Dissertation
submitted to the
Combined Faculties of the Natural Sciences and Mathematics
of the Ruperto-Carola University of Heidelberg, Germany
for the degree of
Doctor of Natural Sciences

Put forward by
Alessio Piucci
Born in: Atessa, Italy
Oral Examination: 16/10/2019

Amplitude analysis of $\mathbf{\Lambda_b^0 \rightarrow \Lambda_c^+ \overline{D}^0 K^-}$ decays and pentaquark searches in the $\mathbf{\Lambda_c^+ \overline{D}^0}$ system at the LHCb experiment

Alessio Piucci

Heidelberg University, Germany

Referees
Prof. Dr. Stephanie Hansmann-Menzemer
Apl. Prof. Dr. Monica Dunford

Abstract

This thesis reports the amplitude analysis of $\Lambda_b^0 \to \Lambda_c^+ \overline{D}^0 K^-$ decays using data collected by the LHCb experiment from proton-proton collisions, corresponding to an integrated luminosity of 9.1 fb^{-1}. A new amplitude fitter has been developed in the context of this analysis, which exploits novel computing concepts and software frameworks.

Numerous models predict large couplings of the pentaquark candidates observed by LHCb [1, 2] to the $\Lambda_c^+ \overline{D}^0$ system. This makes the $\Lambda_b^0 \to \Lambda_c^+ \overline{D}^0 K^-$ channel meaningful to discriminate between models which attempt to describe the internal structure of the pentaquark states.

Amplitude fits are performed to measure the contributions of intermediate resonances to $\Lambda_b^0 \to \Lambda_c^+ \overline{D}^0 K^-$ decays and upper limits are set for the observation of pentaquark states in this channel. The results obtained are in contrast with the expectations from the most popular theory models which describe the pentaquark states as $\Sigma\overline{D}^*$-$\Sigma^*\overline{D}$ molecules.

Kurzfassung

Diese Arbeit berichtet über die Amplitudenanalyse von $\Lambda_b^0 \to \Lambda_c^+ \overline{D}^0 K^-$ Zerfällen unter Verwendung der vom LHCb gesammelten Daten aus Proton-Proton-Kollisionen, die einer integrierten Luminosität von 9.1 fb^{-1} entsprechen. Im Rahmen dieser Analyse wurde ein neuer Amplituden-Fitter entwickelt, der sich neuartige Rechenkonzept und Software-Frameworks zunutze macht.

Zahlreiche Modelle sagen große Kopplungen der von LHCb [1, 2] beobachteten Pentaquark-Kandidaten zum $\Lambda_c^+ \overline{D}^0$ System voraus. Daher ist der $\Lambda_b^0 \to \Lambda_c^+ \overline{D}^0 K^-$ Kanal bedeutsam um zwischen Modellen zu unterscheiden, die versuchen, die interne Struktur der Pentaquark-Zustände zu beschreiben.

Amplitudenfits werden durchgeführt, um die Beiträge von Zwischenresonanzen zu $\Lambda_b^0 \to \Lambda_c^+ \overline{D}^0 K^-$ Zerfällen zu messen. und Obergrenzen für die Beobachtung von Pentaquarkzuständen werden in diesem Kanal gesetzt. Diese Ergebnisse stehen im Gegensatz zu den Erwartungen der weit verbreitesten theoretischen Modelle, die die Pentaquark-Zustände als $\Sigma\overline{D}^*$-$\Sigma^*\overline{D}$-Moleküle beschreiben.

Introduction

The so-called Standard Model of particle physics (SM) describes how particles and fields interact. Three fundamental forces between particles, the *electromagnetic*, *weak* and *strong* interactions, are characterised in the SM and their interaction strength expressed by *coupling constants*. The electromagnetic and weak interactions, described by relatively small couplings, are well studied and consolidated thanks to precise theoretical predictions and experimental results. Instead, the strong interaction between the quarks composing the hadrons is represented by a large coupling value. Large uncertainties affect both the theoretical and experimental aspects of the processes dominated by the strong force. Ultimately, a better characterisation of the strong interaction is of crucial importance for a more complete formulation of the Standard Model.

The difficulty in making predictions of processes involving the strong force makes experimental approaches a key resource for shedding light on the theory models. In this framing, spectroscopy searches hold a particular important role. Among the three fundamental interactions described in the SM, the strong force is the most relevant for forming hadrons. Conventional hadrons are formed by a pair (*mesons*) or by three (*baryons*) quarks, and have been well studied since the second part of the last century. However, the theoretical framework does not forbid quarks to form hadrons made of four (*tetraquarks*) or five (*pentaquarks*) quarks. The first tetraquark candidates have been observed at the beginning of the 21st century. The Belle experiment claimed in 2003 the observation of the $X(3872)$ tetraquark candidate [3], and of the $Z(4430)$ state in 2007 [4]. These states have been later confirmed by the LHCb experiment. On other hands, pentaquarks have a particularly long history of inconclusive experimental searches. A series of claims of observations, since the 1970s to the early 2000s, always revealed to be not statistically significant. Finally, in 2015 the LHCb experiment claimed the observation with striking significance of pentaquark-like candidates in the $\mathrm{J}/\psi\mathrm{p}$ system from $\Lambda_\mathrm{b}^0 \to \mathrm{J}/\psi\mathrm{K}^-\mathrm{p}$ decays [1].

The observation of the pentaquark candidates by LHCb induced a strong interest in the theory community. A large number of models have been developed with the attempt of describing their properties and internal structure, in order to accommodate them into the Quantum ChromoDynamics (QCD) theory framework together with the conventional hadrons. Popular theory models characterise the observed pentaquark candidates as molecular bound systems. Within these models, the pentaquark states are expected to decay to the $\Lambda_\mathrm{c}^+\overline{\mathrm{D}}^{(*)0}$ system with a relatively large decay rate. This makes the channel $\Lambda_\mathrm{b}^0 \to \Lambda_\mathrm{c}^+\overline{\mathrm{D}}^0\mathrm{K}^-$ particularly important for searching for eventual pentaquark candidates.

This thesis reports the amplitude analysis of the $\Lambda_\mathrm{b}^0 \to \Lambda_\mathrm{c}^+\overline{\mathrm{D}}^0\mathrm{K}^-$ decay and the search for eventual pentaquark states, performed using data collected by the LHCb experiment. Amplitude analyses disentangle the decay reaction in *partial waves* [5], corresponding to the partial contributions of the intermediate resonances to the total decay. By performing an amplitude analysis, it is possible to measure both the static properties of the intermediate states, such as mass, width, quantum numbers, and their dynamical behaviour and interference patterns. The LHCb detector is installed on the Large Hadron Collider at the CERN laboratory (Switzerland). It is highly-optimised for studying processes involving hadrons with *beauty* (b) quarks and *charm* (c) quarks, even though it demonstrated to be very versatile. Among the others, high-precision measurements have been performed of rare decays and of processes of electro-weak and heavy-ions physics. Spectroscopy searches in the charm sector, in which this analysis is framed, are also particularly relevant. The full LHCb data set collected during the LHC Run 1 and Run 2 periods is employed in this analysis, corresponding to an integrated luminosity of $9.1\ \mathrm{fb}^{-1}$.

A preliminary analysis [6] of $\Lambda_b^0 \to \Lambda_c^+ \overline{D}^0 K^-$ decays has been performed in the last two years. It observed this channel for the first time, and measured its branching fraction. Major contributions have been made to that measurement: the efficiency evaluation of the data selection, the correction of the data by the efficiency effects, the definition, fetching and preparation of the data samples and of the simulated samples. Also, large contributions have been given to the definition of the analysis workflow, and to the implementation of the strategies of analysis preservation and reproducibility. A dedicated software framework has been implemented for the evaluation and treatment of the selection efficiency. It has been employed by other analyses as well, such as the branching fraction measurement of the $\Lambda_b^0 \to J/\psi \Lambda \phi$ decay, which is currently under internal review of the LHCb experiment. Despite the branching fraction of the $\Lambda_b^0 \to \Lambda_c^+ \overline{D}^0 K^-$ decay has been measured, a full amplitude analysis is required in order to make significant statements about the eventual presence of pentaquark candidates in such decays. In the context of this analysis, a new amplitude fitter has been developed which exploits novel computing paradigms and software libraries such as TensorFlow [7].

This thesis is structured in the following way. A theoretical introduction to the quark model and to the QCD framework is given in Chapter 1. The theoretical interpretation of the observed pentaquark candidates, and the importance of the $\Lambda_b^0 \to \Lambda_c^+ \overline{D}^0 K^-$ channel, are addressed as well. A general description of the LHCb experiment, namely its subdetectors, data-flow and reconstruction strategy, is given in Chapter 2. The outline of the analysis, the relevant statistical concepts and the main software tools used are described in Chapter 3. The selection of the data used by this analysis, and the fits to the Λ_b^0, Λ_c^+ and $\overline{D}^0$ invariant mass distributions are detailed in Chapter 4. The amplitude model used by this analysis is introduced in Chapter 5. The amplitude fit to the data is presented in Chapter 6. Chapter 7 groups the studies performed to verify the stability of the fit results, and to evaluate the systematics uncertainty associated to the analysis results. The assessment of the statistical significance of observation of pentaquark candidates in the $\Lambda_b^0 \to \Lambda_c^+ \overline{D}^0 K^-$ channel is described in Chapter 8. The conclusions of this thesis are summarised in Chapter 9. Supplementary material is given in the Appendix A.

The first part of the doctoral studies has been devoted to the optimisation of a tracking subdetector, the Scintillating Fiber (SciFi) tracker [8], planned to be installed in the upgraded LHCb detector in 2020. Detailed studies with the goal of improving the tracking performances of the SciFi have been realised. Different detector geometries have been implemented in the GEANT [9] simulation framework, and the LHCb reconstruction algorithms have been adapted. The detector layout has been finally optimised in terms of the track reconstruction performances. The studies and their results have been reported in a public note [10].

Contents

Abstract **i**

Introduction **iii**

1 Theoretical background and motivation **1**
1.1 Quantum ChromoDynamics and the quark model 1
1.2 SU(3) and the characterisation of hadrons 6
1.3 Searches for pentaquark states 8
1.4 Theoretical interpretation of the pentaquark candidates observed by LHCb 9
1.5 The role of the $\Lambda_b^0 \to \Lambda_c^+ \overline{D}^0 K^-$ channel 12

2 The LHCb experiment **15**
2.1 Tracking detectors and magnet 16
2.2 Particle identification detectors 20
2.3 LHCb data-flow and reconstruction strategy 22
2.3.1 Online selection of data 22
2.3.2 Reconstruction strategy 23
2.3.3 Offline processing of data 25

3 Analysis outline and tools **27**
3.1 Analysis strategy 27
3.2 Statistical foundations 28
3.2.1 Fundamental concepts 28
3.2.2 Parameter estimation and maximum likelihood 29
3.2.3 *sPlot* technique 31
3.2.4 Hypothesis testing and confidence interval 33
3.2.5 Profile likelihood ratio test 34
3.2.6 Boosted Decision Tree classifiers 36
3.3 Software framework 37
3.3.1 Software for particle identification of final-state tracks 37
3.3.2 Boosted Decision Trees classifiers for selection of charmed hadrons 37
3.3.3 TensorFlow-based framework for amplitude fits 38
3.3.4 Strategies of analysis preservation 39

4 Data selection and mass fits **43**
4.1 Data selection 43
4.1.1 Online selection 43
4.1.2 Selection of the offline processing 45
4.1.3 Final analysis selection 47
4.2 Treatment of multiple signal candidates in the same events 50
4.3 Mass fits to the invariant mass distributions 50
4.3.1 Three-dimensional fits to the Λ_b^0, Λ_c^+, $\overline{D}^0$ invariant mass distributions 50
4.3.2 One-dimensional fits to the Λ_b^0 invariant mass distribution 56

5 Amplitude model **61**
5.1 Helicity frame and coordinate transformations . . . 61
5.2 Matrix elements . . . 64
5.3 K-matrix approach for scattering amplitudes . . . 66
5.4 Coordinate transformations for the $\Lambda_b^0 \to \Lambda_c^+ \overline{D}^0 K^-$ decay channel . . . 70
5.4.1 Coordinate transformations of the $A_i \to \Lambda_c^+ \overline{D}^0$ decay chain . . . 72
5.4.2 Coordinate transformations of the $B_i \to \overline{D}^0 K^-$ decay chain . . . 73
5.4.3 Coordinate transformations of the $C_i \to \Lambda_c^+ K^-$ decay chain . . . 76
5.5 Reduction of the free helicity amplitudes and couplings . . . 77

6 Amplitude fit to data **81**
6.1 Signal *pdf* and extended likelihood . . . 81
6.2 Normalisation samples, Boosted Decision Trees and particle identification efficiencies . 83
6.3 Resonances and amplitude model . . . 84
6.4 Fit fractions and interference terms . . . 92
6.5 Results . . . 92

7 Crosschecks and systematics studies **97**
7.1 Crosschecks of the stability of the fit results . . . 97
7.1.1 Amplitude fit with higher partial waves . . . 97
7.1.2 Amplitude fit without the $\Xi_c^0(2790)$ state . . . 97
7.1.3 Amplitude fit including the $D_{s2}^*(2573)$ state . . . 101
7.1.4 Amplitude fit with a *non-resonant* contribution . . . 101
7.1.5 Amplitude fits with the $\Xi_c^0(2815)$, $\Xi_c^0(2970)$, $\Xi_c^0(3055)$ and $\Xi_c^0(3088)$ states . . . 102
7.1.6 Tighter selection of Λ_c^+ and bachelor K^- candidates . . . 104
7.1.7 K-matrix amplitude with $\overline{D}^0 K^-$ and $D_1^0(2420)K^-$ channels . . . 106
7.1.8 Measurement of eventual Λ_b^0 polarisation . . . 107
7.1.9 Distributions of background data . . . 107
7.1.10 Check of the *s*-weighting procedure . . . 112
7.1.11 Studies on the normalisation samples . . . 113
7.1.12 Fits to LHC Run 1 and Run 2 data sets . . . 116
7.2 Source of systematic uncertainties . . . 117
7.2.1 Size of the normalisation sample . . . 117
7.2.2 Efficiency shapes of the selections based on Boosted Decision Trees classifiers and particle identification . . . 117
7.2.3 Line shape of the $D_{s0}^*(2317)$ state . . . 119
7.2.4 Fit biases . . . 119
7.3 Systematic uncertainties . . . 119

8 Search for pentaquark states **123**
8.1 Expectations from the theory models . . . 123
8.1.1 Amplitude model with pentaquark states . . . 123
8.2 Likelihood ratio test implementation . . . 124
8.3 Hypothesis testing . . . 126
8.4 Extra hidden-charm pentaquarks . . . 133

9 Conclusions **135**

A Appendices **139**
A.1 Data distributions with finer binning . . . 139
A.2 Fit distributions with finer binning . . . 140
A.3 Efficiency maps of the Λ_c^+ and $\overline{D}^0$ selections based on Boosted Decision Trees classifiers 142

A.4 Efficiency maps of the K^- selection based on particle identification 145
A.5 $D_{s1}^*(2700)$ and $D_{s1}^*(2860)$ states parametrised by a sum of Breit-Wigner line shapes 146
A.6 Fit to data with $\Xi_c^0(2970), \Xi_c^0(3055), \Xi_c^0(3080)$ states 148
A.7 Line shape of the $D_{s0}^*(2317)$ state parametrised by a sub-threshold Breit-Wigner distribution 149

References **157**

1 Theoretical background and motivation

One of the most important achievements of modern science is the unification of three of the four known fundamental forces of Nature, the *electromagnetic*, *weak* and *strong* interactions, into the so-called Standard Model (SM) of particle physics. The Standard Model has been formulated in a coherent way starting from the 1960s, and has been able to describe with success most of the interactions at the electroweak and strong nuclear scales of the subatomic particles observed so far. In particular, processes driven by electromagnetic and weak interactions are in general well studied and determined with great precision on both the theoretical and experimental sides.

However, the observation of some processes which are evading the SM predictions make clear that some extensions of the model are required. Some of the key examples include the fact that neutrinos are massive, the existence of dark matter at the level observed in the Universe, and the complexity to incorporate gravity. Nevertheless, some aspects of the Standard Model are not fully determined neither from the theoretical formulation nor from the experimental side. This especially concerns the strong nuclear sector in a wide range of energy regimes. The latter is described by a quantum field theory known as *Quantum ChromoDynamics* (QCD), which is plagued by large modelling uncertainties due to its non-perturbative nature. Moreover, many tests of the electromagnetic and weak interactions rely on studying hadron decays, which are driven by the strong force. Thus, a better understanding of the QCD internal mechanisms is fundamental for a more complete description of the SM, and has an impact on testing theories beyond the Standard Model.

Experimental approaches play a very relevant role in probing the QCD model. Indeed, due to the intrinsic difficulties on formulating precise theory expectations, models are often driven by experimental results. In this sense, a particularly active area in experimental searches is the spectroscopy of hadrons. In recent years a number of resonances resulting from orbital excitation of ground state hadrons have been discovered. Their fitting in the description of strong interaction is extremely valuable for a better comprehension of processes in the non-perturbative regime of QCD.

An introduction to the QCD formulation and to the characterisation of hadrons is given in Sections 1.1-1.2. Section 1.3 introduces the search for exotic hadrons, and in particular for pentaquark states, as experimental probe of the theory. The theoretical interpretation of the pentaquarks observed by LHCb, and the relevance of searches in $\Lambda_\mathrm{b}^0 \to \Lambda_\mathrm{c}^+ \overline{\mathrm{D}}^0 \mathrm{K}^-$ decays, are presented in Sections 1.4-1.5.

1.1 Quantum ChromoDynamics and the quark model

The QCD Lagrangian is based on the Yang-Mills theory [11] of strong interactions, a gauge theory based on the special unitary group $SU(N)$. It was introduced with the aim of describing the behaviour of elementary particles using *non-abelian Lie groups.* These groups are differentiable manifolds with smooth group operations: roughly speaking, a Lie group is a continuous group in which elements are described by several real parameters. The invariance of the Lagrangian under certain Lie groups of *local transformations* [1] characterises a field theory as a gauge theory.

---

[1] A transformation θ is said to be global if it is performed identically at every point of the space ($\theta = const$), in contrast of being local ($\theta = \theta(x)$). The locality represents a stronger constraint.

Let us introduce a set of field operators $\{\phi(x)_{r=1,...,k}\}$ as a k-dimensional vector $\boldsymbol{\phi}(x)$ [2] . The Yang-Mills theory introduces transformations of such field operators, which under $SU(N)$ transform like:

$$\boldsymbol{\phi}(x) \to \tilde{\boldsymbol{\phi}}(x) \equiv U\boldsymbol{\phi}(x) = e^{i\sum_{a=1}^{N^2-1}\theta^a(x)T_a}\boldsymbol{\phi}(x) \tag{1}$$

where N^2-1 stands for the dimensionality of the $SU(N)$ group, and T_a are its generators. The covariant derivative must transforms as the field operators, to assure the Lagrangian to be gauge-invariant under *local* transformations:

$$\mathcal{D}_\mu\boldsymbol{\phi}(x) \to U(\mathcal{D}_\mu\boldsymbol{\phi}(x)) = e^{i\theta^a(x)T_a}\mathcal{D}_\mu\boldsymbol{\phi}(x) \tag{2}$$

where the Einstein notation for summation [12] is used. Equation 2 is fulfilled by a covariant derivative of the form:

$$\mathcal{D}_\mu\boldsymbol{\phi}(x) = [\partial_\mu + igA_\mu^a(x)T_a]\boldsymbol{\phi}(x) \tag{3}$$

with $A_\mu^a(x)$ representing the set of N^2-1 gauge vector fields coupled to $\boldsymbol{\phi}(x)$ by the coupling g. The quanta of the vector fields represent the gauge bosons of the theory. The fields transform like:

$$T^a A_a^\mu(x) \to T^a \tilde{A}_a^\mu(x) \equiv UT^a A_a^\mu(x)U^{-1} + \frac{1}{g_s}(\partial^\mu U)U^{-1} \tag{4}$$

Equation 4 can be explicited by expanding the infinitesimal gauge transformation U:

$$U = e^{-i\theta_a(x)T_a} \simeq 1 - i\theta_a(x)T_a + ... \tag{5}$$

which leads to the following expansion of the gauge field transformations, up to terms linear in $\theta_a(x)$:

$$A_a^\mu(x) \to A_a^\mu(x) - \frac{1}{g_s}\partial^\mu\theta_a(x) + f_{abc}\theta_b(x)A_c^\mu(x) \tag{6}$$

A relation between the gauge fields and the field strength tensor $F_{\mu\nu}^a$ is needed to formulate a locally-gauge invariant Lagrangian. Let us introduce the *structure constants* f_{ab}^c of the group, which are used to explicit the product of two basis vectors in the algebra. This product can be uniquely extended to all the vectors in the vector space, therefore it determines uniquely the product of the algebra. The structure constants define the commutator property of the Lie algebra:

$$[T_a, T_b] = if_{ab}^c T_c \tag{7}$$

which allows to define the commutator between covariant derivatives:

$$[\partial_\mu, \partial_\nu] = -igT_aF_{\mu\nu}^a(x) \tag{8}$$

Following the relations given in Equations 3 and 8, the field strength tensor $F_{\mu\nu}^a(x)$ takes the form:

$$F_{\mu\nu}^a = \partial_\mu A_\nu^a(x) - \partial_\nu A_\mu^a(x) + gf_{bc}^a A_\mu^b(x)A_\nu^c(x) \tag{9}$$

The product of $F_{\mu\nu}^a(x)$ is a gauge-invariant quantity, the *gauge field Lagrangian*:

$$\mathcal{L}_{gf} = -\frac{1}{4}F_a^{\mu\nu}(x)F_{\mu\nu}^a(x) \tag{10}$$

---

[2] This analysis makes use of the bold-italic convention for indicating vector quantities.

Introducing a Dirac field $\phi(x)$ for $\frac{1}{2}$ spin fermions, the Lagrangian is expressed as sum of the gauge field Lagrangian $\mathcal{L}_{gf}$ and of the Lagrangian $\mathcal{L}_0(x)$ for a free Dirac fermion:

$$\begin{aligned} \mathcal{L}(x) &= \mathcal{L}_{gf}(x) + \mathcal{L}_0(x) \\ &= \mathcal{L}_{gf}(x) + \overline{\phi}(x)(i\not{\mathcal{D}} - m)\phi(x) \end{aligned} \tag{11}$$

with $\not{\mathcal{D}} = \gamma^\mu \mathcal{D}_\mu$ being the gauge covariant derivative, $\overline{\phi}(x) = \phi^\dagger(x)\gamma^0$, and m being the mass of the fermion.

The above derivation of a Yang-Mills theory is valid for any $SU(N)$ gauge group. QCD is based on a $SU(3)$ colour charge group described by a Yang-Mills theory. The number of colors has been determined to be three by a series of empirical evidences. Among all, the comparison between predictions and experimental results of the $\pi^0 \to \gamma\gamma$ decay and of the $e^- e^+$ annihilation to hadrons represented striking indications in this direction. To take into account the existence of anticolour, the QCD formulation needs to have irreducible complex representations in addition to the irreducible real ones. The only gauge group with three irreducible real and complex representations, which is also a *compact* and *semi-simple* Lie group results to be $SU(3)$. The compactness of the group refers to its compact topology. This means that it must be closed (i.e. it contains all its limit points) and bounded (all its points lie within a fixed distance of each other). The semi-simplicity implies that any finite-dimensional representation of the group has to be a direct sum of simple, thus irreducible, representations. The local gauge transformations of the $SU(3)$ colour charge group are introduced as:

$$U = e^{-i\theta_a(x)\frac{\lambda_a}{2}} \tag{12}$$

where $\theta_a(x)$ is a real function, $a = 1, 2, ..., 8$ is the index of the eight gauge fields ($3^2 - 1 = 8$ is the group dimensionality) and λ_a are the Gell-Mann matrices [13]. The latter define the $SU(3)$ generator $T_a = \frac{\lambda_a}{2}$. By denoting the gluon field (represented by A in the former Yang-Mills derivation) with G, the covariant derivative takes the form:

$$\mathcal{D}_\mu = \partial_\mu - i g_s G_\mu(x) \tag{13}$$

with g_s being the strong gauge coupling, proportional to a coupling strength α_s of the strong interaction. With the help of Equation 13, the free Lagrangian for quarks reads:

$$\begin{aligned} \mathcal{L}_0 &= \overline{q}_f(i\not{\mathcal{D}} - m_f)q_f \\ &= \overline{q}_f(i\not{\partial} - m_f)q_f + g_s\overline{q}_f\not{G}(x)q_f \\ &= \overline{q}_f(i\not{\partial} - m_f)q_f + g_s\overline{q}_f\not{G}^a(x)\frac{\lambda_a}{2}q_f \end{aligned} \tag{14}$$

with q_f being a quark field (corresponding to the field operator $\phi(x)$), and m_f the quark masses generated by the Higgs mechanism. In the last term of Equation 14, the gluon field has been developed in terms of the Gell-Mann matrices. Using the definition from Equation 9, the gluonic strength tensor is given by:

$$F^a_{\mu\nu} = \partial_\mu G^a_\nu(x) - \partial_\nu G^a_\mu(x) + g_s f^a_{bc} G^b_\mu(x) G^c_\nu(x) \tag{15}$$

Finally, following Equation 11 the Equations 14-15 bring to the QCD Lagrangian:

$$\begin{aligned} \mathcal{L}_{QCD}(x) = &-\frac{1}{4}(\partial_\mu G^a_\nu(x) - \partial_\nu G^a_\mu(x))(\partial^\mu G^\nu_a(x) - \partial^\nu G^\mu_a(x)) + \overline{q}^\alpha_f(i\not{\partial} - m_f)q^\alpha_f \\ &+ g_s\overline{q}^\alpha_f\not{G}^a(x)(\frac{\lambda_a}{2})_{\alpha\beta}q^\beta_f \\ &+ \frac{g_s}{2}f^{bc}_a(\partial_\mu G^a_\nu(x) - \partial_\nu G^a_\nu(x))G^\mu_b(x)G^\nu_c(x) \\ &- \frac{g_s^2}{4}f^{abe}f_{cde}G^\mu_a(x)G^\nu_b(x)G^c_\mu(x)G^d_\nu(x) \end{aligned} \tag{16}$$

with α, β being the colour indices. Factors $\sim m^2 G_a^\mu G_\mu^a$ are not appearing since they would violate gauge invariance (Eq. 4), thus gluons result to be massless. In Equation 16 the first line makes explicit the kinetic terms of the quark and gluon fields, the second the colour interaction between quark and gluons, the third and fourth describe the self-interaction of third- and fourth-order of gluons, respectively. It must be noted that the gluon self-interactions arise from the Lie commutator relation (Eq. 8) even in absence of other fields.

The gluon self-interaction described by this formulation is of key importance to generate the two main properties which characterise the QCD: the *asymptotic freedom* at high energy (i.e. small distance), and the *colour confinement* at low energy (i.e. large distance). The first implies that the quark interaction gets weaker at high energy, allowing for perturbative calculations. This behaviour corresponds to a small coupling of the strong interaction. Instead, the colour confinement describes the experimental evidence that particles with colour charge cannot be isolated or directly observed at low energy scales.

In the regime of asymptotic freedom, the quantum field theory technique of *perturbation theory* can be used to make precise predictions on processes involving the strong interaction. Within the perturbative approach, a set of approximations (from the leading to the higher orders) are added as perturbations to a simple quantum system for which the mathematical solutions are known. If the perturbations are relatively small, they can be calculated used approximated methods. This allows the description of a complex system in terms of a simpler one. Perturbative QCD is nowadays well consolidated, and has been experimentally verified at percent-level. On the other hand, at low energy regime the coupling of the strong force is large and perturbative methods cannot be applied. Non-perturbative QCD calculations are extremely challenging on both the formal and computational sides. Lattice QCD [14] computations are among the most popular and successful approaches to non-perturbative QCD problems. Huge efforts have been spent to formulate a unified, analytical solution valid for both the low- and high-energy ranges of QCD. On the other hand, phenomenological-based models exist which describe relatively precisely the experimental observations. An overview of these models is presented in Section 1.2.

The dependence of the QCD coupling strength α_s on the energy can be formalised as function to a renormalisation scale μ^2, needed for applying perturbative techniques. The measurement of this dependence is shown in Figure 1 [15]. Below the *QCD scale* (or *Landau pole*) $\mu^2 = \Lambda^2_{QCD} \sim 300 - 1000$ MeV [16], QCD becomes a strongly-coupled gauge theory and the perturbative expansion diverges: thus, a perturbative treatment of QCD at low energy is highly challenging and not yet fully successful. Quarks with mass above Λ_{QCD} are usually referred to as heavy quarks, in contrast to the light quarks with mass below this value. Nevertheless, their masses cannot be measured directly because of quark confinement into hadrons, and must often rely to perturbative approaches. Table 1 lists the quark properties [17,18], such as their *bare masses* [3] , the third component of the isospin I_3, the strangeness S, charmness C, bottomness B and topness T. QCD conserves the flavour quantum number, thus hadrons can be referenced to their minimum valence quark content. However, massless virtual gluons compose the numerical majority of particles inside hadrons. Also, the strong force binding energy between quarks composing the hadrons is large enough to create pairs of virtual quarks and antiquarks which continuously appear and annihilate in the hadrons.

---

[3] The bare mass of an elementary particle is evaluated in the limit of infinite energy (i.e. zero distance). It differs from the *invariant mass* because the latter includes the “clothing” of the particle by pairs of virtual particles that are temporarily created by the surrounding force-fields.

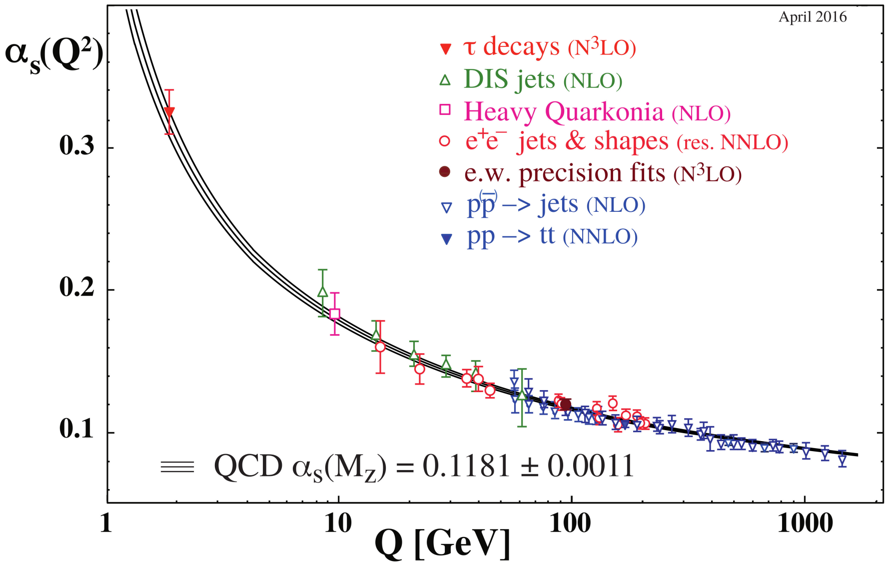

Figure 1: Measurements of the coupling strength α_s as a function of the energy scale $\mu = Q$ [15]. The respective degree of QCD perturbation theory used in the extraction of α_s is indicated in brackets (NLO: next-to-leading order; NNLO: next-to-next-to-leading order; res. NNLO: NNLO matched with resummed next-to-leading logs; N3LO: next-to-NNLO).

Quark	Mass [MeV/c^2]	electric charge [e]	I_3	S	C	B	T
u (up)	$2.2^{+0.6}_{-0.4}$	$+\frac{2}{3}$	$+\frac{1}{2}$	/	/	/	/
d (down)	$4.7^{+0.5}_{-0.4}$	$-\frac{1}{3}$	$-\frac{1}{2}$	/	/	/	/
c (charm)	1280 ± 30	$+\frac{2}{3}$	/	/	+1	/	/
s (strange)	96^{+8}_{-4}	$-\frac{1}{3}$	/	-1	/	/	/
t (top)	173100 ± 600	$+\frac{2}{3}$	/	/	/	+1	/
b (bottom)	4180^{+40}_{-30}	$-\frac{1}{3}$	/	/	/	/	-1

Table 1: Quark properties and quantum numbers [17, 18].

1.2 SU(3) and the characterisation of hadrons

Hadrons have been historically grouped into multiplets of particles with same flavour numbers and approximately same mass, relying on the quark fields to be (approximately) flavour-symmetric [4] . The flavour group $SU(3)$ of u, d and s quarks has two fundamental representations: the $\mathbf{3}$ representation of quarks and its complex conjugate $\overline{\mathbf{3}}$ for the antiquarks. These representations can be sketched in a picturesque way in the $Y - I_3$ plane (Fig. 2). Here $Y = 2(Q - S)$ is the *strong hypercharge*, with Q being the electric charge of the quark and S its strangeness, and I_3 is the third component of the isospin.

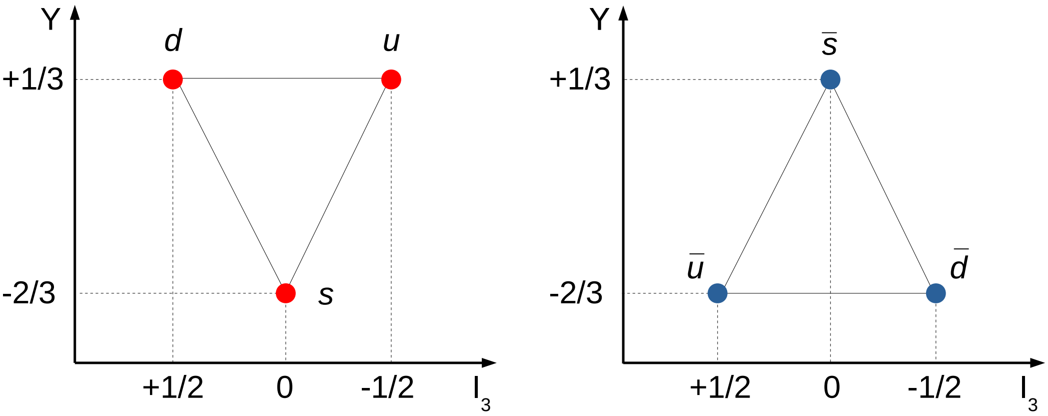

Figure 2: Weight diagrams for the quarks $\mathbf{3}$ (left) and antiquarks $\overline{\mathbf{3}}$ (right) representations of the flavour group $SU(3)$.

Combining pairs of quark and antiquarks ($q\overline{q}$), a nonet of states is formed. These bound states are called *mesons*. The nonet can be decomposed into the trivial $\mathbf{1}$ and the adjoint $\mathbf{8}$ representations:

$$\mathbf{3} \otimes \overline{\mathbf{3}} = \mathbf{8} \oplus \mathbf{1} \tag{17}$$

An example of this decomposition is given in Figure 3, forming the nonet of pseudoscalars mesons with spin 0 and nonet of mesons with spin 1. In the limit of the quark fields to be exactly-flavour symmetric, neglecting the electroweak interactions between quarks, all elements of the nonet would have the same mass. However, symmetry breaking considerations generate different masses for the quarks, and allows for the possibility of mixing between different multiplets.

Let us now consider states composed by three quarks (qqq), referred to as *baryons*. Since quarks are fermions, the spin-statistics theorem [20, 21] implies that the wave function of baryons must be anti-symmetric under exchange of two quarks [5] . This condition can be fulfilled by anti-symmetrising the wave function in colour, and making it symmetric in combination of flavour, spin and space. The anti-symmetry of the colour wave-function is a consequence of the fact that all observable particles are a color singlet (i.e. colour-less), due to the colour confinement in QCD (Sec. 1.1). This also requires baryons to be formed by three quarks: any mixed combination of quarks and antiquarks would not result in a color singlet. The decomposition in flavour for qqq states takes the form of:

$$\begin{aligned} \mathbf{3} \otimes \mathbf{3} \otimes \mathbf{3} &= (\mathbf{6}_S \oplus \overline{\mathbf{3}}_A) \otimes \mathbf{3} \\ &= \mathbf{10}_S \oplus \mathbf{8}_M \oplus \mathbf{8}_M \oplus \mathbf{1}_A \end{aligned} \tag{18}$$

---

[4] In the electroweak interaction the flavour symmetry is broken and flavour-changing processes exist, such as quark flavour mixing and neutrino oscillation.

[5] The spin-statistics theorem applies to *indistinguishable* particles. Mesons are always constituted by distinguishable particles (a quark and an antiquark pair), thus there is no symmetry requirement on their wave functions.

where the indices S, A and M indicate multiplets which are respectively fully symmetric, fully anti-symmetric or with mixed symmetry with respect to flavour. The fully-symmetric decuplet is constituted by states with flavour wave functions of the form:

$$\begin{aligned} \psi &= uuu; \\ \psi &= \frac{uud + udu + duu}{\sqrt{3}} \end{aligned} \tag{19}$$

while the two mixed-symmetric octets are defined by flavour wave functions which are anti-symmetric for exchange of a pair quarks:

$$\begin{aligned} \psi &= \frac{(ud - du)u}{\sqrt{2}} \quad \text{anti-symmetric for 1-2 exchange ;} \\ \psi &= \frac{u(ud - du)}{\sqrt{2}} \quad \text{anti-symmetric for 2-3 exchange} \end{aligned} \tag{20}$$

A third octet can be derived, but is not independent from the previous ones. Finally the flavour singlet is a completely anti-symmetric state represented by:

$$\psi = \frac{uds - usd + dsu - dus + sud - sdu}{\sqrt{6}} \tag{21}$$

The decuplet of baryons with spin $\frac{3}{2}$ and the octet of ground state baryons with spin $\frac{1}{2}$ are shown in Figure 4.

With similar arguments, flavour symmetry can be extended to all quark flavours and the ground states follow the qualitative expectations from the quark model. The top flavour is an exception, since its heavy mass results in a lifetime too short for forming hadrons.

The non-perturbative nature of QCD makes difficult to formulate precise theoretical calculations of nuclear physics phenomena. Thus, experimental hadron spectroscopy plays an important role in hadron physics to shed light on the internal mechanisms which lead to the formation of hadrons. Starting from the ground states, a large number of bound states can be build from radial excitation. The spectra of the charmonium system [22] and of mesons composed of heavy quarks [23] are especially rich. Many of these states have been only recently observed, and the experimental searches are very active in this direction. Similarly, the formation of non-conventional states made of four or five quarks is not forbidden by the quark model. They eluded the experimental observation for decades until recent years [24], and their study is now of primary importance in hadron physics.

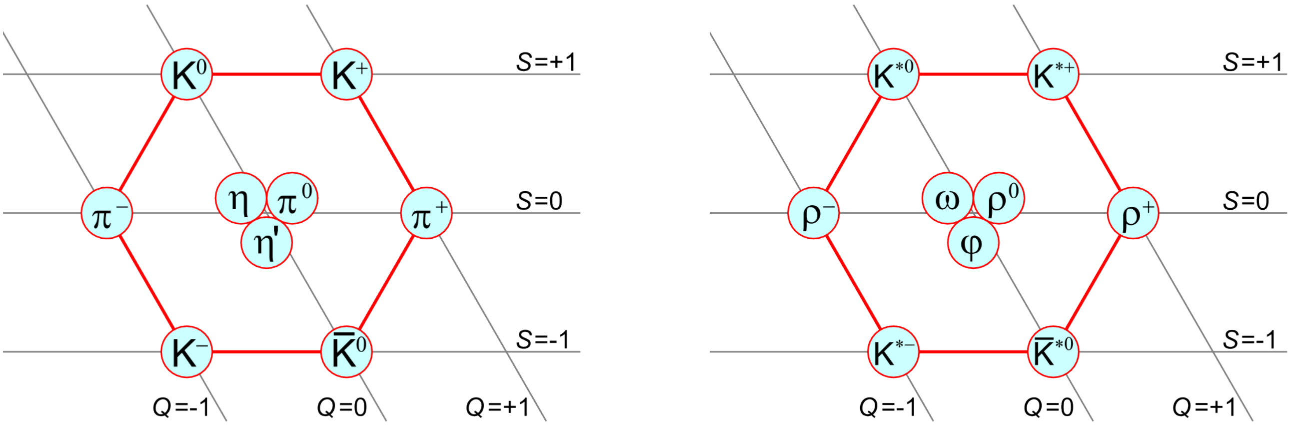

(a) (b)

Figure 3: a) Nonet of pseudoscalar mesons with spin 0. b) Nonet of mesons with spin 1 [19].

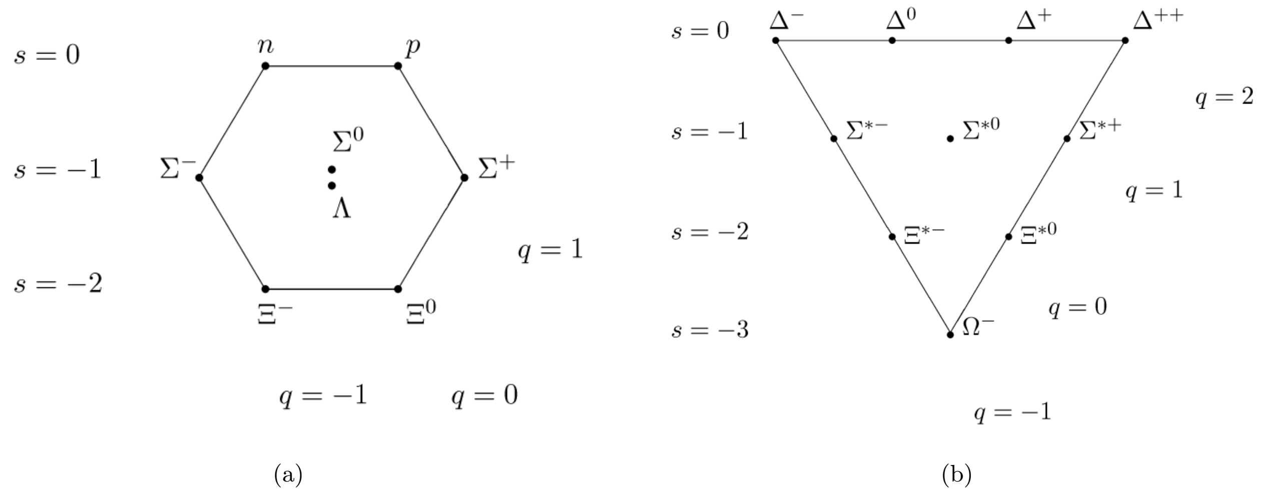

Figure 4: a) Octet of ground state baryons with spin $\frac{1}{2}$. b) Decuplet of baryons with spin $\frac{3}{2}$ [19].

1.3 Searches for pentaquark states

Experimental search for hadrons constituted by more than three valence quarks, called *exotic hadrons*, has been a very active field since the first formulation of the quark model in the 1960s. Especially the existence of pentaquark states $qqqq\bar{q}$ has been predicted since decades, but was always elusive to observe. In the late 1980s, experiments of kaon-nucleon scattering suggested the observation of a series of pentaquark candidates matching the predictions of the so-called Z^+ and Z^0 states. However, their observation revealed to be not significant. In 1997 the existence of a new pentaquark candidate, the Θ^+ with $uudd\bar{s}$ quark content, was predicted by a *chiral quark soliton* model [25]. Within this formulation, light quark masses are considered massless (chiral limit). Baryons are introduced, starting from a description of meson-meson scattering, as soliton solutions to the equations of motion. These are solutions which correspond to a configuration of the meson fields that cannot be expanded in a power series around unity [26]. The model was able to perform striking predictions of the small widths of the baryon antidecuplet states in line with the experimental findings, and it gained in popularity. Basing on these considerations, many experiments focused their searches on the Θ^+. In 2003 the SPring-8 laboratory (Japan) reported its first potential observation [27, 28] of the Θ^+ state in photon-C_{12} scattering. The result was soon followed by similar findings by the CLAS Collaboration at the Jefferson Lab (US) [29], the DIANA experiment at the ITEP laboratory (Russia) [30], the SAPHIR experiment at the ELSA laboratory (Germany) [31]. However, a subsequent re-analyses of the data led to less confidence in the observation of the Θ^+. To resolve this issue, dedicated experiments were set up to perform precise measurements of the pentaquark candidate. Finally, in 2005 a group from the INFN laboratories (Italy), studying the same reaction as the ELSA experiment but with much larger data sample, found no evidence of the Θ^+. Many other experiments later confirmed the non-existence of the Θ^+.

Since then, although searches actively continued, pentaquarks have been considered with scepticism. A turning point finally happened in 2015, with the claim by the LHCb Collaboration of the observation of two pentaquark candidates in the $\mathrm{J}/\psi\mathrm{p}$ system in $\Lambda_\mathrm{b}^0 \to \mathrm{J}/\psi\mathrm{K}^-\mathrm{p}$ decays [1]. A six-dimensional amplitude analysis has been performed to LHC Run 1 data, and the fit with only ordinary known states was not satisfactory. This implied the necessity of including two new states referred to as $P_c(4380)^+$ and $P_c(4450)^+$, with quark content $uudc\bar{c}$. Mass projections of the $\mathrm{J}/\psi\mathrm{p}$ and pK^- systems are shown in Figure 5, with the fit model overimposed. Table 2 lists the measured properties of the two pentaquark states, with the preferred assignments of spin and parity J^P.

A model-independent analysis of the same decay channel was performed by LHCb in 2016 [32], supporting the need for at least one exotic component consistent with the $P_c(4450)^+$ state. This

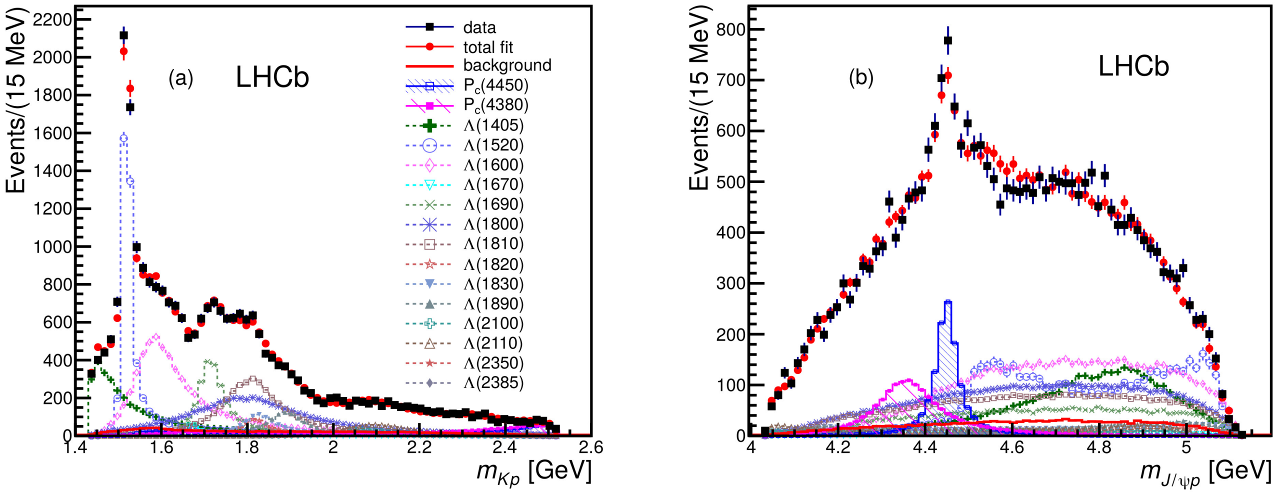

Figure 5: Invariant mass projections of the pK^- (left) and $J/\psi p$ (right) systems from the observation of pentaquark candidates by the LHCb experiment in 2015, using LHC Run 1 data [1]. The fit model (red points) is overimposed.

State	Mass [MeV/c^2]	Width [MeV/c^2]	J^P
$P_c(4380)^+$	4380 ± 8 ± 29	205 ± 18 ± 86	$\frac{3}{2}^{-1}$
$P_c(4450)^+$	4449.8 ± 1.7 ± 2.5	39 ± 5 ± 19	$\frac{5}{2}^{+1}$

Table 2: Measured properties of the pentaquark candidates observed by the LHCb experiment in 2015, using LHC Run 1 data [1]. The assignment of spin and parity J^P of the states is not univocal, and the values reported are the preferred by the measurement.

model-independent approach has not been able to confirm the $P_c(4380)^+$ state because of its large width, though. The $\Lambda_b^0 \to J/\psi\pi^-p$ channel [33], the Cabibbo-suppressed partner of the $\Lambda_b^0 \to J/\psi K^-p$ decay, has been also studied by LHCb. The analysis has not been able to disentangle the two pentaquark states, but exotic contributions were needed to describe the data.

In 2019 the channel $\Lambda_b^0 \to J/\psi K^-p$ [2] has been re-analysed by LHCb, including data collected in the LHC Run 2. An improved selection of the data increased the statistics of observed decays by an order of magnitude with respect to the original analysis. Although a simpler 1-dimensional mass fit has been performed in this analysis, rather than a full amplitude analysis of the process, a new narrow state $P_c(4312)^+$ has been observed. Its measured production rate is too small for having a chance to observe it in the first analysis. The new analysis provided a significant evidence for the $P_c(4450)^+$ to be structured by two components, called $P_c(4440)^+$ and $P_c(4457)^+$. However, this analysis approach has not been able to probe the evidence for a broad state such as the $P_c(4380)^+$. Also, the J^P assignments of the states are ambiguous, and an amplitude analysis would be required to measure them. The measured properties of the pentaquark candidates by this new analysis are reported in Table 3. The listed J^P assignments are desumed from models those predictions reasonably match the properties of the observed candidates.

1.4 Theoretical interpretation of the pentaquark candidates observed by LHCb

The observation of the $P_c(4380)^+$ and $P_c(4450^+$ pentaquark candidates by LHCb arised vivid discussion, especially concerning the nature of their internal structure. Their description would be valuable for a better comprehension of hadrons formation, and ultimately for the description of QCD processes.

Formulations consider the pentaquark states as diquark-diquark-quark [34, 35] or diquark-triquark [36] molecules. Alternative models refer to them as *baryocharmonia* [37], where the pentaquarks are

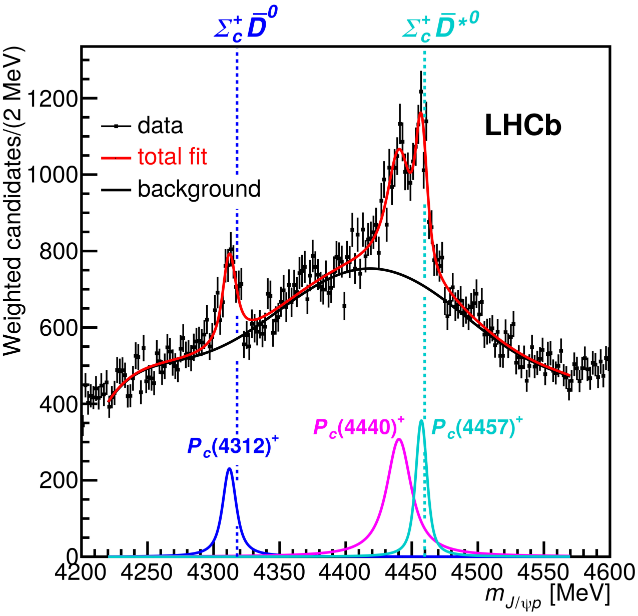

Figure 6: Fit to the invariant mass distribution of the J/ψp system from the re-analysis of the $\Lambda_b^0 \to J/\psi K^- p$ by the LHCb experiment in 2019, using LHC Run 1 and Run 2 data [2].

State	Mass [MeV/c^2]	Width [MeV/c^2]	J^P
$P_c(4312)^+$	4312.0 ± 1.0	< 13.7 (CL = 95%)	$(\frac{1}{2}^-)$
$P_c(4440)^+$	4450.5 ± 2.3	< 69 (CL = 95%)	/
$P_c(4457)^+$	4457.3 ± 3.2	< 13.2 (CL = 95%)	$(\frac{1}{2}^-, \frac{3}{2}^-)$

Table 3: Measured properties of the pentaquark states observed by the LHCb experiment in 2019, using LHC Run 1 and Run 2 data [2]. The assignments of spin and parity J^P are desumed from theory predictions, but not directly measured.

composites of J/ψ and excited nucleon states such as the $N(1440)$ and the $N(1520)$. Other works suggest that the P_c states could be originated from kinematic effects [38] like reflections or anomalous triangle singularities, rather than being real resonances. Particularly popular are models which describe the P_cs as molecular-hidden-charm states [39]. In this picture, the pentaquarks are composed by loosely bound states of charmed and anticharmed hadrons such as $\Sigma_c^*(2520)\overline{D}$, $\Sigma_c(2455)\overline{D}^*$ in non-relativistic regime. Within this class of models, the pentaquark molecules would preferably decay into $\Lambda_c^+\overline{D}^0$ and $\Lambda_c^+\overline{D}^*$, as sketched in Figure 7. In particular, the $P_c(4380)^+$ and $P_c(4450)^+$ decay rates to these channels is expected to be enhanced by factors 5-20 with respect to the first-observation channel $\Lambda_b^0 \to J/\psi K^- p$, as shown in Table 4.

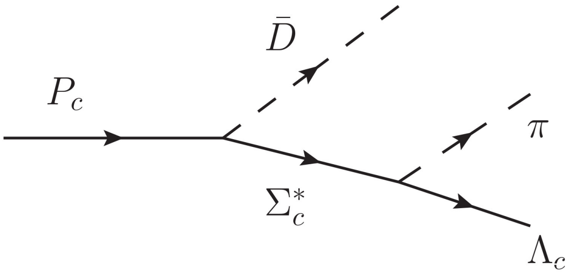

Figure 7: Three-body decay of a P_c state in the $\Sigma_c^*(2520)\overline{D}$ molecular hypothesis [39].

Mode	Widths [MeV/c^2]			
	$P_c(4380)^+$		$P_c(4450)^+$	
	$\overline{\mathrm{D}}\Sigma_c^*(\frac{3}{2}^-)$	$\overline{\mathrm{D}}^*\Sigma_c(\frac{3}{2}^-)$	$\overline{\mathrm{D}}^*\Sigma_c(\frac{3}{2}^-)$	$\overline{\mathrm{D}}^*\Sigma_c(\frac{5}{2}^+)$
$\overline{\mathrm{D}}^*\Lambda_\mathrm{c}^+$	131.3	41.6	80.5	22.6
$\mathrm{J}/\psi\mathrm{p}$	3.8	8.4	8.3	2.0
$\overline{\mathrm{D}}^0\Lambda_\mathrm{c}^+$	1.2	17	41.4	18.8

Table 4: Partial widths of the $P_c(4380)^+$ and $P_c(4450)^+$ states to $\overline{\mathrm{D}}^*\Lambda_\mathrm{c}^+$, $\mathrm{J}/\psi\mathrm{p}$ and $\overline{\mathrm{D}}^0\Lambda_\mathrm{c}^+$ decays, under the hypotheses of being $\Sigma_\mathrm{c}^*(2520)\overline{\mathrm{D}}$ or $\Sigma_\mathrm{c}(2455)\overline{\mathrm{D}}^*$ molecules [39].

J^P	A			B		
	z_R[MeV/c^2]	Couplings $[10^{-3}(\mathrm{MeV}/c^2)^{-\frac{1}{2}}]$		z_R[MeV/c^2]	Couplings $[10^{-3}(\mathrm{MeV}/c^2)^{-\frac{1}{2}}]$	
		$g_{\bar{\mathrm{D}}\Lambda_\mathrm{c}^+}$	$g_{\bar{\mathrm{D}}\Sigma_c}$		$g_{\bar{\mathrm{D}}\Lambda_\mathrm{c}^+}$	$g_{\bar{\mathrm{D}}\Sigma_c}$
$\frac{1}{2}^-$	4295 - i 3.7	1.4 + i 0.2	13.2 + i 0.8	4297 - i 3.0	1.1 + i 0.2	10.9 + i 0.6
$\frac{1}{2}^+$	4334 - i 28	1.1 - i 1.1	-1.9 + i 3.6	4334 - i 30	1.0 - i 1.0	-1.9 + i 3.7
$\frac{3}{2}^+$	4325 - i 54	0.3 - i 1.1	0.8 - i 4.5	425 - i 54	0.3 - i 1.0	0.7 - i 4.6
$\frac{3}{2}^-$	4380 - i 147	0.5 - i 1.9	-1.4 + i 5.6	4378 - i 146	0.5 - i 1.7	-1.3 + i 5.6

Table 5: Pole positions z_R, couplings and spin-parity assignments for the states in the hidden-charm sector with $I = \frac{1}{2}$ [40]. The parameters of the poles refer to two sets of cut-offs A and B used in the model. The properties of the last pole match reasonably well with the $P_c(4380)^+$ candidates observed by LHCb in [1].

Models, while attempting to describe the nature of the observed candidates, also predicts possible pentaquark partners. In particular, a *dynamical coupled-channel* approach [40, 41] concludes that additional hidden-charm states at the ~ 4.3 GeV/c^2 could possibly exist. Their predicted properties are listed in Table 5. In the coupled channel approximation, the interaction potential is constructed by a *finite* sum [6] of contributions from different reactions and partial waves. Within this approximation, pentaquark states emerge naturally from the dynamic of the interaction itself (they are *dynamically generated*). Also, the predicted properties of a pole (Tab. 5) match reasonably well the observation of the $P_c(4380)^+$ state by LHCb.

As already mentioned, the re-analysis of the $\Lambda_\mathrm{b}^0 \to \mathrm{J}/\psi\mathrm{K}^-\mathrm{p}$ channel with much higher statistics changed the scenery. The new state $P_c(4312)^+$ has been observed and a double-peak structure of the previously-claimed $P_c(4450)^+$ state has been determined, originating the $P_c(4440)^+$ and $P_c(4457)^+$ states. The $P_c(4380)^+$ has not been confirmed, due to the simpler analysis technique. A variety of theoretical works precedent the first analysis of 2015 have been predicting the possibility of $\Sigma_\mathrm{c}\overline{\mathrm{D}}$ molecular bound states to exist in correspondence to the new observed states. Therefore, they have not been distracted by the evidence of the first $P_c(4380)^+$ and $P_c(4450)^+$ states.

In one of the first investigations [42, 43], an interaction potential between (anti-)charmed baryons and mesons is introduced, and described by exchange of vector mesons (ρ, ω, ϕ). Within this framing, a $\Sigma_\mathrm{c}\overline{\mathrm{D}}$ bound state arises at ~ 4261 MeV/c^2, well below the observed $P_c(4312)^+$. Also, a $\Sigma_\mathrm{c}\overline{\mathrm{D}}^*$ bound state is predicted at a mass ~ 4416 MeV/c^2, again quite low with respect the $P_c(4440)^+$ and $P_c(4457)^+$ measured masses.

In a more sophisticated model [44], the quark-level forces are implemented via the extended chiral $SU(3)$ constituent quark model. In a simple chiral (i.e. in the limit of massless quarks) $SU(3)$ quark model, only the pseudo-scalar and scalar chiral fields are considered. It is *extended* by including vector meson exchanges, to describe short range interactions [45]. In this formulation, nucleon resonances can be described as baryon-meson resonances generated from the dynamic of the interaction [46, 47]. This

---

[6] In general, the exact solution of the interaction potential cannot be written as a finite sum of contributions.

model allows for an attractive $\Sigma_c\overline{D}$ interaction, forming a state in the 4310-4316 MeV/c^2 mass region. The pentaquark resonance predicted by this model would have the possibility of decaying to the $J/\psi p$ system, and it would fit reasonably well to the observed $P_c(4312)^+$.

Other models introduce a baryon-meson interaction by a *one-boson-exchange potential*. Such a formalism is an extension of the more traditional meson exchange models in nuclear force [48]. An effective boson-exchange potential is first defined in the coordinate or momentum space. Then the scattering problem of two hadrons and the bound state problem are solved. From the obtained binding energy, the resonance properties can be extracted. In this particular one-boson-exchange model [49], $\Sigma_c\overline{D}$ and $\Sigma_c\overline{D}^*$ interactions are described by exchange of light mesons $(\pi, \eta, \rho, \omega, \sigma)$. In this construction, a $\Sigma_c\overline{D}$ bound state is predicted at around the mass of the $P_c(4312)^+$ state. Also, a $\Sigma_c\overline{D}^*$ bound state would be compatible with the $P_c(4457)^+$ candidate, and the same system could potentially be responsible for the $P_c(4440)^+$ state as well.

Analogously, employing coupled-channels models and introducing potentials mediated by exchange of only vector mesons, bound states compatible with the $P_c(4312)^+$ and the $P_c(4457)^+$ are foreseen [50].

1.5 The role of the $\Lambda_b^0 \to \Lambda_c^+\overline{D}^0K^-$ channel

As mentioned in Section 1.4, in the hypotheses of the $P_c(4380)^+$ and $P_c(4450)^+$ being $\Sigma_c^*\overline{D}$, $\Sigma_c\overline{D}^*$ molecular bound states, a large decay rate is predicted to the $\Lambda_c^+\overline{D}^0$ system. This makes the study of the $\Lambda_b^0 \to \Lambda_c^+\overline{D}^0K^-$ decay of crucial importance for discriminating between the different proposed models which attempt to describe the nature of the pentaquark states. Either the observation of the pentaquark states in this channel, or limits put to their decays to $\Lambda_c^+\overline{D}^0$, would be of primary relevance. Moreover, the observation of the pentaquark candidates in different processes, in addition to the $\Lambda_b^0 \to J/\psi K^-p$ decay, would be particularly meaningful. An estimation of the expected yields for the $P_c(4380)^+$ and $P_c(4450)^+$ states to the $\Lambda_b^0 \to \Lambda_c^+\overline{D}^0K^-$, based on the $\Sigma_c^*\overline{D}$-$\Sigma_c\overline{D}^*$ molecular model [39] as in Table 4, is presented in Section 8.1.

Unfortunately, the observation of the $P_c(4312)^+$, $P_c(4440)^+$ and $P_c(4457)^+$ states is too recent for having precise theoretical predictions of their decay rates to the $\overline{D}^0\Lambda_c^+$ system. Nevertheless, the expected decay rates of the $P_c(4380)^+$ and $P_c(4450)^+$ states to $\overline{D}^0\Lambda_c^+$, as presented in Table 4, are based from couplings which are either deduced from experimental data of the decay widths of D^*, Σ_c, and Σ_c^*, or are relatively model-independent [51–54].

Nevertheless, a variety of theory predictions are being formulated in very recent time, which again highlight the role of the $\Lambda_b^0 \to \Lambda_c^+\overline{D}^0K^-$ channel in establishing the nature of the newly-observed pentaquark candidates. Large decay couplings of these states to the $\Lambda_c^+\overline{D}^0$ system are predicted for the $\Sigma_c\overline{D}^{(*)}$ molecular model in [55]. An effective range expansion of the dynamics around the $\Sigma_c\overline{D}^{(*)}$ threshold is considered, assuming a short-ranged scattering potential between the Σ_c and $\overline{D}$ particles. Similarly, large couplings are expected by [56] which makes use of an extended chromomagnetic model. Within this approach [57], only the hyperfine interaction between quarks is retained, and the Coulombic short-ranged and linear long-ranged potentials are described by a constant. Alternative models, as the hadrocharmonium hypothesis [58] of the pentaquarks being bound states of a nucleon and a charm meson, also expect the P_cs to be relatively highly-coupled to the $\Lambda_c^+\overline{D}^0$ system. At the time of this analysis only couplings have been predicted, which are not enough for a direct comparison with the observation channel $\Lambda_b^0 \to J/\psi K^-p$. Indeed, non-trivial factors enter in the calculation of the expected decay rates, such as phase-space terms which are channel-dependent.

On other hands, a very recent modelisation [59] of the interaction of the $\Sigma_c^{(*)}\overline{D}^{(*)}$ channels resulted in considerably different predictions. In this work, it is observed that the largest uncertainties on the different predictions are originated from the subtraction constants needed to regularise the loops involved in the calculations. By tuning these constants to the most recent data taken by LHCb, considerably smaller couplings of the pentaquark decays to the $\Lambda_c^+\overline{D}^0$ system are predicted, with respect to the above-cited models. Following this model, the confidence in observing pentaquark candidates in $\Lambda_b^0 \to \Lambda_c^+\overline{D}^0K^-$ decays is rather little.

The above considerations make clear the potential of the $\Lambda_b^0 \to \Lambda_c^+ \overline{D}^0 K^-$ channel in discriminating between different models which attempt to describe the nature of the observed pentaquark candidates. Either an observation of P_c candidates, or stringent limits to their decays, would represent a valuable input for theory models. Finally, the $\Lambda_b^0 \to \Lambda_c^+ \overline{D}^0 K^-$ channel is also interesting to test for the existence of possible pentaquark partners of further hidden-charm states [40], as presented in Table 5.

2 The LHCb experiment

The LHCb detector is a single-arm forward spectrometer that covers a pseudo-rapidity [7] range of $2 < \eta < 5$. It is installed on the Large Hadron Collider (LHC) at the CERN laboratory (Switzerland), a circular collider of 27 km circumference which accelerates and collides pp, Pb Pb or p Pb beams. The LHC accelerates two pp beams from a center-of-mass energy of 450 GeV up to 13 TeV, or heavy ion beams from 350 GeV to an energy of 5 TeV. The beams are pre-accelerated by a system of linear (LINACs) and circular (PS, SPS) accelerators, and injected to the LHC for the last stage of acceleration. Beams are accelerated by sixteen radiofrequency cavities, and kept in their circular trajectory by 1232 super-conducting dipole magnets which provide a magnetic field of 8 T.

The primary purpose of LHCb is to perform precision measurements in the search for New Physics in CP violation and rare decays of beauty and charm hadrons. Requirements to fulfill such a physics program are excellent tracking performances in terms of momentum, impact parameter and primary vertex resolution, precise decay time resolution and excellent particle identification capabilities. To limit the radiation damage of the detectors and the particle multiplicity, the instantaneous luminosity $\mathcal{L}$ delivered to the LHCb experiment is kept a factor ~ 5 lower than the maximum $\mathcal{L}$ delivered to other experiments installed on the LHC, such as ATLAS and CMS. This allows to deliver to LHCb a constant instantaneous luminosity, thanks to magnetic lenses which slightly tilt the colliding beams over the LHC fills. Keeping a constant luminosity is beneficial for the detector running, and it permits to better control the data taking and online selection conditions of the experiment. In LHCb the luminosity is levelled in order to have on average 1-1.5 primary interactions between protons, per collision. Table 6 shows the average running conditions of LHCb in LHC Run 1 (2011-2012) and Run 2 (2015-2018), where μ is the average number of visible pp interactions per bunch crossing.

Year	Instantaneous luminosity	Collision energy	μ	Colliding bunches	LHCb integrated luminosity
2011	$1-4 \cdot 10^{32}\mathrm{cm}^{-2}\mathrm{s}^{-1}$	7 TeV	1.5	1000-1300	1.11 fb^{-1}
2012	$4 \cdot 10^{32}\mathrm{cm}^{-2}\mathrm{s}^{-1}$	8 TeV	1.7	$\sim$ 1300	2.08 fb^{-1}
2015	$0.5-3.5 \cdot 10^{32}\mathrm{cm}^{-2}\mathrm{s}^{-1}$	13 TeV	1.1	300-1500	0.33 fb^{-1}
2016	$3.5 \cdot 10^{32}\mathrm{cm}^{-2}\mathrm{s}^{-1}$	13 TeV	1.1	1700-2000	1.65 fb^{-1}
2017	$3.5 \cdot 10^{32}\mathrm{cm}^{-2}\mathrm{s}^{-1}$	13 TeV	1.1	1700-2300	1.71 fb^{-1}
2018	$4.4 \cdot 10^{32}\mathrm{cm}^{-2}\mathrm{s}^{-1}$	13 TeV	1.1	$\sim$ 2300	2.19 fb^{-1}
Total					9.07 fb^{-1}

Table 6: Average running conditions of the LHC collider and the LHCb experiment over LHC Run 1 and Run 2. Only the pp collisions are considered in the LHCb integrated luminosity. The energy is referred to the collision center of mass.

Reconstruction of charged particles in LHCb is performed using information from the tracking subdetectors: the Vertex Locator (VELO), the Silicon Tracker (ST) and the Outer Tracker (OT). Particle identification is accomplished by the Ring Čerenkov (RICH) detectors, the calorimetric system

---

[7] Pseudo-rapidity is defined as $\eta = -\ln\tan\frac{\theta}{2}$, with $\theta = \frac{p_z}{p}$ being the angle between the particle trajectory and the beam pipe. For highly-relativistic particles, pseudo-rapidity is almost identical to the rapidity $y = \frac{1}{2}\ln\frac{E+p_zc}{E-p_zc}$ of the particle. Here, E, p and p_z are respectively the particle energy, momentum and projection of the momentum along the beam direction (z direction).

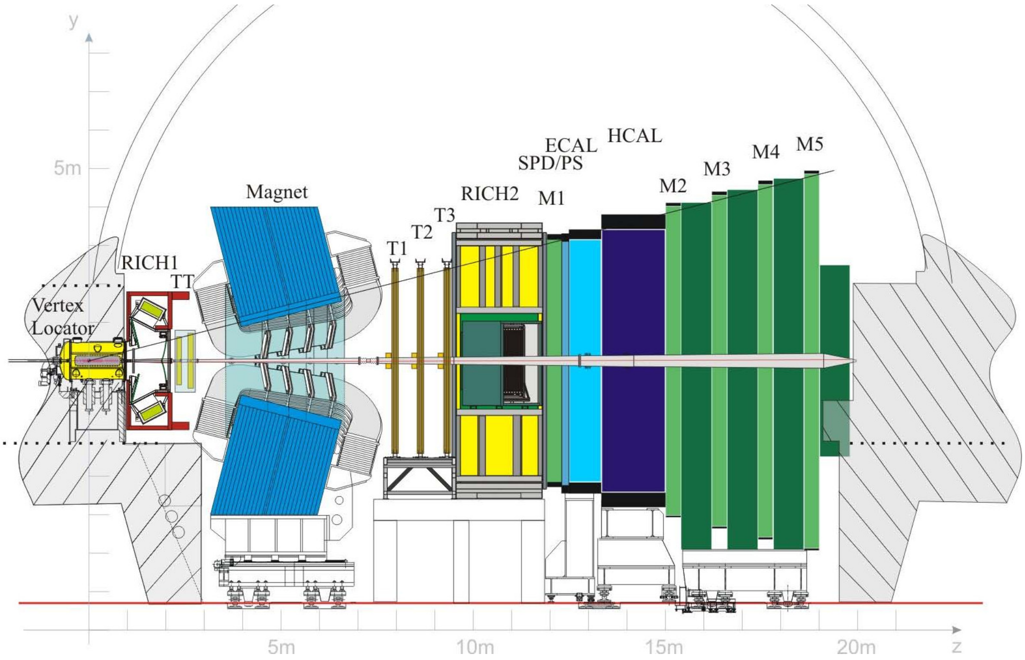

Figure 8: Side view of the LHCb detector [60].

and the muon stations. Figure 8 shows a side view of the LHCb detector. An overview of the subdetectors characteristics is given in Sections 2.1-2.2; more details can be found in [60]. The LHCb data-flow and main reconstruction strategies are presented in Section 2.3.

2.1 Tracking detectors and magnet

Measurements of the particle momenta are made possible by a warm dipole magnet in a window-frame yoke, which match the LHCb detector acceptance. An integrated magnetic field of 4 Tm for 10 m long tracks is provided. This accommodates the requirements of having a field as high as possible between the tracking detectors, and a small field (below 2 mT) within the RICHs envelope. The main magnetic field component is along the y direction [8] , while the B_x and B_z components are negligible within per-cent level. The magnet polarity is periodically switched in opposite-directed magnetic fields, to control possible systematic effects in the detector response and the particle reconstruction. A perspective view of the LHCb dipole magnet and the map of the resulting magnetic field are shown in Figure 9.

Three tracking systems are present in LHCb exploiting different technologies: the Vertex Locator (VELO) surrounding the interaction point; the Trigger Tracker (TT) stations placed upstream of the dipole magnet in the weak fringe magnetic field; and the main tracker (T tracker) installed downstream the magnet. The TT stations provide an approximated value of the particle momentum, while the T tracker measures it with high precision.

The VELO consists of a series of silicon modules displaced in 21 tracking layers, each of them providing a measure of the $r - \phi$ [9] coordinates, arranged along the beam direction nearby the collision region. It provides precise measurement of the track coordinates close to the interaction point, and it is crucial to reconstruct primary and secondary vertices. The precision of the measurement of the particle trajectory close to the interaction point improves as much the detector sensors move closer to the collision point. Therefore the VELO sensors are placed at the closest position to the beams allowed by its mechanical constrains. Their radial distance to the z axis is ≈ 8 mm. However, at a so

---

[8] In the LHCb reference system, the z axis is directed along the beam direction while the y axis is vertically oriented and the x direction is horizontal (see Figure 8).

[9] r is the radial distance to the beam pipe; ϕ is the azimuthal angle with respect the y axis, on the xy plane.

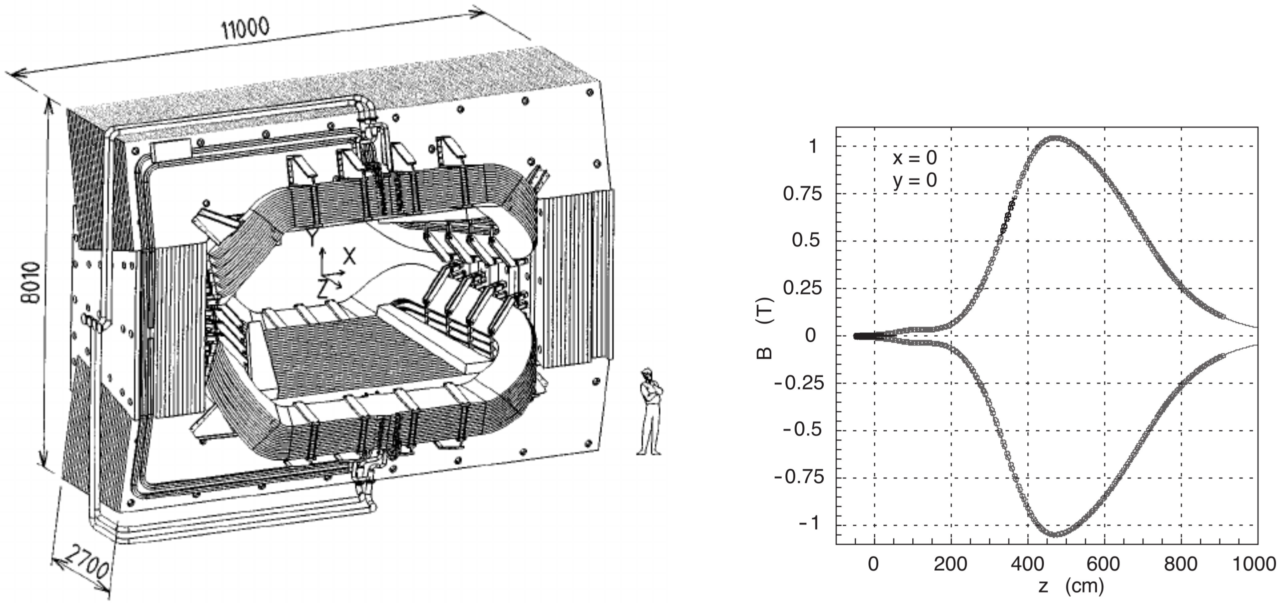

(a) (b)

Figure 9: a) Perspective view of the LHCb dipole magnet. The quoted distances are in units of cm. b) Map of the LHCb magnetic field along the z axis [60]. The B_x and B_z components of the magnetic field are negligible.

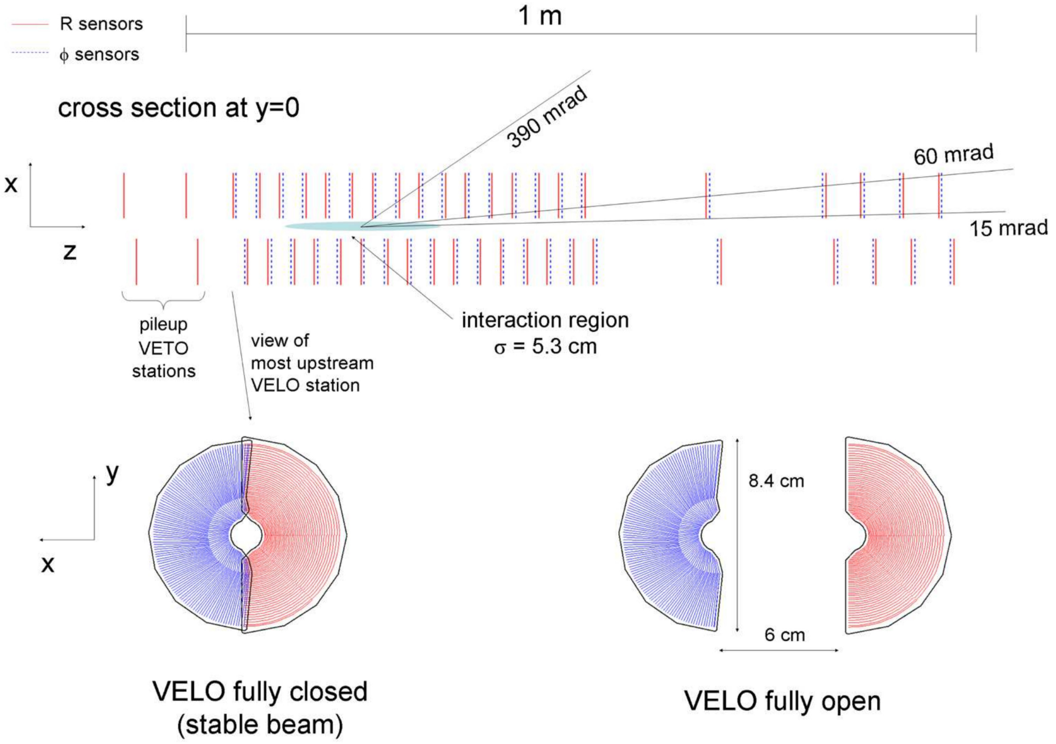

Figure 10: Cross-section of the VELO detector [60]. The z axis corresponds to the beam pipe direction.

small distance to the beams the sensors would be damaged during the injection and acceleration stages of the colliding particles. The tracking modules are therefore retractable and kept at safety distance during beam preparation. Figure 10 shows a cross-section of the VELO detector. The VELO layout has been optimised to minimise the amount of material in the acceptance, which is crucial to minimise the reconstruction uncertainty due to multiple scattering. The sensor active area is about 5 cm x 5 cm in each layer. The radial and angular sensor pitches change with the distance from the layer center, varying from ≈ 40 μm to ≈ 100 μm. Figure 11 shows a cross-section of a VELO layer. The individual hit resolution of the sensors strongly depends on the sensor pitch and *projected angle* of the particle trajectory [10], and varies in the range 10-25 μm.

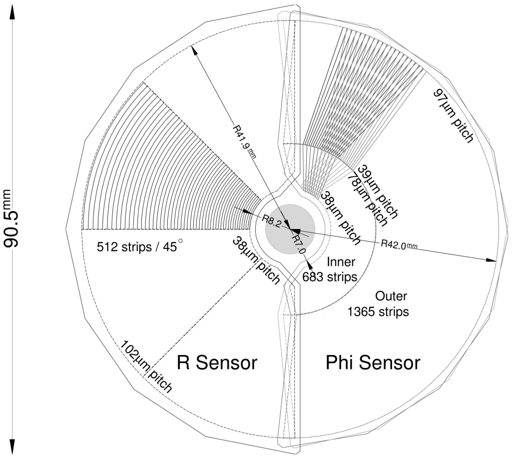

Figure 11: Cross-section of a VELO layer [60]. Each half of the layer is provided of both the r- and ϕ-sensors, placed on its front and back area. The order of the sensors are switched between the two halves of a layer, resulting in each layer face having half r-sensors (left half of the picture) and half ϕ-sensors (right half of the picture).

The Silicon Tracker includes detection layers placed in different tracking subdetectors, the Trigger Tracker (TT) and the Inner Tracker (IT). Both make use of silicon micro-strip sensors, with a strip pitch of ≈ 200 μm. The TT consists of four tracking layers in a x-u-v-x arrangement, where strips are vertical in the first and last layers and are rotated by an angle -5 and $+5$ with respect to the vertical in the second and third layers, respectively. This geometry has been optimised based on the characteristic of the LHCb magnetic field. Since the only non-null component of the magnetic field is directed vertically, particles are bent into the horizontal (xz) plane. The vertical strips of the TT measure the displacement of charged particles onto the x direction due to the bending, while the tilted modules give a rough estimation of the y coordinate of the particle intersection with the layers. Precise measurement of the y coordinate of the intersections is provided by a linear extrapolation of the VELO measurements. TT layers are 150 cm wide and 130 cm high, and they consist of a row of seven silicon sensors. Figure 12 shows a sketch of a TT layer. The strip pitch is ≈ 200 μm, to meet the single-hit resolution of 50 μm required by the reconstruction algorithms.

The Inner Tracker covers the inner region of the tracking stations downstream the magnet (T stations), to cope with the high track occupancy characterising the beam pipe area. The IT is organised in three tracking stations with four layers each. Within each station, the IT layers are arranged in a x-u-v-x layout as for the Trigger Tracker detector. Each IT module consists of either one or two silicon sensors, with strip pitch of about 200 μm. Figure 13 shows a sketch of an IT module.

The outer regions of the T layers are covered by the Outer Tracker (OT), a drift-time detector designed as an array of individual, gas-tight straw-tubes modules. Each module contains two layers of drift-tubes, with inner diameters of 4.9 mm. The single hit resolution of the OT is 200 μm. Analogously to the Inner Tracker, the OT modules are arranged in three station in a x-u-v-x layout. The OT layers are 6 m x 4.8 m sized. Figure 14 shows a sketch of the OT layout.

---

[10] The projected angle α_p is the crossing angle of the particle projected perpendicular to the strips, given by $\tan\alpha_p = \frac{d}{l_\perp}$ [61]. Here, d is the sensor thickness and $l_\perp$ is the track component perpendicular to a strip.

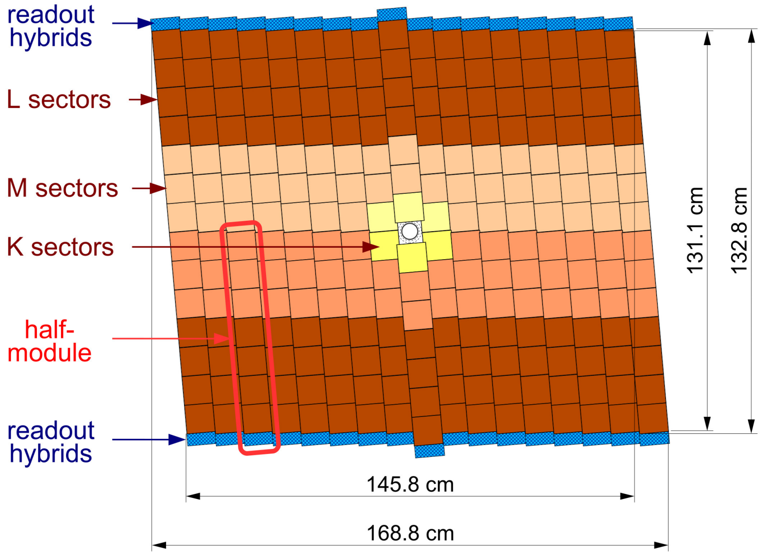

Figure 12: Layout of a TT layer [60]. The sensors are arranged in rows of seven sectors, with the readout placed on top and on the bottom of the layer.

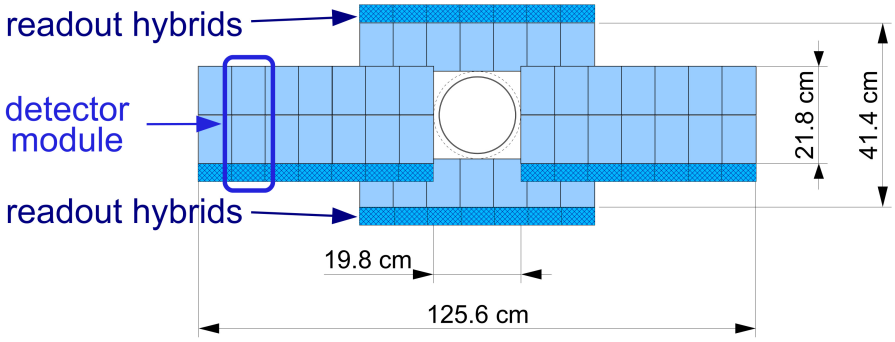

Figure 13: Layout of an IT module [60].

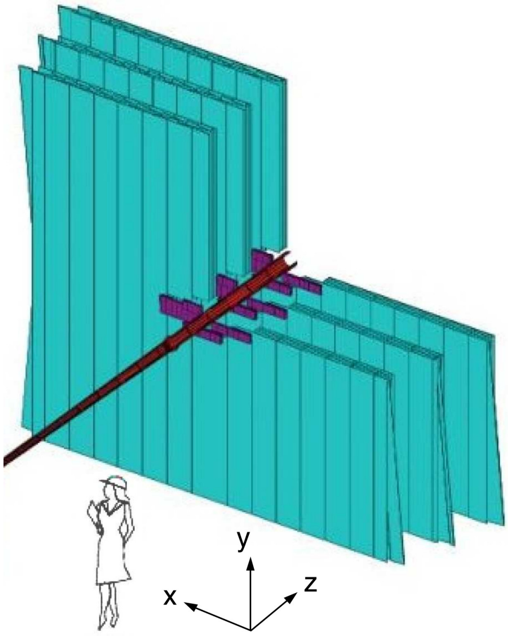

Figure 14: Layout of the T stations, with the OT modules in cyan and the IT modules in purple [60].

2.2 Particle identification detectors

Calorimeters are installed for detection of photons and separation of electrons and hadrons. The muon detection is made possible by muon stations. Finally, two RICH detectors are installed to provide separation of charged hadron species.

The main calorimeter system is constituted by an electromagnetic calorimeter (ECAL) followed by a hadronic calorimeter (HCAL). Two additional detectors, the Scintillator Pad Detector (SPD) and the PreShower (PS) are also present. The calorimeters play an key role for the online selection of events in LHCb. In particular, a good measurement of the electron energy is essential for the electron trigger. Therefore, the ECAL has been optimised to fully contain the showers from high energetic electrons and photons, choosing a thickness of 25 radiation lengths. The HCAL thickness is 5.6 interaction lengths due to space limitations. The calorimetric subdetectors adopts a variable lateral segmentation, since the hit density varies by two orders of magnitude over the calorimeter surface. In all the calorimeters, scintillation light is transmitted to photo-multipliers by wavelength-shifting plastic fibres. A shashlik technology has been adopted by the ECAL, where a sampling scintillator-lead structure is readout by the fibers. The HCAL instead is a sampling device made from iron and scintillating tiles running parallel to the beam axis, as absorber and active material respectively. The energy resolution of ECAL results to be $\sigma_E/E \approx 10\%/\sqrt{E} \oplus 1\%$, with E, the energy of the deposited signal, measured in GeV. The energy resolution of HCAL is $\sigma_E/E = (69\% \pm 5\%)/\sqrt{E} \oplus (9\% \pm 2\%)$, with the energy E measured in GeV. A schematic of the internal cell structure of the HCAL is shown in Figure 15.

The SPD and the PreShower detectors are put in front of the ECAL. Their design is similar, consisting of two scintillating vertical planes each. Charged particles leave in the SPD a signal which is detected, while photons do not interact. A lead sheet of 2.5 radiation length is sandwiched between the two subdetectors. This lead converter initiates the electromagnetic showers, so that both electrons and photons deposit a sizable amount of energy in the PS. Combining the SPD and the PS information with the cluster position reconstructed in the ECAL, the nature of the electromagnetic particle (either electron or photon) is determined. Moreover, the PreShower provides longitudinal segmentation of the electromagnetic shower detection. This characterisation of the shower is essential for the rejection of the large background of charged pions in the electron detection.

The muon chambers also play a key role for the online triggering of events in LHCb, and provide important offline PID information for analysis of decay channels involving muons. The muon detector is composed of five stations, M1-M5. M1 is placed in front of the calorimeters, and it is used to improve the measurement of the particle transverse momentum, p_t, for the online selection. Its inner region make use of triple-GEM detector technology, to ensure good resistance to ageing. The M1 outer region is based on multi-wire proportional chambers. The M2-M5 stations are placed downstream the calorimeters and are interleaved with 80 cm thick iron absorbers to select penetrating muons. These stations are based on multi-wire proportional chambers. A view of the muon detector layout is shown in Figure 15.

Finally, two RICH detectors (RICH1 and RICH2) are employed for particle identification of hadrons trough detection of the Čerenkov emissions of charged particles in radiators. At large polar angles the momentum spectrum of the particles is softer, while at small angles it is harder. Hence, the two RICH detectors have been optimised to cover the full momentum range. RICH1 is placed upstream of the magnet, while RICH2 is installed downstream. RICH1 covers the low momentum charged particle range $\sim 1 - 60$ GeV/c using aerogel and C_4F_10 radiators (only the latter in Run 2). Instead, RICH2 covers the high momentum range from $\sim 15 - 100$ GeV/c using a CF_4 radiator. In both the detectors the Čerenkov light is focused by a combination of spherical and flat mirrors to reflect the image out of the spectrometer acceptance, where Hybrid Photon Detectors used to detect the Čerenkov photons are installed. In RICH1 the optical layout is developed vertically whereas in RICH2 it is horizontal, as sketched in Figure 16.

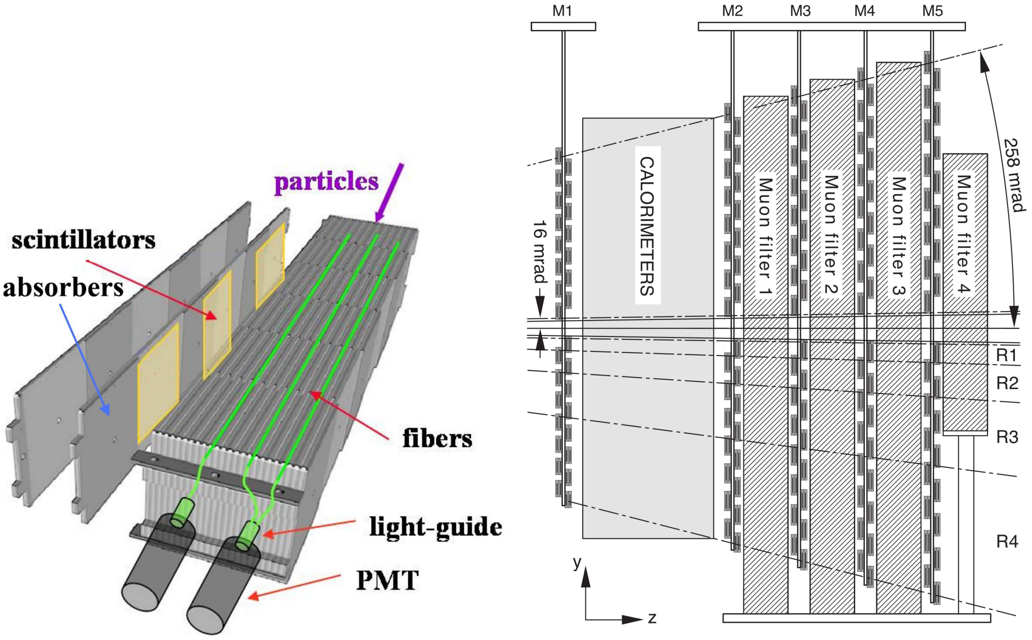

(a) (b)

Figure 15: a) Internal structure of a HCAL cell. b) Side view of the muon detector [60].

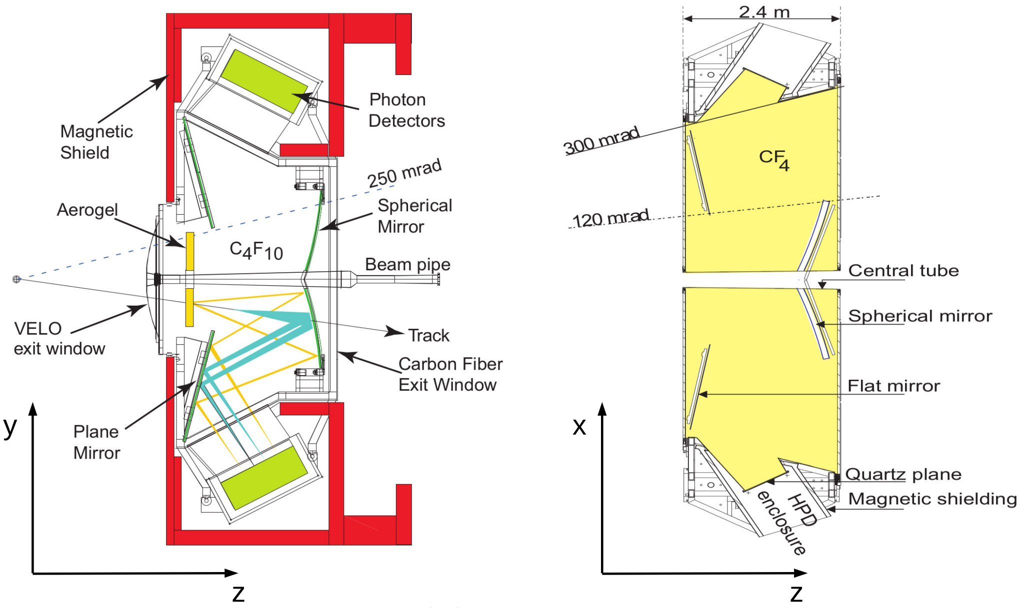

(a) (b)

Figure 16: a) Optical layout of RICH1, developed vertically. b) Optical layout of RICH2, developed horizontally [60].

2.3 LHCb data-flow and reconstruction strategy

The LHCb data-flow consists of an *online* and an *offline* processing steps. In the online processing the bunch crossing rate provided by the colliding beams is reduced to a rate that is possible to be stored permanently. This is followed by the offline step which processes the online-selected data to achieve the best reconstruction quality for the analysis of data. An overview of both the online and offline processings will be given in the following. Also, the particle reconstruction strategy will be discussed [62].

2.3.1 Online selection of data

During Run 1 and Run 2 the LHC provided pp collisions at a rate of 40 MHz, however the LHCb tracking detectors have a readout frequency of 1 MHz. Furthermore, only about $\sim 5-10$ kHz of data rate can be written to permanent storage for offline analysis, because of the limits set by the available computing resources. The required event-rate reduction is achieved by employing a multi-stage trigger consisting in a hardware-based Level 0 (L0) trigger, and in two stages of the High Level Trigger (HLT) implemented in software.

The L0 reduces the initial bunch crossing rate from 40 MHz to 1 MHz using information from the calorimeters and the muon stations. It selects events with hadrons, electrons or photons with high transverse energy or muons with high transverse momentum, which are signatures for the decay of heavy-mass B mesons. A pile-up veto-system in the VELO estimates the number of primary pp collisions in each bunch crossing and rejects events with a high number of interactions.

The HLT algorithms further reduce the data rate from 1 MHz to the permanent storing rate of $\sim 1-5$ kHz making use of the full-detector information. The HLT reconstruction algorithms run on a large event filter farm which in Run 2 consisted of $\sim 51,000$ logical cores. The HLT is split into two stages, the HLT1 and HLT2.

HLT1 takes as input the L0 decisions, and attempts to confirm them based on a partial reconstruction of the events. Information from the tracking system, the calorimeters and the muon stations are used. Primary vertices are reconstructed, and inclusive selections based on single- and two-tracks quantities are performed. The HLT1 reduced the event rate from 1 MHz to 80 kHz in Run 1 and to 150 kHz in Run 2.

HLT2 takes as input the events confirmed by HLT1, and performs a full reconstruction of the event. A mixture of inclusive and exclusive selections are performed, employing particle identification (PID) information from the RICH detectors as well. While the HLT1 stage kept the same basic structure for both Run 1 and Run 2, HLT2 faced a deep evolution over the years.

During Run 1, events passing the L0 and HLT1 selections have been processed sequentially by HLT2, writing to permanent storage a final data rate of ≈ 5 kHz. Because of the limited online computing resources, there have been differences in the algorithms of pattern recognition and particle selections with respect to the offline processing. Also, no hadron identification was provided online. This resulted in a limited accuracy of the reconstruction provided by the HLT2 processing.

The trigger strategy, in particular for what concerns HLT2, drastically evolved in Run 2 with the goal of running *online* an offline-like-quality reconstruction. However, this requires an offline-quality alignment and calibration of the detectors to be performed on real time. This would have not been feasible in the limited time budget per event given the trigger structure in Run 1. Therefore, a *deferred-triggering* strategy has been adopted. Within this approach, events are buffered to disk and processed between fills. Since stable beams are provided by the LHC for about 35% of the data taking periods, the time budget available for processing buffered events increases dramatically. During Run 1 the 20% of L0 accepted events were deferred already, but in Run 2 100% of HLT1-accepted events were moved to a buffer consisting of more than 10 PB of disk space. Embracing this new strategy, the HLT1 output can be used for *online calibration and alignment* of the full detector. This allows the HLT2 stage to perform a full event reconstruction with offline-like-quality, writing to permanent storage at a ≈ 12.5 kHz rate. The layout of the trigger strategies in Run 1 and Run 2 are compared in Figure 17.

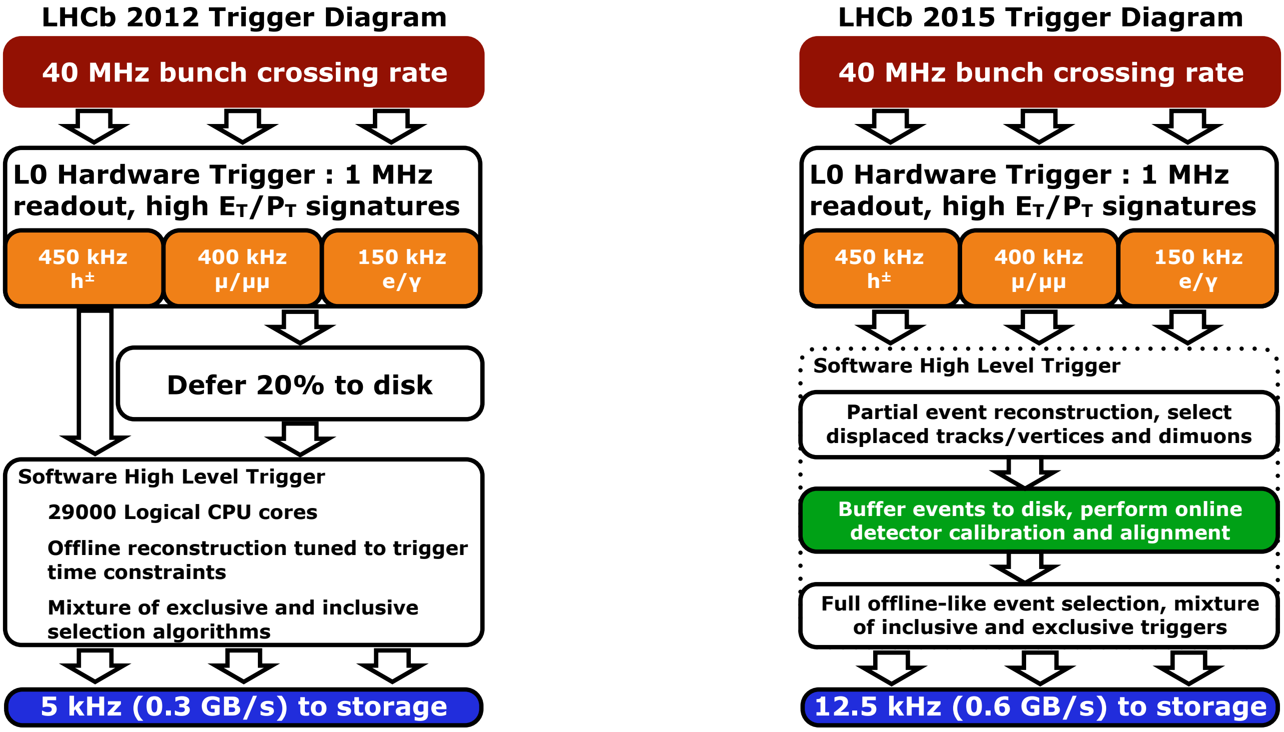

(a) (b)

Figure 17: Layout of the LHCb trigger strategies in Run 1 (a) and Run 2 (b).

Achieving offline-like-quality on real time permits to perform physics analysis with HLT-reconstructed objects. However, it would not be feasible to write on permanent storage the entire HLT2 output, because of the limited amount of tape available. Thus, the so-called *Turbo stream* has been implemented in 2015 [63]. In its first incarnation, only the HLT information related to the signal candidate was stored removing most of the detector raw data. In this way the Turbo stream processing decreased the space required to below 10% with respect the standard data stream. Allowing to loosen the precedent selection criteria used online, Turbo stream revealed to be ideal for high-yield analysis such as for charm-physics. Also, since offline reconstruction is not required to be processed, Turbo data is available for analysis in $\sim days - weeks$ rather than months required by the standard processing. During Run 2, the Turbo concept has evolved offering the possibility to save to disk the full reconstructed event rather than the trigger candidate only (*Turbo++*), or either to choose what kind of particles must be preserved (*Turbo Selective Persistence* [64]), while still skipping the raw information. Therefore, the Turbo streams now covers the whole range of analysis-specific requirements.

2.3.2 Reconstruction strategy

Given the geometry of the LHCb detector, several track types are defined depending on the subdetectors in which the tracks have measurements, as sketched in Figure 18. *Long tracks* intersect the entire tracking system from the vertex locator to the tracking stations downstream the magnet, resulting in the most precise measurements of momentum and impact parameter. *VELO tracks* only have measurements in the vertex locator, and are mainly used for primary vertex reconstruction. *T tracks* only have hits in the downstream tracking stations, and can be originated from the decay of long-lived particles decaying after the upstream tracker. *Upstream tracks* have hits only in the vertex locator and in the tracker downstream the magnet, and they mainly correspond to low-momentum particles which are bent out of the acceptance of the downstream tracker. *Downstream tracks* have measurements in the upstream and downstream trackers only, and usually correspond to daughter particles of long-lived

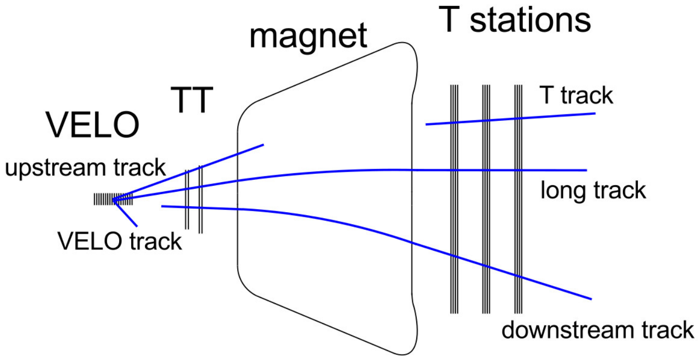

Figure 18: Different types of tracks in LHCb, depending on the intersected subdetectors [62].

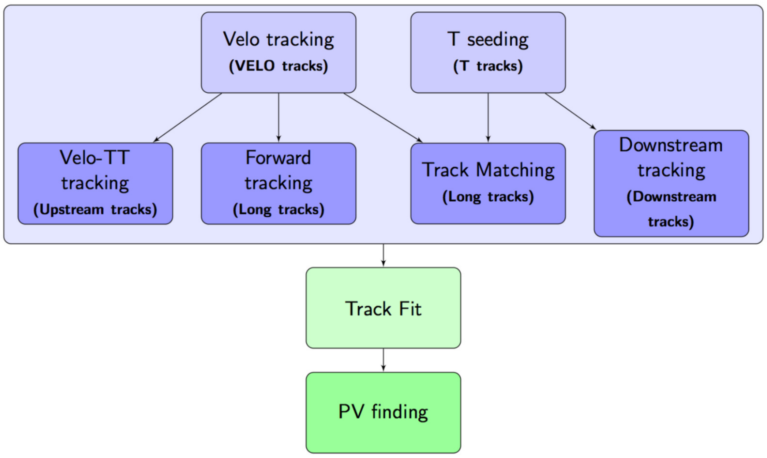

Figure 19: Main tracking algorithms in LHCb [62].

particles decaying out of the vertex locator, such as K^0_S and Λ.

Several tracking algorithms have been developed to reconstruct the different track species, as sketched in Figure 19. *VELO tracking* and *T-seeding* are standalone algorithms to reconstruct VELO tracks and T tracks respectively. The *Forward tracking* is the main algorithm for the reconstruction of long tracks. It takes as input reconstructed VELO tracks and attempts to extrapolate them to the downstream tracking stations. *Track matching* also reconstructs long tracks, but matching tracklets reconstructed independently by the VELO tracking and T-seeding algorithms. Both Forward tracking and track matching reconstruct the same particles, and the reconstructed long tracks are finally matched and merged to compensate the eventual reconstruction inefficiency of the individual algorithms. Finally, *VELO-TT* and *Downstream tracking* reconstruct upstream and downstream tracks. The Forward tracking can also take VELO-TT reconstructed tracks, rather than simple VELO tracks as input. Thanks to the weak fringe magnetic field present in the TT detector, the VELO-TT algorithm provides a rough estimation of the track momentum ($\delta p/p \sim 15\%$) permitting the Forward algorithm to select hits on the downstream tracker considerably faster.

After tracks have been reconstructed, they are fitted by a Kalman Filter fit [65] in order to achieve the most precise measurements of their parameters, in particular an excellent momentum resolution $\delta p/p \approx 0.4\%$. Finally, a multivariate classifier named *ghost probability* [66, 67] combines information from different stages of the track reconstruction and from global event properties to assign to each track a so-called *TrackGhostProbability*. This quantity indicates the probability of the track of being mis-reconstructed and thus of not corresponding to a real particle intersecting the detector. Such tracks are referred to as *ghosts*.

Primary vertex (PV) reconstruction is then performed [68]. An excellent separation between primary and secondary vertices is required to distinguish decay of b- and c-hadrons from the large background of light quarks production. Therefore, the PV reconstruction is of crucial importance for LHCb. It consists of two stages, the initial *seeding* followed by a final fitting. PV seeding searches for primary vertex candidates, defined as point at which a sufficient number of tracks pass close to each other. Once all the PV seeds of an event have been found, a fit based on an *adaptive weighted least square* method [69] is performed on each of them. Excellent primary vertex resolutions on the transverse directions $\delta x, \delta y \approx 0.04 - 0.01$ mm and on the beam direction $\delta z \approx 0.2 - 0.04$ mm are achieved, depending on the track multiplicity.

Once all tracks in the event have been reconstructed, the trajectory of each particle through the RICH radiator volumes can be determined [70]. This allows the computation of an assumed emission point of the emitted photon candidates for each track. The candidate photons for each track are determined by combining the photon emission point with the measured hit positions of the photons. Once the photon candidates have been assigned, the Čerenkov angle can be computed. The trajectory of the photons are determined by an analytical solution of the RICH optics, taking into account the mirror and HPD alignment. In order to determine the particle species for each track, the information of the Čerenkov angle must be combined with the track momentum measured by the tracking algorithms. An overall *event log-likelihood* [11] algorithm is employed [70] to assign the particle type to the particle, where all the tracks in the event are considered. The overall event likelihood is computed assuming all particles are pions; then, for each track in turn, is recomputed varying the mass hypothesis to e, μ, π, K and p. The mass hypothesis which gives the largest increase in the event likelihood is taken as optimal assignment of the track. The differences in the log-likelihood for each track between the mass hypothesis (with respect to the pion mass) are the final results of the particle identification procedure, and are referred to as $PIDe$, $PID\mu$, $PIDp$ and $PIDk$ [71]. These variables, also called *combined Delta Log-Likelihoods* (DLLs), are easy to understand but have some limitations. Multivariate classifiers have therefore been developed combining measurements from all subdetectors, to give a better PID performance. Artificial neural networks are trained on data, obtaining synthetic PID variables referred to as *ProbNN*s [71] which have higher significance to discriminate different particle type assumptions.

2.3.3 Offline processing of data

Data selected online are permanently stored to tape with all the detector raw banks, apart from the samples selected by the Turbo stream. Periodically, an offline processing of the data is performed. Events are reconstructed making use of all the detector information, relaxing the selection criteria used online and achieving the best accuracy on the track and vertex measurements.

Once events are reconstructed offline, they are further selected and categorised by the so-called *stripping* procedure. Signatures of decays and processes are searched for in the data, making use of requirements specified in *stripping lines*. The latter are defined by analysts, and generally one stripping line corresponds to a single (either inclusive or exclusive) process of interest. The output of the stripping lines represents the data actually used by analyses in LHCb, together with the output of the Turbo streams. As example, this analysis makes use of the *X2LcD0KD02KPiBeauty2Charm* stripping line, which is constructed to select events with $\{\Lambda_b^0, B^0, B_s^0\} \to \Lambda_c^+\overline{D}^0K^-$ decays, with the $\overline{D}^0$ decaying into $K^+\pi^-$.

---

[11] The log-likelihood is introduced in Section 3.2.2.

3 Analysis outline and tools

The basic analysis strategy is presented in Section 3.1, in particular for what concerns the decomposition of a decay process in terms of partial waves. Section 3.2 describes the main statistical concepts that are adopted by the analysis. Finally, an overview on the most important software packages and concepts exploited in this analysis is given in Section 3.3.

3.1 Analysis strategy

As seen in Chapter 1, the non-perturbative nature of QCD makes it difficult to calculate processes where light quarks are involved. Therefore, effective models must be build from measured properties of the hadron spectrum, investigating the decay and scattering of hadrons, and identifying the intermediate states contributing to the processes. This can be accomplished by disentangling the reactions in *partial waves* [5], corresponding to the partial contributions of the intermediate resonances to the total decays. The goal of amplitude analyses is to measure both the static properties of the intermediate states, such as mass, width, quantum numbers, and their dynamical behaviour and interference patterns.

The decomposition of a scattering process in terms of partial waves can be accomplished by expanding the scattering wave of the process, defined by the Schrödinger equation, in terms of the Legendre polynomials [5]. Many methods have been developed to construct an amplitude from the partial wave decomposition, which differ by the assumptions which must be taken to group particles and to build the decay chains. This analysis makes use of the so-called *isobar model* [72], an empirical approach in which the decay reaction is disentangled in a sequence of two-body decays. This is sketched in Figure 20, by a three-body decay in which two final state particles are the decay product of an intermediate state. In this approach, the decay of the intermediate state factorizes from the recoil particle, which is involved in conserving the angular-spin properties of the process. The isobar model has proven to work extremely well for most of the hadrons and in very different environments, while being reasonably simple to construct. However more complex reactions exist which cannot be easily treated by the isobar model. In these processes, such as $\omega \to \pi^+\pi^-\pi^0$ and $\eta \to 3\pi$, rescattering between the intermediate state and the recoil particle have a large influence. In some cases the isobar model can be retained if the rescattering process is refactorizable in terms of many isobar reactions. This usually involves the introduction of many parameters, and may not lead to a sufficient description. In those cases model assumptions have to be made. Nevertheless, the isobar approach is generally very accurate in describing most of the decay processes, and it is the most common method followed by amplitude analyses in LHCb.

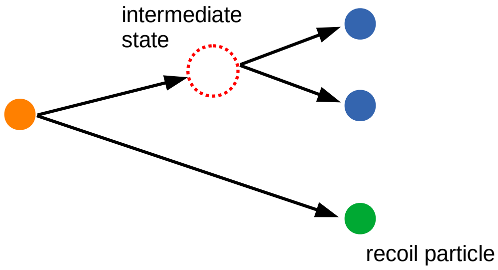

Figure 20: Sketch of a three-body decay, proceeding through an intermediate resonance.

Within the isobar model, each of the decay nodes are expressed by amplitudes. They are consisting of an angular part, defined by the angular-spin properties of the process, and of a dynamical part. There are multiple ways to express the spin structure of the reaction. This analysis makes use of the so-called *helicity formalism* [73], in which a spin quantisation axis is chosen, and two-body decays are defined by rotations with respect to it. In this particular formalism each of the particle spins is quantised parallel to its own flight direction, resulting in the helicity to be diagonal. The amplitudes corresponding to different values of the orbital angular momenta, spin and helicities are related through couplings, determined by a fit to the data. The construction of the amplitude model specific to this analysis is detailed in Chapter 5, and the amplitude fits are presented in Chapter 6.

Before that the amplitude fit can be performed to the data, some preliminary steps are required. The data sample is first selected in order to reject as much background is possible, while keeping the highest fraction of the signal. The selection procedure is described in Chapter 4. After that the selection is applied, a mass fit to the Λ_{b}^{0} invariant mass distribution is performed. This fit is employed to derive the so called *s*-weights, a set of weights which indicate how much a candidate is probable to represent signal or background process. The statistic procedure of extracting the *s*-weights is referred to as *sPlot*, and it is described in Section 3.2. The mass fits are detailed in Chapter 4.

Once the amplitude model is fitted to the data, the statistical significance for the observation of pentaquark candidates in $\Lambda_{\mathrm{b}}^{0} \to \Lambda_{\mathrm{c}}^{+}\overline{\mathrm{D}}^{0}\mathrm{K}^{-}$ decays is assessed. This is done by testing different pentaquark hypotheses performing *profile likelihood ratio tests*, that are introduced in Section 3.2.5. The results of the statistical tests are described in Chapter 8.

3.2 Statistical foundations

This analysis employs several statistical methods and strategies for extracting results which are statistically meaningful and solid. The fundamental concepts [74] are presented in Section 3.2.1. The *maximum likelihood*, the *sPlot* technique and the *profile likelihood ratio test*, which are used for fitting the model to the data and for assessing the statistical significance of observing pentaquark candidates in the $\Lambda_{\mathrm{b}}^{0} \to \Lambda_{\mathrm{c}}^{+}\overline{\mathrm{D}}^{0}\mathrm{K}^{-}$ decay process, are described in Sections 3.2.2-3.2.5. Finally, *Boosted Decision Trees* are introduced in Section 3.2.6, which represent a key tool for selecting the signal candidates in this analysis.

3.2.1 Fundamental concepts

Let us consider a random process, with outcome described by a variable x which can be either discrete or continuous. The probability prediction for x can be expressed by a function $f(x)$. If x is discrete, $f(x)$ is itself a probability. If x is continuous, $f(x)$ is called *probability density function* (*pdf*) and the probability of x of being in the interval of values $A = [x_0, x_1]$ is given by:

$$p(x \in A) = \int_A f(x')dx' \tag{22}$$

If x is a *quantitative* variable [12], for any function $g(x)$ it is defined the so-called *average* or *expected value*:

$$\begin{aligned} E[g] &= \sum g(x')f(x')\ , \\ E[g] &= \int g(x')f(x')dx' \end{aligned} \tag{23}$$

in case of a discrete or continuous variable, respectively. The expected value of $g(x)$ represents its mean value. Particularly important is the expected value of the variable x itself, often denoted by μ.

---

[12] A variable is said *quantitative* if it assumes numerical values, in contrast to a *qualitative* variable.

Another property is the *variance* of the variable x:

$$V[x] \equiv \sigma^2 = E[(x-\mu)^2] = E[(x-E(x))^2] \tag{24}$$

which gives a measure of the variability of the values taken by x, with respect to its expected value μ. Its square root σ is said *standard deviation.*

Supposing to have a *pdf* $f(x, y)$ which is function of two random variables x and y, the *covariance* is defined to be:

$$cov[x,y] \equiv V_{xy} = E[x \cdot y] - E[x] \cdot E[y] \tag{25}$$

The covariance measures the correlation between the variables x and y. A dimensionless alternative to the covariance is the *correlation* ρ_{xy}:

$$\rho_{xy} = \frac{cov[x,y]}{\sigma_x \cdot \sigma_y} \tag{26}$$

Following the above definitions, the self-covariance V_{xx} of a variable x is its variance ($V_{xx} = \sigma_x^2$) and its self-correlation ρ_{xx} is the unity.

3.2.2 Parameter estimation and maximum likelihood

As introduced in the previous section, *pdf* functions involve a variable describing random quantities. They can also be related to one or more *parameters*, generically indicated by θ in what follows. A *pdf* of a variable x depending on a parameter θ is denoted by $f(x|\theta)$. The estimation of parameters from the observed distributions plays a crucial role in the analysis of data. This procedure is said *parameter fitting*, and its main concepts are described in the following.

Let us consider a sample of N measurements $\boldsymbol{x} = (x_1, x_2, ..., x_N)$ which are statistically independent and each follow a *pdf* $f(x)$. The properties of $f(x)$ can be estimated by introducing a functional form $f(x, \boldsymbol{\theta})$, with $\boldsymbol{\theta} = (\theta_1, \theta_2, ..., \theta_m)$ being a set of m parameters. It is possible to estimate the true value θ^* for each of the parameter θ. In the following, the set of true values of the parameters are denoted by $\boldsymbol{\theta^*}$ The estimated values for the parameters $\boldsymbol{\theta}$ are inferred through a statistic, i.e. a function of the data, referred to as *estimator* $\hat{\boldsymbol{\theta}}$:

$$\hat{\boldsymbol{\theta}} = \hat{\boldsymbol{\theta}}(\boldsymbol{x}) : \boldsymbol{x} \to \boldsymbol{\theta} \tag{27}$$

Different ways how to build the estimator exist. This analysis makes use of a *frequentist approach*, and attempts to use estimators which are *unbiased*, *consistent*, *efficient* and *robust* [74]. An estimator is said to be unbiased if its expected value is equal to the true parameter value $\boldsymbol{\theta^*}$:

$$E[\hat{\boldsymbol{\theta}}] = \boldsymbol{\theta^*} \tag{28}$$

The estimator is defined to be consistent when it is asymptotically unbiased, hence it converges to the true value $\boldsymbol{\theta^*}$ in the limits of a large number of measurements:

$$\lim_{N\to\infty} \hat{\boldsymbol{\theta}} = \boldsymbol{\theta^*} \tag{29}$$

Note that an estimator can be biased but consistent, or unbiased but not consistent [13] . An estimator is efficient if it estimates $\boldsymbol{\theta}$ in the *best possible way*, or more quantitatively if it has the smallest variance.

---

[13] As example, given N measurements of decay times $t_1, t_2, ..., t_N$ of a particle, a consistent but biased estimator of its mean lifetime τ is $\hat{\tau} = \frac{\sum_{t_i=t_1}^{N} t_i}{N-1}$, while a unbiased but not consistent estimator is $\hat{\tau} = t_1$. A unbiased and consistent estimator is $\hat{\tau} = \frac{\sum_{t_i=t_1}^{N} t_i}{N}$.

The minimum possible variance of a unbiased estimator is given by the Cramér-Rao-Frechet inequality [75], [76]:

$$V[\hat{\boldsymbol{\theta}}] \geq I(\boldsymbol{\theta})^{-1} \tag{30}$$

with $I(\boldsymbol{\theta})$ being the *information matrix* computed over all the measurements x_i:

$$I_{jk}(\boldsymbol{\theta}) = -E\big[\sum_{i=1}^{N} \frac{\partial^2 \ln f(x_i|\boldsymbol{\theta})}{\partial\theta_i \partial\theta_k}\big] \tag{31}$$

Finally, the estimator is robust when it is not affected by outliers or by relatively small deviations from the model assumptions.

Given a finite sample $\boldsymbol{x}$ of the observed data, a good (in the sense of the above-mentioned properties) estimator is the *(extended) maximum likelihood* [77]: it is consistent, efficient, robust but not unbiased for small statistics. Let us consider the x_i measurements statistically independent, and following each the *pdf* $f(x|\boldsymbol{\theta})$, with $\boldsymbol{\theta}$ being a set of m parameters. The likelihood function is defined as the joint probability density function for the observed values $\boldsymbol{x}$:

$$\mathcal{L}(\boldsymbol{x}|\boldsymbol{\theta}) = \prod_{i=1}^{N} f(x_i|\boldsymbol{\theta}) \tag{32}$$

where the individual *pdf*s factorise because the measurements are independent. The maximum likelihood estimate (MLE) $\hat{\boldsymbol{\theta}}$ of the parameters $\boldsymbol{\theta}$ is the value which *globally* maximises $\mathcal{L}(\boldsymbol{x}|\boldsymbol{\theta})$:

$$\left.\frac{\partial\mathcal{L}}{\partial\theta_i}\right|_{\theta_i=\hat{\theta}_i} = 0 \qquad \text{for each } \theta_i \in \boldsymbol{\theta} \tag{33}$$

Note that here $\hat{\boldsymbol{\theta}}$ denotes the estimate itself of the parameters, and not the estimator function as in Equation 27. Following this construction, the likelihood measures the probability of $\boldsymbol{\theta}$ to take a given value $\boldsymbol{\theta'}$, given the observed values $\boldsymbol{x}$. Equivalently, the MLE minimises the negative log-likelihood defined as:

$$l(\boldsymbol{x}|\boldsymbol{\theta}) = -\ln\mathcal{L}(\boldsymbol{x}|\boldsymbol{\theta}) = -\sum_{i=1}^{N} \ln f(x_i|\boldsymbol{\theta}) \tag{34}$$

The negative log-likelihood is usually preferred to the simple likelihood function, because of computational considerations. In fact, $-\ln\mathcal{L}(\boldsymbol{x}|\boldsymbol{\theta})$ is a convex function; this class of functions holds a prominent role in the field of mathematical optimisation, and the so-called *convex optimisation* is a well studied problem.

While in conventional sampling models experiments consist of taking a pre-determined number of measurements, in this analysis the measurements are taken for a given fixed time and they can occur randomly. This results in a total number of measurements n which fluctuates. A natural extension of the maximum likelihood method, suited for the latter use case, is the *maximum extended likelihood* technique [78]. In this method the normalisation of the standard likelihood function is replaced by a Poissonian statistics:

$$\mathcal{L}_{ext}(\boldsymbol{x}|\boldsymbol{\theta},\nu) = \frac{\nu^n e^{-\nu}}{n!} \prod_{i=1}^{n} f(x_i|\boldsymbol{\theta}) \tag{35}$$

where n is the total number of observed events, being a Poisson random variable with mean value ν.

3.2.3 *sPlot* technique

The so-called *sPlot* technique [79] is a statistical method which allows to unfold the distributions of several contributions co-existing in a unique data sample. In this analysis it is exploited to categorise signal-like and background-like events. The *sPlot* technique makes use of a set of variables for which the distribution of all the sources of events are known, called *discriminating variables*. The latter is used to infer the unknown distributions of a second set of variables, referred to be the *control variables*. A basic assumption for this method to work, is that the discriminating and the control variables must be uncorrelated. In this analysis the discriminating variable is represented by the invariant mass distribution of the Λ_b^0 candidates, while the most relevant control variables are the invariant mass distributions of the $\Lambda_\mathrm{c}^+\overline{\mathrm{D}}^0$, $\overline{\mathrm{D}}^0\mathrm{K}^-$ and $\Lambda_\mathrm{c}^+\mathrm{K}^-$ systems.

Let us introduce a total number n of measurements $\boldsymbol{e} = (e_1, e_2, ..., e_n)$, called *events* in what follows, defining a data sample. Also, let us consider a number n_s of species populating the sample and a number n_k of average expected events for each of the k species ($k = 1, 2, ..., n_s$). Moreover, let $\boldsymbol{y}$ and $\boldsymbol{x}$ be a set of discriminating and control variables, respectively. A set of *pdf*s f_i is defined for the discriminating variables of the species. Finally, let us denote by $\boldsymbol{y}_e$ the values of the discriminating variables for an event e. Knowing the *pdf*s f_i, and having performed a fit to determine the yields of all the species, a weight for a fixed i species can be naïvely defined as:

$$P_i(\boldsymbol{y}_e) = \frac{n_i f_i(\boldsymbol{y}_e)}{\sum_{k=1}^{n_s} n_k f_k(\boldsymbol{y}_e)} \tag{36}$$

with n_i being the yield obtained for the i species. Now let us introduce $\boldsymbol{x}_e$ as the value taken by $\boldsymbol{x}$ for the event e, and a set of values $\boldsymbol{x'}$ defined by a neighbourhood of $\boldsymbol{x}$ of width $\delta\boldsymbol{x}$, centered around the values $\tilde{\boldsymbol{x}}$:

$$\boldsymbol{x'} = (\tilde{\boldsymbol{x}} - \delta\boldsymbol{x}, \tilde{\boldsymbol{x}} + \delta\boldsymbol{x}) \tag{37}$$

The weight P_i defined in Equation 36 can be used to build the distribution $\tilde{M}_i$ of $\boldsymbol{x}$, defining the number of events of the i type:

$$n_i \tilde{M}_i(\tilde{\boldsymbol{x}})\delta\boldsymbol{x} \equiv \sum_{e \subset \boldsymbol{x'}} P_i(\boldsymbol{y}_e) \tag{38}$$

where the sum runs over the events for which $\boldsymbol{x}_e \in \boldsymbol{x'}$. Following this construction, $\boldsymbol{x'}$ represents a bin of $\delta\boldsymbol{x}$ centered in $\boldsymbol{x}$, $n_i\tilde{M}_i(\tilde{\boldsymbol{x}})\delta\boldsymbol{x}$ represents the distribution of $\boldsymbol{x}$ obtained by “histogramming” the events using P_i as weight. On average, this procedures reproduces the *true* distribution $M_n(\tilde{\boldsymbol{x}})$ of $\boldsymbol{x}$. In fact on average, and in the limit of infinitesimal bin widths $\delta\boldsymbol{x}$, the discrete sum in Equation 38 can be replaced by:

$$E[\sum_{e \subset \boldsymbol{x'}}] \rightarrow \int d\boldsymbol{y'} \sum_{k=1}^{n_s} n_k f_k(\boldsymbol{y'}) \cdot \delta(\boldsymbol{x}(\boldsymbol{y'}) - \tilde{\boldsymbol{x}})\delta\boldsymbol{x} \tag{39}$$

Analogously, considering n_i as the expected number of events for the species i, Equation 38 becomes:

$$\begin{aligned} E[n_i\tilde{M}_i(\tilde{\boldsymbol{x}})] &= \int d\boldsymbol{y'} \sum_{k=1}^{n_s} n_k f_k(\boldsymbol{y'}) \cdot \delta(\boldsymbol{x}(\boldsymbol{y'}) - \tilde{\boldsymbol{x}}) \cdot \delta\boldsymbol{x} \cdot P_i(\boldsymbol{y'}) \\ &= \int d\boldsymbol{y'} \sum_{k=1}^{n_s} n_k f_k(\boldsymbol{y'}) \cdot \delta(\boldsymbol{x}(\boldsymbol{y'}) - \tilde{\boldsymbol{x}}) \cdot \delta\boldsymbol{x} \cdot \frac{n_i f_i(\boldsymbol{y'})}{\sum_{k'=1}^{n_s} n_{k'} f_{k'}(\boldsymbol{y'})} \\ &= n_i \int d\boldsymbol{y'}\ \delta(\boldsymbol{x}(\boldsymbol{y'}) - \tilde{\boldsymbol{x}}) f_i(\boldsymbol{y'}) \\ &\equiv n_i M_i(\tilde{\boldsymbol{x}}) \end{aligned} \tag{40}$$

with $M_n(\tilde{\boldsymbol{x}})$ being the true distribution of $\boldsymbol{x}$. However, in this construction the weight P_i implicitly depends on the *pdfs* of $\boldsymbol{x}$ via the test function $\delta(\boldsymbol{x}(\boldsymbol{y}) - \tilde{\boldsymbol{x}})$, which is equivalent to require fits to be performed into sufficient small bins in $\boldsymbol{x}$.

Assuming that the two sets of variables $\boldsymbol{x}$ and $\boldsymbol{y}$ are uncorrelated, the total *pdfs* $f_k(\boldsymbol{x}, \boldsymbol{y})$ which appear in Equation 40 factorize into the product $M_k(\boldsymbol{x}) f_k(\boldsymbol{y})$, leading to:

$$\begin{aligned}
E[n_i \tilde{M}_i(\tilde{\boldsymbol{x}})] &= \int\int d\boldsymbol{y'} d\boldsymbol{x'} \sum_{k=1}^{n_s} n_k M_k(\boldsymbol{x'}) f_k(\boldsymbol{y'}) \cdot \delta(\boldsymbol{x'} - \tilde{\boldsymbol{x}}) \cdot P_i(\boldsymbol{y'}) \\
&= \int d\boldsymbol{y'} \sum_{k=1}^{n_s} n_k M_k(\tilde{\boldsymbol{x}}) f_k(\boldsymbol{y'}) \cdot \frac{n_i f_i(\boldsymbol{y'})}{\sum_{k'=1}^{n_s} n_{k'} f_{k'}(\boldsymbol{y'})} \\
&= n_i \sum_{k=1}^{n_s} M_k(\tilde{\boldsymbol{x}}) \Big(n_k \int d\boldsymbol{y'} \frac{f_n(\boldsymbol{y'}) f_k(\boldsymbol{y'})}{\sum_{k'=1}^{n_s} n_{k'} f_{k'}} \Big) \\
&\neq n_i M_i(\tilde{\boldsymbol{x}})
\end{aligned} \tag{41}$$

Equation 41 does not give the same results as before because of the correction term in parentheses. However the extended log-likelihood can be introduced, which in this case looks:

$$\mathcal{L} = \sum_{e=1}^{n} \ln \Big(\sum_{k=1}^{n_s} n_k f_k(\boldsymbol{y}_e) \Big) - \sum_{k=1}^{n_s} n_k \tag{42}$$

and it can be observed that the correction term in Equation 41 is related to the inverse of the covariance matrix given by the second derivatives of $\mathcal{L}$, which is minimised by the fits:

$$V_{qr}^{-1} = \frac{\partial^2(-\mathcal{L})}{\partial n_q \partial n_r} = \sum_{e=1}^{n} \frac{f_q(\boldsymbol{y}_e) f_r(\boldsymbol{y}_e)}{(\sum_{k'=1}^{n_s} n_{k'} f_{k'}(\boldsymbol{y}_e))^2} \tag{43}$$

On average, and in the limit of small δx:

$$\begin{aligned}
E[V_{qr}^{-1}] &= \int\int d\boldsymbol{y'} d\boldsymbol{x'} \sum_{k'=1}^{n_s} n_{k'} M_{k'}(\boldsymbol{x'}) f_{k'}(\boldsymbol{x'}) \frac{f_q(\boldsymbol{y'}) f_r(\boldsymbol{y'})}{(\sum_{k'}^{n_s} n_{k'} f_{k'}(\boldsymbol{y'}))^2} \\
&= \int d\boldsymbol{y'} \sum_{k'}^{n_s} n_{k'} f_{k'}(\boldsymbol{y'}) \frac{f_q(\boldsymbol{y'}) f_r(\boldsymbol{y'})}{(\sum_{k'}^{n_s} n_{k'} f_{k'}(\boldsymbol{y'}))^2} \cdot \int M_{k'}(\boldsymbol{x'}) d\boldsymbol{x'} \\
&= \int \frac{f_q(\boldsymbol{y'}) f_r(\boldsymbol{y'})}{\sum_{k'=1}^{n_s} n_{k'} f_{k'}(\boldsymbol{y'})} d\boldsymbol{y'}
\end{aligned} \tag{44}$$

which can be used in Equation 41 to rewrite it as:

$$E[\tilde{M}_i(\tilde{\boldsymbol{x}})] = \sum_{k}^{n_s} M_k(\tilde{\boldsymbol{x}}) \cdot n_k \cdot E[V_{ik}^{-1}] \tag{45}$$

and inverting it, the initial distribution of interested is recovered:

$$n_i M_i(\tilde{\boldsymbol{x}}) = \sum_{k}^{n_s} E[V_{ik}] \cdot E[\tilde{M}_i(\tilde{\boldsymbol{x}})] \tag{46}$$

This result can be formulated as follow: when $\boldsymbol{x}$ and $\boldsymbol{y}$ are uncorrelated variables, a new weight P_i^s, referred in the following as *s-weight*, replaces the naïve weight:

$$P_i^s(\boldsymbol{y}_e) = \frac{\sum_{k=1}^{n_s} V_{ik} \cdot f_k(\boldsymbol{y}_e)}{\sum_{k'}^{n_s} n_{k'} f_{k'}(\boldsymbol{y}_e)} \tag{47}$$

With the above defined *s*-weight, the distributions of the control variables can be obtained from the *sPlot* histogram:

$$n_i \tilde{M}_i^s(\tilde{\boldsymbol{x}})\delta \boldsymbol{x} \equiv \sum_{e \subset \boldsymbol{x}'} P_i^s(\boldsymbol{y}_e) \tag{48}$$

and on average the true distributions are reproduced:

$$E[n_i \tilde{M}_i^s(\tilde{\boldsymbol{x}})] = n_i M_i(\boldsymbol{x}) \tag{49}$$

Hence the *s*-weighting procedure results in a set of *s*-weights for each of the species included in the model, for each of the measurements. In this analysis, *s*-weights are used to indicate how much a candidate is likely to belong either to the signal species, or to the background ones.

3.2.4 Hypothesis testing and confidence interval

The agreement between the data and model used in this analysis is assessed by statistical inference. The methods employed are based on the *hypothesis testing* procedure developed by Neyman and Pearson [80], formulated from the *null hypothesis* and *significance test* theories by Fisher [81].

In the Neyman scheme two hypotheses H_0 and H_1, respectively referred to as *null* and *alternate*, are tested based on the observed data. The test assesses the validity of one of the two hypotheses against the other. Let $\boldsymbol{x}$ be a set of measurements x_i, and S the space of all the possible outcomes. The space S is divided in two regions, the *critical region* w and its complementary $\overline{w}$, called *acceptance region.* The level of agreement of a hypothesis with the observations is determined by a function of the observations, called *test statistic* $t(\boldsymbol{x})$. If the test statistics $t(\boldsymbol{x})$ falls in the critical region w, then H_0 is rejected and H_1 is accepted. If $t(\boldsymbol{x})$ lies in the acceptance region $\overline{w}$, H_0 cannot be rejected. However, the separation of the regions could be not perfectly efficient, leading to some observations falling in the wrong partition, with a consequent contamination of the classes.

The test is adjusted by defining a critical region w such that the probability of losses, meaning the probability of rejecting H_0 when it is true, is kept smaller or equal to a fixed value α:

$$p(t \in w | H_0 \text{ is true}) = \int_w g(t' | H_0 \text{ is true})\ dt' \leq \alpha \tag{50}$$

with $g(t)$ being the *pdf* of the test statistic $t(\boldsymbol{x})$. The probability α is said *significance* of the test. On the other hand, the H_1 hypothesis could be rejected while it is true, with a probability β:

$$p(t \in \overline{w} | H_1 \text{ is true}) = \int_{\overline{w}} g(t' | H_1 \text{ is true})\ dt' = \beta \tag{51}$$

The probabilities α and β are called errors of the first and second type respectively. The test is prepared by fixing α, and minimizing β. Finally, the probability of correctly classify H_1 is called *power* of the test:

$$p(t \in w | H_1 \text{ is true}) = \int_w g(t' | H_1 \text{ is true})\ dt' = 1 - \beta \tag{52}$$

and in general it depends on the choice of H_1.

A concept closely related to hypothesis testing is the so-called *confidence interval* (CI) of a value of a unknown parameter θ [82]. The CI is a type of interval estimate that might contain the *true* value θ_{true} of the parameter under consideration, and it is defined from the choice of an associated *confidence level* (CL). The confidence interval is constructed in such a way that, in new possible measurements collected in the same conditions as the already observed ones, θ_{true} would be included in the interval a fraction CL of times, as the number of measurements tends to infinity. The CL quantifies the level of confidence that the true value of the parameter lies in the interval defined by the CI. Following this construction, a given confidence level characterises a *family* of confidence intervals. It is important to stress that a given CL value for a confidence interval does not represent the probability that the parameter value lies within the interval [14] . Instead, the confidence level of a CI gives a measure of the reliability of the estimation procedure.

Following the above definitions, a confidence interval of fixed CL for the parameter θ is constructed by finding all the true hypothetical values θ_{true} which are not rejected in a test of size 1 - CL, given an observed value θ_{obs} of the parameter. Strictly speaking, the confidence interval is built by repeating a hypothesis test for each value in the interval itself. This procedure is said *inversion of a hypothesis test.*

By definition, a confidence interval refers to a single observed value θ_{obs} of the parameter under interest. A *confidence belt* is then introduced as a set of confidence intervals of fixed CL for different possible outcomes of the measurement. This analysis exploits the *profile likelihood ratio test* technique to build confidence belts referred to a variety of hypotheses, as it is described in the next section.

3.2.5 Profile likelihood ratio test

The statistical significance of the results of this analysis is assessed by performing *profile likelihood ratio tests* [83]. Various hypotheses are tested, and hereafter a set of associated confidence intervals are built. In particular this analysis is interested into evaluating the significance of the observation of pentaquark candidates in $\Lambda_b^0 \to \Lambda_c^+ \overline{D}^0 K^-$ decays. The recourse to this procedure is motivated by the Neyman-Pearson lemma [80], which states that the likelihood ratio test is the *most powerful test* (i.e. it guarantees the maximum power 1 - β for a given significance α) to test two statistical hypotheses. The test is introduced in the following.

Let us introduce a model describing the observable μ, which depends on a set of *nuisance parameters* $\boldsymbol{\omega}$. We are interested to test a hypothesised value $\tilde{\mu}$ of the observable. In this analysis, μ is represented by the *strength* of the pentaquark presence in the sample and the remaining parameters of the amplitude model correspond to $\boldsymbol{\omega}$. In the following μ is assumed to be non-negative, which reflects the definition of the physically-allowed region for the observation of pentaquark signals. The *profile likelihood ratio* it is introduced as:

$$\lambda(\tilde{\mu}) \equiv \frac{\mathcal{L}(\tilde{\mu}, \hat{\boldsymbol{\omega}})}{\mathcal{L}(\mu_{MLE}, \boldsymbol{\omega}_{MLE})} \tag{53}$$

where μ_{MLE} and $\boldsymbol{\omega}_{MLE}$ are the maximum-likelihood estimators (MLE) of μ and $\boldsymbol{\omega}$ respectively. They are obtained by maximising the *unconditional*, i.e. with no imposed conditions, likelihood function at the denominator of Equation 53. In the numerator, the observable μ is kept fixed to the value $\tilde{\mu}$ which is under hypothesis, while $\hat{\boldsymbol{\omega}}$ is the MLE estimator of $\boldsymbol{\omega}$ of the *conditional* likelihood. The latter is conditioned having fixed the observable to the constant value $\tilde{\mu}$. From Equation 53 the test statistic $t(\tilde{\mu})$ can be defined as:

$$t(\tilde{\mu}) \equiv -2 \ln \lambda(\tilde{\mu}) \tag{54}$$

The global minimum of $t(\tilde{\mu})$ represents the best compatibility between the data and the hypothesised value $\tilde{\mu}$. Increasing values of $t(\tilde{\mu})$ reflect a higher level of disagreement between the considered hypothesis and the data.

By inversion of the profile likelihood ratio test (Sec. 3.2.4), it is possible to build a confidence interval for the observable μ. This interval contains all values μ_0 such that a *two-sided test* [15] of the null hypothesis $H_0 : \mu = \mu_0$ would not be rejected at a fixed level α of significance. The associated confidence level of the interval is α. Under the assumption of the null hypothesis being true, the Wilks' theorem [84] states that $t(\mu)$ asymptotically follows a χ^2 distribution. Basing on this result and

---

[14] As Neyman was pointing in his original paper [82]: "Consider now the case when a sample is already drawn, and the calculations have given [particular limits]. Can we say that in this particular case the probability of the true value [falling between these limits] is equal to α? The answer is obviously in the negative. The parameter is an unknown constant, and no probability statement concerning its value may be made."

[15] A statistical test is said two-sided if it tests the statistical significance of values which can be smaller or higher than the hypothesised value of the parameter under test.

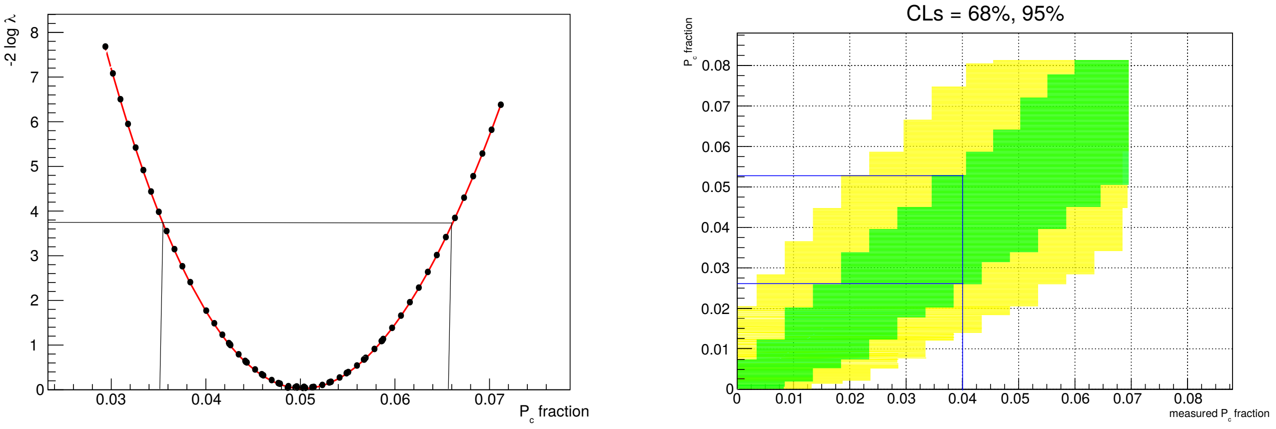

(a)

(b)

Figure 21: a) Profile likelihood ratio distribution obtained from pseudo-experiments, for a true value 0.05 of the P_c fraction. The vertical lines define the shortest CI interval of 95% CL. b) Confidence belt obtained using profile likelihood ratio tests from pseudo-experiments. Coverage region of 68% is highlighted in green, of 95% in yellow. For a measured value 0.04 of the P_c fraction, the [0.025, 0.052] interval with 95% CL is defined by the horizontal lines.

profiling the likelihood ratio in only one parameter (μ), the hypothesis H_0 is not rejected at a level α of significance when the following relation holds [83]:

$$t(\mu) < \chi^2_{1-\alpha}(ndof = 1) \tag{55}$$

Let us consider the particular case of $\alpha = 0.95$ representing a 95% confidence level interval. From Equation 55 the boundaries of the acceptance region are defined by the values of μ such that $t(\mu) = \chi^2_{0.05}(n.d.of. = 1) = 3.84$. Note that the above-defined acceptance region is referred to a unique true value of the parameter μ, which is however unknown when performing the statistical test on real data. Thus, a set of true values of μ are considered, and a profile likelihood ratio test repeated for each of them. The ensemble of acceptance regions obtained in this way defines a confidence belt for the hypothesised values μ_{true}, versus the (potentially) measured values μ_{obs}. A pedagogical example is shown in Figure 21, in which an arbitrary fit fraction value of 5% for a pentaquark state is tested on pseudo-experiments. A pseudo-sample is generated with a fixed pentaquark contribution. Next, a profile likelihood ratio test is performed by fitting the sample with the unconditional likelihood (i.e. fitting the fit fraction of the pentaquark), and for various hypotheses of the pentaquark fit fraction (with the pentaquark fraction being constrained in the fit). This procedure is repeated for a set of *true* contributions of pentaquarks, by generating different pseudo-samples and performing the profile likelihood ratio test over them. The confidence belt is built before the actual measurement of μ from the data, generally employing pseudo-experiments. Once the value of the parameter μ is measured in the experiment, a vertical line is drawn corresponding to it. The lower and upper boundaries of the CI defined by this measurement are given by the true values of μ corresponding to the interceptions of the confidence belt with the above-constructed vertical line. In the example in Figure 21, for a measured value 0.04 of the P_c fit fraction the shortest [16] 95% CL interval is given by the [0.025, 0.052] interval.

The above-described procedure results in confidence belts which are valid for setting *upper limits* and quoting *two-sided confidence intervals* in a *unified way*. The first case refers to the observation of a negligible value (or smaller than the experiment sensitivity) of μ. The latter corresponds to a measurement of μ which is different from zero, in a statistical meaningful way. Thanks to this unified construction, hypotheses a-priori of the measurement regarding the expected value of μ are not required.

---

[16] Remember that a given CL defines a family of confidence intervals. Therefore, a criterion must be defined to choose a CI. In this analysis the *shortest* interval related to a CL is chosen.

Moreover, the confidence belt is built *before* the actual experiment is performed. This is a key aspect, since confidence intervals naïvely built a-posteriori, basing on the observed data, might not fulfill the required coverage [85]. Basing on these properties, this statistical procedure can be considered similar to the unified approach of building confidence intervals proposed by Feldman and Cousins in [85].

3.2.6 Boosted Decision Tree classifiers

A number of techniques exists to address the problem of classifying observations into classes, such as categorising an event as signal or background. Methods based on multivariate-analysis, i.e. capable to combine several discriminating variables into one final discriminator, are particularly powerful. Among them, this analysis makes use of so-called *Boosted Decision Trees* (BDT) classifiers to enhance the signal and background separation in the data sample. A decision tree is defined by a consecutive set of nodes representing rectangular cuts with binary outcome, and by final decisions referred to as leaves. A sketch of a decision tree structure is shown in Figure 22.

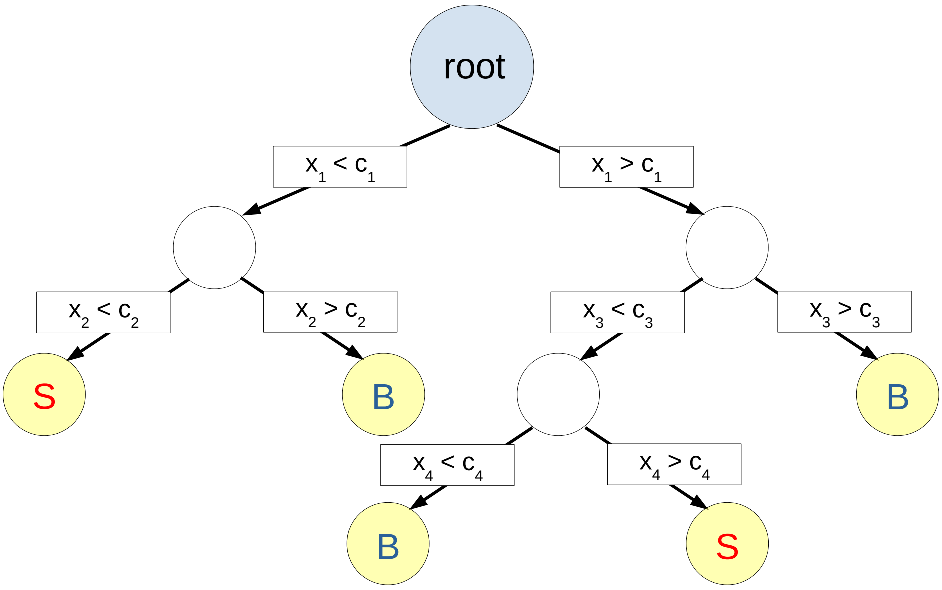

Figure 22: Schematic structure of a decision tree. A consecutive set of nodes represents a rectangular cuts with binary outcome. The final classifier responses (either S or B) are represented by the tree leaves.

A decision tree has to be trained on a data set which already provides the outcome of the classification process, such as simulated samples in which events are a-priori generated and labelled in different categories. An important concept is the *separation gain*, which measures the separation between the different populations consisting the sample, determined by a specific metric function. As example, one of the most used metric is the so-called *Gini-index* [86], measuring the separation as $p(1-p)$, with p being the purity of the partitions determined by the decision tree. The node structure of the classifier is optimised by maximising recursively the separation gain between the nodes. Equivalently, the optimisation of the decision tree proceeds through the minimisation of the *classification loss function*, which represents the mis-classification risk in a classification problem.

Despite decision trees are easy to interpret and relatively fast to train, a single independent tree is not very strong in classification power. A common approach is to consider an ensemble of independent trees, referred to as *random forest*, which combines the outcomes of all the trees to extrapolate its final decision. In this way, many weak learners are combined in a strong classifier. Each tree of the forest is created iteratively, and a weight is assigned to its output representing the related accuracy. Many methods how to train a random forest have been developed. In this analysis the *boosting* method is employed, which assigns to each sample a weight based on its mis-classification, after each iteration.

The importance of mis-classified samples is then enhanced in the next iterations with respect to the correctly-classified ones, so that the next trees improve the classification power over them. Random forests trained with boosting techniques are referred to as boosted decision trees (BDTs). The *gradient boosting* method is employed in this analysis for training BDTs [87]. This technique generalises the definition of the BDT model by allowing the optimisation of arbitrary differentiable loss functions, and proceeds by iteratively choosing a function which points in the negative gradient direction of the loss.

Although their power in addressing classification problems, BDTs are subjected to *overtraining*. By construction, they tend to optimise their classification response to specific features of the training sample which are not representative of a more general (or different) sample. As example, BDTs can be overtrained by statistical fluctuations of the training sample. This issue is approached by exploiting the *bootstrap aggregating* method, also known as *bagging* [88]. Given a training sample, bagging randomly generates a number of sub-samples by sampling uniformly and with replacement the initial sample. This means that the same elements might be included in multiple sub-samples. The BDT is then trained on each of the sub-sample, and the final response is obtained by averaging or voting the single outputs. Following this procedure, the possibility of overtrain a BDT is much reduced.

3.3 Software framework

This analysis makes use of an elaborate software framework, which relies on a number of software packages developed in the specific context of this measurement or which are provided by the LHCb Collaboration. Also, modern strategies of analysis preservation and replicability are employed, to ensure the possibility to reproduce the analysis in a straightforward way and to preserve it in the future. The main software strategies and packages are described in the following.

3.3.1 Software for particle identification of final-state tracks

Usage of particle identification (PID) information is of crucial importance in the LHCb experiment. They hold a key role for defining a highly-efficient selection of signal events and an effective rejection of background constituted by mis-identified particles. Particle identification of charged particles involve all the devoted subdetectors of LHCb such as the RICH detectors, the calorimetric system and the muon detectors (Secs. 2.2-2.3.2). A good description of their combined response, which also depends on the kinematic of the particles, on the beam conditions, and on event-level quantities, is non trivial in the simulation. Hence, data-driven techniques have been developed in LHCb to measure the performances (efficiency and purity) of PID selections of final-state charged particles (protons, muons, charged kaons and pions). Calibration data samples are provided where candidates have been selected without the use of PID information. Then, arbitrary particle identification requirements can be tested. The response of the PID variables (such as the *PIDi* and *ProbNNi* variables introduced in Section 2.3.2) are parametrised in a set of variables, and their performances determined in function of them. Often, the most relevant variables are the particle momentum and the track multiplicity in the event. Parametrised in such a way, the obtained PID performances are valid for any track regardless if it belongs to the calibration sample or not. This allows any analysis in LHCb to rely on the above-described calibration of the PID variables and performance determination.

The *PIDCalib* software package [89], developed by the LHCb Collaboration, collects all the tools needed for evaluating the performances of PID selections. The full parametrisation of the PID performances allows to build efficiency look up tables from which the efficiency of a particular PID selection can be extracted and combined with the efficiencies of the remaining selections.

3.3.2 Boosted Decision Trees classifiers for selection of charmed hadrons

Hadronic decays of beauty hadrons to final states with charmed hadrons play an important role in the LHCb physics program. However, they are experimentally challenging because of the typical large multiplicity of final state charged particles, $\sim 5-8$ tracks, resulting in a large combinatorial background. The latter can be reduced by applying PID selections on the final state particles. However, the PID variables introduced in Section 2.3.2 have an important limitation: they neglect the existing correlations between particles in the same events, and in particular originating from the same decay process. In fact, the PID calibration is performed assuming that all particles are uncorrelated.

A more powerful selection can be achieved by making use of the correlations between the particle identification information of these particles. Within this context, [90] introduced the idea of multivariate classifiers trained to act as PID-like variables on non-prompt charm hadrons. Boosted Decision Trees classifiers have been developed, referred to as *D-from-B BDTs*, and re-optimised in [91] in the context of the branching fraction measurement of $\Lambda_b^0 \to \Lambda_c^+ \overline{D}^0 K^-$ decays. These BDTs are trained in a purely data-driven way, by combining raw-PID information from the PID detectors and kinematic variables of the c-hadron daughters. Calibration samples of $\Lambda_b^0 \to \Lambda_c^+ \pi^-$, $B^- \to D^0 \pi^-$ and $B_s^0 \to D_s^+ \pi^-$ decays are employed to train the BDTs to classify non-prompt $\Lambda_c^+(\to pK^-\pi^+)$, $D^0(\to K^-\pi^+)$, $D_s^+(\to K^+K^-\pi^+)$ charm hadrons in generic b-decays.

D-from-B BDTs have been proved to outperform standard cut-based or likelihood-based selections of c-hadrons in signal selection efficiency and background rejection. Their power mainly comes from the exploitation of the correlations in the responses of the PID detectors to the detection of the c-hadrons daughters, in contrast to selections based on standard PID variables. *D-from-B* BDTs are employed in this analysis for the selection of Λ_c^+ and $\overline{D}^0$ candidates.

3.3.3 TensorFlow-based framework for amplitude fits

TensorFlow [7] is an open-source software library for data-flow programming, which has the potential to cross a large variety of tasks. It has been internally developed by Google within the Google Brain project [92], and released with open-source license at the end of 2015. It was initially developed for machine learning applications, and optimised to process large data-flows in highly-parallelised streams over multiple computational architectures as CPUs and GPUs.

TensorFlow allows developers to create *data-flow graphs*, structures that describe how data moves through a graph, or a series of processing *nodes*. Each node in the graph represents a mathematical operation, and each connection between nodes is a multidimensional data array, or *tensor*. Data-flow graphs are characterised by the relations existing between the data and operations, rather than by the data itself. Therefore they are optimal in order to identify processes that can be executed in parallel, and distributed over multiple devices and architectures.

Despite that the original purpose of TensorFlow has been to address machine learning problems, its flexibility can be exploited to process in an efficient way the large amount of data that the experiments at the LHC have collected in the last years. A pioneering software library based on TensorFlow, *TensorFlowAnalysis* [93], is available in LHCb. It collects a set of scripts and functions useful for data analysis.

In this analysis a complete framework for amplitude fitting has been implemented from first principles, the *TOAST fitter* [94]. It relies on TensorFlow and on the basic functions provided by the TensorFlowAnalysis library, such as the definitions of the main variable types, the mathematical operations and the transformations between reference systems. The TOAST framework implements the core part of the amplitude fit: the definition of the resonances and decays structures, the building of the amplitude model, the handling of the amplitude parameters and the operations between them, the fit itself, the input/output handling of the data and configurations. The framework is integrated with *PyROOT* [95], the Python-based extension of the *ROOT* data analysis framework widely used in High Energy Physics. This grants the access to the vast and standardised collection of libraries, classes and functions implemented in ROOT. In particular, the highly-optimised likelihood minimisation package of ROOT, *Minuit* [96, 97], is exploited by the amplitude fitter.

The TOAST fitter is fully-configurable via configuration files and options provided at command prompt level. Scripts for performing pseudo-experiments, for fitting and for plotting are provided, and they can be configured to be used for the different use-cases. The fitter is fully generic, and applicable to any amplitude fits of decay channels with similar spin structure of the $\Lambda_b^0 \to \Lambda_c^+ \overline{D}^0 K^-$ channel. This implies that, for most of the cases, analysts only need to configure the existing scripts to perform an amplitude fit instead of writing their own fitting routines. Development are ongoing to further generalise the fitter to decays with different spin structures. The fitter is capable to run over CPU- or GPU-based systems either, thanks to the flexibility provided by TensorFlow. The exact same code runs over different architectures, which are enabled by setting a single configurable option. Configurations are provided to run the fitter over local systems, over the CERN login machines *lxplus* [98], and on the centralised batch system of CERN [99]. The fitting framework is integrated with the strategies of analysis preservation and reproducibility that are described in Section 3.3.4. A modularised approach is embraced in the framework: all the external libraries are included as so-called *submodules* [100], in dedicated sub-directories of the fitter repository. This allows to keep the different software libraries independent to each other, a key point in order to be able to develop them independently. The modularised approach is particularly powerful when using libraries which are co-used by other software projects, thus evolving on a time schedule which might be different to the own software. The code of the TOAST fitter [94] is made public with LGPGL license [17] and re-usable. This analysis, and specifically its amplitude fitter TOAST, represents one of the first examples in the LHCb collaboration of application of TensorFlow in amplitude fits.

Considerable efforts have been invested in the implementation of the fitting framework, mainly due to its basing on recent computing paradigm and libraries. On the other hand, the native parallelism offered by TensorFlow grants immediate benefits from the point of view of the fitting execution time. Amplitude fits are renowned for their computational complexity, and with standard code they can take hours to days to be performed. Without any particular optimisation of the TOAST framework code for what concerns the execution time, in this analysis the generation of pseudo-experiments and amplitude fits of data with about ~ 50 variables takes $\sim 5 - 30$ minutes on a 8-threads CPU mounted on a commercial laptop. The most expensive process of the fit is the minimisation of the likelihood: performing it on a non recent laptop GPU takes on average $\approx 40 - 50\%$ less time. A dedicated optimisation of the code would surely improve these performances, especially for running over GPU-based systems. Nevertheless these numbers should be taken with a grain of salt, because the complexity of amplitude fits, and therefore their execution time, widely depends on the particular problem and amplitude model. However, TensorFlow-based frameworks show great potential to drastically reduce the computational resources needed by amplitude fits, even with practically no optimisation of the code.

3.3.4 Strategies of analysis preservation

The LHC provided a un-precedent high number of pp collisions to the experiments, resulting in vast data samples collected over Run 1 and Run 2. Together with the large scale of the collaborations, which extend from hundreds to thousands of scientists, the data preservation and the capability of reproducing analysis results in the future are gaining in importance and they are taking a large role in the analysis "good-practices". A comprehensive summary of the main techniques adopted by CERN experiments for analysis preservation is presented in [102]. The analyses of the $\Lambda_b^0 \to \Lambda_c^+ \overline{D}^0 K^-$ channel (starting with the branching fraction measurement, to the current amplitude analysis) make use of advanced strategies of data preservation, and have represented prototypes of "preserved and reproducible" measurements in LHCb.

The full analysis code [103], comprehending source code and scripts, is hosted on GitLab [104], a web-based Git-repository manager widely used by large technology companies. It provides easy tools for team-collaboration on software development, and all the LHCb software projects are hosted through it. Users can develop their code or improve parts of a software package by working on *branches* or *forks* of the main software repository. They can submit their changes in *merge requests*, so that other developers can review it and spot possible mistakes or room for improvements. Once the merge request

---

[17] *GNU Lesser General Public License* (LGPL) [101] is a free-software license. It allows developers to use and integrate a software component (released under the LGPL) into their own (even proprietary) software without being required to release the source code of their own components. However, any developer who modifies an LGPL-covered component is required to make their modified version available under the same LGPL license.

has been reviewed and accepted, the related code will be part of the main software project. This analysis also embraces the so-called *Continuous Integration* (CI) integrated within GitLab. The CI is a software development practice in which the code is built and tested every time that the developer pushes it to the repository, minimising the occurrences that the changes in the code break the existing software. Continuous Integration builds are running over dedicated servers: some CERN Virtual Machine [105] instances have been configured as CI servers of this analysis, on slots provided by the CERN OpenStack service [106].

The analysis workflow is fully automated exploiting the *Snakemake* functionalities [107]. Snakemake is a workflow management tool focused on creating reproducible and scalable data analyses in a human readable Python language. Snakemake-based workflows are defined by *rules*, each of them have input and output defined by the developer. Once all the input and output relationships between the rules have been defined, Snakemake builds automatically the workflow needed to produce the required outputs. With a well defined workflow, analysis can be literally run with one single command making straightforward to reproduce them. To avoid steps of the analysis, i.e. specific rules, to be re-run when it is not required, Snakemake detects which of the needed outputs are missing, and triggers the execution of the related rules only. If the output of an intermediate rule, which is used as input for a subsequent part of the workflow, needs to be reproduced, all the rules in the workflow which depend of that file are re-run. With a simple adaption of the code, it is also possible to instruct Snakemake to check for eventual modifications of the code between commits of the repository, to trigger a re-run of the related rules. All these features grant a full consistency of the intermediate and final results of the analyses, at the same time optimising the execution time and the computing resources.

Reproducibility of the analysis is finally ensured by detailed instructions provided in the GitLab repository how to set the needed software requirements, and how to run it. Configurations to run the analysis over multiple platforms, like on the *lxplus* machines at CERN, on local clusters of the Heidelberg University or on local machines, are provided.

The analysis is also integrated with the Docker [108] application. Docker is a software that performs operating-system-level virtualisation, by running software packages called *containers*. Containers are isolated from each other and bundle their own application, tools, libraries and configurations. All containers are run by a single operating-system kernel and are thus more lightweight than standard virtual machines. Containers are created from *images* that specify their precise contents. Docker images into which is possible to run the analysis are also shipped with the analysis code. They allow to run the analysis on any local or cluster system with Docker installed, without any specific software requirement on the hosting machine. Docker images are also used to configure the instances of the CI servers.

Data and simulated samples used for this analysis are stored on dedicated EOS [109] space at CERN, for preservation and to make easier the analysis to be reproduced. EOS is a disk-based, low-latency storage service provided by CERN. The main target area for the service is physics data analysis, which is characterised by many concurrent users, a significant fraction of random data access and a large file-open rate.

4 Data selection and mass fits

The data sample used in this analysis must first be selected online by the L0, HLT1 and HLT2 trigger systems of LHCb introduced in Section 2.3.3, then reconstructed offline, and selected by a dedicated stripping selection (Sec. 2.3.3). Finally, the sample is refined by selection criteria specific to this analysis. The online and offline selections are detailed in Section 4.1.

Once the signal data sample is defined, eventual multiple signal candidates present in the same event are removed as it is described in Section 4.2. Events are then categorised to be signal- and background-like by performing mass fits based on the *sPlot* technique introduced in Section 3.2.3. In the branching fraction measurement of the channel under analysis [6], three-dimensional fits in the Λ_b^0, Λ_c^+, $\overline{D}^0$ invariant mass distributions were required in order to fit the partially-reconstructed channel $\Lambda_b^0 \to \Lambda_c^+ \overline{D}^{0*} K^-$. In this analysis only the fully-reconstructed decay $\Lambda_b^0 \to \Lambda_c^+ \overline{D}^0 K^-$ is investigated, thus a simpler and more stable one-dimensional fit in the Λ_b^0 invariant mass distribution is considered. Three-dimensional and one-dimensional fits on the signal channel $\Lambda_b^0 \to \Lambda_c^+ \overline{D}^0 K^-$ are compared in Sections 4.3.

4.1 Data selection

The $\Lambda_b^0 \to \Lambda_c^+ \overline{D}^0 K^-$ process investigated in this analysis proceeds through sequential decays of the Λ_b^0, Λ_c^+ and $\overline{D}^0$ particles, as sketched in Figure 23. The Λ_b^0 is produced in the primary vertex (*PV*) of the pp interaction, and flies in the detector for ∼mm-cm before decaying into the Λ_c^+, $\overline{D}^0$ and K^-. The Λ_c^+ and $\overline{D}^0$ fly for a similar distance, before decaying into their stable daughters. Reconstructing the final state particles of the overall decay (the bachelor K^- from the Λ_b^0 and the Λ_c^+, $\overline{D}^0$ daughters), the secondary vertices (SVs) of the Λ_b^0, Λ_c^+ and $\overline{D}^0$ decays can be reconstructed. The flight distance of the decaying particles is large enough to be directly measured in the vertex detector. Thus requirements on the displacement of particles with respect the PV and the SVs are the key ingredients for discriminating signal candidates from background. Candidates are also required to have a relatively large momentum, in order to reject background from soft collisions. These are the main requirements applied by the online trigger selection, and they are detailed in Section 4.1.1.

The offline selection is more sophisticated, and makes use of particle identification information and BDT classifiers trained to reject background. It is described in Sections 4.1.2-4.1.3.

4.1.1 Online selection

Events are first processed by the L0 hardware trigger. For the specific case of this analysis, all events passing the *L0Physics* decision are considered. This decision is positive if at least one of the L0 physics-trigger lines [18] results in a positive decision. The most relevant L0 trigger line for the signal channel of this analysis is the *L0HadronDecision* line. It selects events with a relatively large transverse energy deposit in the hadronic calorimeter, to reject background events of elastic or soft collisions. The *L0HadronDecision* energy thresholds are listed in Table 7, depending on the year of data taking. The efficiency of the L0 trigger selection on $\Lambda_b^0 \to \Lambda_c^+ \overline{D}^0 K^-$ decays is $\sim 35-45\%$ for Λ_b^0 particles decaying in the detector acceptance. The L0 trigger efficiency for this channel is not too high mainly because of

---

[18] L0 trigger lines are split between physics and operational ones. The latter are implemented for luminosity measurement and rejection of events with too high pile-up.

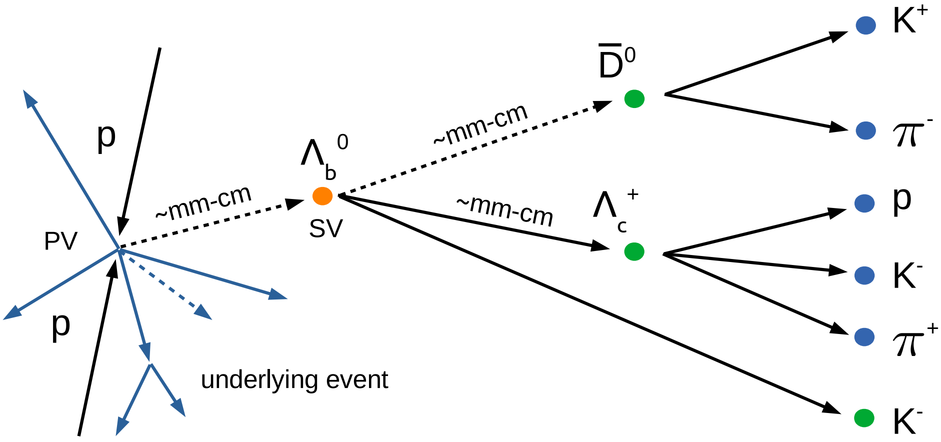

Figure 23: Sketch of the $\Lambda_b^0 \to \Lambda_c^+\overline{D}^0K^-$signal decay. The Λ_b^0 is produced from the primary vertex (PV) of the pp interactions and flies for ~mm-cm, before decaying into the Λ_c^+, $\overline{D}^0$, K^- particles (green dots). The Λ_c^+ and $\overline{D}^0$ further decay into the final-state particles (blue dots). Dotted lines represent the path of neutral states, which cannot be detected by the tracking detectors. Other particles produced in the PV, and their eventual decay products, represent background from the underlying event.

the large number of final-state particles, which result in a relatively high chance for particles to escape from the calorimeter acceptance.

	2011	2012	2015	2016	2017, 2018
E_t threshold	3.5 GeV	3.7 GeV	3.6 GeV	4.0 GeV	3.8 GeV

Table 7: Thresholds of the transverse energy deposited in the hadronic calorimeters for the *L0HadronDecision* trigger line, depending on the year of data taking.

Events must then trigger a positive *Hlt1TrackAllL0* decision [110]. This trigger line selects events which include a well reconstructed track with a sufficient number of hits in the tracking detectors and a small track-χ^2 from the HLT1 reconstruction. The track is also required to have a relatively large transverse momentum and impact parameter (IP) from the primary vertex, to reject prompt background. The requirements are specified in Table 8. The selection efficiency of the HLT1 requirements on the $\Lambda_b^0 \to \Lambda_c^+\overline{D}^0K^-$ channel is $\sim 50-55\%$, on L0-selected events. The trigger efficiency is limited by the relatively small momenta carried by the final-state particles of this channel, since the initial Λ_b^0 momentum has to be spread between the six final particles.

Quantity	Cut value
Kinematic cuts	$p > 10$ GeV$/c, p_t > 1.7$ GeV$/c$
Minimum number of VELO hits	10
Minimum number of IT hits (x2) + OT hits	17
Reconstruction cuts	$track\text{-}\chi^2/ndof < 2.$
Displacement cut	$IP(PV) > 100\ \mu$m, $IP\ \chi^2(PV) > 16.$

Table 8: Requirements of the *Hlt1TrackAllL0* trigger line. Each hit of the Inner Tracker (IT) is given a weight of 2 to account for the smaller number of tracking layers in the IT region, with respect the number of active sensor layers in the Outer Tracker region (see Section 2.1).

Finally, events must pass at least one of the *Hlt2Topological* trigger lines [111], a set of inclusive trigger lines based on BDT classifiers trained to select $n = 2, 3, 4$-body B decays with high signal efficiency and large background rejection. Tracks which are input to the HLT2 topological lines are required to have a relatively large momentum. A small track-χ^2 from the HLT2 reconstruction and a large $IP\ \chi^2$ are required to suppress background from ghosts (reconstructed tracks which do not correspond to real particles intersecting the detector) and prompt particles. A summary of the requirements on the input particles of the *Hlt2Topological* trigger lines is listed in Table 9. The selection efficiency of the HLT2 requirements on the $\Lambda_b^0 \to \Lambda_c^+ \overline{D}^0 K^-$ channel is $\sim 50\%$, on L0- and HLT1-selected events.

Quantity	Cut value
Kinematic cuts	$p > 5$ GeV$/c, p_t > 0.5$ GeV$/c$
Reconstruction cuts	$track\text{-}\chi^2/ndof < 5.$
Displacement cut	$IP\ \chi^2(PV) > 16.$

Table 9: Requirements on the input particles of the *Hlt2Topological* trigger lines.

An important point of the HLT2 topological trigger lines is how the candidates are built. Two input particles are combined to form a two-body object. Another input particle is added to the two-body object to build a three-body object. A fourth particle is added to the three-body object to constitute a four-body candidate. Thus, an n-body candidate is formed by combining an (n - 1)-body candidate and an additional particle, not by combining n particles. This is a crucial difference, and it greatly improves the efficiency of the HLT2 topological lines [111].

4.1.2 Selection of the offline processing

Events which pass the online trigger selection are reconstructed offline, and further selected by the *X2LcD0KD02KPiBeauty2Charm* stripping line. This line is constructed to select $\{\Lambda_b^0, B^0, B_s^0\} \to \Lambda_c^+ \overline{D}^0 K^-$ decays, with the $\overline{D}^0$ decaying into $K^+\pi^-$. The line requires that events have passed any of the *Hlt2Topological* trigger lines or any of the *Hlt2*IncPhi* lines. The latter are not relevant for this analysis. Events with more than 500 tracks reconstructed as long tracks are discarded by the stripping line, since a too high track multiplicity could lead to a too large rate of fake signal candidates built from combinatorial background. In 2018, the data taking period with the highest track multiplicity per event, the average number of reconstructed long tracks has been ~ 100 per event and about 98% of events had less than 500 long tracks.

The reconstructed final state particles p, K, π which are input to the stripping selection are required to be reconstructed as long tracks, and to fulfil a requirement on the *clone distance* [112]. This quantity is useful to reject clone tracks which are sharing only few hits in the tracking detectors but are very close in phase-space. Loose cuts on the momentum are applied to the final state particles p, K, π. They are required to be well reconstructed based on their $track\text{-}\chi^2/ndof$ value resulting from the Kalman fit performed in the offline reconstruction, and to have a small *track ghost-probability* (see Section 2.3.2). Finally, they are required to be displaced from the primary vertex of the pp interaction by requiring a large impact parameter χ^2 resulting from the vertex fit. A summary of these base cuts on the final state particles is listed in Table 10.

As next step, the intermediate Λ_c^+ and $\overline{D}^0$ are built from the previously-selected final state particles applying further selection cuts. Loose particle identification requirements are applied to the p, K and π particles. In particular, it is asked that the pions a have small probability to be identified as kaons. All two-particle combinations used to form the c-hadrons are required to have a small distance of closest approach. A cut on the minimum value of the summed transverse momentum of the c-hadron daughters is applied, and at least one daughter is required to have large momentum and to be well reconstructed. Finally, the combined invariant masses of the daughters must be close enough to the masses of the respective c-hadrons. These selection cuts are detailed in Table 11, and are applied

Quantity	Cut value
Kinematic cuts	$p > 1$ GeV/$c, p_t > 0.1$ GeV/c
Reconstruction cuts	$track\text{-}\chi^2/ndof < 3.$, $track\ ghost\text{-}probability < 0.4$
Displacement cut	$IP\ \chi^2(PV) > 4.$

Table 10: Base selection cuts applied to the final state particles by the *X2LcD0KD02KPiBeauty2Charm* stripping line.

Quantity	Cut value
PID on p and K	$PIDp > -10.$, $PIDK > -10.$
PID on π	$PIDK < 20.$
Distance of closest-approach	$DOCA < 0.5$ mm
Sum of daughters' p_t	$\sum_{i\in\{daughters\}} p_{t,i} > 1.8$ GeV/c
Leading daughter	$track\text{-}\chi^2/ndof < 2.5$, $p > 5.$ GeV/$c, p_t > 0.5$ GeV/c
Combined invariant mass, Λ_c^+	$\lvert m - m_{\Lambda_c^+}\rvert < 0.1$ GeV/c^2
Combined invariant mass, $\overline{D}^0$	1764.85 MeV/$c^2 < m < 1964.84$ MeV/c^2

Table 11: Selection cuts applied by the stripping selection to the final state particles, to form the Λ_c^+ and $\overline{D}^0$. The $PIDj$ variables are the differences in the log-likelihood for each track between the j mass hypothesis and the pion mass assignment, as defined in Section 2.3.2. The cuts are applied independently to the Λ_c^+ and $\overline{D}^0$ candidates.

independently to the Λ_c^+ and $\overline{D}^0$.

After that, a vertex fit is performed combining the c-hadron daughter particles, and cuts are applied to the Λ_c^+ and $\overline{D}^0$ candidates. Prompt c-hadrons are rejected by cutting on the χ^2-distance calculated with respect to the related primary vertex. The decay vertices of the c-hadrons are required to be well reconstructed by the vertex fit. The c-hadrons also have to point downstream with respect to the PV, using the cosine of the angle between the hadron momentum and the vector pointing from the PV to the hadron vertex. The above-mentioned selection is listed in Table 12.

The Λ_b^0 signal candidates are formed from the previously-built c-hadron candidates and the bachelor K^-, applying the final stripping selection. The bachelor track is required to have large momentum, and to be well reconstructed. A cut on the minimum value of the summed transverse momentum of the b-hadron (including eventual soft photons) is applied. At least one b-daughter (referred to as *b-leading daughter*) is required to have large momentum, to be well reconstructed, and to be displaced from any PV having large impact parameter value and χ^2. The b-hadron candidate must point back to the best primary vertex, using the cosine of the angle between its momentum and the vector pointing from the PV to the decay vertex. The b-hadron is required to originate from the best primary vertex selecting on the impact parameter χ^2, and its decay vertex has to be well reconstructed. Combinatorial background from the PV is rejected requiring the b-hadron to have a sufficiently large lifetime computed with respect the best primary vertex. Finally, the combined invariant mass of the b-daughters must be close

Quantity	Cut value
Distance to the PV	$\chi^2 - distance(PV) > 36.$
Decay vertex quality	$vertex\text{-}\chi^2/ndof < 10.$
Decay direction	$\cos(\frac{\boldsymbol{p}_{c-hadron}\cdot \hat{dir}(PV \to decay\ vertex)}{\lvert \boldsymbol{p}_{c-hadron}\rvert}) > 0.$

Table 12: Selection cuts applied by the stripping selection to the Λ_c^+ and $\overline{D}^0$ candidates.

enough to the Λ_b^0 mass. The cuts used to build the Λ_b^0 signal candidates are reported in Table 13.

Quantity	Cut value
Bachelor K	$\textit{track-}\chi^2/ndof < 2.5$, $p > 5.$ GeV$/c, p_t > 0.5$ GeV$/c$
Sum of b-daughters p_t	$\sum_{i\in\{b-daughters\}} > 5.$ GeV$/c$
Leading b-daughter	$\textit{track-}\chi^2/ndof < 2.5$, $p > 10.$ GeV$/c, p_t > 1.7$ GeV$/c$, $\chi^2 - IP(any\ PV) > 4.$, $IP(any\ PV) > 0.1$ mm
Decay direction	$\cos\left(\frac{\boldsymbol{p}_{\Lambda_b^0}\cdot \hat{dir}(PV\rightarrow decay\ vertex)}{\lvert\boldsymbol{p}_{\Lambda_b^0}\rvert}\right) < 0.999$
b-hadron production vertex	$\chi^2 - IP(PV) < 25.$
Decay vertex quality	$\textit{vertex-}\chi^2/ndof < 10.$
b-hadron lifetime	$\textit{lifetime} > 0.2$ ps
b-daughters comb. invariant mass	5.2 GeV$/c^2 < m < 6.$ GeV$/c^2$

Table 13: Selection cuts applied by the stripping selection to the Λ_c^+, $\overline{D}^0$ and bachelor K^- to form the Λ_b^0 candidates. The leading b-daughter is the daughter which satisfies all the requirements specified; the leading daughter can be ambiguous.

4.1.3 Final analysis selection

In this analysis additional cuts are applied on top of the stripping selection, to purify and better identify the signal candidates. The analysis selection is based on that of the first observation and branching fraction measurement of the $\Lambda_b^0 \to \Lambda_c^+\overline{D}^0K^-$ decay channel [6]. A more detailed discussion on the selection criteria can be found in [6], while in this Section they are only summarised.

The signal decay could be affected by a variety of background channels where a final state particle has been mis-identified. This could possibly lead to narrow structures peaking in the mass distributions. Four narrow peaks are present in the signal channel, as shown in Figures 24-25. Two are in the K^+K^- mass distribution, originated from ϕ mesons where a kaon has been misidentified as the proton from the Λ_c^+ decay. Similarly, two $D^*(2010)^-$ peaks are visible in the $\overline{D}^0\pi^-$ mass distribution, where to the K^- (the bachelor particle, or the Λ_c^+ daughter) is assigned the π^- mass. These background channels are vetoed by excluding the ϕ and $D^*(2010)^-$ peaks in the $K^+K^-$and $\overline{D}^0\pi^-$ mass distributions respectively.

Particle identification requirements are of crucial importance to efficiently suppress background in decays with a large number of final state particles like in this analysis. A standard *ProbNNK* PID cut is applied to the bachelor K^-, and cuts based on the responses of the *D-from-B* BDT classifiers are applied to select the Λ_c^+ and $\overline{D}^0$ (see Section 3.3.2).

Cuts are applied to the p $K^-\pi^+$, $K^+\pi^-$, $\Lambda_c^+\overline{D}^0K^-$ invariant mass combinations around the Λ_c^+, $\overline{D}^0$ and Λ_b^0 nominal masses, respectively. The mass cuts are relatively loose, to allow a proper parametrisation of the combinatorial background by the *sPlot* technique employed in the mass fits.

Finally, a kinematic fiducial region is defined in the transverse momentum and pseudo-rapidity space of the Λ_b^0 candidate.

A summary of the analysis selection cuts is listed in Table 14.

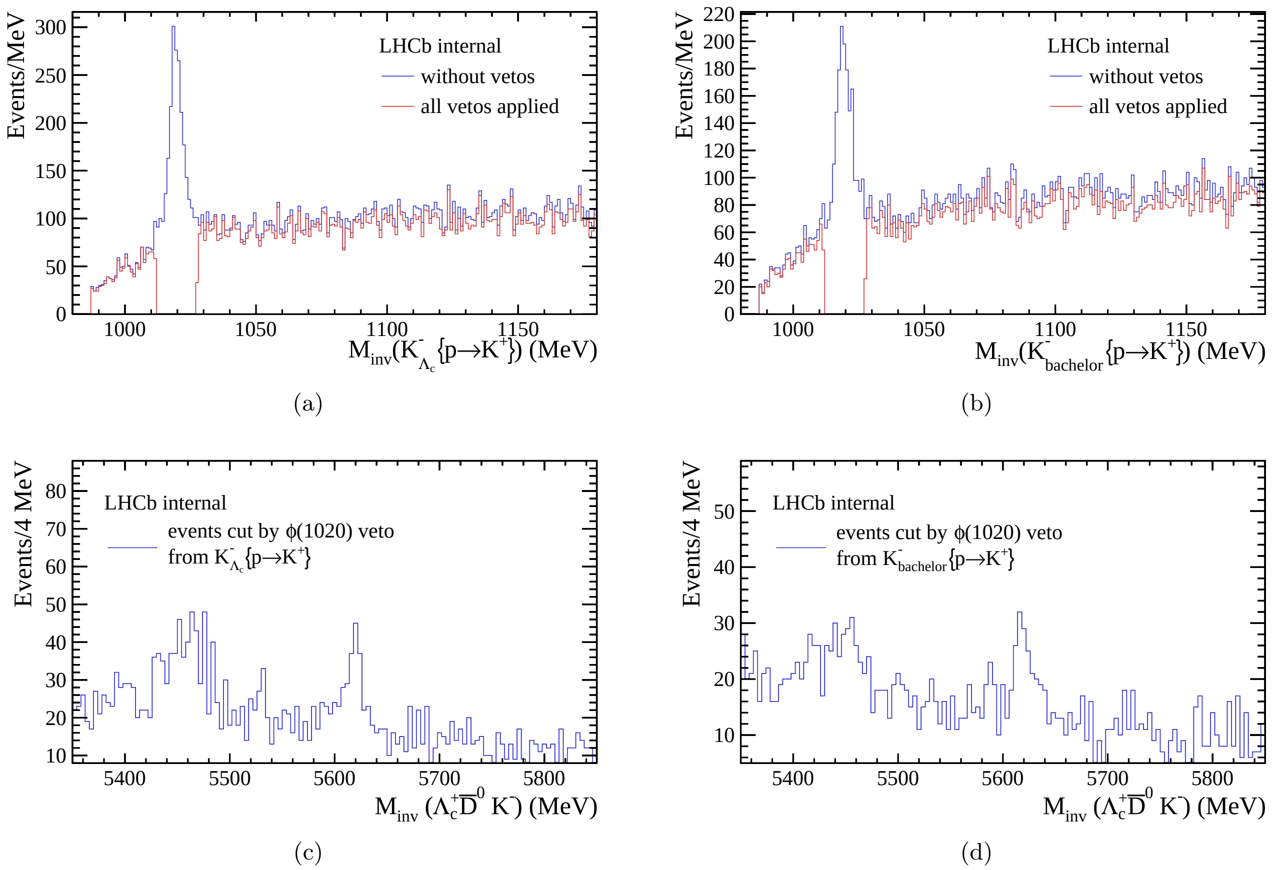

Figure 24: K^+K^- invariant mass distributions with the vetoed ϕ signal (a, b), and Λ_b^0 invariant mass distribution of the events rejected by the vetos (c, d). The kaon mass is assigned to the proton candidate, which is then combined either with the kaon from the Λ_c^+ decay (a, c), or with the bachelor kaon (b, d). A ϕ veto is applied to the invariant mass distributions.

Cut type	Cut value
Fiducial	$5.5\ \text{GeV}/c < p_{t,\Lambda_b^0} < 30.\ \text{GeV}/c,\ 2.5 < y_{t,\Lambda_b^0} < 4.$
ϕ veto	$1011.7\ \text{MeV}/c^2 < m(\text{K}^-{}_{\Lambda_c^+}, \text{p} \rightarrow \text{K}^+) < 1027.7\ \text{MeV}/c^2,$
	$1011.7\ \text{MeV}/c^2 < m(\text{K}^-{}_{bach}, \text{p} \rightarrow \text{K}^+) < 1027.7\ \text{MeV}/c^2$
$\text{D}^*(2010)^-$ veto	$2010.4\ \text{MeV}/c^2 < m(\overline{\text{D}}^0, \text{K}^-{}_{bach} \rightarrow \pi^-) < 2013.4\ \text{MeV}/c^2,$
	$2010.4\ \text{MeV}/c^2 < m(\overline{\text{D}}^0, \text{K}^-{}_{\Lambda_c^+} \rightarrow \pi^-) < 2013.4\ \text{MeV}/c^2$
PID	$ProbNNK(K_{bach}) > 0.18,\ BDT(\Lambda_c^+) > -0.15, BDT(\overline{\text{D}}^0) > -0.25$
Invariant mass	$2258.\ \text{MeV}/c^2 < m(\text{pK}^-\pi^+) < 2318.\ \text{MeV}/c^2,$
	$1822.\ \text{MeV}/c^2 < m(\text{K}^+\pi^-) < 1912.\ \text{MeV}/c^2,$
	$5560.\ \text{MeV}/c^2 < m(\Lambda_c^+\overline{\text{D}}^0\text{K}^-) < 5850.\ \text{MeV}/c^2$

Table 14: Criteria defining the final analysis selection.

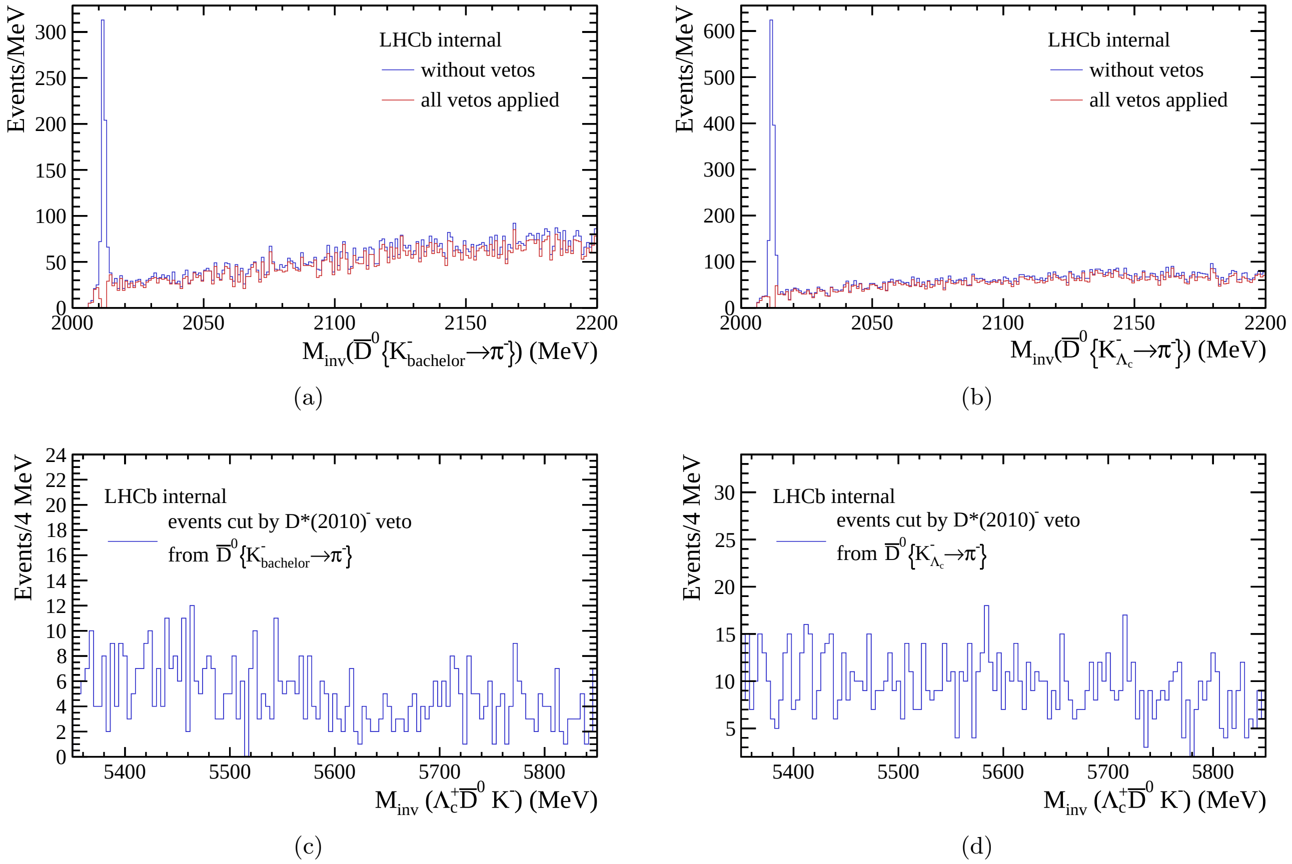

Figure 25: $\overline{\mathrm{D}}^0\pi^-$ invariant mass distributions with the vetoed $\mathrm{D}^*(2010)^-$ signal (a, b), and Λ_b^0 invariant mass distribution of the events rejected by the vetos (c, d). The pion mass is assigned either to the kaon candidate from the Λ_c^+ decay (a, c), or to the bachelor kaon (b, d). It is then combined with the $\overline{\mathrm{D}}^0$ candidate. A $\mathrm{D}^*(2010)^-$ veto is applied to the invariant mass distributions.

4.2 Treatment of multiple signal candidates in the same events

The probability of having more than one signal decay per collision is negligible. However, it occurs that multiple signal candidates are reconstructed in one single event, especially in case of events with high track multiplicity. These *multiple candidates* are either built from completely uncorrelated particles, or they are sharing part of the reconstructed decays, but with the Λ_{b}^0, Λ_{c}^+ or $\overline{\mathrm{D}}^0$ candidates being built from different tracks. In the first case only one candidate is potentially a pure-signal candidate, and all the others are pure-combinatorics background. In the latter, the multiple candidates are sharing part of the correct signal decay, thus their identification is more challenging. The presence of multiple candidates could affect the sensitivity of a measurement contributing to the background present in the data set, or they could even bias the result if treated as pure-signal events. To correct for this effect, in this analysis multiple candidates are randomly-removed from the data sample: for each event with multiple Λ_{b}^0 candidates, all but one are removed in a random way. This reduces the statistical power of the data set lowering the number of signal candidates, but does not introduce any bias in the measurement.

Multiple candidates are identified in the data sample, after the baseline selection described in the previous section is applied. About 5% of events have multiple candidates, and $\approx 95\%$ of them have two candidates passing the selection. A large fraction of them ($\sim 80\%$) are uncorrelated candidates, while the rest are mainly formed sharing the same bachelor K^-. After that the multiple candidates are removed, the data sample is reduced by 1186 reconstructed candidates ($\sim 5.3\%$ of the initial sample). The final number of candidates in the data sample surviving the selection and the removal of multiple candidates are listed in Table 15, depending on the period of data taking.

Year of data taking	Candidates
2011	1393
2012	3383
2015	953
2016	5482
2017	5215
2018	4410
Sum	20836

Table 15: Number of decay candidates in the data sample after the selection and the removal of multiple candidates, for the different periods of data taking. The baseline data selection, as introduced in Section 4.1, is considered.

4.3 Mass fits to the invariant mass distributions

4.3.1 Three-dimensional fits to the Λ_{b}^0, Λ_{c}^+, $\overline{\mathrm{D}}^0$ invariant mass distributions

Two main background components are expected to contribute in the data sample. First, combinatorial background is formed by reconstructed tracks which are randomly picked from the underlying event to form the Λ_{b}^0 candidate. Secondly, the so-called *charmless channels* in which the Λ_{b}^0 decays to the same final-state particles as the signal channel, but with only one of the two intermediate *c*-hadrons: $\Lambda_{\mathrm{b}}^0 \to \Lambda_{\mathrm{c}}^+[\to \mathrm{p}\mathrm{K}^-\pi^+]\ \mathrm{K}^+\pi^-\mathrm{K}^-$ referred to as Λ_{c}^+-*charmless* decay, or $\Lambda_{\mathrm{b}}^0 \to \mathrm{p}\mathrm{K}^-\pi^+\overline{\mathrm{D}}^0[\to \mathrm{K}^+\pi^-]\ \mathrm{K}^-$ called $\overline{\mathrm{D}}^0$-*charmless* channel. Combinatorial components are also present in the charmless channels. The case where the Λ_{b}^0 decays into the final-state particles with no intermediate resonances ("doubly-charmless channel", with $\Lambda_{\mathrm{b}}^0 \to \mathrm{p}\mathrm{K}^-\pi^+\mathrm{K}^+\pi^-\mathrm{K}^-$) is indistinguishable by the combinatorial background, and thus is not modelled.

The combinatorial background is expected to follow a decreasing exponential shape over the mass range, so a one-dimensional fit to the mass distribution of the Λ_b^0 candidates would be sufficient to model it. Instead, the Λ_c^+-charmless candidates appear as signal-like in the Λ_c^+ mass distribution and as combinatorial background in the $\overline{D}^0$ mass distribution. Additionally, they peak under the signal region of the Λ_b^0 invariant mass distribution. An analogous reasoning applies to the $\overline{D}^0$-charmless candidates. Therefore, a three-dimensional fit in the Λ_b^0, Λ_c^+ and $\overline{D}^0$ mass distributions is required to disentangle the signal and background contributions in the charmless decays. In the following, the *pdf* used to describe the different components of the fit are presented in a general way. The actual fit observables and nuisance parameters are discussed afterwards.

The signal *pdf*s used to fit the Λ_b^0, Λ_c^+ and $\overline{D}^0$ projections are the sum of two Crystal Ball distributions [113]. This function is used to model peaking but asymmetric shapes, and it consists of a Gaussian core with mean μ and width σ, and an exponential tail below a certain threshold determined by a parameter α:

$$CB(x,\mu,\sigma,\alpha,n) = \frac{1}{\sigma N_{CB}} \cdot \begin{cases} \exp(-\frac{(x-\mu)^2}{2\sigma^2}) & \text{for } \frac{x-\mu}{\sigma} > \alpha \\ (\frac{n}{|\alpha|})^n \cdot e^{-\alpha^2/2} \cdot (\frac{n}{|\alpha|} - |\alpha| - \frac{x-\mu}{\sigma})^{-n} & \text{for } \frac{x-\mu}{\sigma} \leq \alpha \end{cases} \tag{56}$$

with x being the observable variable, n describing the slope of the exponential tail, and N_{CB} being a normalisation factor:

$$N_{CB} = \frac{ne^{-\alpha^2/2}}{|\alpha|(n-1)} + \sqrt{\frac{\pi}{2}}[1 + \text{erf}(\frac{|\alpha|}{\sqrt{2}})] \tag{57}$$

where the *error function* erf is defined by [114]:

$$\text{erf}(x) = \frac{1}{\pi} \int_{-x}^{x} e^{-y^2} dy \tag{58}$$

The two summed Crystal Ball functions have common mean μ and tail parameters n. The width σ and the tail parameter α of the first Crystal Ball are expressed as functions of the parameters of the second one, through multiplicative factors $\sigma_{k,f}$ and $\alpha_{k,f}$, respectively. Finally, the first Crystal Ball is multiplied by a scaling factor f_k. In this description, k is an index to discriminate between the Λ_b^0, Λ_c^+ and $\overline{D}^0$ signal *pdf*s. Finally, the signal *pdf*s take the form:

$$\begin{aligned} \mathcal{F}_{signal,k} =& f_k \cdot CB(x = m_k, \mu = \mu_k, \sigma = \sigma_k, \alpha = \alpha_k, n = n_k) \\ &+ CB(x = m_k, \mu = \mu_k, \sigma = \sigma_{k,f} \cdot \sigma_k, \alpha = \alpha_{k,f} \cdot \alpha_k, n = n_k) \end{aligned} \tag{59}$$

with m_k being the observable of the fit, i.e. the invariant mass of the $pK^-\pi^+K^+\pi^-K^-$, $pK^-\pi^+$ and $K^+\pi^-$ combinations, respectively in the Λ_b^0, Λ_c^+ and $\overline{D}^0$ mass projections. The overall signal component of the $\Lambda_b^0 \to \Lambda_c^+\overline{D}^0K^-$ decay is therefore modelled by a combination of signal *pdf*s in all the three systems:

$$\mathcal{F}_{signal} = \mathcal{F}_{signal,\Lambda_b^0} \cdot \mathcal{F}_{signal,\Lambda_c^+} \cdot \mathcal{F}_{signal,\overline{D}^0} \tag{60}$$

A falling exponential distribution is used to describe the *pdf* of the combinatorial backgrounds:

$$\mathcal{F}_{comb,k'} = \exp(-\frac{m'_k}{\tau'_k}) \tag{61}$$

with k' indexing the invariant mass distribution (Λ_b^0, Λ_c^+ or $\overline{D}^0$) in which the combinatorics is modelled. The purely-combinatorial background of the signal channel consists of candidates which are built from random tracks in all the three systems:

$$\mathcal{F}_{bkg} = \mathcal{F}_{comb,\Lambda_b^0} \cdot \mathcal{F}_{comb,\Lambda_c^+} \cdot \mathcal{F}_{comb,\overline{D}^0} \tag{62}$$

or from final-state particles from the decay of a single c-*hadron*, but combined with random tracks to form the Λ_b^0 and the other c-*hadron*:

$$
\begin{aligned}
\mathcal{F}_{bkg,\Lambda_\mathrm{c}^+} &= \mathcal{F}_{comb,\Lambda_\mathrm{b}^0} \cdot \mathcal{F}_{signal,\Lambda_\mathrm{c}^+} \cdot \mathcal{F}_{comb,\overline{\mathrm{D}}^0} \\
\mathcal{F}_{bkg,\overline{\mathrm{D}}^0} &= \mathcal{F}_{comb,\Lambda_\mathrm{b}^0} \cdot \mathcal{F}_{comb,\Lambda_\mathrm{c}^+} \cdot \mathcal{F}_{signal,\overline{\mathrm{D}}^0}
\end{aligned}
\tag{63}
$$

where $\mathcal{F}_{bkg,\Lambda_\mathrm{c}^+}$ corresponds to a *good* Λ_c^+ candidate combined with a $\overline{\mathrm{D}}^0$ candidate built from background tracks, and $\mathcal{F}_{bkg,\overline{\mathrm{D}}^0}$ to a *good* $\overline{\mathrm{D}}^0$ combined with a background Λ_c^+. Finally, a combinatorial source is constituted by particles coming from the decay of both the Λ_c^+ and $\overline{\mathrm{D}}^0$, but combined with a random kaon assigned to be the bachelor K^- of the $\Lambda_\mathrm{b}^0 \to \Lambda_\mathrm{c}^+\overline{\mathrm{D}}^0\mathrm{K}^-$ decay:

$$
\mathcal{F}_{bkg,\Lambda_\mathrm{c}^+-\overline{\mathrm{D}}^0} = \mathcal{F}_{comb,\Lambda_\mathrm{b}^0} \cdot \mathcal{F}_{signal,\Lambda_\mathrm{c}^+} \cdot \mathcal{F}_{signal,\overline{\mathrm{D}}^0}
\tag{64}
$$

The charmless contributions are modelled in the Λ_b^0 projection by the sum of two Gaussian distributions with common mean $\mu_{\Lambda_\mathrm{b}^0}$, fixed to the value of the mean of the signal Λ_b^0 *pdf* (Eq. 60), and with widths related by a factor $\sigma_{k'-cl,f}$:

$$
\mathcal{F}_{k'-cl,\Lambda_\mathrm{b}^0} = f_{k'-cl} \cdot G(\mu = \mu_{\Lambda_\mathrm{b}^0}, \sigma = \sigma_{k'-cl}) + G(\mu = \mu_{\Lambda_\mathrm{b}^0}, \sigma = \sigma_{k'-cl,f} \cdot \sigma_{k'-cl})]
\tag{65}
$$

where k' is an index distinguishing between the Λ_c^+ and $\overline{\mathrm{D}}^0$ charmless channels. In Equation 65 the Λ_b^0 subscript is used to stress that this *pdf* is only used to model the Λ_b^0 projection of the total fit. The resonating components (Λ_c^+ or $\overline{\mathrm{D}}^0$) of the charmless channels are modelled by the respective signal *pdf*s introduced in Equation 59. The non-resonating components are modelled by background *pdf*s as in Equation 61. Finally, the *pdf*s of the Λ_c^+- and $\overline{\mathrm{D}}^0$-charmless components are given respectively by:

$$
\begin{aligned}
\mathcal{F}_{\Lambda_\mathrm{c}^+-cl} &= \mathcal{F}_{\Lambda_\mathrm{c}^+-cl,\Lambda_\mathrm{b}^0} \cdot \mathcal{F}_{signal,\Lambda_\mathrm{c}^+} \cdot \mathcal{F}_{bkg,\overline{\mathrm{D}}^0} \\
\mathcal{F}_{\overline{\mathrm{D}}^0-cl} &= \mathcal{F}_{\overline{\mathrm{D}}^0-cl,\Lambda_\mathrm{b}^0} \cdot \mathcal{F}_{bkg,\Lambda_\mathrm{c}^+} \cdot \mathcal{F}_{signal,\overline{\mathrm{D}}^0}
\end{aligned}
\tag{66}
$$

The total *pdf* used to fit the data is finally:

$$
\begin{aligned}
\mathcal{F}_{tot} =& N_{\Lambda_\mathrm{b}^0} \cdot [\mathcal{F}_{signal} + f_{\Lambda_\mathrm{c}^+-cl,N_{\Lambda_\mathrm{b}^0}} \cdot \mathcal{F}_{\Lambda_\mathrm{c}^+-cl} + f_{\overline{\mathrm{D}}^0-cl,N_{\Lambda_\mathrm{b}^0}} \cdot \mathcal{F}_{\overline{\mathrm{D}}^0-cl}] \\
&+ N_{bkg} \cdot (f_{bkg,\Lambda_\mathrm{b}^0} \cdot \mathcal{F}_{bkg,\Lambda_\mathrm{b}^0} + f_{bkg,\Lambda_\mathrm{c}^+} \cdot \mathcal{F}_{bkg,\Lambda_\mathrm{c}^+} + f_{bkg,\overline{\mathrm{D}}^0} \cdot \mathcal{F}_{bkg,\overline{\mathrm{D}}^0} + f_{bkg,\Lambda_\mathrm{b}^0-\overline{\mathrm{D}}^0} \cdot \mathcal{F}_{bkg,\Lambda_\mathrm{c}^+-\overline{\mathrm{D}}^0})
\end{aligned}
\tag{67}
$$

with $N_{\Lambda_\mathrm{b}^0}$ representing the yield of Λ_b^0 signal candidates, N_{bkg} the total number of events from combinatorial background, and f_i the fractions of $N_{\Lambda_\mathrm{b}^0}$ or N_{bkg} for the i-th component.

The tail parameters $\alpha_k, n_k, s_{k,f}$ and the fractions f_k of the Crystal Balls distributions in the signal *pdf* (Eq. 60) are not fitted to data, but extracted from three-dimensional fits performed to simulated samples of the $\Lambda_\mathrm{b}^0 \to \Lambda_\mathrm{c}^+\overline{\mathrm{D}}^0\mathrm{K}^-$ signal channel. These samples are generated simulating both signal and background processes, but the latter are excluded from the fitted data set by making use of the so-called *truth-information.* It represents the *a-priori* knowledge of the characteristics of the simulated decays, from the generation stage. The fits to the simulated samples are shown in Figure 26. All the remaining parameters are fit to data.

The charmless channels are challenging to be described on data, since they peak under the signal region in the Λ_b^0 mass projection. A variety of fit models are considered to investigate the charmless contamination in the data sample. Three-dimensional fits without charmless contributions, with only

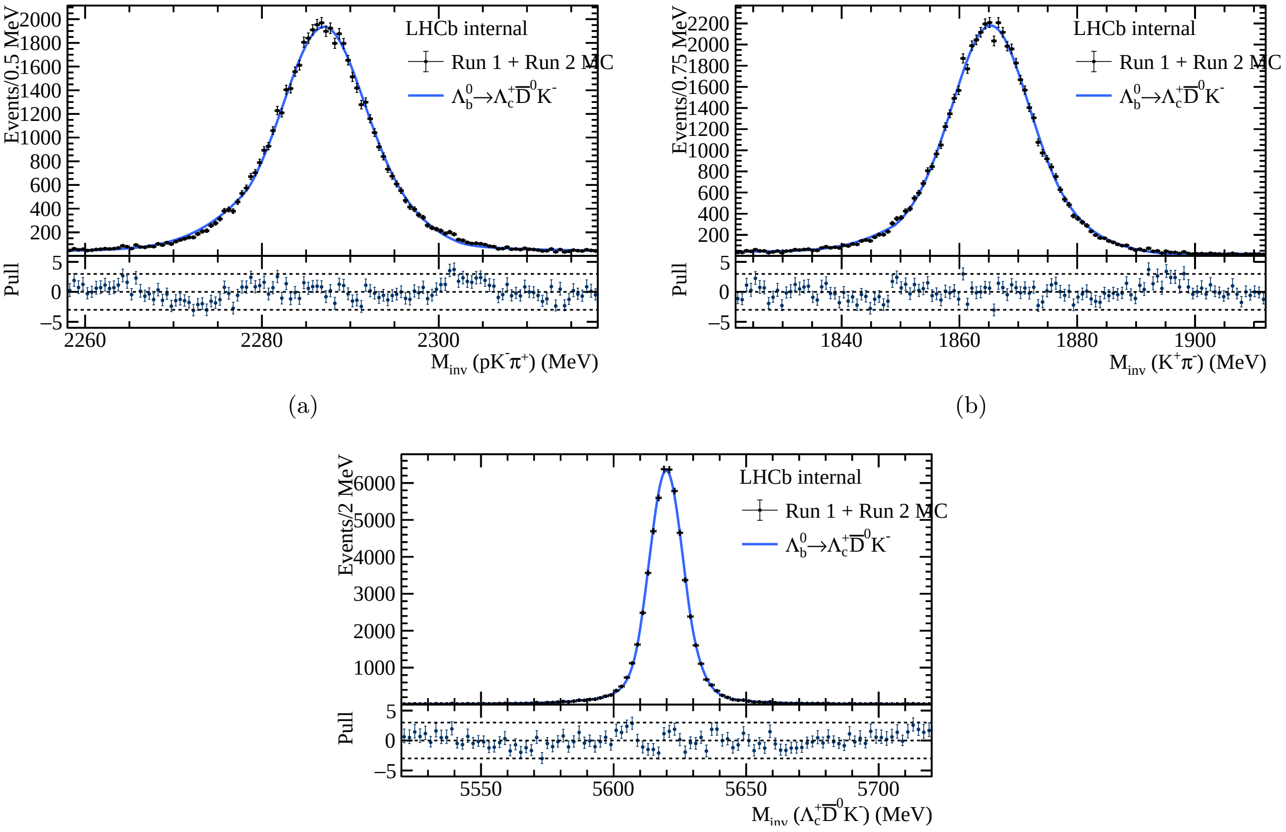

(a)

(b)

(c)

Figure 26: Projections in the Λ_c^+ (a), $\overline{\mathrm{D}}^0$ (b) and Λ_b^0 (c) invariant mass distributions of the three-dimensional fits to the $\Lambda_b^0 \to \Lambda_c^+\overline{\mathrm{D}}^0\mathrm{K}^-$ simulated sample. Background candidates are removed from the sample making use of the *truth-information* introduced in the text.

Cut variable	Loose selection	Tight selection
$m_{\Lambda_b^0}$	[5560, 5850] MeV/c^2	[5560, 5700] MeV/c^2
$BDT_{\Lambda_c^+}$	> -0.15	> -0.05
$BDT_{\overline{\mathrm{D}}0}$	> -0.25	> -0.15

Table 16: *D-from-B* BDT cut values and cuts on the Λ_c^+, $\overline{\mathrm{D}}^0$, Λ_b^0 invariant masses for the loose and tight selections of the three-dimensional mass fits.

one of them, and with both of them are performed. The main fit results which are useful to estimate the charmless contributions are shown in Table 17, in particular the signal and background yields. The fit projections are shown in Figure 27. Note that in order to correctly describe the combinatorial backgrounds in all three mass projections, a considerable amount of background events must be included in the Λ_b^0 invariant mass distribution, reducing the purity of the data sample.

A tight selection of the data sample with more strict cuts on the Λ_b^0 invariant mass and *D-from-B* BDT is defined, for crosschecks of the obtained results. The set of cuts defining the old (*loose*) and new (*tight*) selections are listed in Table 16. The fit results on the tight-selected sample are shown in Table 18. For both the selections, the introduction of the charmless contributions in the total *pdf* (Eq. 60) does not effect the signal yields, but the background description only. The fractions $f_{\overline{\mathrm{D}}0-cl,N_{\Lambda_b^0}}$,

$f_{\Lambda_\mathrm{c}^+-cl,N_{\Lambda_\mathrm{b}^0}}$ of the charmless contributions are negligible. A negligible contamination from the charmless channels allows to perform a simpler one-dimensional fit to the Λ_b^0 invariant mass distribution, in contrast to the three-dimensional fit investigated so far.

Fit parameter	no charmless	only $\overline{\mathrm{D}}^0$-charmless	only Λ_c^+-charmless	$\overline{\mathrm{D}}^0$- and Λ_c^+-charmless
$N_{\Lambda_\mathrm{b}^0}$	5535 ± 91	5530 ± 100	5511 ± 96	5512 ± 100
$N_{bkg,\Lambda_\mathrm{b}^0}$	15300 ± 130	15200 ± 380	15230 ± 160	15200 ± 1500
$f_{\overline{\mathrm{D}}^0-cl,N_{\Lambda_\mathrm{b}^0}}$	/	0.02 ± 0.24	/	0.01 ± 0.28
$f_{\Lambda_\mathrm{c}^+-cl,N_{\Lambda_\mathrm{b}^0}}$	/	/	0.017 ± 0.021	0.016 ± 0.027

Table 17: Results of the three-dimensional fit to data for different modelling of the charmless contributions: no charmless components are considered, only the $\overline{\mathrm{D}}^0$- or Λ_c^+- component is described, or both the contributions are used in the model.

Fit parameter	no charmless	only $\overline{\mathrm{D}}^0$-charmless	only Λ_c^+-charmless	$\overline{\mathrm{D}}^0$- and Λ_c^+-charmless
$N_{\Lambda_\mathrm{b}^0}$	5253 ± 82	5252.1 ± 5.3	5257 ± 88	5230 ± 280
N_{bkg}	6393 ± 89	6393.3 ± 5.7	6389 ± 94	6120 ± 300
$f_{\overline{\mathrm{D}}^0-cl,N_{\Lambda_\mathrm{b}^0}}$	/	0 ± 3.9e-06	/	0.0025 ± 0.0010
$f_{\Lambda_\mathrm{c}^+-cl,N_{\Lambda_\mathrm{b}^0}}$	/	/	0 ± 0.00092	0.0532 ± 0.0036

Table 18: Results of the three-dimensional fit to data for different modelling of the charmless contributions, for tighter *D-from-B* BDT cuts on the Λ_c^+ and $\overline{\mathrm{D}}^0$ and mass cut to the Λ_b^0 invariant mass. No charmless components are considered, only the $\overline{\mathrm{D}}^0$- or Λ_c^+- component is described, or both the charmless contributions are used in the model.

Further checks are performed employing simulated samples of the $\Lambda_\mathrm{b}^0 \to \Lambda_\mathrm{c}^+\mathrm{K}^+\pi^-\mathrm{K}^-$ decay, corresponding to the Λ_c^+-charmless background. The simulated events are selected by the same stripping and analysis selections used for the $\Lambda_\mathrm{b}^0 \to \Lambda_\mathrm{c}^+\overline{\mathrm{D}}^0\mathrm{K}^-$ signal channel, apart from the *D-from-B* BDT selections of Λ_c^+ and $\overline{\mathrm{D}}^0$. The latter cannot be applied to the simulated samples, since the *D-from-B* classifiers have been trained on data and they make use of variables which are not well reproduced in simulation (Sec. 3.3.2). In order to be able to apply the PID selection on the bachelor K^-, the simulated samples are resampled in the response of the *ProbNN* classifiers (Sec. 2.3.2) using *PIDGen* [115], a dedicated software developed within LHCb [19] . The number of simulated candidates passing the selections, and which are *truth-matched* is shown in Table 19. The results are compared to what was obtained with the simulated sample of the signal channel $\Lambda_\mathrm{b}^0 \to \Lambda_\mathrm{c}^+\overline{\mathrm{D}}^0\mathrm{K}^-$. Because of the method used to apply the selection to the $\Lambda_\mathrm{b}^0 \to \Lambda_\mathrm{c}^+\mathrm{K}^+\pi^-\mathrm{K}^-$ channel, the charmless reconstructed candidates which are truth-matched are overestimated by a factor 15%-20%. The *D-from-B* BDT selection on the $\overline{\mathrm{D}}^0$ would further suppress the eventual charmless reconstructed candidates by a considerably large fraction. Indeed, this selection has proven to be highly efficient on signal (> 85%) while rejecting most of the background (> 80%) [6], thus it would remove most of the $\Lambda_\mathrm{b}^0 \to \Lambda_\mathrm{c}^+\mathrm{K}^+\pi^-\mathrm{K}^-$ candidates in Table 19. The *D-from-B* BDT selection on the Λ_c^+ would act in a similar way on both the $\Lambda_\mathrm{b}^0 \to \Lambda_\mathrm{c}^+\overline{\mathrm{D}}^0\mathrm{K}^-$ and the $\Lambda_\mathrm{b}^0 \to \Lambda_\mathrm{c}^+\mathrm{K}^+\pi^-\mathrm{K}^-$, removing in equal proportions Λ_c^+ truth-matched candidates wrongly identified as background. Hence, it would not modify the picture of the results presented here. Based

---

[19] The *PIDGen* software library [115] uses techniques of kernel density estimation of the PID *pdf*s from calibration data samples, in order to achieve a reasonably good PID response in the simulated samples.

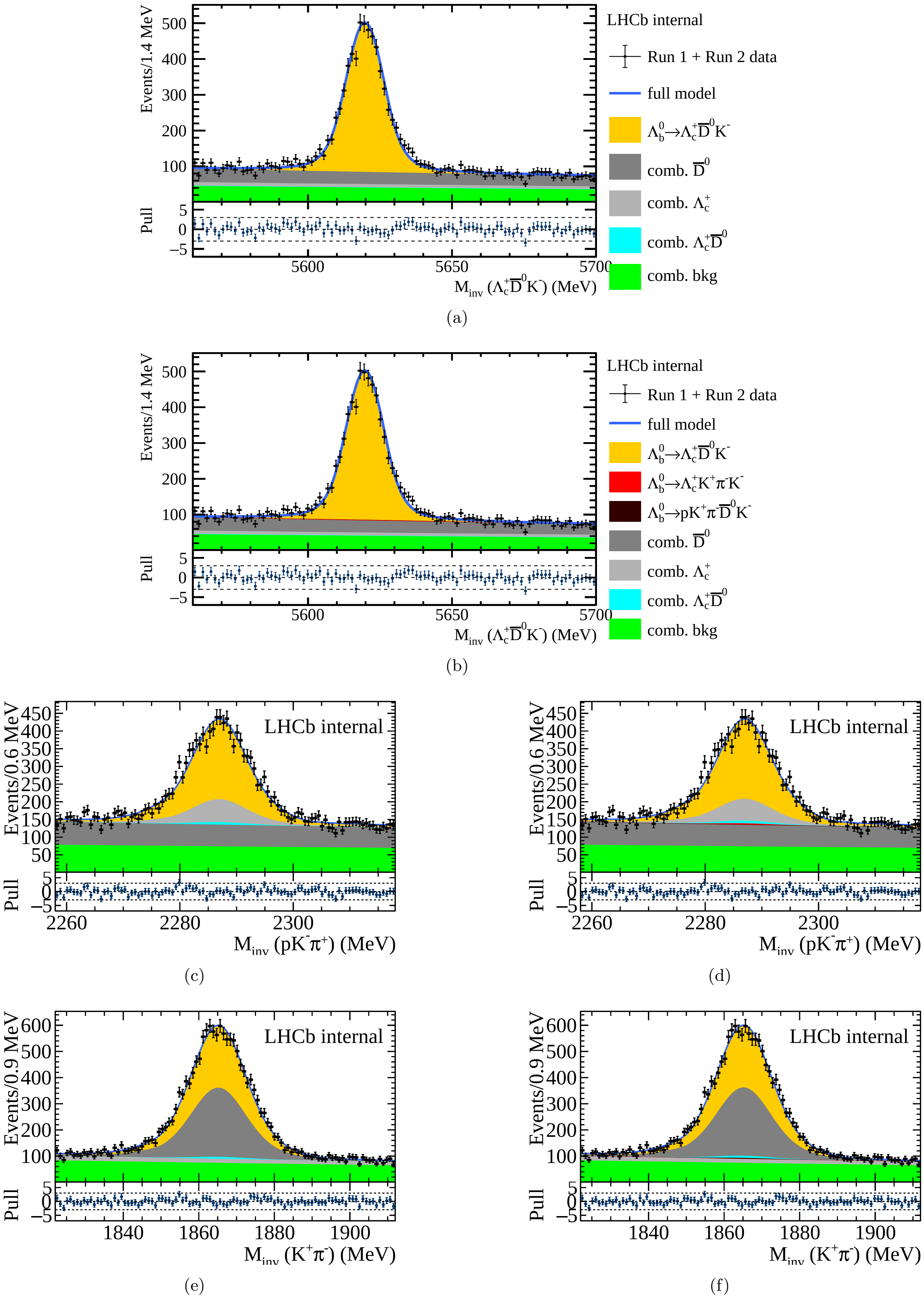

(a)

(b)

(c)

(d)

(e)

(f)

Figure 27: Projections of the three-dimensional fits to data in the Λ_b^0 (a, b), Λ_c^+ (c, e), $\overline{D}^0$ (d, f) invariant mass distributions. a, c, e) The charmless contributions are not modelled. b, d, f) Both the charmless contributions are included in the fit model.

class of events	$\Lambda_b^0 \to \Lambda_c^+ \overline{D}^0 K^-$	$\Lambda_b^0 \to \Lambda_c^+ K^+ \pi^- K^-$
generated events	1.34 M	1.18 M
events after stripping selection	48258	8514
events after stripping selection — truth-matched	17447	552
events after analysis selection — truth-matched	12694	92

Table 19: Comparison of the generated and reconstructed events for the $\Lambda_b^0 \to \Lambda_c^+ \overline{D}^0 K^-$ signal channel and the $\Lambda_b^0 \to \Lambda_c^+ K^+ \pi^- K^-$ charmless channel, from simulated samples. The *D-from-B* BDT selections on the Λ_c^+ and $\overline{D}^0$ are not applied.

Cut variable	Loose selection	Tight selection
$m_{\Lambda_c^+}$	[2258, 2318] MeV/c^2	[2270, 2302] MeV/c^2
$m_{\overline{D}^0}$	[1822, 1912] MeV/c^2	[1840, 1895] MeV/c^2
$m_{\Lambda_b^0}$	[5570, 5670] MeV/c^2	[5580, 5660] MeV/c^2
$BDT_{\Lambda_c^+}$	> -0.15	> -0.05
$BDT_{\overline{D}^0}$	> -0.25	> -0.15

Table 20: *D-from-B* BDT cut values and cuts on the Λ_c^+, $\overline{D}^0$, Λ_b^0 invariant masses for the loose and tight selections of the 1-dimensional mass fits.

on these considerations and on the results in Table 19, the suppression of the charmless channel is estimated to be by a factor $1.5 \cdot 10^{-3}$ with respect to the signal channel.

The studies on simulated samples cannot be considered conclusive, since their results depend on the production rate of the Λ_c^+-charmless decay in the real collisions, which is unknown. Nevertheless, they corroborate the conclusion from the three-dimensional fits that the contamination of the charmless channels in the data sample is negligible.

4.3.2 One-dimensional fits to the Λ_b^0 invariant mass distribution

In the previous section, the charmless contributions to the data sample have been proved to be negligible. This allows to perform one-dimensional mass fits on the Λ_b^0 mass projection rather than the three-dimensional fits investigated so far, gaining in simplicity and stability of the fit. Also, this permits to cut away most of the background events which were needed to describe the Λ_c^+ and $\overline{D}^0$ background and signal components in the charmless contributions. This is done by tightening the mass range of their invariant mass distributions.

The Λ_b^0 projection of the one-dimensional fit to the $\Lambda_c^+ \overline{D}^0 K^-$ invariant mass distribution is shown in Figure 28. The purity of the data sample is important in the amplitude fits, thus a tighter selection is introduced with more strict cuts on the Λ_c^+, $\overline{D}^0$, Λ_b^0 invariant masses and on the *D-from-B* BDT selections. The criteria defining the old (*loose*) and new (*tight*) selections are compared in Table 20.

After the tight selection is applied to the data sample, about 3% of events have multiple candidates. Following the procedure detailed in Section 4.2, 228 multiple candidates are removed, reducing the size of the data sample by $\sim 3.4\%$. The number of candidates passing the tight selection and the removal of multiple candidates are listed in Table 21.

The Λ_b^0 mass projection of the fit for the tight selection is also shown in Figure 28, and the fit results for both the selections are listed in Table 22. The average mass and width values of the Λ_b^0 signal contribution are compatible within the uncertainties, for both the selections.

The tight selection defined in Table 20 keeps a large fraction of the signal, $\sim 90\%$, while rejecting

Year of data taking	Candidates
2011	388
2012	926
2015	312
2016	1632
2017	1650
2018	1657
Sum	6565

Table 21: Number of signal and background candidates in the data sample after the selection and the removal of multiple candidates, for the different periods of data taking.

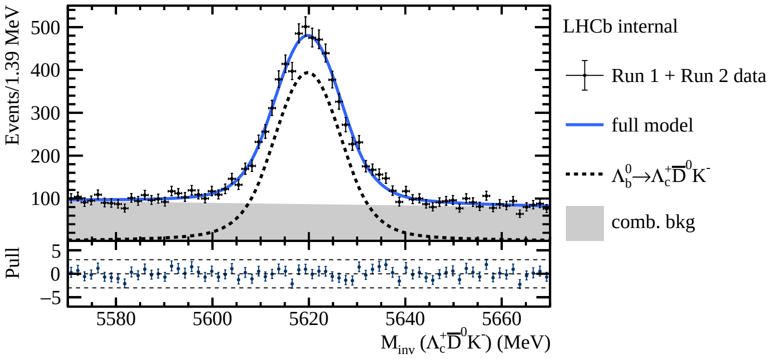

(a)

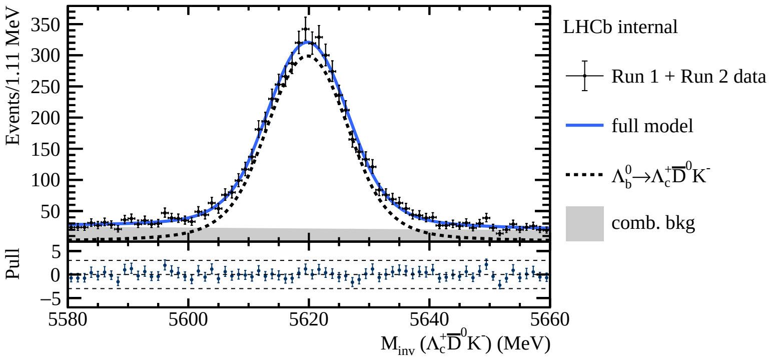

(b)

Figure 28: One-dimensional fit to the $\Lambda_c^+ \overline{D}^0 K^-$ invariant mass for loose (a) and tight (b) cuts on the Λ_c^+, $\overline{D}^0$ invariant masses and on the *D-from-BDT* BDT selection.

most of the background, $\sim 75\%$. Thus it considerably improves the purity of the data sample, and it is used as a baseline in the following. The correlation matrix of the baseline mass fit is presented in Table 23.

Fit parameter	Loose selection	Tight selection
$N_{\Lambda_b^0}$	5400 ± 110	4971 ± 92
N_{bkg}	6260 ± 110	1594 ± 71
$\mu_{\Lambda_b^0}$	5619.78 ± 0.15	5619.82 ± 0.13
$\sigma_{\Lambda_b^0}$	6.99 ± 0.16	6.84 ± 0.14
$\tau_{\Lambda_b^0}$	-0.00167 ± 0.00046	-0.0031 ± 0.0013

Table 22: Fit results for the one-dimensional mass fits with looser (left) and tighter (right) cuts on the Λ_c^+, $\overline{\mathrm{D}}^0$ invariant masses and on the BDT selection.

	$N_{\Lambda_b^0}$	N_{bkg}	$\mu_{\Lambda_b^0}$	$\sigma_{\Lambda_b^0}$	$\tau_{\Lambda_b^0}$
$N_{\Lambda_b^0}$	1.				
N_{bkg}	0.53	1.			
$\mu_{\Lambda_b^0}$	0.0048	-0.0062	1.		
$\sigma_{\Lambda_b^0}$	-0.38	0.49	-0.01	1.	
$\tau_{\Lambda_b^0}$	-0.052	0.068	-0.22	0.05	1.

Table 23: Correlation matrix of the fit parameters from the Λ_b^0 mass fit. The baseline data selection, as introduced in Section 4.3.2, is considered.

5 Amplitude model

This analysis employs to the helicity formalism to parametrise the amplitude model used to describe $\Lambda_b^0 \to \Lambda_c^+ \overline{D}^0 K^-$ decays, as introduced in Section 3.1. The coordinate transformations between reference systems, which stand at the base of such a formalism, are developed in Section 5.1.

As introduced in Section 3.1, the isobar model is used to express the process in terms of subsequent two-body decays. This decomposition is introduced in Section 5.2, and detailed in the next sections. The K-matrix description for scattering amplitudes, a key element for this analysis, is described in Section 5.3.

The discussion in this Chapter follows the notation used by the first observation of pentaquark states by LHCb [1].

5.1 Helicity frame and coordinate transformations

Let us consider a two-body decay $A \to BC$. A coordinate system $\hat{\boldsymbol{r}}_0^A = (\hat{x}_0^A, \hat{y}_0^A, \hat{z}_0^A)$ is defined in the rest frame of A, with $\hat{k}$ being the unit vector directed along the k axis. $\hat{z}_0^A$ is chosen to be the quantisation direction of the spin of the particle A. Helicity is defined as the projection of the particle spin onto the direction of its momentum. When the z axis coincides with the direction of the particle momentum, its spin projection onto it is denoted as λ. Following the prescriptions of the helicity formalism, the initial $\hat{\boldsymbol{r}}_0^A$ coordinate system is rotated to align the z axis to the direction of the momentum of one of the daughter particles. Let us align the z axis to the momentum of $\boldsymbol{p}_B$ the particle B, obtaining the $\hat{\boldsymbol{r}}_3^A = (\hat{x}_3^A, \hat{y}_3^A, \hat{z}_3^A)$ coordinate system as sketched in Figure 29. In this reference system the relation $\hat{z}_3^A || \boldsymbol{p}_B$ holds. In the following, $\hat{\boldsymbol{r}}_3^A$ is referred to as the *helicity frame* of the B particle.

A generic rotation can be formally expressed by an operator $R(\alpha, \beta, \gamma)$ in the three-dimensional space, which first performs a rotation by the angle α around the $\hat{z}_0$ axis, then a rotation by the angle β around the rotated $\hat{y}_1$ axis, and finally a rotation by the angle γ around the rotated $\hat{z}_2$ axis.

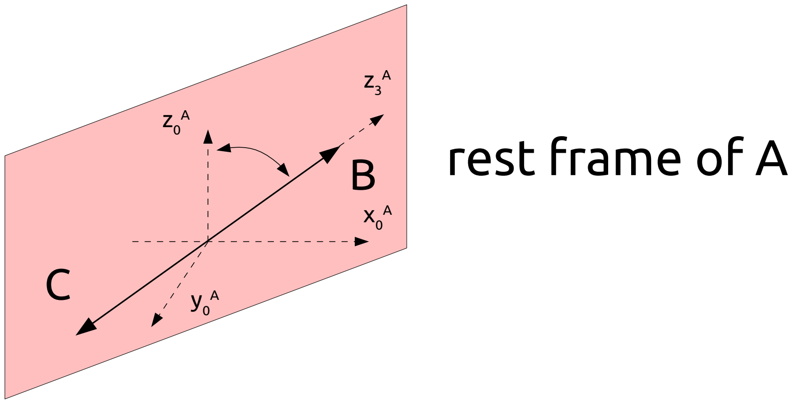

Figure 29: Definition of the helicity frame $\hat{r}_3^A$ of the particle B, obtained rotating the coordinate system $\hat{r}_0^A$ defined in the rest frame of the particle A, in such a way to align the quantisation axis of the particle A, $\hat{z}_0^A$, to the momentum direction of the particle B, $\hat{z}_3^A$.

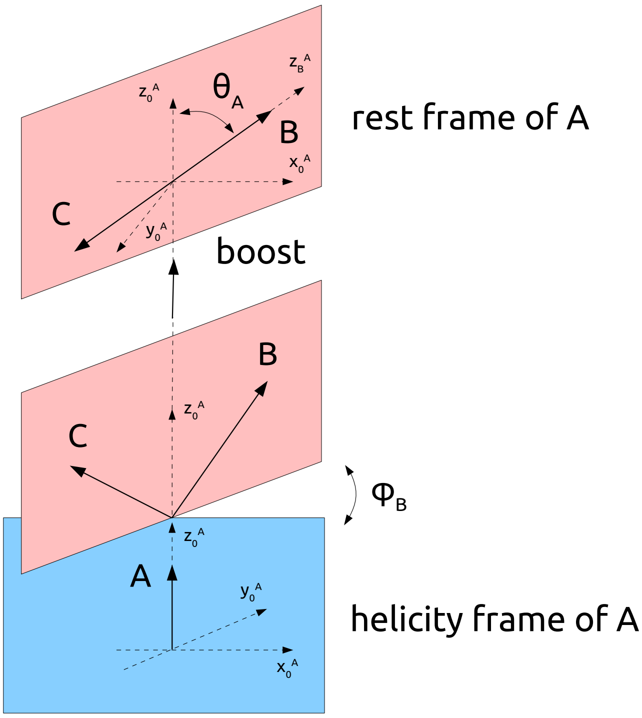

Figure 30: Rotation of the helicity frame of the particle A into the helicity frame of the particle B, by using the azimuthal ($\phi_B^A = \alpha$) and polar ($\theta_A^A = \beta$) angles of the momentum of B in the rest frame of the particle A.

The $|J_A, j_A>$ spin eigenstates of the particle A in the $\hat{\boldsymbol{r}}_0^A$ reference can be expressed in the basis of its spin eigenstates $|J_A, j_A^{'}>$ in the rotated $\hat{\boldsymbol{r}}_3^A$ reference, using the *Wigner D-matrices* $D^{J_A}_{j_A, j_A^{'}}$ [116]:

$$|J_A, j_A> = \sum_{j_A^{'}} D^{J_A}_{j_A, j_A^{'}}(\alpha, \beta, \gamma)^* |J_A, j_A^{'}> \tag{68}$$

where the complex conjugates of the D-matrices are expressed as function of the *small D-matrices* $d^{J_A}_{j_A, j_A^{'}}$ [116]:

$$\begin{aligned} D^{J_A}_{j_A, j_A^{'}}(\alpha, \beta, \gamma)^* &= < J_A, j_A | R(\alpha, \beta, \gamma) | J_A, j_A^{'} >^* \\ &= e^{i j_A \alpha} d^{J_A}_{j_A, j_A^{'}}(\beta) e^{i j_A^{'} \gamma} \end{aligned} \tag{69}$$

The exact dependence of the $d^{J_A}_{j_A, j_A^{'}}$ on the angular and spins values is described in Section 5.2. In Equation 68 the angular momentum conservation imposes $j_A^{'} = j_B^{'} + j_C^{'} = \lambda_B - \lambda_C$, where $j_C^{'} = -\lambda_C$ because $\boldsymbol{p}_C^A$ points in the opposite direction to $\hat{z}_3^A$. A rotation of the helicity frame of the particle A is now performed into the helicity frame of the particle B. This is accomplished by using the azimuthal ($\phi_B^A = \alpha$) and polar ($\theta_A^A = \beta$) angles of the momentum of B in the rest frame of the particle A, as sketched in Figure 30. As shown in Figure 30, the third rotation defined by the operator $R(\alpha, \beta, \gamma)$, namely of the z_2^A axis onto the final z_3^A axis, is not needed. Therefore, the angle γ is set to zero.

In the following, θ^A_B is the *helicity angle* θ_A of the particle A, and ϕ^A_B is denoted by ϕ_B. These angles are given by:

$$
\begin{aligned}
\phi_B &= \mathrm{atan2}(p^A_{B_y}, p^A_{B_x}) \\
&= \mathrm{atan2}(\hat{y}^A_0 \cdot \boldsymbol{p}^A_B, \hat{x}^A_0 \cdot \boldsymbol{p}^A_B) = \mathrm{atan2}((\hat{z}^A_0 \times \hat{x}^A_0) \cdot \boldsymbol{p}^A_B, \hat{x}^A_0 \cdot \boldsymbol{p}^A_B), \\
\cos\theta_A &= \hat{z}^A_0 \cdot \hat{p}^A_B
\end{aligned}
\tag{70}
$$

It must be noted that the choice of the first set of coordinates $\hat{\boldsymbol{r}}^A_0$ is arbitrary, but the transformation to the frame of the particle B is fixing a convention that must be propagated consistently between all the subsequent transformations to different decays chains.

If the particle B subsequentially decays ($B \to DE$), a second coordinate transformation is needed to align the z axis of the rest frame of the particle B along the momentum of the particle D, defining the $\hat{z}^B_D$ direction. The four-momenta of the daughters D and E must be first boosted to the rest frame of B along the $\hat{z}^A_3$ direction, which here coincides with $\hat{z}^A_2$ since the third rotation is not performed. The rotated $\hat{r}^A_3$ coordinate system becomes now the initial coordinate system of quantisation of the spin of the particle B, in its rest frame:

$$
\begin{aligned}
\hat{x}^B_0 &= \hat{x}^A_3, \\
\hat{y}^B_0 &= \hat{y}^A_3, \\
\hat{z}^B_0 &= \hat{z}^A_3
\end{aligned}
\tag{71}
$$

This set of directions defines a reference frame referred to as $\hat{\boldsymbol{r}}^B_0$. Using Equation 71, $\hat{z}^B_0$ is set to the direction of the momentum of the particle B in the rest frame of A:

$$
\hat{z}^B_0 \equiv \hat{z}^A_3 = \hat{p}^A_B \tag{72}
$$

To define the y^B_0 and x^B_0 directions as introduced in Equation 71, the intermediate axes of the $\hat{x}^A_1$, $\hat{x}^A_2$ directions must be derived as follows. After the first rotation by the ϕ_B angle around $\hat{z}^A_0$, the $\hat{x}^A_1$ axis is directed along the $\hat{p}^A_B$ component perpendicular to the $\hat{z_0}^A$ axis:

$$
\begin{aligned}
\boldsymbol{\omega}^A_{B\perp z_0} &\equiv (\boldsymbol{p}^A_B)_{\perp \hat{z}^A_0} = \boldsymbol{p}^A_B - (\boldsymbol{p}^A_B)_{||\hat{z}^A_0} \\
&= \boldsymbol{p}^A_B - (\boldsymbol{p}^A_B \cdot \hat{z}^A_0)\hat{z}^A_0, \\
\hat{x}^A_1 = \hat{\omega}^A_{B\perp z_0} &= \frac{\boldsymbol{\omega}^A_{B\perp z_0}}{|\boldsymbol{\omega}^A_{B\perp z_0}|}
\end{aligned}
\tag{73}
$$

After the second rotation by the angle θ_A around $\hat{y}^A_1$, the following holds:

$$
\hat{z}^A_2 = \hat{z}^A_3 = \hat{p}^A_B \tag{74}
$$

and the $\hat{x}^A_2 = \hat{x}^A_3$ direction is anti parallel to the $\hat{z}^A_0$ component which is perpendicular to the transformed z axis ($\hat{p}^A_B$) :

$$
\begin{aligned}
\boldsymbol{\alpha}^A_{z_0\perp B} &= (\hat{z_0}^A)_{\perp \boldsymbol{p}^A_B} = \hat{z}^A_0 - (\hat{z}^A_0 \cdot \hat{p}^A_B)\hat{p}^A_B, \\
\hat{x}^B_0 = \hat{x}^A_3 &= -\hat{\alpha}^A_{z_0\perp B} = -\frac{\boldsymbol{\alpha}^A_{z_0\perp B}}{|\hat{\alpha}^A_{z_0\perp B}|}
\end{aligned}
\tag{75}
$$

From Equations 72-75, $\hat{y}_0^B$ is finally given by:

$$\hat{y}_0^B = \hat{z}_0^B \times \hat{x}_0^B \tag{76}$$

Once the $(\hat{x}_0^B, \hat{y}_0^B, \hat{z}_0^B)$ directions are derived, $\hat{z}_D^B$ can be determined with the same transformations introduced to align the z axis of the rest frame of A along the momentum direction of the particle B (Eq. 70).

5.2 Matrix elements

The essential ingredient that defines the signal *pdf* used to fit the model to the data is a matrix element M of the decay process of interest. It expresses both the kinematic and angular dependence of the process. The connection between the decay matrix element and the signal *pdf* is detailed in Chapter 6.

Let us consider a decay process which proceeds through intermediate resonances. In the helicity formalism the complete matrix element, which includes all the processes j of the intermediate states, is expressed as sum over the initial- (λ_i) and final-state (λ_f) helicities:

$$|M|^2 = \sum_{\lambda_i, \lambda_f} |\sum_j M^j_{\lambda_i, \lambda_f}|^2 \tag{77}$$

In this formulation, a three-body decay $A \to BCD$ is decomposed into two subsequent two-body decays, namely $A \to BX$ and $X \to CD$, where X is an intermediate resonance. The intermediate matrices $M^j_{\lambda_i, \lambda_f}$ in Equation 77 are expressed by coherent sums over the intermediate-state helicities λ_X:

$$M^X_{\lambda_A, \lambda_B, \lambda_C, \lambda_D} = \sum_{\lambda_X} M^{A \to BX}_{\lambda_A, \lambda_B, \lambda_X} \cdot M^{X \to CD}_{\lambda_X, \lambda_C, \lambda_D} \tag{78}$$

$M^{A \to BX}_{\lambda_A, \lambda_B, \lambda_X}$ and $M^{X \to CD}_{\lambda_X, \lambda_C, \lambda_D}$ are two-body decay matrix elements which include the *helicity amplitudes* H, the angular dependence through the small D-matrices $d(\theta)$ and the resonance shapes $R(m)$:

$$M^{X \to CD}_{\lambda_X, \lambda_C, \lambda_D} = H^{X \to CD}_{\lambda_C, \lambda_D} \cdot d^{J_X}_{\lambda_X, \lambda_C - \lambda_D}(\theta) \cdot e^{i\lambda_X \cdot \phi} \cdot R(m_{C,D}) \tag{79}$$

and similarly for $M^{A \to BX}_{\lambda_A, \lambda_B, \lambda_X}$. The sum is performed over $|\lambda_C| <= J_C$, $|\lambda_D| <= J_D$, $|\lambda_C - \lambda_D| <= J_X$ with J denoting the spin assignment of the states. In Equation 79, $m_{C,D}$ is the mass value of the C and D invariant mass distribution. In what follows, the form of the terms H, $d(\theta)$ and $R(m)$ are detailed for the $X \to CD$ two-body decay. The construction for the $A \to BX$ decay matrix is analogous.

The helicity amplitudes H are complex parameters, defined in general as:

$$H^{X \to CD}_{\lambda_C, \lambda_D} = a_{\lambda_C, \lambda_D} \cdot e^{i\phi_{\lambda_C, \lambda_D}} \tag{80}$$

where a_{λ_C, λ_D} and $\phi_{\lambda_C, \lambda_D}$ are the magnitude and phase of the polar representation of complex numbers. This results in a different set of magnitude and phase for each possible combination of $\{\lambda_C,\ \lambda_D\}$ which have to be determined from a fit to data, leading to a large number of free parameters. An alternative definition of the helicity amplitudes relates them to the Clebsch-Gordan coefficients $< J_C, J_D, S|\lambda_C, -\lambda_D, \lambda_C - \lambda_D >$ and $< L, S, J_X|0, \lambda_C, -\lambda_D, \lambda_C - \lambda_D >$, with $\boldsymbol{S} = \boldsymbol{J_C} + \boldsymbol{J_D}$ being the total spin of the daughter particles, and $\boldsymbol{L}$ the orbital angular momentum between them.

Introducing the complex parameters B_{LS}, referred to as B_{LS} *couplings*, the helicity amplitude $H^{X\to CD}_{\lambda_C,\lambda_D}$ takes the form:

$$
\begin{aligned}
H^{X\to CD}_{\lambda_C,\lambda_D} = \sum_L \sum_S \sqrt{\frac{2L+1}{2J_X+1}} \cdot B_{LS} \cdot < J_C, J_D, S|\lambda_C, -\lambda_D, \lambda_C - \lambda_D > \\
\cdot < L, S, J_X|0, \lambda_C, -\lambda_D, \lambda_C - \lambda_D >
\end{aligned}
\tag{81}
$$

where the (L, S) subscripts of the B_{LS} couplings denote that one coupling is needed to describe each possible combination of the allowed values for L and S. The B_{LS} couplings are the actual parameters of the signal *pdf* that must be fit to data, together with the parameters of the line shape $R(m)$.

The formulation of the helicity amplitude in Equation 81 can be used to reduce the effective number of independent free parameters. In fact, if the decay process conserves parity, the helicity amplitudes are related by the P_X, P_C, P_D parity values of the particles X, C, D:

$$
H^{X\to CD}_{-\lambda_C,-\lambda_D} = P_X \cdot P_C \cdot P_D \cdot (-1)^{J_C+J_D-J_X} \cdot H^{X\to CD}_{\lambda_C,\lambda_D}
\tag{82}
$$

leading to a reduction of the number of independent amplitudes that must be summed.

The Wigner small d-matrices in Equation 79 express the angular dependence:

$$
\begin{aligned}
d^{J_X}_{\lambda_X,\lambda_C-\lambda_D}(\theta) = \sqrt{(J_X+\lambda_C)! \cdot (J_X-\lambda_C)! \cdot (J_X+\lambda_D)! \cdot (J_X-\lambda_D)!} \\
\cdot \sum_s [\frac{(-1)^s}{(J_X+\lambda_D-s)!s!(\lambda_C-\lambda_D+s)!(J_X-\lambda_C-s)!} \\
\cdot (cos\frac{\theta}{2})^{2J_X+\lambda_D-\lambda_C-2s} \cdot (sin\frac{\theta}{2})^{\lambda_C-\lambda_D+2s})]
\end{aligned}
\tag{83}
$$

where s is running over integers that make the factorials non negative.

Finally, the term $R(m_{C,D})$ in Equation 79 describes the shape of the X resonance appearing in the invariant mass distribution of the C and D particles of the 3-body decay $A \to BCD$:

$$
R(m_{C,D}) = B_{L_{X,B}}(p, p_0, d_{X,B})(\frac{p}{p_0})^{L_{X,B}} \cdot f(m_{C,D}|m_X, \Gamma_X) \cdot B_{L_{C,D}}(q, q_0, d_{C,D})(\frac{q}{q_0})^{L_{C,D}}
\tag{84}
$$

where $L_{X,B}$ and $L_{C,D}$ are respectively the orbital angular momentum between X and the spectator particle B and between the X daughters, C and D. The invariant mass of the $C-D$ system is denoted by $m_{C,D}$, and p is the momentum of the X resonance in the rest frame of A:

$$
p = \sqrt{\frac{(m^2_{C,D} - (m_C+m_D)^2) \cdot (m^2_{C,D} - (m_C-m_D)^2}{4\ m^2_{C,D}}}
\tag{85}
$$

while p_0 is evaluated at the resonance peak ($m_{C,D} = m_X$). Analogously, q is the momentum of the C particle in the X rest frame, and q_0 is evaluated at the resonance peak of X. The B_L terms are the *orbital angular momentum barrier factors* also called Blatt-Weisskopf functions [117]. They describe how it is likely to create an orbital angular momentum L depending on the momenta p, q and radii of the decaying particle $d_{A\to XB}$ and of the resonance $d_{X\to CD}$.

The $f(m,\Gamma)$ term in Equation 84 is the *line shape function*. It is mostly commonly parametrised by the relativistic Breit-Wigner distribution:

$$f(m_{C,D}|m_X,\Gamma_X) = \frac{1}{m_X^2 - m_{C,D}^2 - im_X\Gamma(m_{C,D})} \tag{86}$$

where $\Gamma(m_{C,D})$ is the mass-dependent width:

$$\Gamma(m_{C,D}) = \Gamma_0 \cdot (\frac{q}{q_0})^{2L_{C,D}+1} \cdot \frac{m_X}{m_{C,D}} \cdot B_{L_{C,D}}(q,q_0,d_{C,D})^2 \tag{87}$$

If the resonance X peaks near the $C-D$ threshold ($m_{C,D} = m_C + m_D$), its line shape is better parametrised by the Flatté distribution [118], rather than by a Breit-Wigner description. An effective pole mass $\tilde{m}$ is defined as follows:

$$\tilde{m} = m_{min} + (m_{max} - m_{min}) \cdot \frac{1 + \tan\chi}{2} \tag{88}$$

with m_{min}, m_{max} being the mass values kinematically allowed:

$$\begin{aligned} m_{min} &= m_C + m_D; \\ m_{max} &= m_A - m_B \end{aligned} \tag{89}$$

and χ defined as:

$$\chi = \frac{m_X - \frac{m_{min}+m_{max}}{2}}{m_{max} - m_{min}} \tag{90}$$

In the evaluation of the p_0, q_0 parameters in Equation 84, m_X is replaced by $\tilde{m}$. Also, a two-widths parametrisation is used, replacing the width Γ in the relativistic Breit-Wigner distribution by $\tilde{\Gamma}$:

$$\tilde{\Gamma} = \frac{2\rho_1\Gamma_1 \cdot 2\rho_2\Gamma_2}{m_X} \tag{91}$$

with Γ_1, Γ_2 being parameters which act as decay widths, and ρ_1, ρ_2 given by:

$$\begin{aligned} \rho_1 &= \frac{2q}{m_{C,D}} \\ \rho_2 &= \frac{2q'}{m_{C,D}} \end{aligned} \tag{92}$$

where q' is evaluated from the dominant decay channel of X.

In some cases, the Breit-Wigner and Flatté parametrisation are not sufficient for a satisfactory description of the line shape function. A more advanced formulation involves the so-called K-matrix amplitude, which is described in the next Section.

5.3 *K*-matrix approach for scattering amplitudes

The above-described formulation of decay amplitudes is rooted in the *S-matrix formalism* of scattering [119]. Formally, the S-matrix is represented by a *unitary* and *analytic* operator. Its unitarity, expressed by the relation:

$$S^\dagger S = I \tag{93}$$

is related to the normalisation to unity of the sum of all probabilities of decay and scattering processes. The analyticity means that S can be locally expressed by a convergent power series.

The element of the S-matrix connecting an initial-state a to a final-state b is defined by:

$$S_{ab} = I_{ab} - 2i\sqrt{\rho_a}T_{ab}\sqrt{\rho_b} \tag{94}$$

with ρ_a and ρ_b being phase-space terms. T is the so-called scattering matrix, which describes the interactions between the initial and final states. As consequence of the unitarity of the S-matrix, the following holds:

$$\mathrm{Im}(T) = \rho|T|^2 \tag{95}$$

where all the channels contributing to the decay and scattering processes have to be taken into account. Equation 95 is usually referred to as optical theorem [120].

Within the S-matrix formalism, physical states appear as poles of S, either on the physical sheet (for bound states) or on the un-physical ones (for resonances). A pole is represented in the complex S-plane by a complex quantity. Although both the real and imaginary parts of the pole are important for describing its position and the properties of the associated state, measurements are performed only on the real axis of the S-plane. This usually corresponds to the measurement of invariant mass distributions.

Let us consider a pole P corresponding to a state X, represented in the S-plane by the coordinates:

$$s_P = s_R - i\gamma \tag{96}$$

The amplitude $g(s)$ can be expanded around the pole, assuming small values of γ:

$$g(s) = (s - s_P)T(s) \tag{97}$$

where s is the squared invariant mass, which represents the observable under measurement. The expansion around the pole has a characteristic radius of convergence, determined by the closest threshold or pole as sketched in Figure 31. Expanding the amplitude in terms of Taylor series, $g(s)$ reads:

$$g(s) = g(s_P) + (s - s_P)g'(s_P) + ... \tag{98}$$

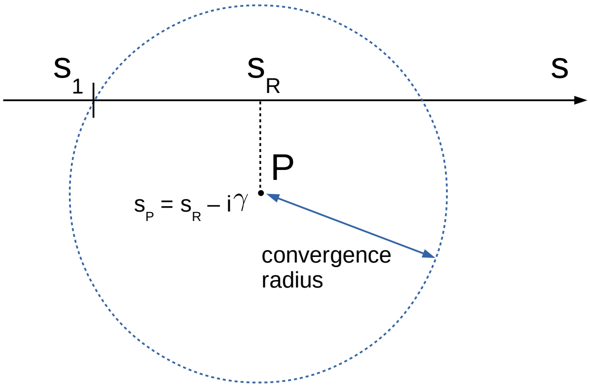

Figure 31: Sketch of a pole P, with real part s_R and imaginary component $-\gamma$. The amplitude around the pole can be expanded in terms of Taylor series, with a given radius of convergence. The latter is determined by the closest threshold or pole. s_1 is a threshold in the example.

At the first order, $g(s) \approx g(s_P)$ and the $T(s)$ matrix is given by:

$$T(s) \approx \frac{-g(s_P)}{s_R - s - i\gamma} \tag{99}$$

which corresponds to a Breit-Wigner distribution with fixed width, with the real part of the pole giving the mass M_X of the state, and its imaginary part being related to the width Γ_X:

$$\begin{aligned} s_R &= M_X^2 \\ \gamma &= M_X \cdot \Gamma_X \end{aligned} \tag{100}$$

Following the above derivation, it appears that the Breit-Wigner description is just the most simplistic extrapolation of the measurement of the real part of the pole into the complex plane. Also, it must be remembered that this formulation is only valid for small values of γ, i.e. for relatively narrow states. Under this assumption and for only one pole, the unitarity condition $\mathrm{Im}(T) = \rho|T|^2$ (Eq. 95) of the scattering matrix T holds, with $\rho = \sqrt{1 - 4M_X^2/s}$. In presence of two or more poles, writing the scattering matrix as simple sum of Breit-Wigner distributions:

$$T = -\frac{A_1^2}{s - M_1^2 + iM_1\Gamma_1} - \frac{A_2^2}{s - M_2^2 + iM_2\Gamma_2} - ... \tag{101}$$

violates unitarity. In fact, for the simplest case of two poles and with $\sigma = M_i\Gamma_i/A_i^2$:

$$\begin{aligned} \mathrm{Im}(T) &= \frac{A_1^2 M_1 \Gamma_1}{(s - M_1)^2 + M_1^2 + \Gamma_1^2} + \frac{A_2^2 M_2 \Gamma_2}{(s - M_2^2) + M_2^2\Gamma_2^2} \\ \rho|T|^2 &= \frac{A_1^2 M_1 \Gamma_1}{(s - M_1)^2 + M_1^2 + \Gamma_1^2} + \frac{A_2^2 M_2 \Gamma_2}{(s - M_2^2) + M_2^2\Gamma_2^2} \\ &\quad +2\rho\mathrm{Re}(\frac{A_1^2}{s - M_1^2 + iM_1\Gamma_1}\frac{A_2^2}{s - M_2^2 - iM_2\Gamma_2}) \end{aligned} \tag{102}$$

where the last factor, expressing the interference between the two poles, violates the unitarity. Moreover, the presence of a second pole limits the convergence radius of the expansion in Equation 98, weakening the analyticity of the theory. Similarly, the convergence of the Breit-Wigner approximation is not ensured in presence of thresholds of other channels. These behaviours are sketched in Figure 32.

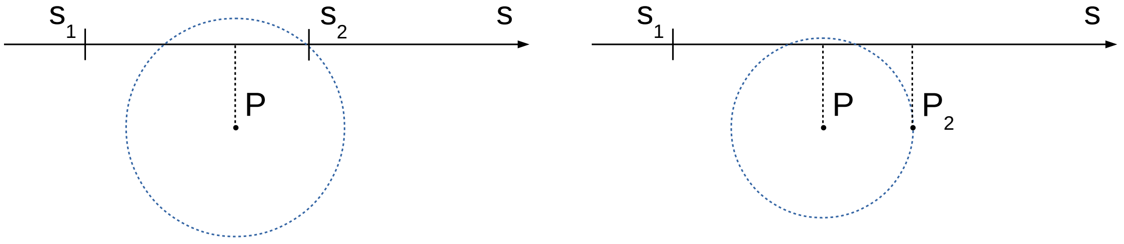

(a) (b)

Figure 32: Sketch of cases where the radius of convergence of the amplitude around a pole P is limited by the presence of a second threshold s_2 (a), or of a second pole P_2 (b).

It has been shown that the usage of Breit-Wigner distributions is problematic for describing states with large width, or close to thresholds of other channels. Also, the sum of Breit-Wigner functions for describing multiple poles breaks unitarity. This last point is especially problematic for states which are close in mass, and share the same quantum numbers. In such cases, the unitarity can be enforced by adopting the so-called *K-matrix formalism* [119] for constructing decay amplitudes. This analysis makes use of this approach, which is described in the following.

Let us consider a particle H decaying into a a number N of intermediate resonances R_n, and a spectator particle. The resonances R_n further decay in a number c of final-state channels labelled by the indices a and b in the following. This decay decomposition is sketched in Figure 33.
The decay amplitude of H can be written as:

$$A_a^H(s) = \gamma_a(s) D_{ab} P_b^H(s) \tag{103}$$

where s is the mass squared, and P_b^H is a vector in the channel space parametrised by:

$$P_b^H(s) = p_b(s) - \sum_{n=1}^{N} \frac{g_{nb}\alpha_n^H}{s - M_n^2} \tag{104}$$

with α_n^H being the coupling of H to the resonance R_n, g_{nb} the coupling of R_n to the channel b, and R_n having bare mass M_n. The factor $p_b(s)$ represents the coupling of H to the channel b, and in literature is often called *background term*.

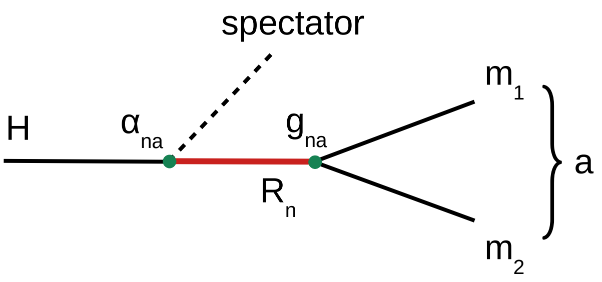

(a)

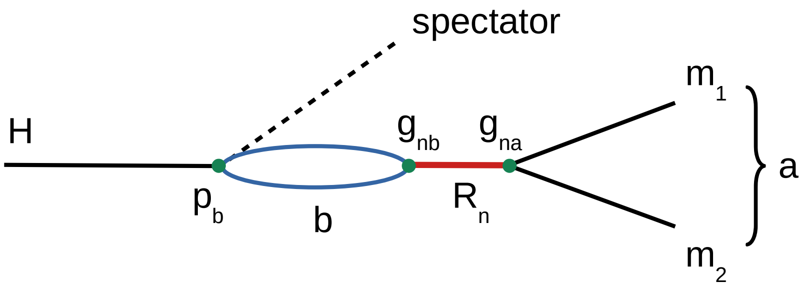

(b)

Figure 33: Sketch of the decay of a particle H to an intermediate resonance R_n and a spectator particle, in the K-matrix formalism. The resonance R_n decays to its final states having mass m_1 and m_2. The total decay amplitude is the sum of the direct process through the single decay channel a (a), and the decay where the other channels b contribute (b).

The matrix D in Equation 103 is given by:

$$D_{ab} = [1 - V^R(s)\Sigma(s)]^{-1}_{ab} \tag{105}$$

with Σ being the *self-energy*:

$$\Sigma_a(s) = i\rho_a(s)\gamma_a(s)^2 \tag{106}$$

and V^R being the *normalised vertex function*:

$$V^R_{ab} = -\sum_{n=1}^{N} \frac{g_{nb}g_{na}}{s - M_n^2} \tag{107}$$

where the coupling g_{na} of R_n to the channel a appears. In the self-energy (Eq. 106), ρ is the phase-space factor and γ is the angular momentum barrier term.

In two-body decays into products with masses m_1 and m_2, the two-body phase-space factor is given by:

$$\rho_a(s) = \frac{1}{16\pi} \cdot 2\frac{q_a(s)}{\sqrt{s}} \tag{108}$$

with q being the *two-body breakup momentum* defined as:

$$q_a(s) = \sqrt{\frac{(s - s_a^2)(s - d_a^2)}{4s}} \tag{109}$$

where $s_a = m_1 + m_2$ and $d_a = m_1 - m_2$ (neglecting the channel indices in the masses). The angular momentum barrier γ in Equation 106 takes the form:

$$\gamma_a(s) = q_a^{L_a} \tag{110}$$

where L_a denotes the angular momentum of the decay products.

Within the K-matrix approach, the only parameters of the model are the masses M_n, the couplings α_n^H, g_{na}, g_{nb} and the term p_b. The widths of the resonances are generated by the scattering amplitude itself, thus are not direct observables of the model. This leads to a more difficult application of the K-formalism to practical uses in fit to data, with respect to the construction described in Section 5.2. Also, a proper description of the K-matrix amplitude would require to sum over all the decay channels a, b. However, for heavy states this is often challenging due to the large number of channels potentially contributing, and the sum is usually truncated to the most relevant terms. Finally, the K-formalism breaks the analyticity of the theory: the phase-space factor in Equation 108 is not well defined for $s = 0$, and for unequal masses it develops a un-physical cut. Methods to improve the analyticity of the model when using the K-matrix approach have been developed [121–124], but are more formally enveloped.

The scattering amplitude $A_a^H(s)$ of Equation 103 replaces the line shape function $R(m)$ (Eq. 79) of the construction presented in Section 5.2. The description of the orbital angular momentum barrier effect, taken into account by the $\gamma_a(s)$ function in Equation 110, can be improved by introducing the Blatt-Weisskopf functions as in Equation 84.

5.4 Coordinate transformations for the $\Lambda_b^0 \to \Lambda_c^+\overline{D}^0K^-$decay channel

In this Section the above-described derivation of the decay matrix elements is actualised to the specific decay channel of this analysis. Intermediate resonance states can decay to all possible two-body system combinations of the Λ_c^+, $\overline{D}^0$, K^- particles. In the following, the notation $A_i \to \Lambda_c^+\overline{D}^0$, $B_i \to \overline{D}^0K^-$

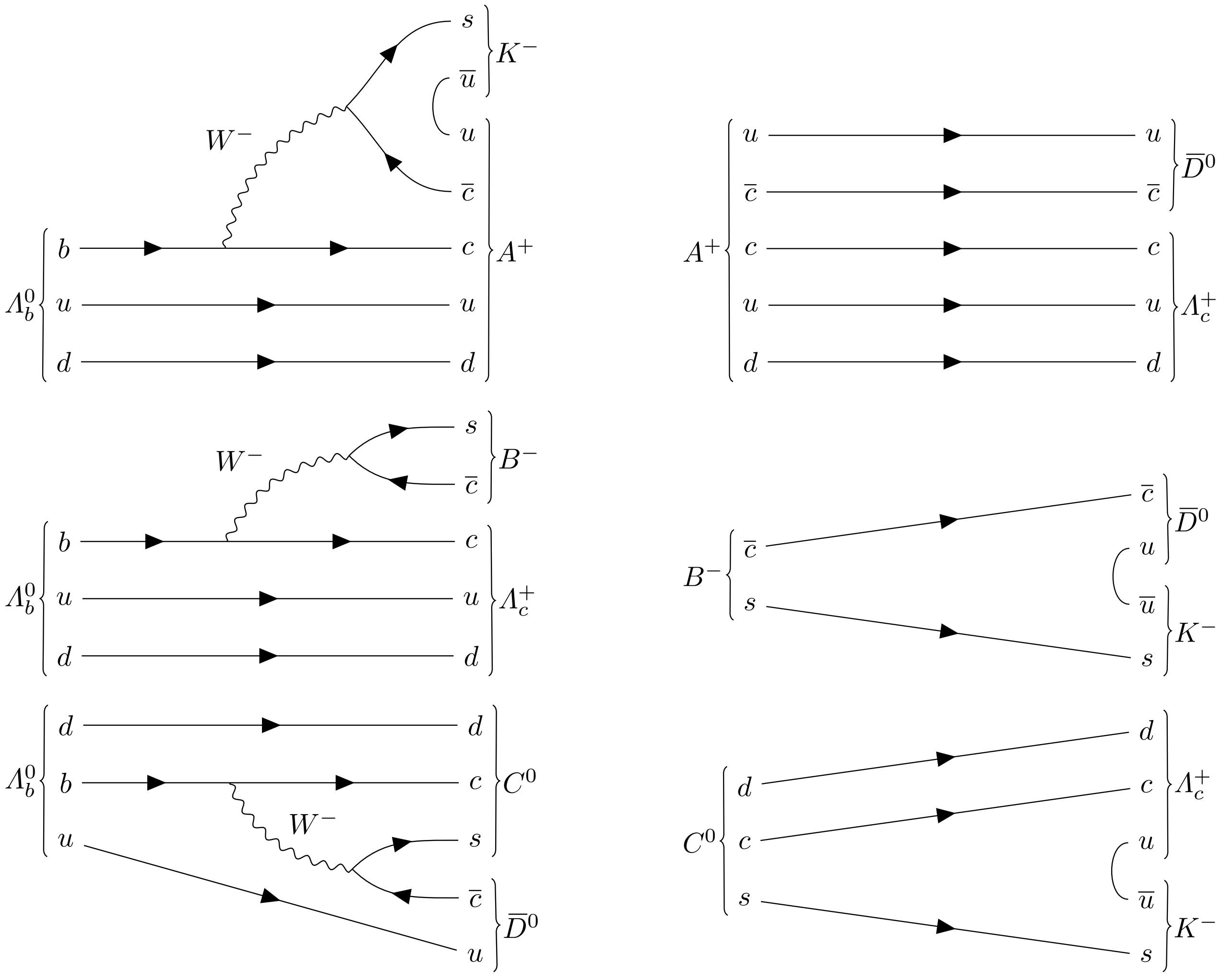

Figure 34: Feynman diagrams describing the $\Lambda_{\rm b}^0$ and subsequent decays for the $A \to \Lambda_{\rm c}^+\overline{\rm D}^0$, $B \to \overline{\rm D}^0{\rm K}^-$ and $C \to \Lambda_{\rm c}^+{\rm K}^-$ decay chains.

and $C_i \to \Lambda_{\rm c}^+{\rm K}^-$ is used to denote the possible types of intermediate resonances A_i, B_i, C_i [20]. The complete matrix element is expressed as sum of all the contributing decays over the initial- ($\lambda_{\Lambda_{\rm b}^0}$) and final-state ($\lambda_{\Lambda_{\rm c}^+}$) helicities:

$$|M|^2 = \sum_{\lambda_{\Lambda_{\rm b}^0},\lambda_{\Lambda_{\rm c}^+}} |\sum_{A_i} M^{\Lambda_{\rm c}^+\overline{\rm D}^0}_{\lambda_{\Lambda_{\rm b}^0},\lambda_{\Lambda_{\rm c}^+}} + \sum_{B_i} M^{\overline{\rm D}^0{\rm K}^-}_{\lambda_{\Lambda_{\rm b}^0},\lambda_{\Lambda_{\rm c}^+}} + \sum_{C_i} M^{\Lambda_{\rm c}^+{\rm K}^-}_{\lambda_{\Lambda_{\rm b}^0},\lambda_{\Lambda_{\rm c}^+}}|^2 \qquad (111)$$

The Feynman diagrams describing those decays are shown in Figure 34. In the following, the matrix elements for the A, B, C decay chains are described under the assumption that the $\Lambda_{\rm b}^0$ and $\Lambda_{\rm c}^+$ particles are not polarised. Eventual polarisations can be taken into account introducing additional parameters multiplying the incoherent sum of the decay amplitudes in Equation 111, as it is described in Section 7.1.8.

---

[20] The current notation A_i, B_i, C_i for the intermediate resonances of the $\Lambda_{\rm b}^0 \to \Lambda_{\rm c}^+\overline{\rm D}^0{\rm K}^-$channel is not related to the notation of the A, B, C particles used in the previous sections to introduce the coordinate transformations and matrix elements.

5.4.1 Coordinate transformations of the $A_i \to \Lambda_c^+ \overline{D}^0$ decay chain

The choice of the $\hat{z}_0{}^{\Lambda_b^0}$ direction for the Λ_b^0 spin quantisation is arbitrary. Previous studies of Λ_b^0 decays in the LHCb experiment did not find evidence for Λ_b^0 polarisation [125,126], thus $\hat{z}_0{}^{\Lambda_b^0}$ is chosen to be the direction of the Λ_b^0 momentum in the laboratory frame. With this choice, its spin projection onto $\hat{z}_0{}^{\Lambda_b^0}$ gives the $\lambda_{\Lambda_b^0}$ helicity. In the Λ_b^0 rest frame, the $\hat{z}_0{}^{\Lambda_b^0}$ direction is defined by the direction of the boost from the laboratory frame:

$$\hat{z}_0{}^{\Lambda_b^0} = \hat{p}^{lab}_{\Lambda_b^0} \tag{112}$$

as shown in Figure 35. The $\theta^A_{\Lambda_b^0}$ helicity angle is given by:

$$\cos\theta^A_{\Lambda_b^0} = \hat{p}^{lab}_{\Lambda_b^0} \cdot \hat{p}^{\Lambda_b^0}_{K^-} \tag{113}$$

Parity conservation in the strong interaction forbids the Λ_b^0 to be longitudinally polarised, thus the helicity values $\lambda_{\Lambda_b^0} = +\frac{1}{2}$, $\lambda_{\Lambda_b^0} = -\frac{1}{2}$ are equally likely.

The choice of the $\hat{x}_0{}^{\Lambda_b^0}$ direction in the Λ_b^0 rest frame is also arbitrary. The $\Lambda_b^0 \to AK^-$ decay plane in the laboratory frame is used to define it, setting $\phi^A_{K^-} = 0$ by definition.

The θ_A, $\phi_{\Lambda_c^+}$ are the polar and azimuthal angles of the Λ_c^+ in the A rest frame. The $\hat{z}_0{}^A$ direction is defined by the boost direction from the Λ_b^0 rest frame to the A rest frame, which coincides with the $-\hat{p}^A_{K^-}$ direction in this frame. The θ_A helicity angle is then given by:

$$\cos\theta_A = -\hat{p}^A_{K^-} \cdot \hat{p}^A_{\Lambda_c^+} \tag{114}$$

From Equations 75-112, the following holds:

$$\begin{aligned} \boldsymbol{\omega}^{\Lambda_b^0}_{z_0\perp A} &= \hat{p}^{lab}_{\Lambda_b^0} - (\hat{p}^{lab}_{\Lambda_b^0} \cdot \hat{p}_A^{\Lambda_b^0})\hat{p}_A^{\Lambda_b^0}, \\ \hat{x}^A_0 = x_3^{\Lambda_b^0} &= -\frac{\boldsymbol{\omega}^{\Lambda_b^0}_{z_0\perp A}}{|\boldsymbol{\omega}^{\Lambda_b^0}_{z_0\perp A}|} \end{aligned} \tag{115}$$

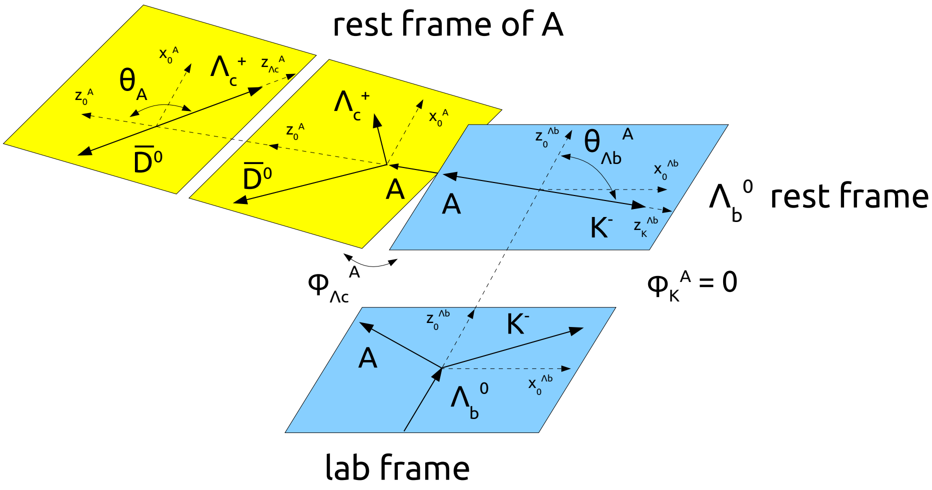

Figure 35: Decomposition of the helicity planes for the $\Lambda_b^0 \to A(\to \Lambda_c^+\overline{D}^0)K^-$ decay.

The $\phi^A_{\Lambda_\mathrm{c}^+}$ angle is finally given in the rest frame of A by Equation 70:

$$\phi^A_{\Lambda_\mathrm{c}^+} = \mathrm{atan2}(-(\hat{p}^A_{\mathrm{K}^-} \times \hat{x}^A_0) \cdot \hat{p}^A_{\Lambda_\mathrm{c}^+}, \hat{x}^A_0 \cdot \hat{p}^A_{\Lambda_\mathrm{c}^+}) \tag{116}$$

Finally, the intermediate matrices of the $\Lambda_\mathrm{b}^0 \to A\mathrm{K}^-$ and $A \to \Lambda_\mathrm{c}^+\overline{\mathrm{D}}^0$ processes are given by coherent sums over the intermediate-state (λ_A) helicities:

$$\begin{aligned}
M^{\Lambda_\mathrm{c}^+\overline{\mathrm{D}}^0}_{\lambda_{\Lambda_\mathrm{b}^0},\lambda_{\Lambda_\mathrm{c}^+}} &= \sum_{\lambda_A} M^{\Lambda_\mathrm{b}^0\to A\mathrm{K}^-}_{\lambda_{\Lambda_\mathrm{b}^0},\lambda_A} \cdot M^{A\to\Lambda_\mathrm{c}^+\overline{\mathrm{D}}^0}_{\lambda_A,\lambda_{\Lambda_\mathrm{c}^+}}, \\
M^{\Lambda_\mathrm{b}^0\to A\mathrm{K}^-}_{\lambda_{\Lambda_\mathrm{b}^0},\lambda_A}(\theta^A_{\Lambda_\mathrm{b}^0}) &= H^{\Lambda_\mathrm{b}^0\to A\mathrm{K}^-}_{\lambda_A} \cdot d^{J_{\Lambda_\mathrm{b}^0}=\frac{1}{2}}_{\lambda_{\Lambda_\mathrm{b}^0},\lambda_A}(\theta^A_{\Lambda_\mathrm{b}^0}), \\
M^{A\to\Lambda_\mathrm{c}^+\overline{\mathrm{D}}^0}_{\lambda_A,\lambda_{\Lambda_\mathrm{c}^+}}(\theta_A,\phi^A_{\Lambda_\mathrm{c}^+}) &= H^{A\to\Lambda_\mathrm{c}^+\overline{\mathrm{D}}^0}_{\lambda_{\Lambda_\mathrm{c}^+}} \cdot d^{J_A}_{\lambda_A,\lambda_{\Lambda_\mathrm{c}^+}}(\theta_A) \cdot e^{i\lambda_A\cdot\phi^A_{\Lambda_\mathrm{c}^+}} \cdot R(m_{\Lambda_\mathrm{c}^+\overline{\mathrm{D}}^0})
\end{aligned} \tag{117}$$

It must be noted that the resonance shape term can be neglected in the two-body decay matrix of the decaying Λ_b^0. In fact, strictly speaking the resonance line shape represents the probability of a resonance to be formed as function of the invariant mass of the daughter particles. This term is needed to describe the intermediate resonances A, B, C which can *potentially* occur in the decay of the Λ_b^0. On the other hand, *all* the decays are originated from a Λ_b^0 particle, which consequentially does not require a line shape term for being described.

5.4.2 Coordinate transformations of the $B_i \to \overline{\mathrm{D}}^0\mathrm{K}^-$ decay chain

Similarly to Equation 113, the $\theta^B_{\Lambda_\mathrm{b}^0}$ helicity angle in the B decay chain, as shown in Figure 36, is given by:

$$\cos\theta^B_{\Lambda_\mathrm{b}^0} = \hat{p}^{lab}_{\Lambda_\mathrm{b}^0} \cdot \hat{p}^{\Lambda_\mathrm{b}^0}_{\Lambda_\mathrm{c}^+} \tag{118}$$

The $\hat{x}^{\Lambda_\mathrm{b}^0}$ axis has been defined already by fixing by the ϕ_{K^-} convention, thus $\phi_{\Lambda_\mathrm{c}^+}$ cannot be set to zero. Equation 75, leads to:

$$\begin{aligned}
\boldsymbol{\omega}^{\Lambda_\mathrm{b}^0}_{\Lambda_\mathrm{c}^+\perp z_0} &= \boldsymbol{p}^{\Lambda_\mathrm{b}^0}_{\Lambda_\mathrm{c}^+} - (\boldsymbol{p}^{\Lambda_\mathrm{b}^0}_{\Lambda_\mathrm{c}^+} \cdot \hat{p}^{lab}_{\Lambda_\mathrm{b}^0})\hat{p}^{lab}_{\Lambda_\mathrm{b}^0}, \\
\hat{x}^{\Lambda_\mathrm{b}^0}_0 &= \frac{\boldsymbol{\omega}^{\Lambda_\mathrm{b}^0}_{\Lambda_\mathrm{c}^+\perp z_0}}{|\boldsymbol{\omega}^{\Lambda_\mathrm{b}^0}_{\Lambda_\mathrm{c}^+\perp z_0}|}
\end{aligned} \tag{119}$$

and $\phi^B_{\Lambda_\mathrm{c}^+}$ results to be:

$$\phi^B_{\Lambda_\mathrm{c}^+} = \mathrm{atan2}((\hat{p}^{lab}_{\Lambda_\mathrm{b}^0} \times \hat{x}^{\Lambda_\mathrm{b}^0}_0) \cdot \hat{p}^{\Lambda_\mathrm{b}^0}_{\Lambda_\mathrm{c}^+}, \hat{x}^{\Lambda_\mathrm{b}^0}_0 \cdot \hat{p}^{\Lambda_\mathrm{b}^0}_{\Lambda_\mathrm{c}^+}) \tag{120}$$

The $\hat{z}^B_0$ direction is defined by the boost direction from the Λ_b^0 to the rest frame of the B particle, which coincides with the $-\hat{p}^B_{\Lambda_\mathrm{c}^+}$ direction. The θ_B helicity angle is then given by:

$$\cos\theta_B = -\hat{p}^B_{\Lambda_\mathrm{c}^+} \cdot \hat{p}^B_{\overline{\mathrm{D}}^0} \tag{121}$$

The $\hat{x}^B_0$ direction is fixed by the convention used in the Λ_b^0 rest frame. From Equation 73, the following relation holds:

$$\begin{aligned}\boldsymbol{\omega}^{\Lambda_b^0}_{z_0\perp B} &= \boldsymbol{p}^{lab}_{\Lambda_b^0} - (\hat{p}^{lab}_{\Lambda_b^0} \cdot \hat{p}_B^{\Lambda_b^0})\hat{p}_B^{\Lambda_b^0}, \\ \hat{x}_0^B &= \frac{\boldsymbol{\omega}^{\Lambda_b^0}_{z0\perp B}}{|\boldsymbol{\omega}^{\Lambda_b^0}_{z_0\perp B}|}\end{aligned} \tag{122}$$

The $\phi^B_{\overline{\mathrm{D}}^0}$ angle is finally given in the rest frame of the B particle by:

$$\phi^B_{\overline{\mathrm{D}}^0} = \mathrm{atan2}(-(\hat{p}^B_{\overline{\mathrm{D}}^0} \times \hat{x}_0^B) \cdot \hat{p}_{\overline{\mathrm{D}}^0}, \hat{x}_0^B \cdot \hat{p}_{\overline{\mathrm{D}}^0} \cdot \hat{p}^B) \tag{123}$$

The intermediate matrix elements for the $\Lambda_\mathrm{b}^0 \to B\Lambda_\mathrm{c}^+$ decays are coherent sums over the intermediate-state helicities λ_B:

$$M^B_{\lambda_{\Lambda_\mathrm{b}^0}, \lambda^B_{\Lambda_\mathrm{c}^+}} = \sum_{\lambda_B} M^{\Lambda_\mathrm{b}^0 \to B\Lambda_\mathrm{c}^+}_{\lambda_{\Lambda_\mathrm{b}^0}, \lambda_B, \lambda^B_{\Lambda_\mathrm{c}^+}} \cdot M^{B \to \overline{\mathrm{D}}^0\mathrm{K}^-}_{\lambda_B} \tag{124}$$

In Equation 124 the Λ_c^+ helicity is labelled with a B superscript to show that the spin quantisation axis is different than in the A decay chain. The Λ_c^+ helicity axes are different because the particle comes from a decay of different particles, in the A and B decay chains: the quantisation axes are always along the Λ_c^+ direction in both the A (in the A decay chain) and Λ_b^0 (in the B decay chain) rest frames, but they are different. These axes are anti-parallel to the particles recoiling against the Λ_c^+, i.e. the $\overline{\mathrm{D}}^0$ and the B in the A and B decay chains respectively, and their directions are preserved when boosting to the Λ_c^+ rest frame. Then it is possible to define a polar angle $\theta^{AB}_{\Lambda_\mathrm{c}^+}$ between the two quantisation axes of the Λ_c^+. It is given by the opening angle between $\overline{\mathrm{D}}^0$ and the particle B in the Λ_c^+ rest frame, as shown in Figure 37:

$$\cos\theta^{AB}_{\Lambda_\mathrm{c}^+} = \hat{p}^{\Lambda_\mathrm{c}^+}_{\overline{\mathrm{D}}^0} \cdot \hat{p}^{\Lambda_\mathrm{c}^+}_B \tag{125}$$

The azimuthal angle $\alpha_{\Lambda_\mathrm{c}^+}$ which aligns the two Λ_c^+ helicity frames can be determined from:

$$\alpha_{\Lambda_\mathrm{c}^+} = \mathrm{atan2}((\hat{z}_0{}^{\Lambda_\mathrm{c}^+(A)} \times \hat{x}_0{}^{\Lambda_\mathrm{c}^+(A)}) \cdot \hat{x}_0{}^{\Lambda_\mathrm{c}^+(B)}, \hat{x}_0{}^{\Lambda_\mathrm{c}^+(A)} \cdot \hat{x}_0{}^{\Lambda_\mathrm{c}^+(B)}) \tag{126}$$

where all the vectors are computed in the Λ_c^+ rest frame. $\hat{x}_0{}^{\Lambda_\mathrm{c}^+(B)}$ is pointing to the direction of the x axis when boosting from the B rest frame, $\hat{x}_0{}^{\Lambda_\mathrm{c}^+(A)}$ and $\hat{z}_0{}^{\Lambda_\mathrm{c}^+(A)}$ are in the directions of the x and z

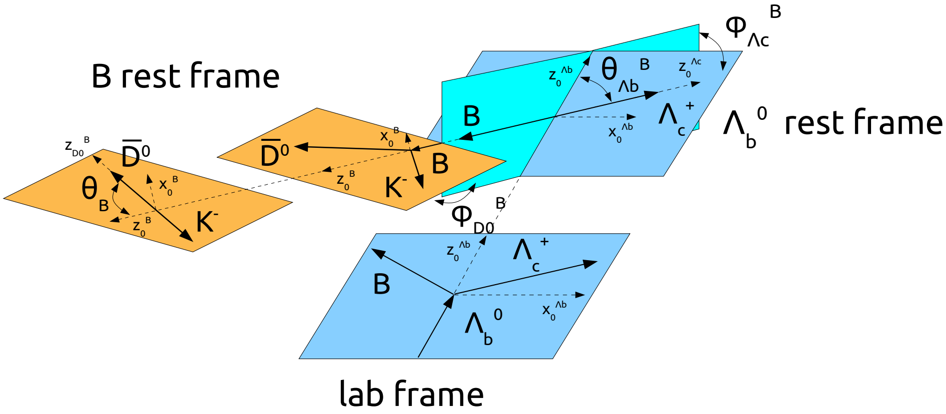

Figure 36: Decomposition of the helicity planes for the $\Lambda_\mathrm{b}^0 \to B(\to \overline{\mathrm{D}}^0\mathrm{K}^-)\Lambda_\mathrm{c}^+$ decay.

axes when boosting from the rest frame of A. In the Λ_{c}^{+} rest frame, $\hat{z_0}^{\Lambda_{\mathrm{c}}^{+}(A)} = -\hat{p}_{\overline{\mathrm{D}}^0}^{\Lambda_{\mathrm{c}}^{+}(A)}$ holds. Also, $\hat{z_0}^{A} = -\hat{p}^{A}_{\mathrm{K}^-}$ and the $\hat{x_0}^{\Lambda_{\mathrm{c}}^{+}(A)}$ direction is derived following Equation 75:

$$\begin{aligned} \boldsymbol{\omega}^{A}_{z_0\perp\overline{\mathrm{D}}^0} &= -\hat{p}^{A}_{\mathrm{K}^-} + (\hat{p}^{A}_{\mathrm{K}^-}\cdot\hat{p}^{A}_{\overline{\mathrm{D}}^0})\hat{p}^{A}_{\overline{\mathrm{D}}^0}, \\ \hat{x_0}^{\Lambda_{\mathrm{c}}^{+}(A)} &= \frac{\boldsymbol{\omega}^{A}_{z_0\perp\overline{\mathrm{D}}^0}}{|\boldsymbol{\omega}^{A}_{z_0\perp\overline{\mathrm{D}}^0}|} \end{aligned} \tag{127}$$

Similarly, $\hat{x_0}^{\Lambda_{\mathrm{c}}^{+}(B)}$ is given by:

$$\begin{aligned} \boldsymbol{\omega}^{\Lambda_{\mathrm{b}}^0(B)}_{z_0\perp B} &= \hat{z}_0^{\Lambda_{\mathrm{b}}^0(B)} - (\hat{z}_0^{\Lambda_{\mathrm{b}}^0(B)}\cdot\hat{p}_B^{\Lambda_{\mathrm{b}}^0(B)})\hat{p}_B^{\Lambda_{\mathrm{b}}^0(B)}, \\ \hat{x_0}^{\Lambda_{\mathrm{c}}^{+}(B)} &= \frac{\boldsymbol{\omega}^{\Lambda_{\mathrm{b}}^0(B)}_{z_0\perp B}}{|\boldsymbol{\omega}^{\Lambda_{\mathrm{b}}^0(B)|}_{z_0\perp B}} \end{aligned} \tag{128}$$

Finally the relation between the $\lambda_{\Lambda_{\mathrm{c}}^{+}}$ and $\lambda^{B}_{\Lambda_{\mathrm{c}}^{+}}$ states is given by:

$$|\lambda_{\Lambda_{\mathrm{c}}^{+}}> = \sum_{\lambda^{B}_{\Lambda_{\mathrm{c}}^{+}}} D^{J_{\Lambda_{\mathrm{c}}^{+}}}_{\lambda^{B}_{\Lambda_{\mathrm{c}}^{+}},\lambda_{\Lambda_{\mathrm{c}}^{+}}}(\alpha_{\Lambda_{\mathrm{c}}^{+}}, \theta^{AB}_{\Lambda_{\mathrm{c}}^{+}}, 0)^{*}|\lambda^{B}_{\Lambda_{\mathrm{c}}^{+}}> \tag{129}$$

It must be noted that the azimuthal angle $\alpha_{\Lambda_{\mathrm{c}}^{+}}$ results to be zero by construction. Indeed, because of momentum conservation the three final state particles in the Λ_{b}^0 rest frame are always lying on the same decay plane. Then, in the Λ_{b}^0 rest frame the A and B decay planes are the same, resulting in a null angle $\alpha_{\Lambda_{\mathrm{c}}^{+}}$.

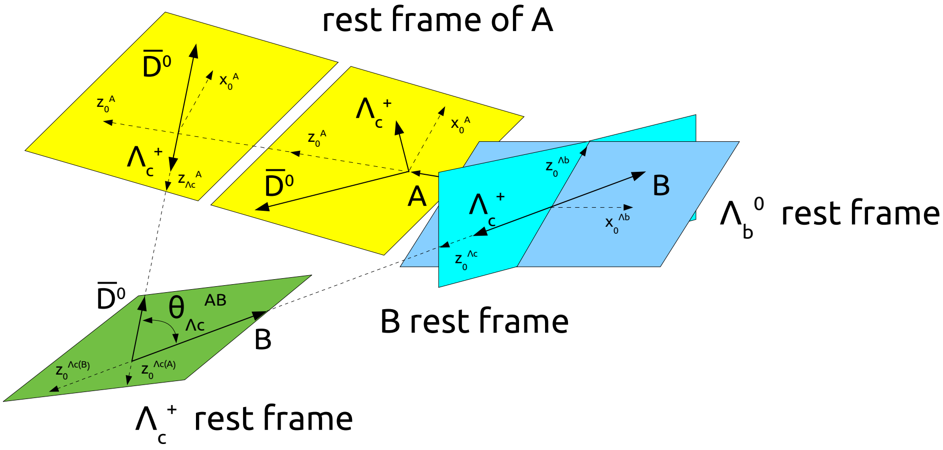

Figure 37: Definition of the $\theta^{AB}_{\Lambda_{\mathrm{c}}^{+}}$ angle between the quantisation axes of the Λ_{c}^{+} in the references of the A and B decay chains.

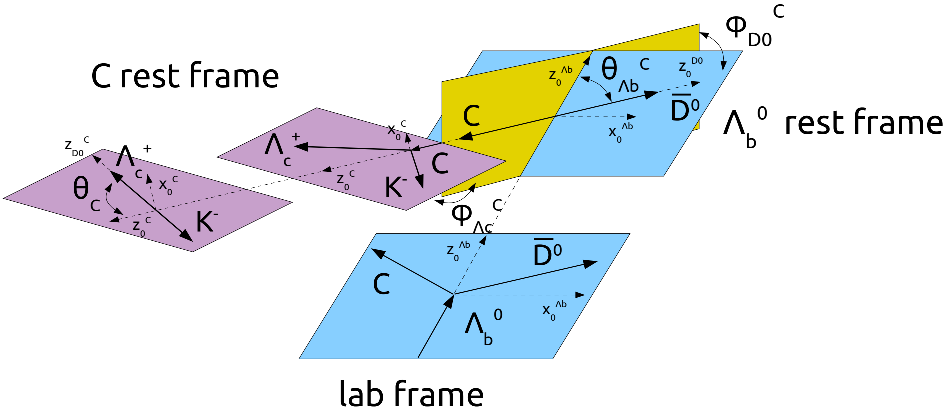

Figure 38: Decomposition of the helicity planes for the $\Lambda_{\mathrm{b}}^{0} \to C(\to \Lambda_{\mathrm{c}}^{+}\mathrm{K}^{-})\overline{\mathrm{D}}{}^{0}$ decay.

The matrix element of the B decay chain (Eq. 124) must take into account the following additional term in the $M^{\Lambda_{\mathrm{b}}^{0}\to B\Lambda_{\mathrm{c}}^{+}}_{\lambda_{\Lambda_{\mathrm{b}}^{0}},\lambda_B,\lambda_{\Lambda_{\mathrm{c}}^{+}}}$ matrix element:

$$
\begin{aligned}
M^{\Lambda_{\mathrm{b}}^{0}\to B\Lambda_{\mathrm{c}}^{+}}_{\lambda_{\Lambda_{\mathrm{b}}^{0}},\lambda_B,\lambda_{\Lambda_{\mathrm{c}}^{+}}}(\theta^{AB}_{\Lambda_{\mathrm{c}}^{+}},\theta^{B}_{\Lambda_{\mathrm{b}}^{0}},\phi^{B}_{\Lambda_{\mathrm{c}}^{+}}) &= \sum_{\lambda^{B}_{\Lambda_{\mathrm{c}}^{+}}} D^{J_{\Lambda_{\mathrm{c}}^{+}}}_{\lambda^{B}_{\Lambda_{\mathrm{c}}^{+}},\lambda_{\Lambda_{\mathrm{c}}^{+}}}(0,\theta^{AB}_{\Lambda_{\mathrm{c}}^{+}},0)^{*}\cdot \\
&\quad \cdot H^{\Lambda_{\mathrm{b}}^{0}\to B\Lambda_{\mathrm{c}}^{+}}_{\lambda_B,\lambda^{B}_{\Lambda_{\mathrm{c}}^{+}}} \cdot d^{J_{\Lambda_{\mathrm{b}}^{0}}=\frac{1}{2}}_{\lambda_{\Lambda_{\mathrm{b}}^{0}},\lambda_B-\lambda^{B}_{\Lambda_{\mathrm{c}}^{+}}}(\theta^{B}_{\Lambda_{\mathrm{b}}^{0}})\cdot e^{i\lambda_{\Lambda_{\mathrm{b}}^{0}}\cdot\phi^{B}_{\Lambda_{\mathrm{c}}^{+}}} \\
&= \sum_{\lambda^{B}_{\Lambda_{\mathrm{c}}^{+}}} d^{J_{\Lambda_{\mathrm{c}}^{+}}=\frac{1}{2}}_{\lambda^{B}_{\Lambda_{\mathrm{c}}^{+}},\lambda_{\Lambda_{\mathrm{c}}^{+}}}(\theta^{AB}_{\Lambda_{\mathrm{c}}^{+}})\cdot H^{\Lambda_{\mathrm{b}}^{0}\to B\Lambda_{\mathrm{c}}^{+}}_{\lambda_B,\lambda^{B}_{\Lambda_{\mathrm{c}}^{+}}} \cdot d^{J_{\Lambda_{\mathrm{b}}^{0}}=\frac{1}{2}}_{\lambda_{\Lambda_{\mathrm{b}}^{0}},\lambda_B-\lambda^{B}_{\Lambda_{\mathrm{c}}^{+}}}(\theta^{B}_{\Lambda_{\mathrm{b}}^{0}})\cdot e^{i\lambda_{\Lambda_{\mathrm{b}}^{0}}\cdot\phi^{B}_{\Lambda_{\mathrm{c}}^{+}}}, \\
M^{B\to\overline{\mathrm{D}}{}^{0}\mathrm{K}^{-}}_{\lambda_B}(\theta_B,\phi^{B}_{\overline{\mathrm{D}}{}^{0}}) &= H^{B\to\overline{\mathrm{D}}{}^{0}\mathrm{K}^{-}}\cdot d^{J_B}_{\lambda_B}(\theta_B)\cdot e^{i\lambda_B\cdot\phi^{B}_{\overline{\mathrm{D}}{}^{0}}}\cdot R(m_{\overline{\mathrm{D}}{}^{0}\mathrm{K}^{-}})
\end{aligned}
\tag{130}
$$

5.4.3 Coordinate transformations of the $C_i \to \Lambda_{\mathrm{c}}^{+}\mathrm{K}^{-}$ decay chain

Analogously to Equations 113, 118 the helicity angle $\theta_{\Lambda_{\mathrm{b}}^{0}}$, as defined in Figure 38, is given by:

$$\cos\theta^{C}_{\Lambda_{\mathrm{b}}^{0}} = \hat{p}^{lab}_{\Lambda_{\mathrm{b}}^{0}}\cdot\hat{p}^{\Lambda_{\mathrm{b}}^{0}}_{\overline{\mathrm{D}}{}^{0}} \tag{131}$$

and similarly to Equation 120 the azimuthal angle $\phi^{C}_{\overline{\mathrm{D}}{}^{0}}$ is:

$$\phi^{C}_{\overline{\mathrm{D}}{}^{0}} = \mathrm{atan2}((\hat{p}^{lab}_{\Lambda_{\mathrm{b}}^{0}}\times\hat{x}_0^{\Lambda_{\mathrm{b}}^{0}})\cdot\hat{p}^{\Lambda_{\mathrm{b}}^{0}}_{\overline{\mathrm{D}}{}^{0}}, \hat{x}_0^{\Lambda_{\mathrm{b}}^{0}}\cdot\hat{p}^{\Lambda_{\mathrm{b}}^{0}}_{\overline{\mathrm{D}}{}^{0}}) \tag{132}$$

The angle θ_C can be derived following Equations 114, 121:

$$\cos\theta_C = -\hat{p}^{C}_{\overline{\mathrm{D}}{}^{0}}\cdot\hat{p}^{C}_{\Lambda_{\mathrm{c}}^{+}} \tag{133}$$

and following Equations 116, 123 the angle $\phi^{C}_{\Lambda_{\mathrm{c}}^{+}}$ results to be:

$$\phi^{C}_{\Lambda_{\mathrm{c}}^{+}} = \mathrm{atan2}(-(\hat{p}^{C}_{\Lambda_{\mathrm{c}}^{+}}\times\hat{x}_0^{C})\cdot\hat{p}^{C}_{\Lambda_{\mathrm{c}}^{+}}, \hat{x}_0^{C}\cdot\hat{p}^{C}_{\Lambda_{\mathrm{c}}^{+}}) \tag{134}$$

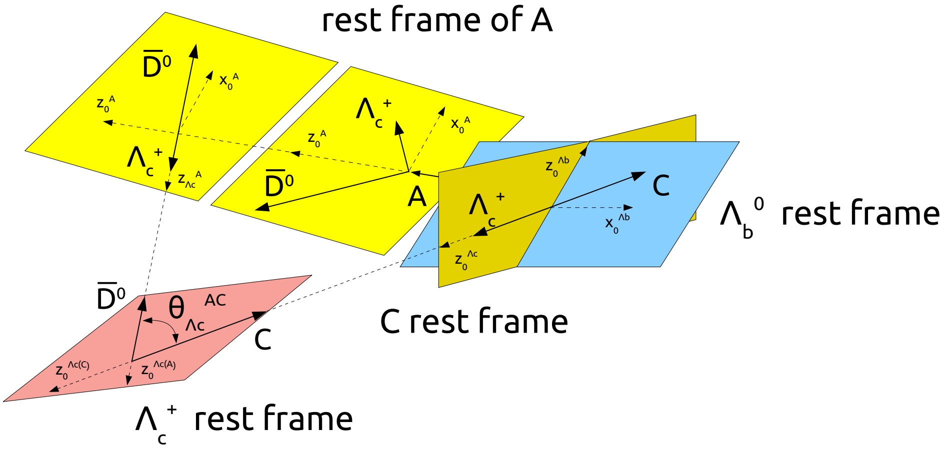

Figure 39: Definition of the $\theta^{AC}_{\Lambda_c^+}$ angle between the quantisation axes of the Λ_c^+ in the references of the A and C decay chains.

The same considerations about the spin quantisation axis of the Λ_c^+, described in the previous subsection, apply here. The $\theta^{AC}_{\Lambda_c^+}$ polar angle between the two quantisation axes of the Λ_c^+, as sketched in Figure 39, can be derived similarly to Equation 125 :

$$\cos\theta^{AC}_{\Lambda_c^+} = \hat{p}^{\Lambda_c^+}_{\overline{D}^0} \cdot \hat{p}^{\Lambda_c^+}_{C} \tag{135}$$

The final matrix element $M^C_{\lambda_{\Lambda_b^0},\lambda^C_{\Lambda_c^+}}$ and the intermediate matrices are listed below:

$$\begin{aligned}
M^C_{\lambda_{\Lambda_b^0},\lambda_{\Lambda_c^+}} &= \sum_{\lambda_C} M^{\Lambda_b^0\to C\overline{D}^0}_{\lambda_{\Lambda_b^0},\lambda_C} \cdot M^{C\to\Lambda_c^+\mathrm{K}^-}_{\lambda_C,\lambda_{\Lambda_c^+}}, \\
M^{\Lambda_b^0\to C\overline{D}^0}_{\lambda_{\Lambda_b^0},\lambda_C}(\theta^C_{\Lambda_b^0},\phi^C_{\overline{D}^0}) &= H^{\Lambda_b^0\to C\overline{D}^0}_{\lambda_C} \cdot d^{J_{\Lambda_b^0}=\frac{1}{2}}_{\lambda_{\Lambda_b^0},\lambda_C}(\theta^C_{\Lambda_b^0}) \cdot e^{i\lambda_{\Lambda_b^0}\cdot\phi^C_{\overline{D}^0}}, \\
M^{C\to\Lambda_c^+\mathrm{K}^-}_{\lambda_C,\lambda_{\Lambda_c^+}}(\theta^{AC}_{\Lambda_c^+},\theta_C,\phi^C_{\Lambda_c^+}) &= \sum_{\lambda^C_{\Lambda_c^+}} d^{J_{\Lambda_c^+}=\frac{1}{2}}_{\lambda^C_{\Lambda_c^+},\lambda_{\Lambda_c^+}}(\theta^{AC}_{\Lambda_c^+}) \cdot H^{C\to\Lambda_c^+\mathrm{K}^-}_{\lambda^C_{\Lambda_c^+}} \cdot d^{J_C}_{\lambda_C,\lambda^C_{\Lambda_c^+}}(\theta_C) \cdot e^{i\lambda_C\cdot\phi^C_{\Lambda_c^+}} \cdot R(m_{\Lambda_c^+\mathrm{K}^-})
\end{aligned} \tag{136}$$

5.5 Reduction of the free helicity amplitudes and couplings

Each X resonance introduces helicity amplitudes at the top-level decay of the Λ_b^0 and for its subsequent decay, namely $H^{\Lambda_b^0}$ and H^X, which depend on the helicities of the initial-, intermediate- and final-state particles as shown in Equation 79.

The Λ_b^0 decays into the state A and a spin-less particle, thus the λ_A helicity can take only values $\pm\frac{1}{2}$ to conserve angular momentum, independent of the spin of A. If A decays through strong interaction, the parity conservation in the decay implies:

$$H^{A\to\Lambda_c^+\overline{D}^0}_{\lambda_{\Lambda_c^+}=-\frac{1}{2}} = P_{\Lambda_c^+}\cdot P_{\overline{D}^0}\cdot P_A\cdot(-1)^{J_{\Lambda_c^+}-J_A}\cdot H^{A\to\Lambda_c^+\overline{D}^0}_{\lambda_{\Lambda_c^+}=+\frac{1}{2}} \tag{137}$$

lowering the number of free parameters to be fitted.

The same reasoning applies for the decays involving the intermediate states C, because both the $\overline{D}^0$ and the K^- are spin-less particles and they can be treated in the same way as in the previous case.

In particular, for strong decays of the C states the parity conservation implies that the $H^{C\to\Lambda_c^+K^-}_{\lambda_{\Lambda_c^+}}$ amplitudes are related by:

$$H^{C\to\Lambda_c^+K^-}_{\lambda_{\Lambda_c^+}=-\frac{1}{2}} = P_C \cdot P_{\Lambda_c^+} \cdot P_{K^-} \cdot H^{C\to\Lambda_c^+K^-}_{\lambda_{\Lambda_c^+}=+\frac{1}{2}} \tag{138}$$

The $B \to \overline{D}^0K^-$ decay is described by one single helicity amplitude $H^{B\to\overline{D}^0K^-}$ which does not show any dependence on the helicities of the B daughters, since they are spin-less particles.

From Equation 81, each partial wave contributing to the helicity amplitudes introduces two free parameters to fit, leading to a high number of free parameters when considering all the possible waves contributing to an amplitude. However, their number can be reduced thanks to considerations about angular momentum and spins. The decomposition of the helicity amplitude in partial waves depends on S, total spin of the daughters combination, and on L, orbital momentum in the decay. If the energy release of the decay $Q = M - m_1 - m_2$ is small compared to the mass M of the decaying particle (where m_i are the masses of the daughter particles), then high values of L are suppressed (*angular momentum barrier* effect) lowering the number of partial waves contributing to the amplitude. This results in a reduction of the fit parameters. Furthermore, for strong decays $A \to BC$ the parity conservation constrains the values that can be taken by L:

$$P_A \equiv P_B \cdot P_C \cdot (-1)^L \tag{139}$$

where P_i are the parities of the particles.

6 Amplitude fit to data

Amplitude fits to data are performed based on the helicity formalism as introduced in Chapter 5. The *s*-weighting procedure, described in Section 3.2.3, is employed to distinguish between signal-like and background-like candidates in the same data set. An alternative fitting procedure which does not rely on the *s*-weighting of the candidates is presented in Chapter 7.

The matrix elements of the decay chains A, B, C introduced in Chapter 5 depend on the angular variables defined in the different coordinate systems, and on the invariant masses $m(\Lambda_c^+\overline{D}^0)$, $m(\overline{D}^0K^-)$, $m(\Lambda_c^+K^-)$. However, all the angular and mass variables can be expressed in terms of only three angles and one invariant mass, via rotations and boosts. Ultimately, the amplitude fit is performed in only four dimensions: the angular variables of the intermediate states A decaying to the $\Lambda_c^+\overline{D}^0$ system ($\cos\theta_{\Lambda_b^0}$, $\cos\theta_A$, $\phi_{\Lambda_c^+}$) and the $m(\Lambda_c^+\overline{D}^0)$ invariant mass distribution. In the following, the angular variable $\cos\theta_A$ is referred to as $\cos\theta_{P_c}$ and the $\Lambda_c^+\overline{D}^0$ invariant mass is denoted by $m_{\Lambda_c^+\overline{D}^0}$.

The signal *pdf* used to fit the data is introduced in Section 6.1. The amplitude model is detailed in Section 6.3, and the results of the amplitude fits presented in Section 6.5.

6.1 Signal *pdf* and extended likelihood

In general, the signal *pdf* $\mathcal{P}$ depends on the $m_{\Lambda_c^+\overline{D}^0}$ invariant mass, on the angular variables of the decay chain of the states A (which is referred to as Ω in the following), and on the fit parameters $\boldsymbol{w}$:

$$\mathcal{P}(m_{\Lambda_c^+\overline{D}^0},\Omega|\boldsymbol{w}) = \frac{1}{N(\boldsymbol{w})}|M(m_{\Lambda_c^+\overline{D}^0},\Omega|\boldsymbol{w})|^2 \cdot \epsilon_{sig}(m_{\Lambda_c^+\overline{D}^0},\Omega)\cdot\phi(m_{\Lambda_c^+\overline{D}^0}) \tag{140}$$

where $M(m_{\Lambda_c^+\overline{D}^0},\Omega)$ is the matrix element describing the complete decay process from the Λ_b^0 to the final-state particles Λ_c^+, $\overline{D}^0$, K^-. ϵ_{sig} is the efficiency of selecting signal events, ϕ is the phase-space factor and $N(\boldsymbol{w})$ is a normalisation factor:

$$N(\boldsymbol{w}) = C\cdot I(\boldsymbol{w}) \tag{141}$$

with C being a constant and $I(\boldsymbol{w})$ having the form:

$$I(\boldsymbol{w}) = \int |M(m_{\Lambda_c^+\overline{D}^0},\Omega|\boldsymbol{w})|^2\cdot dm_{\Lambda_c^+\overline{D}^0}d\Omega \propto \sum_{i=0}^{N_{MC}} |M_i(m_{\Lambda_c^+\overline{D}^0},\Omega|\boldsymbol{w})|^2 \tag{142}$$

The normalisation integral $I(\boldsymbol{w})$ is computed using a phase-space simulated signal sample, meaning that the direct $\Lambda_b^0\to\Lambda_c^+\overline{D}^0K^-$ decay is simulated without contributions from any intermediate state. In Equation 142 the sum runs over the events of the simulated sample, of number N_{MC}. The trigger, reconstruction and analysis selections steps which are based on cuts over kinematic variables of the candidates are simulated in the normalisation sample. On the contrary, the *D-from-B* BDT selections of the Λ_c^+ and $\overline{D}^0$, and the PID-based selection of the bachelor K^- are not simulated. In fact, the variables on which these selections depend are not sufficiently well described in simulation. In particular, the number of tracks in the events are relatively largely underestimated in the simulation. This is a relevant quantity for the response of the PID classifiers used for the selection of the bachelor K^-. Analogously, the response of the *D-from-B* BDT classifiers cannot be easily reproduced in the simulation.

The kinematic efficiency factor $\epsilon_{sig,kin}$ can be omitted in the signal *pdf* (Eq. 140), since it is implicitly taken into account in the normalisation sample. On the other hand, the terms related to the PID and *D-from-B* BDT selections must be explicitly included. The normalisation sample is simulated within the detector acceptance, thus it implicitly includes the phase-space factor ϕ of the signal *pdf.* These considerations lead to a signal *pdf* of the form:

$$\begin{aligned}\mathcal{P}(m_{\Lambda_c^+\overline{D}^0}, \Omega|\boldsymbol{w}) =&\frac{1}{N(\boldsymbol{w})}|M(m_{\Lambda_c^+\overline{D}^0}, \Omega|\boldsymbol{w})|^2 \\ &\cdot \epsilon_{BDT_{\Lambda_c^+}}(m_{\Lambda_c^+\overline{D}^0}, \Omega) \cdot \epsilon_{BDT_{\overline{D}^0}}(m_{\Lambda_c^+\overline{D}^0}, \Omega) \cdot \epsilon_{PID_{K^-}}(m_{\Lambda_c^+\overline{D}^0}, \Omega)\end{aligned} \tag{143}$$

with $\epsilon_{BDT_{\Lambda_c^+}}$ and $\epsilon_{BDT_{\overline{D}^0}}$ denoting the efficiencies of the *D-from-B* BDT selections for the Λ_c^+ and $\overline{D}^0$, respectively. Here it is assumed that the *D-from-B* BDT and PID selection efficiencies are uncorrelated, since the selections are performed over different particles. This assumption is verified in Section 6.2 and Appendix A.3. The fitting strategy of this analysis is to minimise the negative logarithm of the extended likelihood $\mathcal{L}(m_{\Lambda_c^+\overline{D}^0}, \Omega|\boldsymbol{w})_{ext}$, defined following Equation 35:

$$\mathcal{L}(\boldsymbol{w}, \nu)_{ext} \equiv \frac{\nu^N e^{-\nu}}{N!}\prod_{i=1}^{N} p(m_{\Lambda_c^+\overline{D}^0}{}_i, \Omega_i|\boldsymbol{w}) \tag{144}$$

where N is the number of observed events, being a Poisson random variable with mean value ν, and p is the probability density function afore-introduced. The *pdf* $\mathcal{P}$ is normalised to unity:

$$\int \mathcal{P}(m_{\Lambda_c^+\overline{D}^0}, \Omega) dm_{\Lambda_c^+\overline{D}^0} d\Omega = 1 \tag{145}$$

In the following, the amplitude variables $m_{\Lambda_c^+\overline{D}^0}, \Omega$ are summarised as ξ. Using Equation 143 this relation holds:

$$\mathcal{L}(\boldsymbol{w}, \nu)_{ext} = \frac{\nu^N e^{-\nu}}{N!}\prod_{i=1}^{N} \frac{|M(\xi_i|\boldsymbol{w})|^2 \cdot \epsilon_{BDT}(\xi_i)}{\int_{MC} |M(\xi|\boldsymbol{w})|^2 \, d\xi} \tag{146}$$

where the integral in the denominator is computed over the simulated sample used for normalisation of the signal *pdf.* Equation 146 can be further simplified observing that ν expresses the expected number of events predicted by the model:

$$\nu = \int_{MC} |M(\xi|\boldsymbol{w})|^2 \, d\xi \tag{147}$$

obtaining the following formulation for the extended likelihood:

$$\mathcal{L}(\boldsymbol{w}, \nu)_{ext} = \frac{e^{-\nu}}{N!}\prod_{i=1}^{N} \nu \cdot \frac{|M(\xi_i|\boldsymbol{w})|^2 \cdot \epsilon_{BDT}(\xi_i)}{\int_{MC} |M(\xi|\boldsymbol{w})|^2 \, d\xi} = \frac{e^{-\nu}}{N!}\prod_{i=1}^{N} |M(\xi_i|\boldsymbol{w})|^2 \cdot \epsilon_{BDT}(\xi_i) \tag{148}$$

Finally the logarithm of $\mathcal{L}(\boldsymbol{w}, \nu)_{ext}$ results to be:

$$\begin{aligned}\ln \mathcal{L}(\boldsymbol{w}, \nu)_{ext} &= \sum_{i=1}^{N} \ln |M(\xi_i|\boldsymbol{w})|^2 \cdot \epsilon_{BDT}(\xi_i) - \nu - \ln N! \\ &= \sum_{i=1}^{N} \ln |M(\xi_i|\boldsymbol{w})|^2 \cdot \epsilon_{BDT}(\xi_i) - \nu + const\end{aligned} \tag{149}$$

In the data set of this analysis the reconstructed candidates are weighted by *s*-weights, thus the quantity to minimise is the weighted extended likelihood [127, 128]:

$$\mathcal{L}(\boldsymbol{w}, \nu)_{ext} \equiv \frac{\nu^N e^{-\nu}}{N!} \prod_{i=1}^{N} \mathcal{P}(\xi_i, \boldsymbol{w})^{s_i} \tag{150}$$

leading to:

$$\begin{aligned} - \ln \mathcal{L}(\boldsymbol{w}, \nu)_{ext} &= -\alpha(\sum_i s_i \ln |M(\xi_i|\boldsymbol{w})|^2 \cdot \epsilon_{BDT}(\xi_i) + \ln \nu \cdot \sum_i (1 - s_i) - \nu \ ) \\ &= -\alpha(\sum_i s_i \ln |M(\xi_i|\boldsymbol{w})|^2 \cdot \epsilon_{BDT}(\xi_i) + \ln(\int_{MC} |M(\xi|\boldsymbol{w})|^2 \, d\xi) \cdot \sum_i (1 - s_i) \\ &\quad - \int_{MC} |M(\xi|\boldsymbol{w})|^2 \, d\xi \ ) \end{aligned} \tag{151}$$

where s_i is the *s*-weight of the candidate, the constant term is dropped out having no effect in the minimisation of the likelihood, and α is a constant factor which takes into account the statistical uncertainty due to the *s*-weighting procedure:

$$\alpha = \frac{\sum_i s_i}{\sum_i s_i^2} \tag{152}$$

As already said, the phase-space factor $\phi(m_{\Lambda_c^+ \overline{D}^0})$ in the signal *pdf* is taken into account by simulating events within the detector acceptance, and thus must not be explicitly added in the likelihood calculation.

6.2 Normalisation samples, Boosted Decision Trees and particle identification efficiencies

Phase-space simulated samples are used to normalise the signal *pdf* as described in the previous section, and they represent an implicit correction of the data for the kinematic efficiencies. Samples are simulated through the standard LHCb simulation framework for different conditions of the colliding beams. The most representative conditions of LHCb data taking from 2011 to 2017 are simulated, split evenly between the two magnet polarities as in data taking. At the time of performing this analysis, simulated samples representing 2018 conditions have not yet been available. Nevertheless, 2018 data taking conditions have been similar to the ones in 2017, and no major issues are expected to arise using samples simulated with 2017 conditions for 2018 data. The sizes of the simulated samples approximately reflect the size proportions between the samples of real data. This avoids the introduction of eventual biases which might originate from different efficiencies over different periods. Note that 2017 samples have roughly double the size than the 2017 data sample, to take into account 2018 data as well. The number of simulated events of the normalisation samples is listed in Table 24.

The Λ_c^+ and $\overline{D}^0$ selections based on the response of the *D-from-B* BDT classifiers lead to efficiency terms to be explicitly taken into account in the signal *pdf*. Efficiency maps binned in the flight distance χ^2 of the two *c*-hadrons and in the number of tracks of the event are available from the *D-from-B* software package [91]. These maps are computed making use of an adaptive-binning technique developed in the context of the branching fraction measurement of the $\Lambda_b^0 \to \Lambda_c^+ \overline{D}^0 K^-$ channel [129]. Within this approach the binning scheme is not defined by constant bin widths, but by a minimum number of events that must be contained in each of the bins, defined by the analyst. Thus, the adaptive-binning approach allows to reduce the systematic effects originated by fluctuations in the number of events used to describe the efficiency shapes. For each reconstructed Λ_b^0 candidate, the efficiency values of the Λ_c^+ and $\overline{D}^0$ selections are retrieved, basing on the number of tracks in the event and on the flight distance of the two *c*-hadrons. The efficiencies are then combined assuming the selections to be independent.

Year of data taking	Generated signal events	Signal events after selection
2011	436,783	4,465
2012	1,097,239	10,373
2015	458,104	5,389
2016	1,662,019	22,575
2017	2,348,228	46,381
Sum	6,002,373	89,183

Table 24: Number of simulated events of the normalisation samples, before and after the trigger, reconstruction and analysis selections. The *D-from-B* BDT- and PID- based selections are not applied.

The per-candidate efficiency is weighted by the candidate *s*-weight and efficiency maps are computed over the angular variables, invariant mass distributions and Dalitz variables. They are presented in Appendix A.3. The individual and combined efficiencies of the two *D-from-B* BDT classifiers do not strongly depend on any of the variables. Also, the individual classifiers are proven to factorise and to be independent. This is shown in Appendix A.3. This allows to combine the two *D-from-B* BDT efficiency terms as multiplicative factors, as shown in Equation 143.

Figure 40 shows two-dimensional efficiency maps of the combined classifiers, over the possible combinations of the angular variables and the invariant mass distributions, with the resulting correlation between the binning variables. The efficiency map binned in the $cos\theta_{P_c}$ and $m_{\Lambda_c^+\overline{D}^0}$ variables, which show the highest correlation, is used in the signal *pdf* and smoothed exploiting a kernel algorithm implemented in the ROOT framework for data analysis [130].

As introduced in Section 3.3.1, the *PIDCalib* software package is employed to derive PID efficiency maps parametrised in the number of tracks in the event, and in the momentum p and pseudo-rapidity η of the bachelor K^-. A traditional binning scheme with constant bin widths is used for the PID efficiency maps. Per-candidate efficiencies are retrieved following a similar approach to what has been described for the *D-from-B* BDT efficiencies. Figure 41 shows two-dimensional efficiency maps of the PID selection over the combinations of the amplitude variables, weighted by the candidate *s*-weights. The efficiency map binned in the $cos\theta_{P_c}$ and $m_{\Lambda_c^+\overline{D}^0}$ variables, which show the highest correlation, is used in the signal *pdf*, and smoothed similarly to the efficiency maps of the *D-from-B* BDT selections. Efficiency maps over the angular and mass variables are presented in Appendix A.4.

6.3 Resonances and amplitude model

Various known D_s^* and Ξ_c^0 resonances are expected to decay to the $\overline{D}^0K^-$ and $\Lambda_c^+K^-$ systems, respectively. Following the notation introduced in Section 5.4, they correspond to the B and C decay chains. Eventual pentaquarks would decay to the $\Lambda_c^+\overline{D}^0$ system, representing the A decay chain. The D_s^* and Ξ_c^0 intermediate states which could possibly contribute to $\Lambda_b^0 \to \Lambda_c^+\overline{D}^0K^-$ decays are in Table 25. The related energy release Q of the Λ_b^0 and resonance decays, normalised to their masses, are presented as well. Theory expectations [131, 132] predict the $D_{sJ}(3040)$ state to have *unnatural parity* assignment $J^P = 1^+$, preventing it to decay to the $\overline{D}^0K^-$ system due to parity conservation in strong decays. Note that the mass of the $D_{s0}^*(2317)$ state is right below the physically-allowed mass threshold of the $\overline{D}^0K^-$ system. Nevertheless, this does not prevent the state to possibly contribute to the amplitude model. In the following, the general B, C notations in the variables of the related decay chains are replaced by the D_s^*, Ξ_c^0 indices, respectively. Similarly, the P_c notation replaces the A labelling.

Figure 42 shows the distributions of the amplitude variables on data weighted by the signal *s*-weights. Their comparison with the phase-space distributions of the simulated samples is useful to identify structures which are potentially arising from decays of intermediate resonances. A finer binning of these distributions is proposed in Appendix A.1. Figure 43 shows the signal *s*-weighted data over the Dalitz

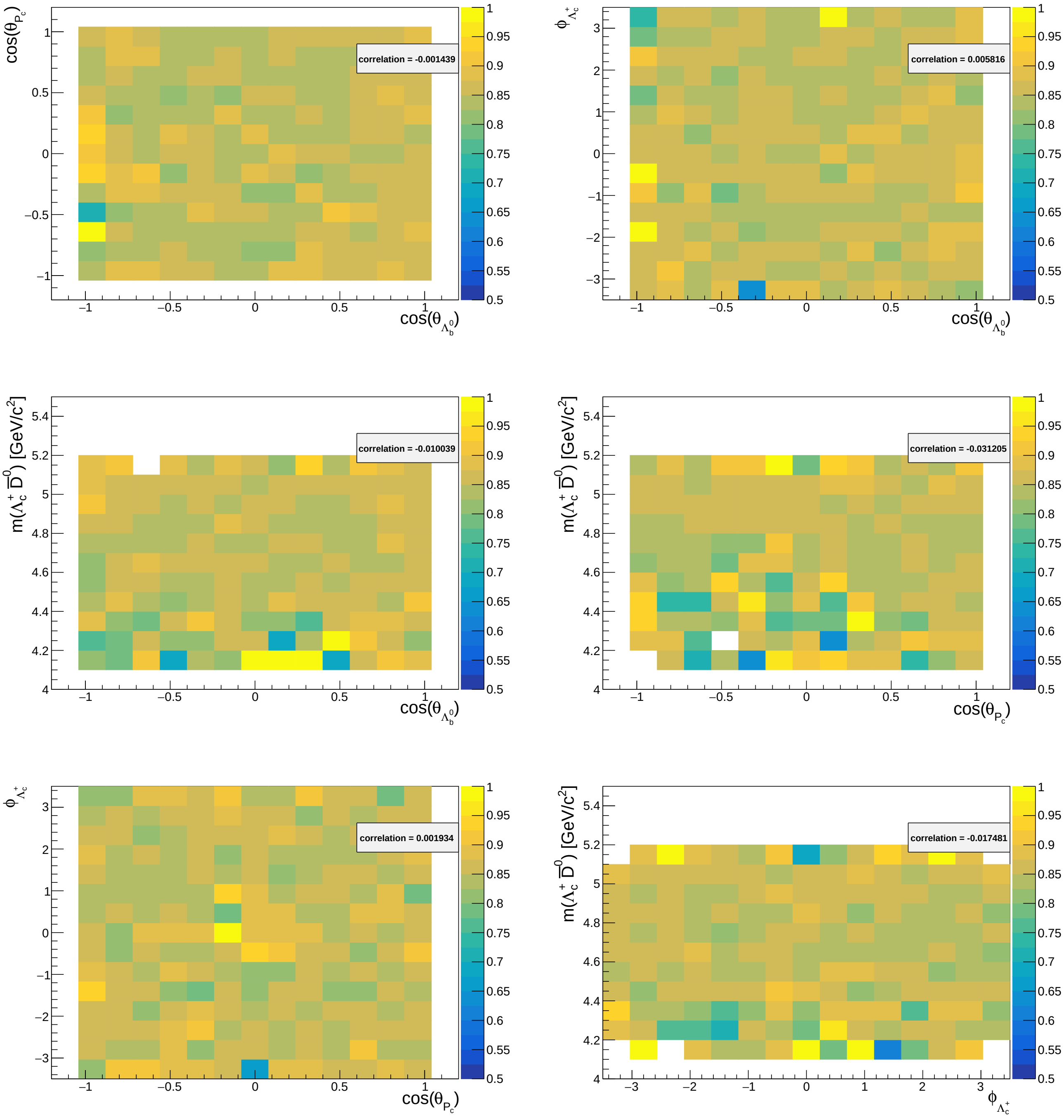

Figure 40: Efficiency of the combined *D-from-B* BDT classifiers used to select the Λ_c^+ and $\overline{\mathrm{D}}^0$ hadrons, over the two-dimensional combinations of the angular variables and invariant mass distributions.

variables. The Dalitz plots suggest the presence of a $\overline{\mathrm{D}}^0\mathrm{K}^-$ state corresponding to $\sim (2.7)^2\ \mathrm{GeV}^2/c^4$ which could be identified as the $\mathrm{D}^*_{s\,1}(2700)$ state. Also, this state possibly shows interference with Ξ_c^0 states at low mass region. A deep fall in the $m(\overline{\mathrm{D}}^0\mathrm{K}^-)$ invariant mass distribution is visible at $\sim 2.9 - 2.92\ \mathrm{GeV}/c^2$, which corresponds to the opening of the $\mathrm{D}_1^0(2420)\mathrm{K}^-$ threshold, placed at $2.914\ \mathrm{GeV}/c^2$. Some minor structures appear at the low-mass region of the same distribution, which could be related to the presence of the $\mathrm{D}^*_{s\,2}(2573)$ state and to the threshold of the $\mathrm{D}^{*0}(2007)\mathrm{K}^-$ channel at $2.500\ \mathrm{GeV}/c^2$. Multiple structures appear in the $m(\Lambda_c^+\mathrm{K}^-)$ invariant mass distribution, which might be related to Ξ_c^0 states.

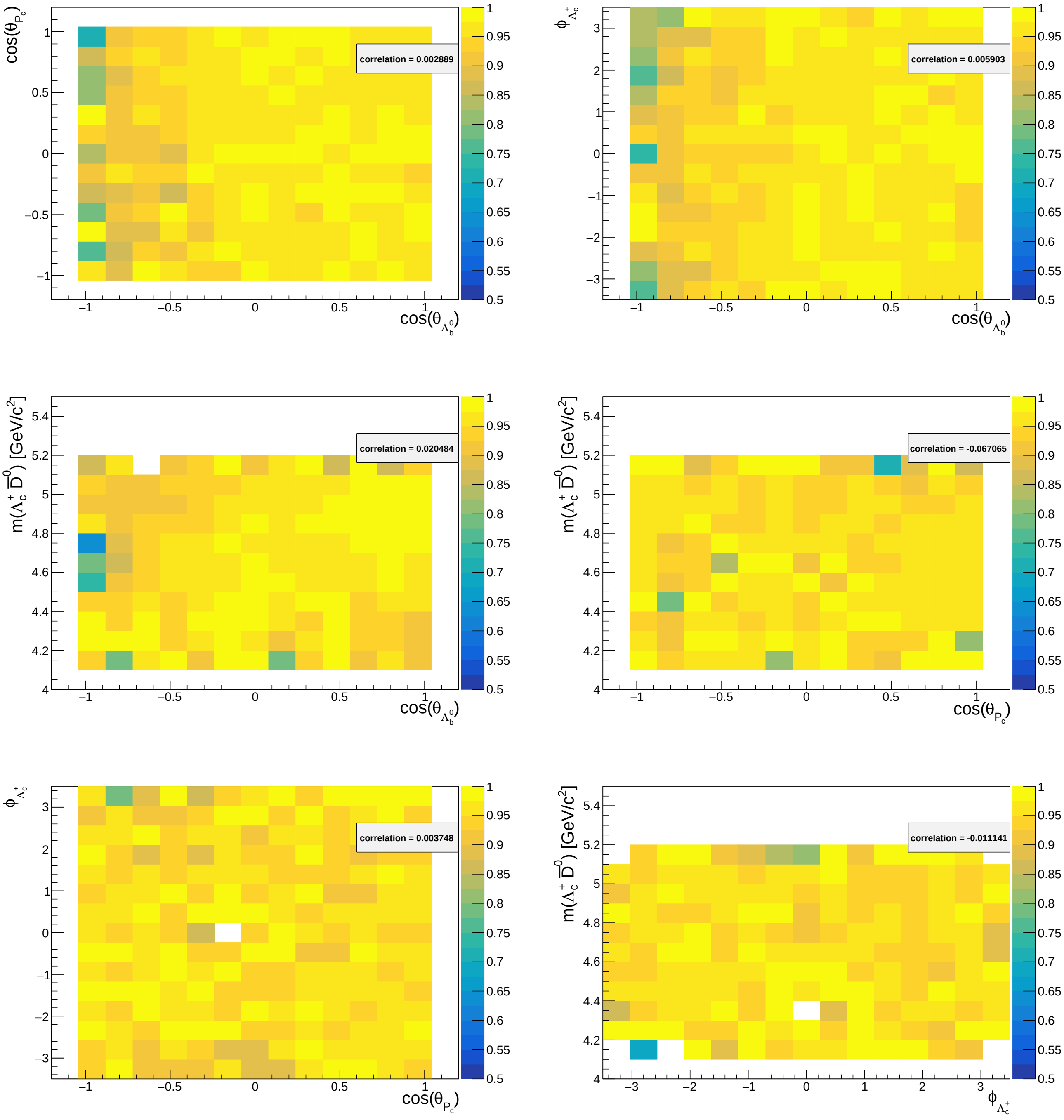

Figure 41: Efficiency of the *ProbNNk* classifier used to select the bachelor K^-, over the two-dimensional combinations of the angular variables and invariant mass distributions.

As explained in Section 5.5, if the energy release Q of the decay of the Λ_b^0 and of the resonances is small compared to the mass of the decaying particle, only one partial wave per process contributes significantly to the amplitude. This wave corresponds to the minimum allowed value of the orbital angular momentum of the decay, L_{min}. From Table 25, the energy releases $Q^{\Lambda_b^0}$ of the Λ_b^0 decays are not negligible for any of the listed decays. Therefore, partial waves with higher orbital angular momentum L than L_{min} might be relevant for the amplitude model. However, the D_s^* states decay to two scalar particles ($\overline{\mathrm{D}}^0$ and K^-), and only one value of orbital angular momentum L is possible between them, which is L_{min}.

State	Mass [MeV/c^2]	Width [MeV/c^2]	J^P	$Q^{\Lambda^0_b}/m_{\Lambda^0_b}$	Q^{res}/m_{res}
$D^*_{s0}(2317)$	2317.7 ± 0.6	< 3.8 (CL = 95%)	0^+	0.18	-0.01
$D^*_{s2}(2573)$	2569.1 ± 0.8	16.9 ± 0.7	2^+	0.14	0.08
$D^*_{s1}(2700)$	2708.3 ± 3.6	120 ± 11	1^-	0.11	0.13
$D^*_{s1}(2860)$	2859 ± 27	159 ± 80	1^-	0.08	0.17
$D^*_{s3}(2860)$	2860 ± 7	53 ± 10	3^-	0.08	0.17
$D_{sJ}(3040)$	3044^{+31}_{-9}	239 ± 60	/	0.05	0.22
$\Xi^0_c(2790)$	2792.8 ± 1.2	10.0 ± 1.1	$\frac{1}{2}^-$	0.17	0.005
$\Xi^0_c(2815)$	2820.22 ± 0.32	2.54 ± 0.25	$\frac{3}{2}^-$	0.17	0.01
$\Xi^0_c(2930)$	2929 ± 12	20 ± 11	/	0.15	0.05
$\Xi^0_c(2970)$	2967.8 ± 0.8	28.1 ± 3.7	/	0.14	0.05
$\Xi^0_c(3080)$	3079.9 ± 1.4	5.6 ± 2.2	/	0.12	0.10

Table 25: Established resonances expected to contribute in the $\overline{D}^0K^-$ (on the top part) and $\Lambda_c^+K^-$ (on the bottom part) mass spectra. The energy releases Q of the Λ^0_b and resonance decays are normalised to their masses.

The amplitude model used to fit the data has been optimised is such a way to include the minimum number of states and parameters which are needed for a satisfactory description of the data. In fact, increasing the number of free parameters in the fit could potentially reduce stability, large correlations and uncertainties could arise between the fit parameters, and there is an increased risk of over-fitting the data. Thus, the amplitude description is optimised by starting to fit the data with the most general model including all possible resonances and partial waves. The model is then simplified by removing step-by-step the components which are not contributing significantly. More quantitative statement about this optimisation procedure are given in Chapter 7.

Finally, an amplitude model including the $D^*_{s0}(2317)$, $D^*_{s1}(2700)$, $D^*_{s1}(2860)$, $D^*_{s3}(2860)$, $\Xi^0_c(2790)$ states is considered. The $D^*_{s1}(2700)$ and $D^*_{s1}(2860)$ states share the same quantum numbers and they are relatively close in mass, considering their large widths. Hence they are described by a K-matrix amplitude (Sec. 5.3). In spite of the considerations presented above, in the baseline model higher partial waves are considered only for the K-matrix amplitude. The validity of this approximation is investigated in Chapter 7. The complete matrix element defining the amplitude model takes the form:

$$M = \sum_{\lambda_{\Lambda^0_b},\lambda_{\Lambda_c^+}} \left| \sum_{\lambda_{D^*_{s0}(2317)}} M^{D^*_{s0}(2317)} + \sum_{\lambda_{D^*_s\mathrm{Kmat}}} M^{D^*_s\mathrm{Kmat}} + \sum_{\lambda_{D^*_{s3}(2860)}} M^{D^*_{s3}(2860)} + \sum_{\lambda_{\Xi^0_c(2790)}} M^{\Xi^0_c(2790)} \right|^2 \tag{153}$$

where the K-matrix contribution is labelled by the D^*_sKmat index. Note that the helicity values taken by the $D^*_{s1}(2700)$ and $D^*_{s1}(2860)$ states are the same, since they share the same quantum numbers. These helicity values are denoted by $\lambda_{D^*_s\mathrm{Kmat}}$.

Each intermediate resonance introduces helicity amplitudes at the top-level decay of the Λ^0_b, and for its subsequent decay to the final-state particles (Eqs. 78-79). A summary of the amplitudes included in the model is listed in Tables 26-28. The matrix elements of the resonance processes in Equation 153 are given by multiplying the amplitudes by the resonance line shapes (Sec. 5.2). The afore-mentioned amplitudes are complex quantities, and they enter in the matrix element as a product (Eq. 78) resulting in a product of two magnitudes and phases. Hence, it is not possible to measure the absolute values of all the magnitudes and phases, but only their relative ratio. An overall magnitude and phase convention must be set, by fixing some of the amplitudes to arbitrary values. The helicity amplitudes $H^{\Lambda^0_b}_{\lambda_{D^*_{s3}(2860)}=-1,\lambda_{\Lambda_c^+}=-\frac{1}{2}}$, $H^{\Lambda^0_b}_{\lambda_{\Xi^0_c(2790)}=-\frac{1}{2}}$ of the Λ^0_b decays in the $D^*_{s3}(2860)$ and $\Xi^0_c(2790)$ amplitudes are

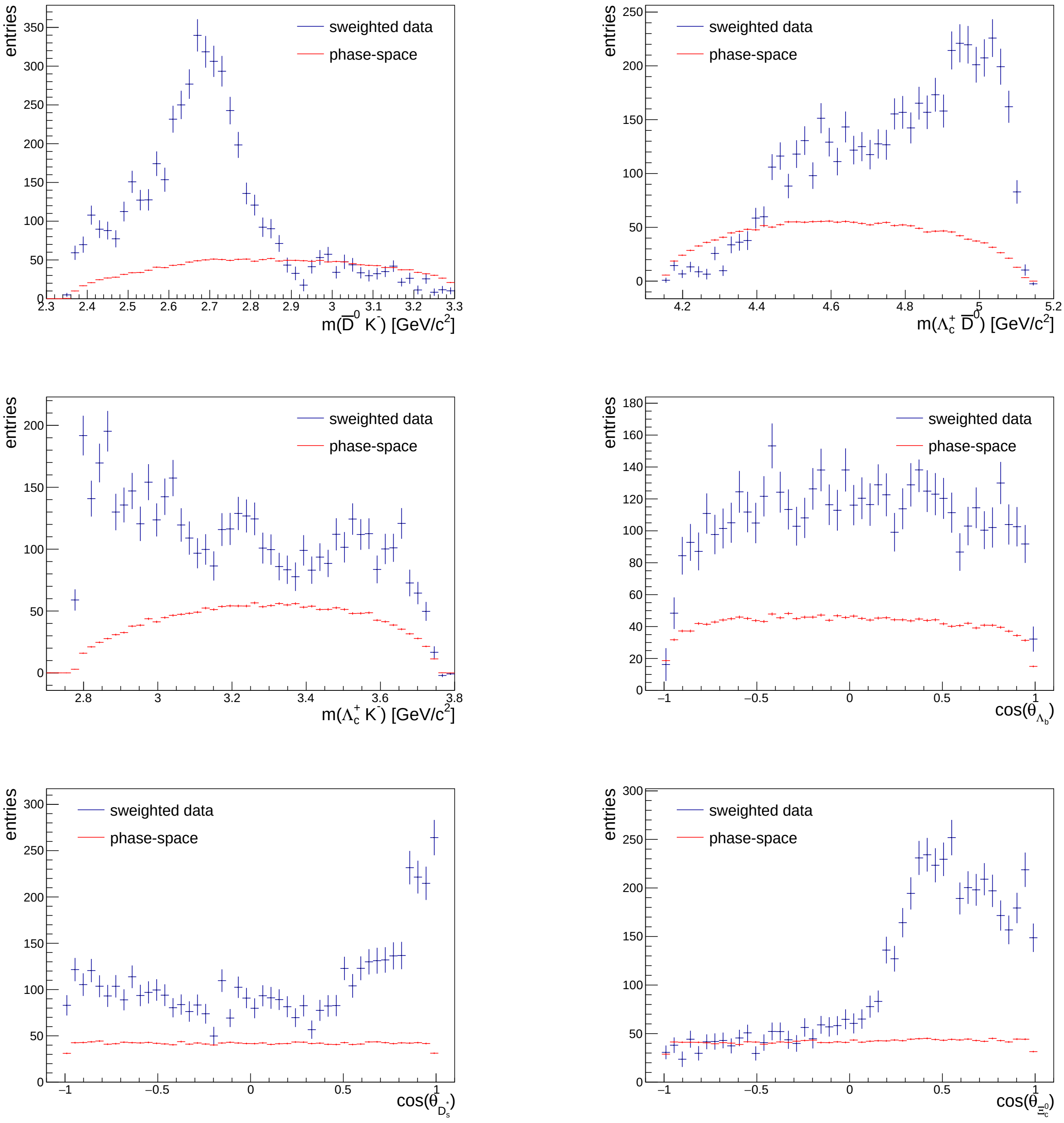

Figure 42: Distributions of the amplitude variables on s-weighted signal candidates compared to the distributions from the phase-space simulated sample.

set to the unity. Additionally, the coupling $B_{0,0}^{\mathrm{D}^*_{s0}(2317)\to\overline{\mathrm{D}}^0\mathrm{K}^-}$ of the $\mathrm{D}^*_{s0}(2317)$ decay is set to unity, corresponding to fix the related amplitude and resulting into fewer free parameters.

Following the construction from Section 5.2, the amplitudes are known functions of the angular variables, and they depend on the B_{LS} couplings. The latter are complex quantities, and their real and imaginary parts represent the main fit parameters of the amplitude model. Additional fitted quantities are some of the line shape parameters and the couplings of the K-matrix amplitude.

The B_{LS} couplings on which the amplitudes depend are summarised in Table 29. Being the B_{LS} couplings complex quantities, each of them introduces two free parameters. All the real and imaginary parts of the B_{LS} couplings are fitted to the data.

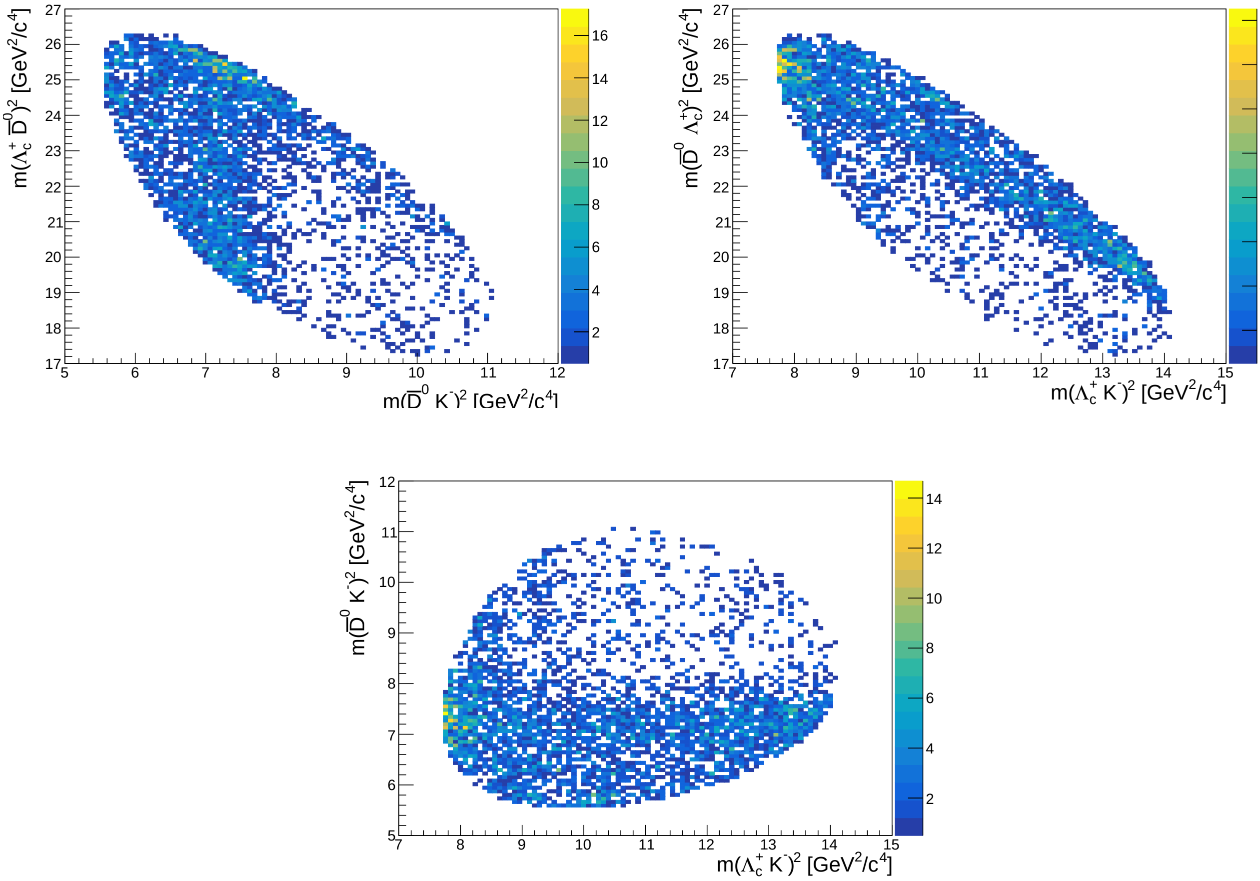

Figure 43: Distributions of the Dalitz variables on s-weighted signal candidates.

$\lambda_{\Lambda_\mathrm{b}^0}$	$\lambda_{\Lambda_\mathrm{c}^+}$	$\lambda_{\mathrm{D}_{\mathrm{s}0}^*(2317)}$	Amplitudes
$\frac{1}{2}$	$\frac{1}{2}$	0	$\left[\sum_{\lambda'=\pm\frac{1}{2}} d^{\frac{1}{2}}_{\lambda',\frac{1}{2}}(\theta^{P_c\mathrm{D}_\mathrm{s}^*}_{\Lambda_\mathrm{c}^+})\cdot H^{\Lambda_\mathrm{b}^0}_{0,\lambda'}\cdot d^{\frac{1}{2}}_{\frac{1}{2},-\lambda'}(\theta^{\mathrm{D}_\mathrm{s}^*}_{\Lambda_\mathrm{b}^0})\cdot e^{i\frac{1}{2}\cdot\phi^{\mathrm{D}_\mathrm{s}^*}_{\Lambda_\mathrm{c}^+}}\right]\cdot H^{\mathrm{D}_\mathrm{s}^*}\cdot d^{J_{\mathrm{D}_\mathrm{s}^*}}_{0,0}(\theta_{\mathrm{D}_\mathrm{s}^*})\cdot e^{i\cdot\phi^{\mathrm{D}_\mathrm{s}^*}_{\overline{\mathrm{D}}^0}}$
$\frac{1}{2}$	- $\frac{1}{2}$	0	$\left[\sum_{\lambda'=\pm\frac{1}{2}} d^{\frac{1}{2}}_{\lambda',-\frac{1}{2}}(\theta^{P_c\mathrm{D}_\mathrm{s}^*}_{\Lambda_\mathrm{c}^+})\cdot H^{\Lambda_\mathrm{b}^0}_{0,\lambda'}\cdot d^{\frac{1}{2}}_{\frac{1}{2},-\lambda'}(\theta^{\mathrm{D}_\mathrm{s}^*}_{\Lambda_\mathrm{b}^0})\cdot e^{i\frac{1}{2}\cdot\phi^{\mathrm{D}_\mathrm{s}^*}_{\Lambda_\mathrm{c}^+}}\right]\cdot H^{\mathrm{D}_\mathrm{s}^*}\cdot d^{J_{\mathrm{D}_\mathrm{s}^*}}_{0,0}(\theta_{\mathrm{D}_\mathrm{s}^*})$
- $\frac{1}{2}$	$\frac{1}{2}$	0	$\left[\sum_{\lambda'=\pm\frac{1}{2}} d^{\frac{1}{2}}_{\lambda',\frac{1}{2}}(\theta^{P_c\mathrm{D}_\mathrm{s}^*}_{\Lambda_\mathrm{c}^+})\cdot H^{\Lambda_\mathrm{b}^0}_{0,\lambda'}\cdot d^{\frac{1}{2}}_{-\frac{1}{2},-\lambda'}(\theta^{\mathrm{D}_\mathrm{s}^*}_{\Lambda_\mathrm{b}^0})\cdot e^{-i\frac{1}{2}\cdot\phi^{\mathrm{D}_\mathrm{s}^*}_{\Lambda_\mathrm{c}^+}}\right]\cdot H^{\mathrm{D}_\mathrm{s}^*}\cdot d^{J_{\mathrm{D}_\mathrm{s}^*}}_{0,0}(\theta_{\mathrm{D}_\mathrm{s}^*})$
- $\frac{1}{2}$	- $\frac{1}{2}$	0	$\left[\sum_{\lambda'=\pm\frac{1}{2}} d^{\frac{1}{2}}_{\lambda',-\frac{1}{2}}(\theta^{P_c\mathrm{D}_\mathrm{s}^*}_{\Lambda_\mathrm{c}^+})\cdot H^{\Lambda_\mathrm{b}^0}_{0,\lambda'}\cdot d^{\frac{1}{2}}_{-\frac{1}{2},-\lambda'}(\theta^{\mathrm{D}_\mathrm{s}^*}_{\Lambda_\mathrm{b}^0})\cdot e^{-i\frac{1}{2}\cdot\phi^{\mathrm{D}_\mathrm{s}^*}_{\Lambda_\mathrm{c}^+}}\right]\cdot H^{\mathrm{D}_\mathrm{s}^*}\cdot d^{J_{\mathrm{D}_\mathrm{s}^*}}_{0,0}(\theta_{\mathrm{D}_\mathrm{s}^*})$

Table 26: Amplitudes of the $\Lambda_\mathrm{b}^0 \to \Lambda_\mathrm{c}^+\mathrm{D}_{\mathrm{s}0}^*(2317)$ decay included in the amplitude model.

The line shapes of the $\mathrm{D}_{\mathrm{s}3}^*(2860)$ and $\Xi_\mathrm{c}^0(2790)$ states are parametrised by the relativistic Breit-Wigner distribution, using $d_{\Lambda_\mathrm{b}^0} = 1.5~\mathrm{GeV}^{-1}$ and $d_{\mathrm{D}_\mathrm{s}^{*n}} = 5~\mathrm{GeV}^{-1}$ (Eq. 84). The $\mathrm{D}_{\mathrm{s}0}^*(2317)$ state, which is below-threshold, is instead parametrised by a Flatté distribution with the dominant decay channel $\mathrm{D}_{\mathrm{s}0}^*(2317) \to \mathrm{D}_\mathrm{s}^+\pi^0$. The line shapes of the $\mathrm{D}_{\mathrm{s}1}^*(2700)$ and $\mathrm{D}_{\mathrm{s}1}^*(2860)$ states are represented by a single K-matrix amplitude. An alternative amplitude model which describe them as two, independent Breit-Wigner contributions is described in Appendix A.5. The mass and width values used to describe

$\lambda_{\Lambda_b^0}$	$\lambda_{\Lambda_c^+}$	$\lambda_{\mathrm{D_s^*}}$	Amplitudes
$\frac{1}{2}$	$\frac{1}{2}$	1, 0	$\left[\sum_{\lambda'=\pm\frac{1}{2}} d^{\frac{1}{2}}_{\lambda^{\mathrm{D_s^*}},\frac{1}{2}}(\theta^{P_c\mathrm{D_s^*}}_{\Lambda_c^+}) \cdot H^{\Lambda_b^0}_{1,\lambda'} \cdot d^{\frac{1}{2}}_{\frac{1}{2},1-\lambda'}(\theta^{\mathrm{D_s^*}}_{\Lambda_b^0}) \cdot e^{i\frac{1}{2}\cdot\phi^{\mathrm{D_s^*}}_{\Lambda_c^+}}\right] \cdot H^{\mathrm{D_s^*}} \cdot d^{J_{\mathrm{D_s^*}}}_{1,0}(\theta_{\mathrm{D_s^*}}) \cdot e^{i\cdot\phi^{\mathrm{D_s^*}}_{\overline{\mathrm{D}}0}}$ $+ \left[\sum_{\lambda'=\pm\frac{1}{2}} d^{\frac{1}{2}}_{\lambda',\frac{1}{2}}(\theta^{P_c\mathrm{D_s^*}}_{\Lambda_c^+}) \cdot H^{\Lambda_b^0}_{0,\lambda'} \cdot d^{\frac{1}{2}}_{\frac{1}{2},-\lambda'}(\theta^{\mathrm{D_s^*}}_{\Lambda_b^0}) \cdot e^{i\frac{1}{2}\cdot\phi^{\mathrm{D_s^*}}_{\Lambda_c^+}}\right] \cdot H^{\mathrm{D_s^*}} \cdot d^{J_{\mathrm{D_s^*}}}_{0,0}(\theta_{\mathrm{D_s^*}}) \cdot e^{i\cdot\phi^{\mathrm{D_s^*}}_{\overline{\mathrm{D}}0}}$
$\frac{1}{2}$	- $\frac{1}{2}$	0, -1	$\left[\sum_{\lambda'=\pm\frac{1}{2}} d^{\frac{1}{2}}_{\lambda',-\frac{1}{2}}(\theta^{P_c\mathrm{D_s^*}}_{\Lambda_c^+}) \cdot H^{\Lambda_b^0}_{0,\lambda'} \cdot d^{\frac{1}{2}}_{\frac{1}{2},-\lambda'}(\theta^{\mathrm{D_s^*}}_{\Lambda_b^0}) \cdot e^{i\frac{1}{2}\cdot\phi^{\mathrm{D_s^*}}_{\Lambda_c^+}}\right] \cdot H^{\mathrm{D_s^*}} \cdot d^{J_{\mathrm{D_s^*}}}_{0,0}(\theta_{\mathrm{D_s^*}})$ $+ \left[\sum_{\lambda'=\pm\frac{1}{2}} d^{\frac{1}{2}}_{\lambda',-\frac{1}{2}}(\theta^{P_c\mathrm{D_s^*}}_{\Lambda_c^+}) \cdot H^{\Lambda_b^0}_{-1,\lambda'} \cdot d^{\frac{1}{2}}_{\frac{1}{2},-1-\lambda'}(\theta^{\mathrm{D_s^*}}_{\Lambda_b^0}) \cdot e^{i\frac{1}{2}\cdot\phi^{\mathrm{D_s^*}}_{\Lambda_c^+}}\right] \cdot H^{\mathrm{D_s^*}} \cdot d^{J_{\mathrm{D_s^*}}}_{-1,0}(\theta_{\mathrm{D_s^*}}) \cdot e^{-i\cdot\phi^{\mathrm{D_s^*}}_{\overline{\mathrm{D}}0}}$
- $\frac{1}{2}$	$\frac{1}{2}$	1, 0	$\left[\sum_{\lambda'=\pm\frac{1}{2}} d^{\frac{1}{2}}_{\lambda',\frac{1}{2}}(\theta^{P_c\mathrm{D_s^*}}_{\Lambda_c^+}) \cdot H^{\Lambda_b^0}_{1,\lambda'} \cdot d^{\frac{1}{2}}_{-\frac{1}{2},1-\lambda'}(\theta^{\mathrm{D_s^*}}_{\Lambda_b^0}) \cdot e^{-i\frac{1}{2}\cdot\phi^{\mathrm{D_s^*}}_{\Lambda_c^+}}\right] \cdot H^{\mathrm{D_s^*}} \cdot d^{J_{\mathrm{D_s^*}}}_{1,0}(\theta_{\mathrm{D_s^*}}) \cdot e^{i\cdot\phi^{\mathrm{D_s^*}}_{\overline{\mathrm{D}}0}}$ $+ \left[\sum_{\lambda'=\pm\frac{1}{2}} d^{\frac{1}{2}}_{\lambda',\frac{1}{2}}(\theta^{P_c\mathrm{D_s^*}}_{\Lambda_c^+}) \cdot H^{\Lambda_b^0}_{0,\lambda'} \cdot d^{\frac{1}{2}}_{-\frac{1}{2},-\lambda'}(\theta^{\mathrm{D_s^*}}_{\Lambda_b^0}) \cdot e^{-i\frac{1}{2}\cdot\phi^{\mathrm{D_s^*}}_{\Lambda_c^+}}\right] \cdot H^{\mathrm{D_s^*}} \cdot d^{J_{\mathrm{D_s^*}}}_{0,0}(\theta_{\mathrm{D_s^*}})$
- $\frac{1}{2}$	- $\frac{1}{2}$	0, -1	$\left[\sum_{\lambda'=\pm\frac{1}{2}} d^{\frac{1}{2}}_{\lambda',-\frac{1}{2}}(\theta^{P_c\mathrm{D_s^*}}_{\Lambda_c^+}) \cdot H^{\Lambda_b^0}_{0,\lambda'} \cdot d^{\frac{1}{2}}_{-\frac{1}{2},-\lambda'}(\theta^{\mathrm{D_s^*}}_{\Lambda_b^0}) \cdot e^{-i\frac{1}{2}\cdot\phi^{\mathrm{D_s^*}}_{\Lambda_c^+}}\right] \cdot H^{\mathrm{D_s^*}} \cdot d^{J_{\mathrm{D_s^*}}}_{0,0}(\theta_{\mathrm{D_s^*}})$ $+ \left[\sum_{\lambda'=\pm\frac{1}{2}} d^{\frac{1}{2}}_{\lambda',-\frac{1}{2}}(\theta^{P_c\mathrm{D_s^*}}_{\Lambda_c^+}) \cdot H^{\Lambda_b^0}_{-1,\lambda'} \cdot d^{\frac{1}{2}}_{-\frac{1}{2},-1-\lambda'}(\theta^{\mathrm{D_s^*}}_{\Lambda_b^0}) \cdot e^{-i\frac{1}{2}\cdot\phi^{\mathrm{D_s^*}}_{\Lambda_c^+}}\right] \cdot H^{\mathrm{D_s^*}} \cdot d^{J_{\mathrm{D_s^*}}}_{-1,0}(\theta_{\mathrm{D_s^*}}) \cdot e^{-i\cdot\phi^{\mathrm{D_s^*}}_{\overline{\mathrm{D}}0}}$

Table 27: Amplitudes of the $\Lambda_b^0 \to \Lambda_c^+\mathrm{D_s^*}$ decays included in the amplitude model, for $\mathrm{D_s^*}$ states with $J > 0$.

the $\mathrm{D^*_{s3}}(2860)$, $\Xi_c^0(2790)$, and $\Xi_c^0(2815)$ line shapes are fixed to those listed in the Particle Data Group (PDG) review of 2018 [17]. The mass of the $\mathrm{D^*_{s0}}(2317)$ state is fixed to its PDG value. As discussed in Section 5.2, the two widths used in the Flatté line shape parametrisation do not directly correspond to physical widths of states. The main goal of this analysis is not to measure the static properties of the resonances, thus these widths are considered as more "abstract" parameters useful to describe the Flatté distribution. In the amplitude model, one of them is fixed to the value 15 MeV/c^2, while the other one is fitted.

The K-matrix amplitude is constructed by considering two poles corresponding to the $\mathrm{D^*_{s1}}(2700)$ and $\mathrm{D^*_{s1}}(2860)$ states, and two contributing channels, the $\overline{\mathrm{D}}^0\mathrm{K}^-$ and the $\mathrm{D}^{*0}(2007)\mathrm{K}^-$. The latter are the two channels expected to contribute the most to the $\mathrm{D^*_{s1}}(2700)$ decays, according to the PDG. An alternative choice of the channels is considered in Section 7.1.7, as crosscheck. Following the notation introduced in Section 5.3, two couplings α_n of the Λ_b^0 to the intermediate resonances are required. Analogously, two couplings g_{nb} of the resonances to the channel $\mathrm{D}^{*0}(2007)\mathrm{K}^-$ are needed. These couplings are complex quantities, and all their real and imaginary components are fitted to data. The background term $p(s)$ is a two-dimensional vector with real components. They are considered to be constant not depending on the mass squared s, and they are both fitted to data. Finally the bare masses of the $\mathrm{D^*_{s1}}(2700)$ and $\mathrm{D^*_{s1}}(2860)$ states are fitted. The orbital angular momentum barrier effect is taken into account by multiplying the K-matrix amplitude by two Blatt-Weisskopf functions, as shown in Equation 84. The parameters q_0 and p_0 of these functions must be evaluated at the resonance peak, but the K-matrix amplitude describes two poles together. Hence, q_0 and p_0 are evaluated at the average of the two fitted values of the pole masses.

$\lambda_{\Lambda_{\mathrm{b}}^0}$	$\lambda_{\Lambda_{\mathrm{c}}^+}$	$\lambda_{\Xi_{\mathrm{c}}^0}$	Amplitudes
$\frac{1}{2}$	$\frac{1}{2}$	$\pm\frac{1}{2}$	$H^{\Lambda_{\mathrm{b}}^0}_{\frac{1}{2}} \cdot d^{\frac{1}{2}}_{\frac{1}{2},\frac{1}{2}}(\theta^{\Xi_{\mathrm{c}}^0}_{\Lambda_{\mathrm{b}}^0}) \cdot e^{i\frac{1}{2}\cdot\phi^{\Xi_{\mathrm{c}}^0}_{\overline{\mathrm{D}}^0}} \cdot\left[\sum_{\lambda'=\pm\frac{1}{2}} d^{\frac{1}{2}}_{\lambda',\frac{1}{2}}(\theta^{P_c\Xi_{\mathrm{c}}^0}_{\Lambda_{\mathrm{c}}^+}) \cdot H^{\Xi_{\mathrm{c}}^0}_{\lambda'} \cdot d^{J_{\Xi_{\mathrm{c}}^0}}_{\frac{1}{2},\lambda'}(\theta_{\Xi_{\mathrm{c}}^0}) \cdot e^{i\frac{1}{2}\cdot\phi^{\Xi_{\mathrm{c}}^0}_{\Lambda_{\mathrm{c}}^+}}\right]$ $+H^{\Lambda_{\mathrm{b}}^0}_{-\frac{1}{2}} \cdot d^{\frac{1}{2}}_{\frac{1}{2},-\frac{1}{2}}(\theta^{\Xi_{\mathrm{c}}^0}_{\Lambda_{\mathrm{b}}^0}) \cdot e^{i\frac{1}{2}\cdot\phi^{\Xi_{\mathrm{c}}^0}_{\overline{\mathrm{D}}^0}} \cdot\left[\sum_{\lambda'=\pm\frac{1}{2}} d^{\frac{1}{2}}_{\lambda',\frac{1}{2}}(\theta^{P_c\Xi_{\mathrm{c}}^0}_{\Lambda_{\mathrm{c}}^+}) \cdot H^{\Xi_{\mathrm{c}}^0}_{\lambda'} \cdot d^{J_{\Xi_{\mathrm{c}}^0}}_{-\frac{1}{2},\lambda'}(\theta_{\Xi_{\mathrm{c}}^0}) \cdot e^{-i\frac{1}{2}\cdot\phi^{\Xi_{\mathrm{c}}^0}_{\Lambda_{\mathrm{c}}^+}}\right]$
$\frac{1}{2}$	$-\frac{1}{2}$	$\pm\frac{1}{2}$	$H^{\Lambda_{\mathrm{b}}^0}_{\frac{1}{2}} \cdot d^{\frac{1}{2}}_{\frac{1}{2},\frac{1}{2}}(\theta^{\Xi_{\mathrm{c}}^0}_{\Lambda_{\mathrm{b}}^0}) \cdot e^{i\frac{1}{2}\cdot\phi^{\Xi_{\mathrm{c}}^0}_{\overline{\mathrm{D}}^0}} \cdot\left[\sum_{\lambda'=\pm\frac{1}{2}} d^{\frac{1}{2}}_{\lambda',-\frac{1}{2}}(\theta^{P_c\Xi_{\mathrm{c}}^0}_{\Lambda_{\mathrm{c}}^+}) \cdot H^{\Xi_{\mathrm{c}}^0}_{\lambda'} \cdot d^{J_{\Xi_{\mathrm{c}}^0}}_{\frac{1}{2},\lambda'}(\theta_{\Xi_{\mathrm{c}}^0}) \cdot e^{i\frac{1}{2}\cdot\phi^{\Xi_{\mathrm{c}}^0}_{\Lambda_{\mathrm{c}}^+}}\right]$ $+H^{\Lambda_{\mathrm{b}}^0}_{-\frac{1}{2}} \cdot d^{\frac{1}{2}}_{\frac{1}{2},-\frac{1}{2}}(\theta^{\Xi_{\mathrm{c}}^0}_{\Lambda_{\mathrm{b}}^0}) \cdot e^{i\frac{1}{2}\cdot\phi^{\Xi_{\mathrm{c}}^0}_{\overline{\mathrm{D}}^0}} \cdot\left[\sum_{\lambda'=\pm\frac{1}{2}} d^{\frac{1}{2}}_{\lambda',-\frac{1}{2}}(\theta^{A\Xi_{\mathrm{c}}^0}_{\Lambda_{\mathrm{c}}^+}) \cdot H^{\Xi_{\mathrm{c}}^0}_{\lambda'} \cdot d^{J_{\Xi_{\mathrm{c}}^0}}_{-\frac{1}{2},\lambda'}(\theta_{\Xi_{\mathrm{c}}^0}) \cdot e^{-i\frac{1}{2}\cdot\phi^{\Xi_{\mathrm{c}}^0}_{\Lambda_{\mathrm{c}}^+}}\right]$
$-\frac{1}{2}$	$\frac{1}{2}$	$\pm\frac{1}{2}$	$H^{\Lambda_{\mathrm{b}}^0}_{\frac{1}{2}} \cdot d^{\frac{1}{2}}_{-\frac{1}{2},\frac{1}{2}}(\theta^{\Xi_{\mathrm{c}}^0}_{\Lambda_{\mathrm{b}}^0}) \cdot e^{-i\frac{1}{2}\cdot\phi^{\Xi_{\mathrm{c}}^0}_{\overline{\mathrm{D}}^0}} \cdot\left[\sum_{\lambda'=\pm\frac{1}{2}} d^{\frac{1}{2}}_{\lambda',\frac{1}{2}}(\theta^{A\Xi_{\mathrm{c}}^0}_{\Lambda_{\mathrm{c}}^+}) \cdot H^{\Xi_{\mathrm{c}}^0}_{\lambda'} \cdot d^{J_{\Xi_{\mathrm{c}}^0}}_{\frac{1}{2},\lambda'}(\theta_{\Xi_{\mathrm{c}}^0}) \cdot e^{i\frac{1}{2}\cdot\phi^{\Xi_{\mathrm{c}}^0}_{\Lambda_{\mathrm{c}}^+}}\right]$ $+H^{\Lambda_{\mathrm{b}}^0}_{-\frac{1}{2}} \cdot d^{\frac{1}{2}}_{-\frac{1}{2},-\frac{1}{2}}(\theta^{\Xi_{\mathrm{c}}^0}_{\Lambda_{\mathrm{b}}^0}) \cdot e^{-i\frac{1}{2}\cdot\phi^{\Xi_{\mathrm{c}}^0}_{\overline{\mathrm{D}}^0}} \cdot\left[\sum_{\lambda'=\pm\frac{1}{2}} d^{\frac{1}{2}}_{\lambda',\frac{1}{2}}(\theta^{P_c\Xi_{\mathrm{c}}^0}_{\Lambda_{\mathrm{c}}^+}) \cdot H^{\Xi_{\mathrm{c}}^0}_{\lambda'} \cdot d^{J_{\Xi_{\mathrm{c}}^0}}_{-\frac{1}{2},\lambda'}(\theta_{\Xi_{\mathrm{c}}^0}) \cdot e^{-i\frac{1}{2}\cdot\phi^{\Xi_{\mathrm{c}}^0}_{\Lambda_{\mathrm{c}}^+}}\right]$
$-\frac{1}{2}$	$-\frac{1}{2}$	$\pm\frac{1}{2}$	$H^{\Lambda_{\mathrm{b}}^0}_{\frac{1}{2}} \cdot d^{\frac{1}{2}}_{-\frac{1}{2},\frac{1}{2}}(\theta^{\Xi_{\mathrm{c}}^0}_{\Lambda_{\mathrm{b}}^0}) \cdot e^{-i\frac{1}{2}\cdot\phi^{\Xi_{\mathrm{c}}^0}_{\overline{\mathrm{D}}^0}} \cdot\left[\sum_{\lambda'=\pm\frac{1}{2}} d^{\frac{1}{2}}_{\lambda',-\frac{1}{2}}(\theta^{P_c\Xi_{\mathrm{c}}^0}_{\Lambda_{\mathrm{c}}^+}) \cdot H^{\Xi_{\mathrm{c}}^0}_{\lambda'} \cdot d^{J_{\Xi_{\mathrm{c}}^0}}_{\frac{1}{2},\lambda'}(\theta_{\Xi_{\mathrm{c}}^0}) \cdot e^{i\frac{1}{2}\cdot\phi^{\Xi_{\mathrm{c}}^0}_{\Lambda_{\mathrm{c}}^+}}\right]$ $+H^{\Lambda_{\mathrm{b}}^0}_{-\frac{1}{2}} \cdot d^{\frac{1}{2}}_{-\frac{1}{2},-\frac{1}{2}}(\theta^{\Xi_{\mathrm{c}}^0}_{\Lambda_{\mathrm{b}}^0}) \cdot e^{-i\frac{1}{2}\cdot\phi^{\Xi_{\mathrm{c}}^0}_{\overline{\mathrm{D}}^0}} \cdot\left[\sum_{\lambda'=\pm\frac{1}{2}} d^{\frac{1}{2}}_{\lambda',-\frac{1}{2}}(\theta^{P_c\Xi_{\mathrm{c}}^0}_{\Lambda_{\mathrm{c}}^+}) \cdot H^{\Xi_{\mathrm{c}}^0}_{\lambda'} \cdot d^{J_{\Xi_{\mathrm{c}}^0}}_{-\frac{1}{2},\lambda'}(\theta_{\Xi_{\mathrm{c}}^0}) \cdot e^{-i\frac{1}{2}\cdot\phi^{\Xi_{\mathrm{c}}^0}_{\Lambda_{\mathrm{c}}^+}}\right]$

Table 28: Amplitudes of the $\Lambda_{\mathrm{b}}^0 \to \Xi_{\mathrm{c}}^0\mathrm{K}^-$ decays included in the amplitude model.

Decay	B_{LS} couplings
$\Lambda_{\mathrm{b}}^0 \to \mathrm{D}^*_{\mathrm{s}0}(2317)\Lambda_{\mathrm{c}}^+$	$B^{\Lambda_{\mathrm{b}}^0\to\mathrm{D}^*_{\mathrm{s}0}(2317)\Lambda_{\mathrm{c}}^+}_{0,\frac{1}{2}}$, $[B^{\Lambda_{\mathrm{b}}^0\to\mathrm{D}^*_{\mathrm{s}0}(2317)\Lambda_{\mathrm{c}}^+}_{1,\frac{1}{2}}$,] $B^{\mathrm{D}^*_{\mathrm{s}0}(2317)\to\overline{\mathrm{D}}^0\mathrm{K}^-}_{0,0}$
$\Lambda_{\mathrm{b}}^0 \to \mathrm{D}^*_{\mathrm{s}3}(2860)\Lambda_{\mathrm{c}}^+$	$B^{\Lambda_{\mathrm{b}}^0\to\mathrm{D}^*_{\mathrm{s}3}(2860)\Lambda_{\mathrm{c}}^+}_{2,\frac{5}{2}}$, $B^{\mathrm{D}^*_{\mathrm{s}3}(2860)\to\overline{\mathrm{D}}^0\mathrm{K}^-}_{3,0}$
$\Lambda_{\mathrm{b}}^0 \to \Xi_{\mathrm{c}}^0(2790)\overline{\mathrm{D}}^0$	$B^{\Lambda_{\mathrm{b}}^0\to\Xi_{\mathrm{c}}^0(2790)\overline{\mathrm{D}}^0}_{0,\frac{1}{2}}$, $[B^{\Lambda_{\mathrm{b}}^0\to\Xi_{\mathrm{c}}^0(2790)\overline{\mathrm{D}}^0}_{1,\frac{1}{2}}$,] $B^{\Xi_{\mathrm{c}}^0(2790)\to\Lambda_{\mathrm{c}}^+\mathrm{K}^-}_{0,\frac{1}{2}}$
K-matrix amplitude	$B^{\Lambda_{\mathrm{b}}^0\ decay}_{0,\frac{1}{2}}$, $B^{\Lambda_{\mathrm{b}}^0\ decay}_{1,\frac{1}{2}}$, $B^{\Lambda_{\mathrm{b}}^0\ decay}_{1,\frac{3}{2}}$, $B^{\mathrm{D}_s^*\mathrm{Kmat}}_{1,0}$

Table 29: Couplings of the decays included in the amplitude model. Elements in parentheses correspond to partial waves which are not included in the baseline amplitude model.

6.4 Fit fractions and interference terms

The contribution of an intermediate state to the total decay amplitude is expressed by the so-called *fit fraction*. The fit fraction $\mathcal{F}_i$ for a given i resonance is defined as ratio of integrals computed over pseudo-samples. Two set of pseudo-experiments are performed, in one case describing an amplitude model which includes the contributions from all the intermediate states (Eq. 153), and secondly a model consisting of only the i resonance. The fit fraction $\mathcal{F}_i$ is then expressed by:

$$\mathcal{F}_i = \frac{\int_{MC} \sum_{\lambda_{\Lambda^0_\mathrm{b}},\lambda_{\Lambda^+_\mathrm{c}}} |M^i_{\lambda_{\Lambda^0_\mathrm{b}},\lambda_{\Lambda^+_\mathrm{c}}}|^2 \, d\xi}{\int_{MC} \sum_{\lambda_{\Lambda^0_\mathrm{b}},\lambda_{\Lambda^+_\mathrm{c}}} |\sum_k M^k_{\lambda_{\Lambda^0_\mathrm{b}},\lambda_{\Lambda^+_\mathrm{c}}}|^2 \, d\xi} \tag{154}$$

where the amplitude variables are summarised as ξ, the dependence of the matrix elements on them is omitted, and k is running over all the contributing amplitudes of the full model. In general, the sum of all the fit fractions is not necessarily the unity, due to the potential interference between resonances. The *interference term* between two resonances i and j is given by:

$$\mathcal{F}_{ij} = \frac{\int_{MC} \sum_{\lambda_{\Lambda^0_\mathrm{b}},\lambda_{\Lambda^+_\mathrm{c}}} 2\,\mathrm{Re}(M_i M_j^*) \, dm_{\Lambda^+_\mathrm{c}\overline{\mathrm{D}}^0} d\Omega}{\int_{MC} \sum_{\lambda_{\Lambda^0_\mathrm{b}},\lambda_{\Lambda^+_\mathrm{c}}} |\sum_i M_i|^2 \, dm_{\Lambda^+_\mathrm{c}\overline{\mathrm{D}}^0} d\Omega} \tag{155}$$

and the unitarity condition can be finally expressed by:

$$\sum_i \mathcal{F}_i + \sum_{i,j}^{i<j} \mathcal{F}_{ij} \equiv 1 \tag{156}$$

The fit to data only provides the uncertainties on the fitted parameters, namely the couplings and the line shape parameters. The uncertainties on the measured fit fractions and interference terms are computed using pseudo-experiments, by sampling the fit parameters in the *uncorrelated space* as described in the following. The covariance matrix resulting from the amplitude fit is diagonalised decomposing it in its eigenvalues. The latter define a basis for a new space, where the fit parameters are uncorrelated with each other. The fit parameters are transformed in the uncorrelated space and sampled within their uncorrelated uncertainties, following a Gaussian sampling. The sampled parameter values are finally transformed back in the original parameter space. The parameters are sampled 250 times, and for each set of parameters a pseudo-experiment is performed generating 100,000 events. A large number of events, with respect to the number of signal candidates in the data set of this analysis, is required in order to not add additional statistical uncertainties arising from the generation of the pseudo-samples. The standard deviation of the distributions of generated fit fractions and interference terms are assigned as statistical uncertainties on fitted quantities.

6.5 Results

The fitted fractions of the intermediate states contributing to the amplitude model, and their interference terms, are listed in Tables 30-31 with their uncertainties. The D_s^* K-matrix component is contributing the most to the amplitude model. The interference between the states are negligible. The components of the model are not independent, but constrained by the condition expressed in Equation 156. Thus, the uncertainty on the sum of the fit fractions is not the sum in quadrature of the uncertainties of the individual components.

Component	Fit fraction
$\mathrm{D}^*_{\mathrm{s}0}(2317)$	0.099 ± 0.013
$\mathrm{D_s}$ K-matrix	0.862 ± 0.029
$\mathrm{D}^*_{\mathrm{s}3}(2860)$	0.0181 ± 0.0077
$\Xi^0_\mathrm{c}(2790)$	0.0257 ± 0.0051
Sum	1.0029 ± 0.0041

Table 30: Fitted resonance fractions.

	$\mathrm{D_s}$ K-matrix	$\mathrm{D}^*_{\mathrm{s}3}(2860)$	$\Xi^0_\mathrm{c}(2790)$
$\mathrm{D}^*_{\mathrm{s}0}(2317)$	-0.012 ± 0.015	0.00006 ± 0.00079	-0.0059 ± 0.0021
$\mathrm{D_s}$ K-matrix	/	-0.00015 ± 0.00053	0.0059 ± 0.0099
$\mathrm{D}^*_{\mathrm{s}3}(2860)$		/	0.0021 ± 0.0013

Table 31: Fitted interference terms between the components of the amplitude model.

Table 32 reports the fit results and related uncertainties for the parameters of the amplitude model, where for each resonance of name *state* the notation is:

- *state_M_Bl<i>s<j>* are the B_{LS} couplings of the Λ^0_b decay for $L = i$, $S = j$ values;
- *state_res_Bl<i>s<j>* are the B_{LS} couplings of the resonance decay for $L = i$, $S = j$ values.

The *Ds_Kmatrix_alpha*, *Ds_Kmatrix_g* and *Ds_Kmatrix_background* parameters are the components of the couplings and of the background term of the K-matrix amplitude, as introduced in Section 5.3.

In order to plot the fitted amplitude model, a pseudo-sample is generated with the values of the amplitude model parameters set to the results of the fit to data. The distributions of the amplitude variables in such a sample, overimposed to the data, are shown in Figure 44. The bin uncertainties shown for the fit model are derived from the same pseudo-samples used to assess the uncertainties of the fit fractions and interference terms. Plots with finer binnings of the fit projections are proposed in Appendix A.2.

Parameter	Fitted value	Parameter	Fitted value
$\mathrm{D}^*_{\mathrm{s}0}$(2317)_width	0.030 ± 0.016	Ds_Kmatrix_g_0_Real	-8.37 ± 0.43
$\mathrm{D}^*_{\mathrm{s}0}$(2317)_M_Bl0s1_Real	-0.017 ± 0.014	Ds_Kmatrix_g_1_Real	6.54 ± 0.13
$\mathrm{D}^*_{\mathrm{s}0}$(2317)_M_Bl0s1_Imag	-0.1256 ± 0.0055	Ds_Kmatrix_g_2_Real	6.6 ± 1.2
Ds_Kmatrix_M_Bl0s1_Real	-1.8 ± 1.0	Ds_Kmatrix_g_3_Real	-3.38 ± 0.25
Ds_Kmatrix_M_Bl0s1_Imag	4.4 ± 1.9	Ds_Kmatrix_background_0	0.0135 ± 0.0017
Ds_Kmatrix_M_Bl2s1_Real	-7.05 ± 0.56	Ds_Kmatrix_background_1	0.0867 ± 0.0045
Ds_Kmatrix_M_Bl2s1_Imag	-4.06 ± 0.57	$\mathrm{D}^*_{\mathrm{s}3}$(2860)_M_Bl4s5_Real	0.32 ± 0.46
Ds_Kmatrix_M_Bl2s3_Real	4.69 ± 0.72	$\mathrm{D}^*_{\mathrm{s}3}$(2860)_M_Bl4s5_Imag	-0.33 ± 0.37
Ds_Kmatrix_M_Bl2s3_Imag	-4.73 ± 0.60	$\mathrm{D}^*_{\mathrm{s}3}$(2860)_res_Bl6s0_Real	-0.036 ± 0.014
Ds_Kmatrix_res_Bl2s0_Real	-1.064 ± 0.048	$\mathrm{D}^*_{\mathrm{s}3}$(2860)_res_Bl6s0_Imag	0.015 ± 0.018
Ds_Kmatrix_res_Bl2s0_Imag	-0.722 ± 0.076	Ξ^0_c(2790)_M_Bl0s1_Real	-0.53 ± 0.32
Ds_Kmatrix_Ds12700_mass	2.7136 ± 0.0042	Ξ^0_c(2790)_M_Bl0s1_Imag	0.69 ± 0.35
Ds_Kmatrix_Ds12860_mass	2.9671 ± 0.0099	Ξ^0_c(2790)_res_Bl0s1_Real	-0.0149 ± 0.0072
Ds_Kmatrix_alpha_0_Real	0.00272 ± 0.00024	Ξ^0_c(2790)_res_Bl0s1_Imag	-0.0295 ± 0.0051
Ds_Kmatrix_alpha_0_Imag	-0.00715 ± 0.0002		
Ds_Kmatrix_alpha_1_Real	-0.00111 ± 0.00014		
Ds_Kmatrix_alpha_1_Imag	0.00394 ± 0.00025		

Table 32: Fitted values of the amplitude model parameters.

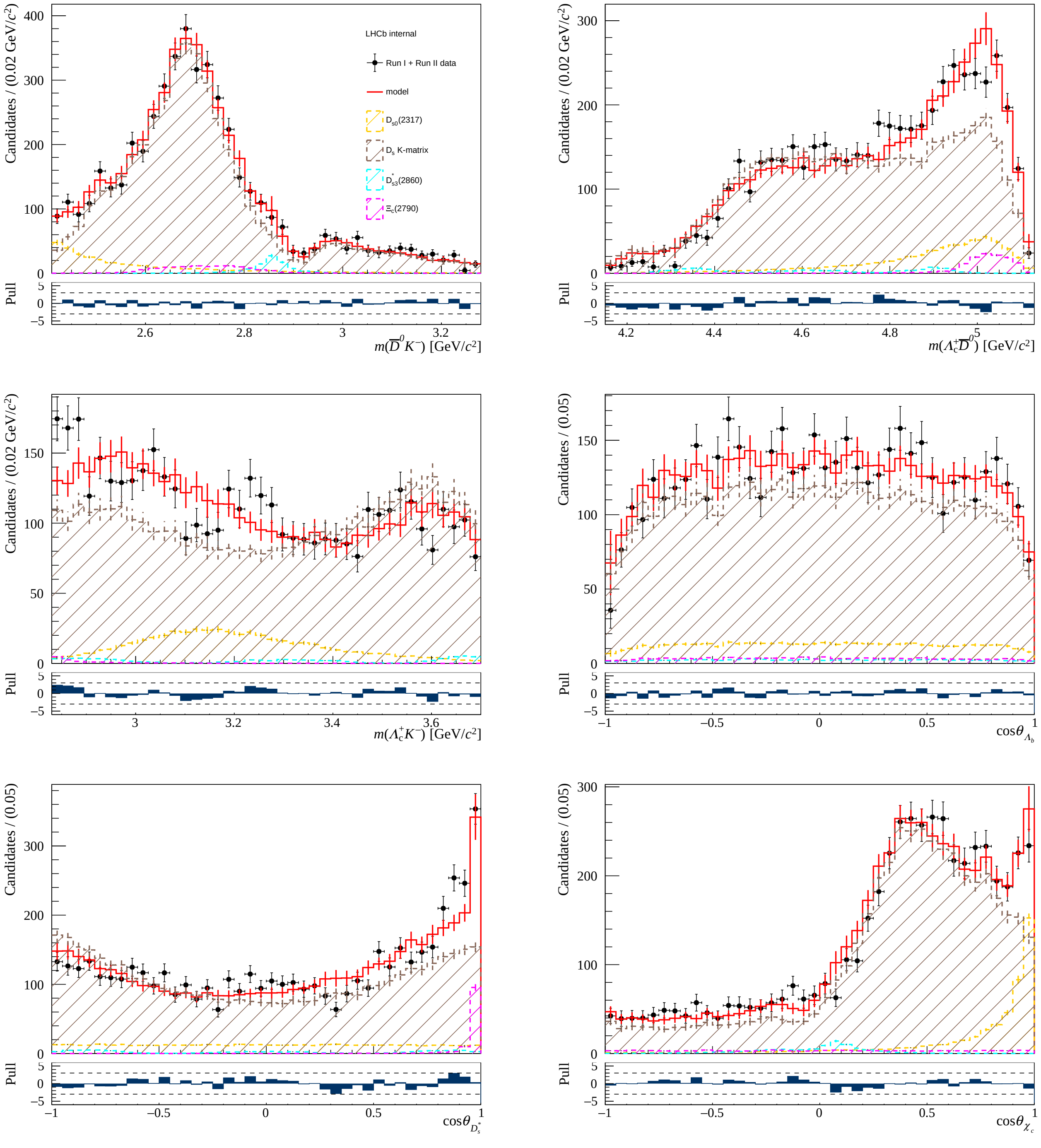

Figure 44: Projections of the amplitude fit over the amplitude variables, overimposed to the data.

The consistency between the data distributions and the fit model is quantified by the distribution of pulls δ:

$$\delta = \frac{data - fit}{\sqrt{\sigma_{data}^2 + \sigma_{fit}^2}} \tag{157}$$

with σ_{data} being the statistical Poissonian uncertainty of the data, and σ_{fit} the fit uncertainty. In the pull distributions, the horizontal dashed lines correspond to $\pm 3\sigma$ levels of discrepancy between data and the fit model.

The fitted amplitude model shows a general good agreement with the data. Although the absolute contribution of the $\Xi_c^0(2790)$ to the model results to be small, this state is crucial for a good description of the data at high values of $\cos(\theta_{D_s^*})$. This is verified in Chapter 7.

Nevertheless, tensions arise especially in the $m(\Lambda_c^+ K^-)$ invariant mass distribution. The data distribution is characterised by an overall falling trend for increasing mass values, with three main structures at $2.96 - 3.08$ GeV/c^2, $3.12 - 3.3$ GeV/c^2 and $3.4 - 3.65$ GeV/c^2. These structures are not well captured by the fit model, which attempts to interpolate them. The pulls of the mass region from ~ 3.1 GeV/c^2 to the end of the spectrum are overall smaller than 2.5σ because of the relatively large uncertainties of both the data and fit model distributions. However a larger discrepancy is present in the low mass region, with $\approx 2 - 2.5\sigma$ significance.

The validity and stability of the obtained fit results have been assessed by performing a number of crosschecks, which are presented in Chapter 7. In the same Chapter it is shown that alternative amplitude models do not particularly improve the fit results. It must be noted that the description of the $\Lambda_c^+ K^-$ system is particularly challenging in this analysis, due to the relatively small natural width of the $\Xi_c^0(2790)$ state. This value is in the same range of the characteristic mass resolution of the channel $\Lambda_b^0 \to \Lambda_c^+ \overline{D}^0 K^-$. A complete treatment of this aspect would require sophisticated methods such as the convolution of the line shape distribution with a resolution function, and it is exceeding the aim of this analysis. Related to this issue, the relatively bad description of the $m(\Lambda_c^+ K^-)$ distribution is reflected in a unsatisfactory description of the data at large values of the $\cos(\theta_{D_s^*})$ angle. Possible improvements in describing the $m(\Lambda_c^+ K^-)$ distribution, which would translate in a better characterisation of the $\cos(\theta_{D_s^*})$ distribution, are investigated in Chapter 7.

7 Crosschecks and systematics studies

The stability of the obtained fit results is verified by performing different checks, which are presented in this Chapter in Section 7.1. In particular, alternative models which could improve the description of the data in the $m(\Lambda_c^+ K^-)$ invariant mass distribution are considered. More general amplitude models to the one used in the baseline fit, meaning including more intermediate states and partial waves which could possibly contribute to the description of the data, are tested as well.

This Chapter also presents the studies performed to assess the systematic uncertainties on the fit results. The final systematic uncertainties are reported in Section 7.3.

7.1 Crosschecks of the stability of the fit results

In the next paragraphs, the choice of the data selection and amplitude model of the baseline fit are validated by performing consistency checks of the results. Alternative selection criteria and amplitude models are considered, and fits to data are repeated. The results are considered to be consistent with the baseline fit if they do not differ from more than one standard deviation of the statistical uncertainties.

Amplitude models with additional states are also tested. In such cases, the contributions from the latter are considered negligible if their fit fractions and interference terms are smaller than 1%, and compatible with zero at 1σ-level of the statistical uncertainties.

7.1.1 Amplitude fit with higher partial waves

The baseline amplitude model includes only partial waves corresponding to the lowest possible orbital angular momentum L_{min} for the $D_{s0}^*(2317)$, $D_{s3}^*(2860)$ and $\Xi_c^0(2790)$ states. Higher partial waves were considered only for the K-matrix amplitude. However, higher partial waves for the other states could in principle contribute in the amplitude fit to data.

A new amplitude model is constructed, including all the possible partial waves for all the states. The amplitude fit to data is repeated, and its projections are shown in Figure 45. The fitted resonance fractions are listed in Table 33. Although the results are consistent with the baseline amplitude fit, the uncertainties are now much larger, as consequence of the higher number of free parameters which have to be fitted to data. In fact, each additional partial wave carries one B_{LS} coupling (i.e. two free parameters) to be determined from data. These results confirm the validity of the approximation made in the baseline amplitude fit, where only the lowest partial waves for the $D_{s0}^*(2317)$, $D_{s3}^*(2860)$ and $\Xi_c^0(2790)$ states have been considered.

7.1.2 Amplitude fit without the $\Xi_c^0(2790)$ state

The absolute contribution of the $\Xi_c^0(2790)$ state to the fitted amplitude model is small, with a measured fit fraction $(2.57 \pm 0.51)\%$ (Tab. 30). Nevertheless, its inclusion in the model is necessary in order to correctly describe the data. This can be seen especially in the $\cos(\theta_{P_c})$ and $\cos(\theta_{D_s^*})$ angular distributions shown in Figure 46, by comparing the baseline fit results with a fit model which does not include the $\Xi_c^0(2790)$ contribution. The low-spectrum of the $\cos(\theta_{P_c})$ distribution and the region of large $\cos(\theta_{D_s^*})$ angles require the presence of the $\Xi_c^0(2790)$ state, to give a satisfactory description of the data.

Component	Baseline model	Model with all possible partial waves
$\mathrm{D}^{*}_{\mathrm{s}\,0}(2317)$	0.099 ± 0.013	0.094 ± 0.046
$\mathrm{D_s}$ K-matrix	0.862 ± 0.029	0.844 ± 0.067
$\mathrm{D}^{*}_{\mathrm{s}\,3}(2860)$	0.0181 ± 0.0077	0.030 ± 0.023
$\Xi^{0}_{\mathrm{c}}(2790)$	0.0257 ± 0.0051	0.026 ± 0.013
Sum	1.0029 ± 0.0041	0.9942 ± 0.0059

Table 33: Fitted resonance fractions. The baseline amplitude model, which includes only the lowest partial waves for the $\mathrm{D}^{*}_{\mathrm{s}\,0}(2317)$, $\mathrm{D}^{*}_{\mathrm{s}\,3}(2860)$ and $\Xi^{0}_{\mathrm{c}}(2790)$ states, is compared with a model which includes all possible partial waves for all states.

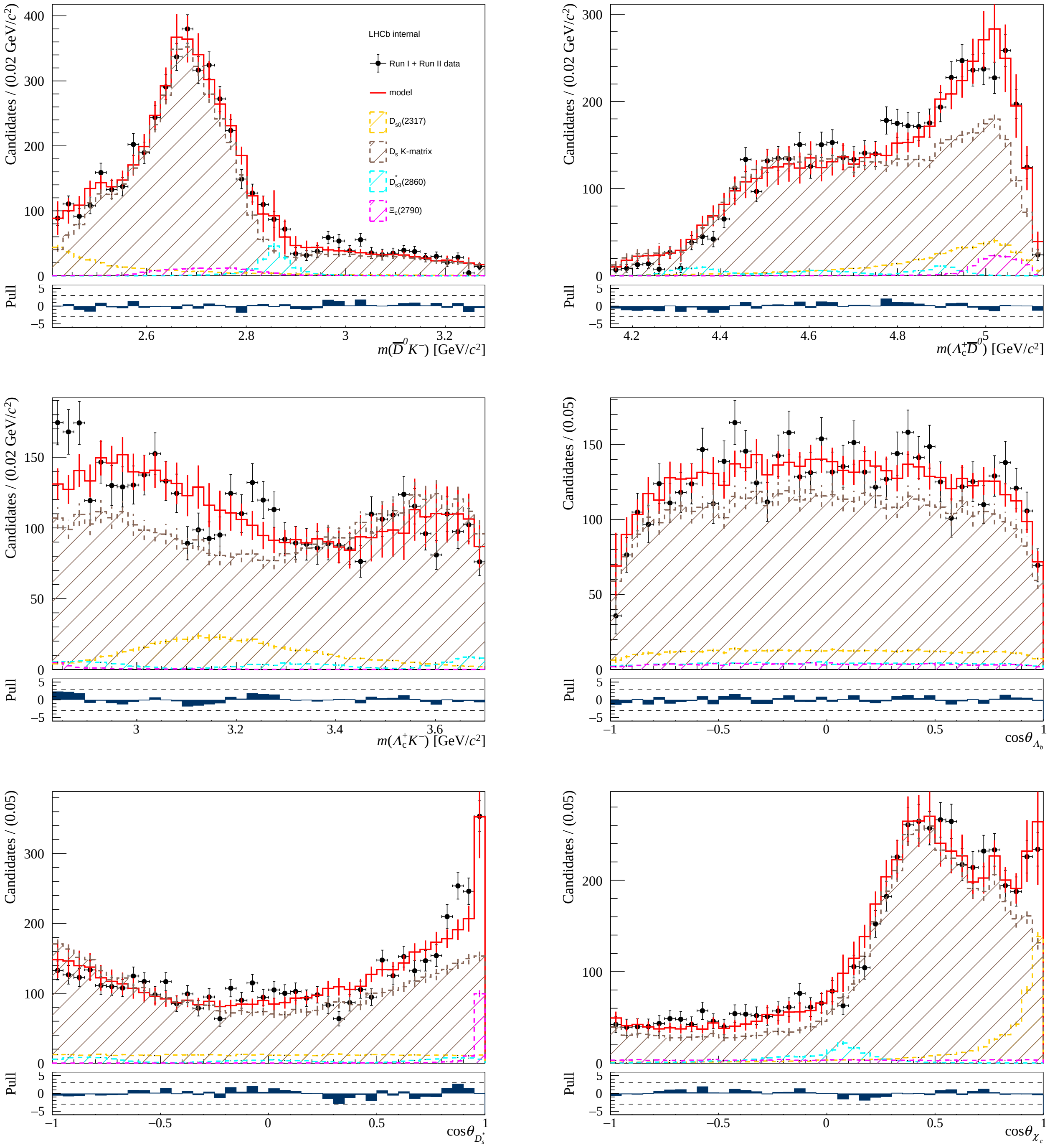

Figure 45: Projections of the amplitude fit to data. All possible partial waves are considered for all the states.

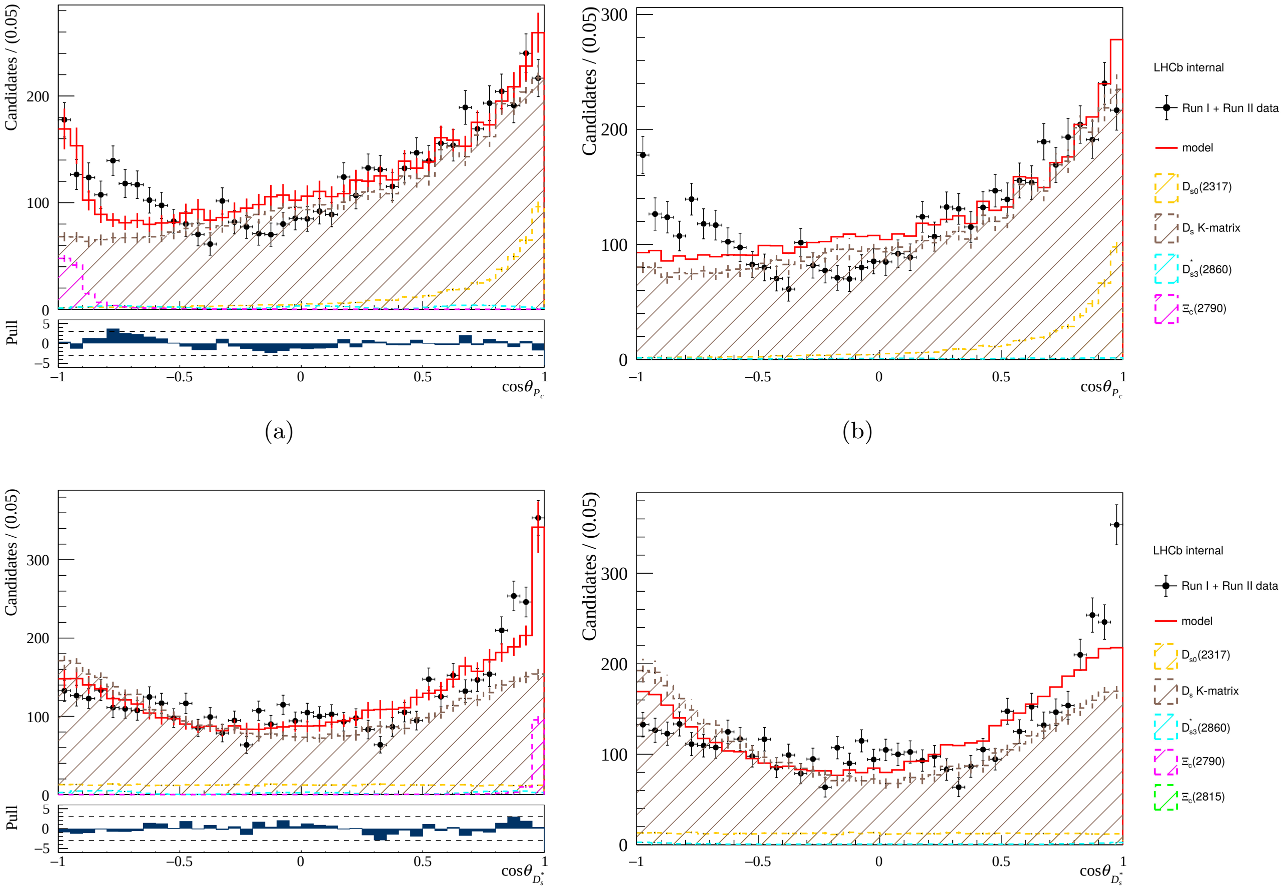

(a) (b)

(d) (e)

Figure 46: Projections of the amplitude fits to data over the $\cos(\theta_{P_c})$ (a, b) and $\cos(\theta_{D_s^*})$ (c, d) distributions. a, c) Baseline amplitude model. b, d) Amplitude model without the $\Xi_c^0(2790)$ state.

7.1.3 Amplitude fit including the $\mathrm{D}^*_{\mathrm{s}2}(2573)$ state

The baseline amplitude model presented in Chapter 6 does not include the $\mathrm{D}^*_{\mathrm{s}2}(2573)$ state, which could potentially contribute to the description of the data. This is checked by defining an amplitude model which includes it, and repeating the amplitude fit to the data. The $m(\overline{\mathrm{D}}^0\mathrm{K}^-)$ projection of the fit is presented in Figure 47, compared to the baseline fit. The values of the fit fractions are reported in Table 34. The contribution of the $\mathrm{D}^*_{\mathrm{s}2}(2573)$ state results to be negligible, and the baseline amplitude model describes better the mass region ≈ 2.52 GeV/c^2 in the $m(\overline{\mathrm{D}}^0\mathrm{K}^-)$ distribution.

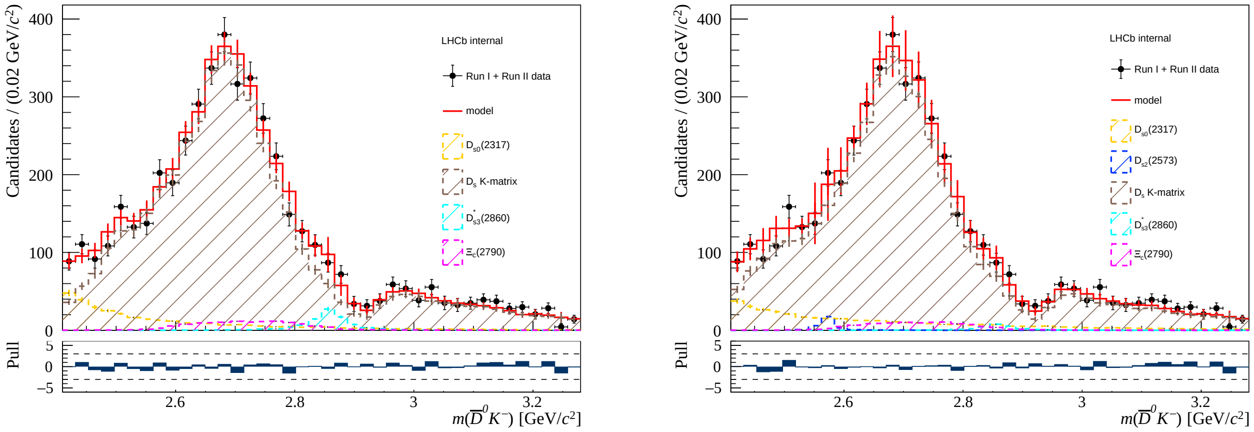

(a)

(b)

Figure 47: Projections of the amplitude fits to data over the $m(\overline{\mathrm{D}}^0\mathrm{K}^-)$ distribution. a) Baseline amplitude model, without the $\mathrm{D}^*_{\mathrm{s}2}(2573)$ contribution. b) Amplitude model including the $\mathrm{D}^*_{\mathrm{s}2}(2573)$ state.

Component	Baseline model	With $\mathrm{D}^*_{\mathrm{s}2}(2573)$ contribution
$\mathrm{D}^*_{\mathrm{s}0}(2317)$	0.099 ± 0.013	0.106 ± 0.018
$\mathrm{D}^*_{\mathrm{s}2}(2573)$	/	$0.0064^{+0.0072}_{-0.0064}$
$\mathrm{D_s}$ K-matrix	0.862 ± 0.029	0.861 ± 0.035
$\mathrm{D}^*_{\mathrm{s}3}(2860)$	0.0181 ± 0.0077	0.0052 ± 0.0037
$\Xi^0_{\mathrm{c}}(2790)$	0.0257 ± 0.0051	0.023 ± 0.0066
Sum	1.0029 ± 0.0041	1.0021 ± 0.0048

Table 34: Fitted resonance fractions adding the $\mathrm{D}^*_{\mathrm{s}2}(2573)$ contribution to the amplitude model, compared to the baseline fit.

7.1.4 Amplitude fit with a *non-resonant* contribution

In Chapter 6, only resonating contributions have been considered in the amplitude model. However an additional flat contribution is often included, parametrised by a real quantity describing the size of its amplitude. This contribution is usually referred to as *non-resonant contribution*, since it describes the direct decay from the initial- to the final-state particles without any intermediate decays of resonances. Anyhow this definition is un-precise, as this term could potentially describe eventual background present in the data set, as well. Moreover, the non-resonant and the background contributions to the amplitude cannot be disentangled within this term.

A new amplitude model is considered, adding to the matrix element in Equation 153 (here denoted by M_{res}) a non-resonant contribution of size $A_{non-res}$:

$$M = M_{res} + |A_{non-res}|^2 \tag{158}$$

The amplitude fit to data are repeated with the new model, and the fitted value of the non-resonant size results to be:

$$A_{non-res} = 0.00 \pm 0.013 \tag{159}$$

where the $A_{non-res}$ parameter has been allowed to take negative values as well. Hence, the non-resonant contribution in the amplitude fit of this analysis results to be negligible.

7.1.5 Amplitude fits with the $\Xi_c^0(2815)$, $\Xi_c^0(2970)$, $\Xi_c^0(3055)$ and $\Xi_c^0(3088)$ states

In the baseline amplitude model, only the $\Xi_c^0(2790)$ state is included in the $\Lambda_c^+K^-$ system. However other Ξ_c^0 states might contribute, as listed in Table 25. Their inclusion could potentially improve the fit quality, especially in the projection of the $m(\Lambda_c^+K^-)$ invariant mass distribution.

The well-established $\Xi_c^0(2815)$ state is included in the amplitude model, and the amplitude fit to data is repeated. All the possible partial waves of the Λ_b^0 and resonances decays are included in the model. The fit fractions are reported in Table 35, and the fit projections are shown in Figure 48. The contribution of the $\Xi_c^0(2815)$ state results to be negligible within the related fit uncertainties, and the fit is not notably improved by its inclusion.

Component	Baseline model	With $\Xi_c^0(2815)$ and higher partial waves
$D_{s0}^*(2317)$	0.099 ± 0.013	0.106 ± 0.022
D_s K-matrix	0.862 ± 0.029	0.863 ± 0.035
$D_{s3}^*(2860)$	0.0181 ± 0.0077	0.0149 ± 0.0066
$\Xi_c^0(2790)$	0.0257 ± 0.0051	0.0225 ± 0.0062
$\Xi_c^0(2815)$	/	0.00129 ± 0.0010
Sum	1.0029 ± 0.0041	1.0076 ± 0.0052

Table 35: Fitted resonance fractions. The $\Xi_c^0(2815)$ state is added to the baseline amplitude model, and all possible partial waves of the Λ_b^0 and resonances decays are included.

Other Ξ_c^0 states, the $\Xi_c^0(2970)$, $\Xi_c^0(3055)$ and $\Xi_c^0(3088)$ resonances, are established and could contribute in the $\Lambda_b^0 \to \Lambda_c^+\overline{D}^0K^-$ decays. However, their quantum numbers have not been established by previous measurements yet. Hence, amplitude models are considered for different hypotheses of the spin assignments for these states. All possible combinations between the assignments $J^P = \frac{1}{2}^-, \frac{3}{2}^-$ are considered, resulting in eight different amplitude models tested. The fit fractions resulting from the amplitude fits to data are listed in Table 36, while the projections of the latter in the $m(\Lambda_c^+K^-)$ spectrum are reported in Appendix A.6. In all cases, the Ξ_c^0 states do not significantly contribute to the amplitude model. The uncertainties on the fit fractions have not been computed since it would have required huge computing resources for generating the required pseudo-experiments, without affecting the outcome of these studies.

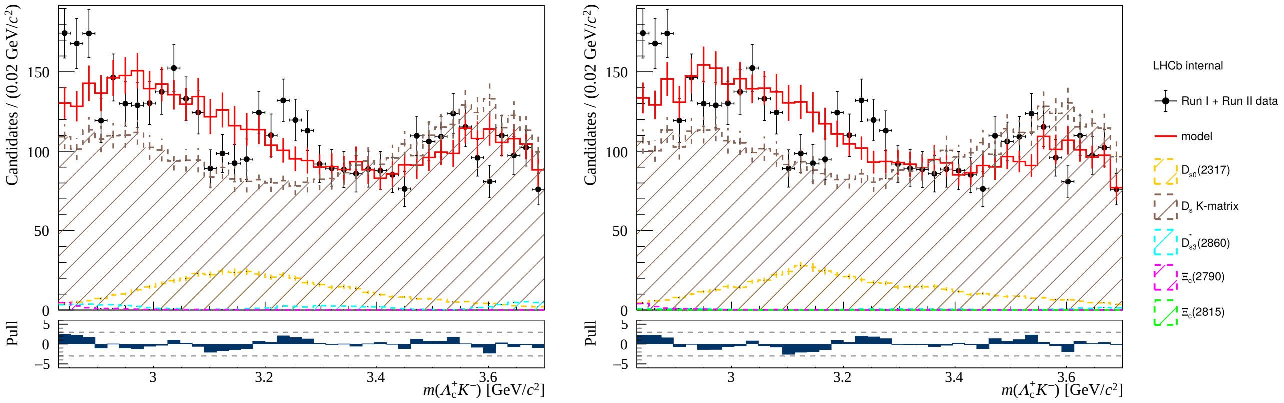

(a) (b)

Figure 48: Projections of the amplitude fit to data over the $m(\Lambda_c^+ K^-)$ distribution. a) Baseline amplitude model. b) The $\Xi_c^0(2815)$ state is added to the amplitude model, and all possible partial waves of the Λ_b^0 and resonances decays are included.

Component	Baseline model	$[\frac{1}{2}^-, \frac{1}{2}^-, \frac{1}{2}^-]$	$[\frac{1}{2}^-, \frac{1}{2}^-, \frac{3}{2}^-]$	$[\frac{1}{2}^-, \frac{3}{2}^-, \frac{1}{2}^-]$	$[\frac{1}{2}^-, \frac{3}{2}^-, \frac{3}{2}^-]$	$[\frac{3}{2}^-, \frac{1}{2}^-, \frac{1}{2}^-]$	$[\frac{3}{2}^-, \frac{1}{2}^-, \frac{3}{2}^-]$	$[\frac{3}{2}^-, \frac{3}{2}^-, \frac{1}{2}^-]$	$[\frac{3}{2}^-, \frac{3}{2}^-, \frac{3}{2}^-]$
$\Xi_c^0(2790)$	0.0257 ± 0.0051	0.0235	0.0260	0.0234	0.0227	0.0235	0.0236	0.0233	0.0236
$\Xi_c^0(2815)$	/	0.0021	0.0031	0.0022	0.0023	0.0021	0.0021	0.0021	0.0020
$\Xi_c^0(2970)$	/	0.00012	0.0012	0.00015	0.000086	0.00059	0.00044	0.00045	0.00027
$\Xi_c^0(3055)$	/	0.0018	0.0038	0.0062	0.0041	0.0016	0.0029	0.0061	0.0072
$\Xi_c^0(3088)$	/	0.0020	0.0015	0.0030	0.0017	0.0021	0.0011	0.0030	0.0017

Table 36: Fitted resonance fractions including the $\Xi_c^0(2815)$, $\Xi_c^0(2970)$, $\Xi_c^0(3055)$ and $\Xi_c^0(3088)$ states to the baseline amplitude model.. Different hypotheses for the spin assignments of the $\Xi_c^0(2970)$, $\Xi_c^0(3055)$, $\Xi_c^0(3088)$ states are considered. The first value within brackets refer to the spin assignment of the $\Xi_c^0(2970)$, the second value to the spin of the $\Xi_c^0(3055)$, the third value to the spin of the $\Xi_c^0(3088)$. All possible partial waves of the Λ_b^0 and resonances decays are included in the amplitude model.

7.1.6 Tighter selection of Λ_c^+ and bachelor K^- candidates

The structures in the $m(\Lambda_c^+K^-)$ invariant mass distribution (Fig. 44) could in principle be generated by peaking background due to mis-reconstructed or mis-identified Λ_c^+ and K^- particles. This is checked by defining tighter *D-from-B* BDT and PID selections and by performing mass and amplitude fits on the newly selected data sample. A Λ_c^+ *D-from-B* BDT cut value of 0.2 and a *ProbNNk* cut value on the bachelor K^- of 0.5 are chosen. These values have been determined from the *D-from-B* BDT and PID response distributions on the raw and *s*-weighted data, shown in Figure 49, from the baseline selection. The mass fit to the new data set is presented in Figure 50, and the results are listed in Table 37. The $m(\Lambda_c^+K^-)$ invariant mass distribution selected by the tighter *D-from-B* BDT and PID cut values is presented in Figure 50, showing a similar shape to what was obtained with the baseline selection.

Fit parameter	Baseline selection	Tighter Λ_c^+ and K^- selections
$N_{\Lambda_b^0}$	4971 ± 92	4062 ± 78
N_{bkg}	1594 ± 71	640 ± 51
$\mu_{\Lambda_b^0}$	5619.82 ± 0.13	5619.73 ± 0.14
$\sigma_{\Lambda_b^0}$	6.84 ± 0.14	6.8 ± 0.14
$\tau_{\Lambda_b^0}$	-0.0031 ± 0.0013	-0.0074 ± 0.0023

Table 37: Results of the fits to the $m(\Lambda_c^+\overline{D}^0K^-)$ invariant mass distribution for the baseline and tighter selection of the Λ_c^+ and K^- particles.

Amplitude fits are performed to the new data set using the same amplitude model as for the default selection. The resulting fit fractions are listed in Table 38, and the fit projections to the $m(\Lambda_c^+K^-)$ distributions are shown in Figure 51. The two selections give compatible results.

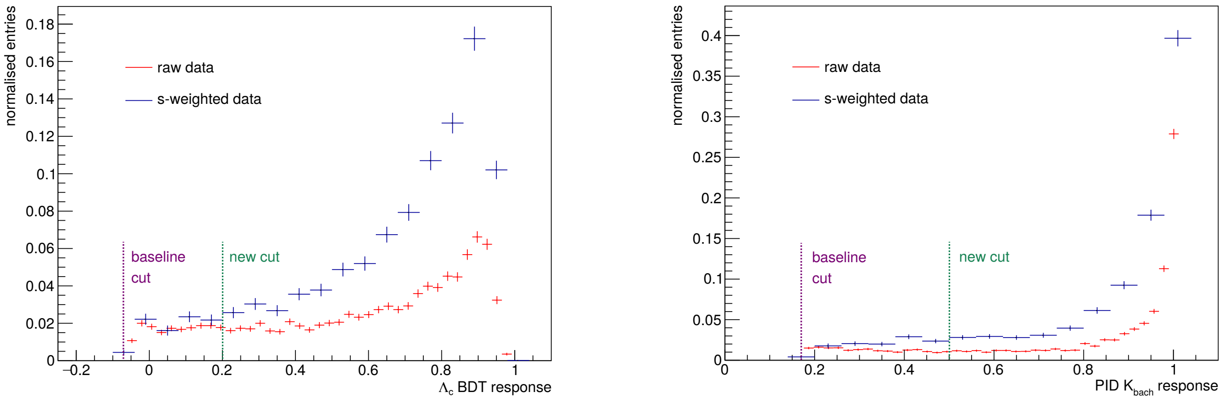

(a) (b)

Figure 49: Λ_c^+ *D-from-B* BDT response (a) and *ProbNNk* response on the bachelor K^- (b) on raw (blue) and *s*-weighted (red) data. The latter have been *s*-weighted by the mass fit performed on the data set defined by the baseline selection. The tighter cut values of the two selections are pointed by the vertical, green dashed lines. The cut values of the baseline selection are highlighted by the vertical, violet dashed lines.

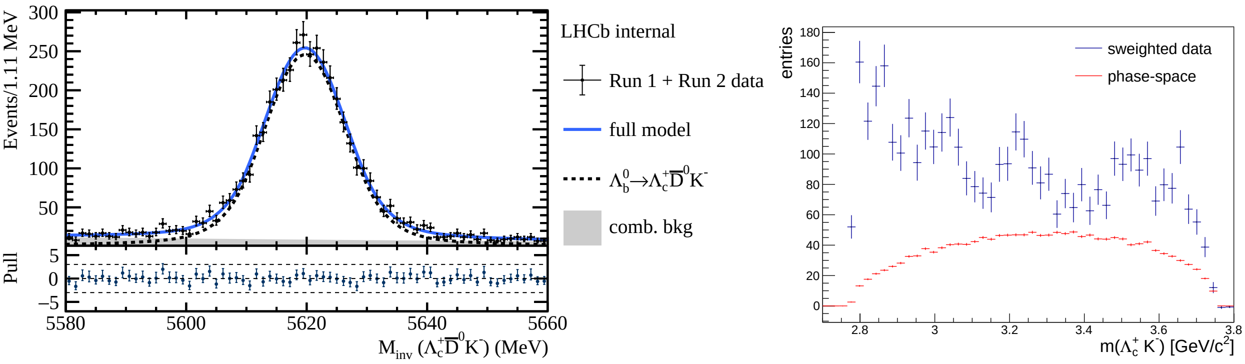

(a) (b)

Figure 50: Mass fit to the $m(\Lambda_c^+ \overline{D}^0 K^-)$ invariant mass distribution (a) and *s*-weighted $m(\Lambda_c^+ K^-)$ distribution (b) with tighter *D-from-B* BDT and PID selection on the Λ_c^+ and bachelor K^- respectively.

Component	Baseline selection	Tighter Λ_c^+ and K^- selections
$D_{s0}^*(2317)$	0.099 ± 0.013	0.109 ± 0.033
D_s *K*-matrix	0.862 ± 0.029	0.845 ± 0.049
$D_{s3}^*(2860)$	0.0181 ± 0.0077	0.011 ± 0.0061
$\Xi_c^0(2790)$	0.0257 ± 0.0051	0.026 ± 0.013
Sum	1.0029 ± 0.0041	0.986 ± 0.010

Table 38: Comparison of the fit fractions obtained with the baseline selection, and with tighter *D-from-B* BDT and PID selections of the Λ_c^+ and K^- particles.

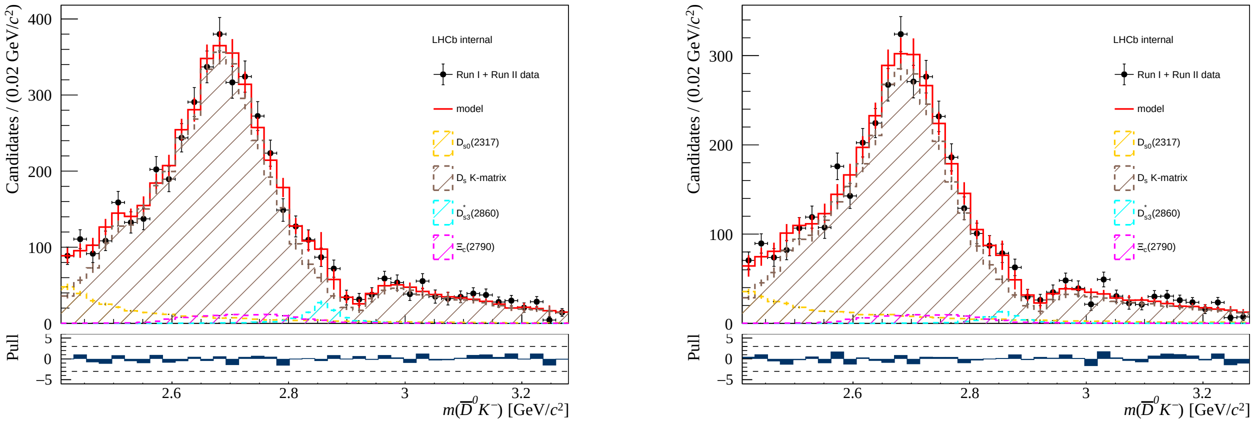

(a) (b)

Figure 51: Projections of the amplitude fit over the $m(\Lambda_c^+ K^-)$ invariant mass distribution. a) Baseline selection. b) Tighter *D-from-B* BDT and PID selections of the Λ_c^+ and K^- particles.

7.1.7 K-matrix amplitude with $\overline{\mathrm{D}}^0\mathrm{K}^-$ and $\mathrm{D}_1^0(2420)\mathrm{K}^-$ channels

In the baseline amplitude model, the K-matrix amplitude is constructed considering the channels $\overline{\mathrm{D}}^0\mathrm{K}^-$ and $\mathrm{D}_1^0(2420)\mathrm{K}^-$. However, all channels which might contribute to the process should be included to obtain a correct description of the decay amplitude.

An additional channel which might be coupled to the $\mathrm{D}_{s1}^*(2700)$ and $\mathrm{D}_{s1}^*(2860)$ states is the $\mathrm{D}_1^0(2420)\mathrm{K}^-$, corresponding to a threshold placed at 2.914 GeV/c^2 in the $m(\Lambda_c^+\overline{\mathrm{D}}^0)$ invariant mass distribution. A complete description of the K-matrix amplitude should include all the three channels $\overline{\mathrm{D}}^0\mathrm{K}^-$, $\mathrm{D}^{*0}(2700)\mathrm{K}^-$ and $\mathrm{D}_1^0(2420)\mathrm{K}^-$. However, the amplitude model gets considerably more complex, and the amplitude fit does not converge properly. Therefore, the stability of the fit results is checked by defining a new amplitude model in which the $\mathrm{D}^{*0}(2007)\mathrm{K}^-$ channel in the K-matrix amplitude is replaced by the $\mathrm{D}_1^0(2420)\mathrm{K}^-$ one. The fit to data is then repeated. The resulting fit fractions are presented in Table 39. The projection of the fit in the $m(\Lambda_c^+\overline{\mathrm{D}}^0)$ invariant mass distribution is shown in Figure 52, compared to the baseline fit. Fit projections with a finer binning are proposed in Appendix A.2. The results are compatible with the baseline amplitude fit. Also, the latter better describes the structure at ~ 2.5 GeV/c^2, and in general it shows smaller uncertainties. Hence, including only the $\overline{\mathrm{D}}^0\mathrm{K}^-$ and $\mathrm{D}^*(2007)\mathrm{K}^-$ channels in the K-matrix amplitude is considered to be a good approximation.

Component	$\mathrm{D}^{*0}(2007)\mathrm{K}^-$ - $\overline{\mathrm{D}}^0\mathrm{K}^-$ channels	$\mathrm{D}_1^0(2420)\mathrm{K}^-$ - $\overline{\mathrm{D}}^0\mathrm{K}^-$ channels
$\mathrm{D}_{s0}^*(2317)$	0.099 ± 0.013	0.090 ± 0.023
$\mathrm{D_s}$ K-matrix	0.862 ± 0.029	0.873 ± 0.039
$\mathrm{D}_{s3}^*(2860)$	0.0181 ± 0.0077	0.0054 ± 0.0042
$\Xi_c^0(2790)$	0.0257 ± 0.0051	0.0255 ± 0.0067
Sum	1.0029 ± 0.0041	0.9943 ± 0.0047

Table 39: Comparison of the fit fractions obtained with the baseline amplitude model, and in the model where the $\mathrm{D}^{*0}(2007)\mathrm{K}^-$ channel has been replaced by the $\mathrm{D}_1^0(2420)\mathrm{K}^-$ channel in the K-matrix amplitude.

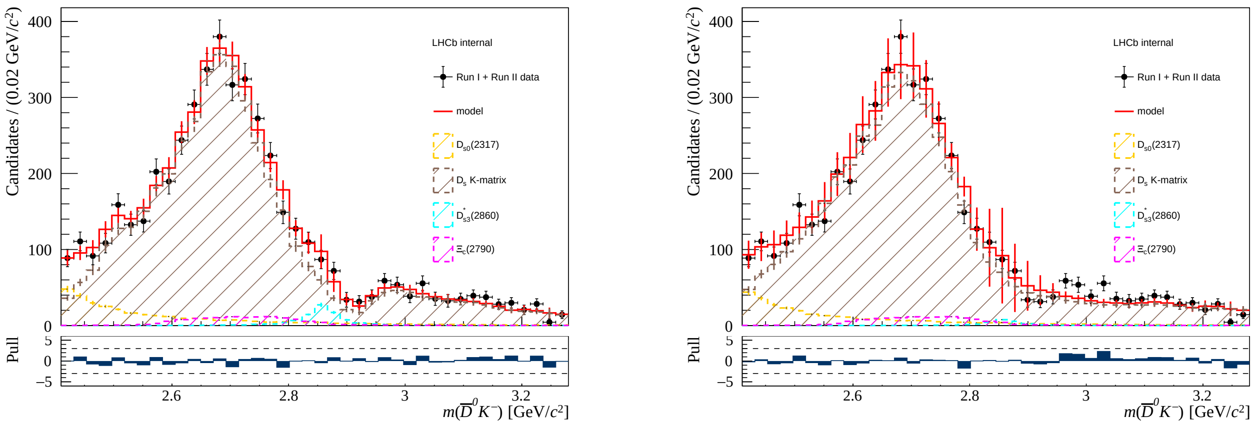

(a)

(b)

Figure 52: Projections of the amplitude fit over the $m(\Lambda_c^+\overline{\mathrm{D}}^0)$ invariant mass distribution. The $\mathrm{D}^{*0}(2007)\mathrm{K}^-$ channel of the baseline amplitude model (a) has been replaced by the $\mathrm{D}_1^0(2420)\mathrm{K}^-$ channel (b), in the K-matrix amplitude.

7.1.8 Measurement of eventual Λ_b^0 polarisation

Previous LHCb measurements of $\Lambda_b^0 \to J/\psi\Lambda$ decays did not find evidence for Λ_b^0 polarisation [125,126]. This is verified in this analysis. Eventual polarisation of the Λ_b^0 particle is taken into account by introducing additional parameters $P_{\lambda_{\Lambda_b^0},\lambda_{\Lambda_c^+}}$ which depend on the Λ_b^0 and Λ_c^+ helicity values. These parameters are included in the total matrix element of Equation 153, as follows:

$$M = \sum_{\lambda_{\Lambda_b^0},\lambda_{\Lambda_c^+}} P_{\lambda_{\Lambda_b^0},\lambda_{\Lambda_c^+}} \left| \sum_X \sum_{\lambda_X} M_{\lambda_X}^X \right|^2 \tag{160}$$

where the sums are running over the matrix elements describing the decay processes of the resonances X. It can be shown that in the $\Lambda_b^0 \to \Lambda_c^+ \overline{D}^0 K^-$ decays the polarisation factors of the Λ_b^0, Λ_c^+ are related by:

$$P_{\lambda_{\Lambda_b^0}=\pm1,\lambda_{\Lambda_c^+}=\pm1} = P_{\lambda_{\Lambda_b^0}=\mp1,\lambda_{\Lambda_c^+}=\mp1} \tag{161}$$

An amplitude model is constructed in which $P_{\lambda_{\Lambda_b^0}=1,\lambda_{\Lambda_c^+}=1} = P_{\lambda_{\Lambda_b^0}=-1,\lambda_{\Lambda_c^+}=-1}$ are set to unity, $P_{\lambda_{\Lambda_b^0}=1,\lambda_{\Lambda_c^+}=-1}$ is fitted and $P_{\lambda_{\Lambda_b^0}=\pm-1,\lambda_{\Lambda_c^+}=1}$ is constrained to be equal to it. Amplitude fits to data are performed, resulting in a Λ_b^0 polarisation factor:

$$P_{\lambda_{\Lambda_b^0}=1,\lambda_{\Lambda_c^+}=-1} = 1.03 \pm 0.10 \tag{162}$$

The result shows non significant Λ_b^0 polarisation, agreeing with the previous LHCb measurements.

7.1.9 Distributions of background data

Eventual peaking backgrounds can be identified by selecting pure-background candidates from the Λ_b^0 invariant mass sidebands, defined by the [5560, 5600] MeV/c^2, [5640, 5680] MeV/c^2 mass ranges. Figures 53-54 show the distributions of the angular, invariant mass and Dalitz variables from sidebands data. It is relevant to note that there are no clear structures visible neither in the $m(\Lambda_c^+ K^-)$ distribution, or in the Dalitz variables.

It is also useful to check eventual background structures generating in the s-weighted-background distributions, i.e. in the distributions of candidates weighted by the combinatorial background s-weights rather than by signal weights. Figures 55-56 show the amplitude variables and Dalitz plots of the s-weighted background candidates. Analogously to the previous case, no significant peaking structures arise in the distributions.

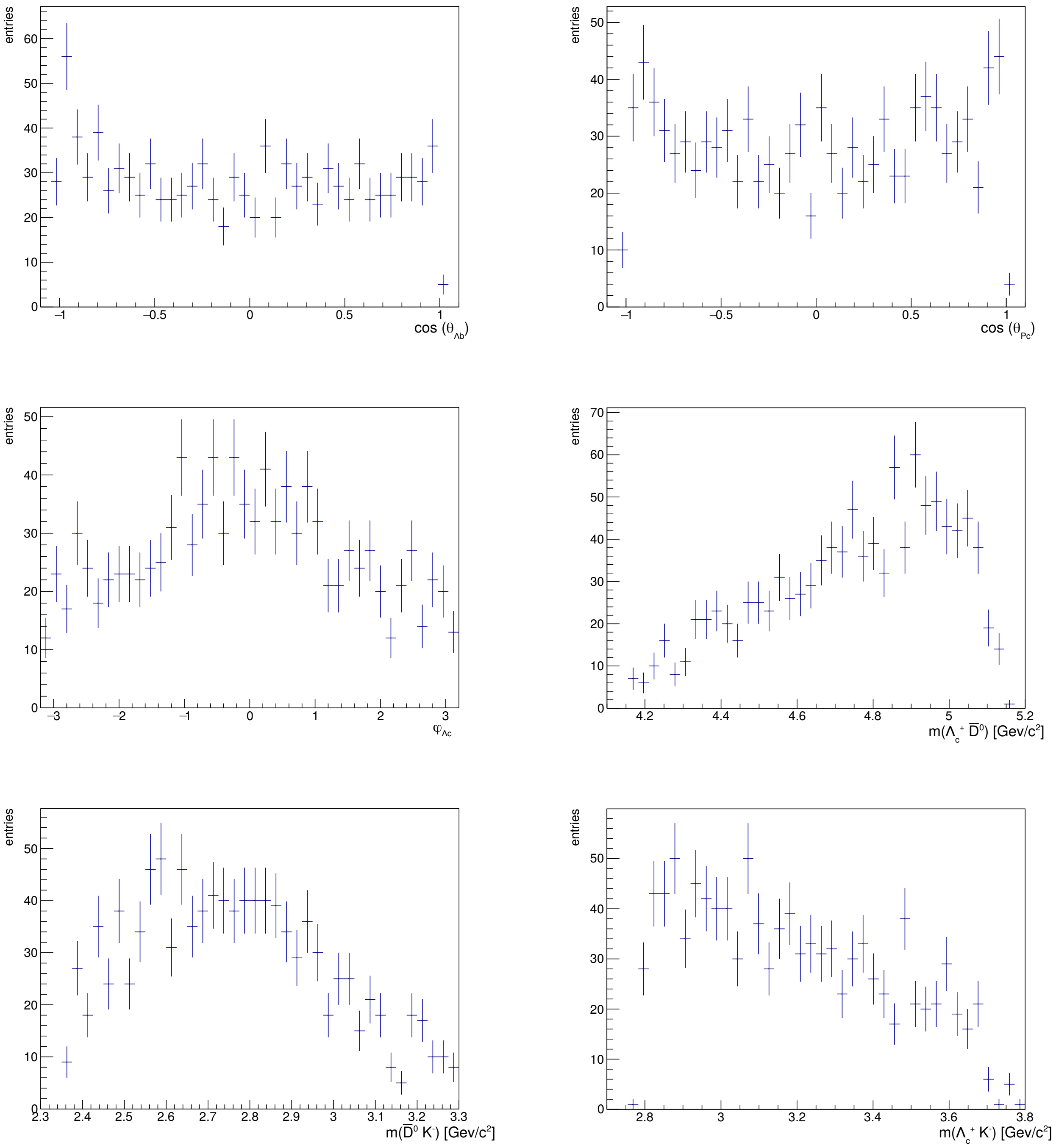

Figure 53: Angular and invariant mass distributions from sidebands candidates, defined by the [5560, 5600] MeV/c^2, [5640, 5680] MeV/c^2 ranges of the Λ_b^0 invariant mass distribution.

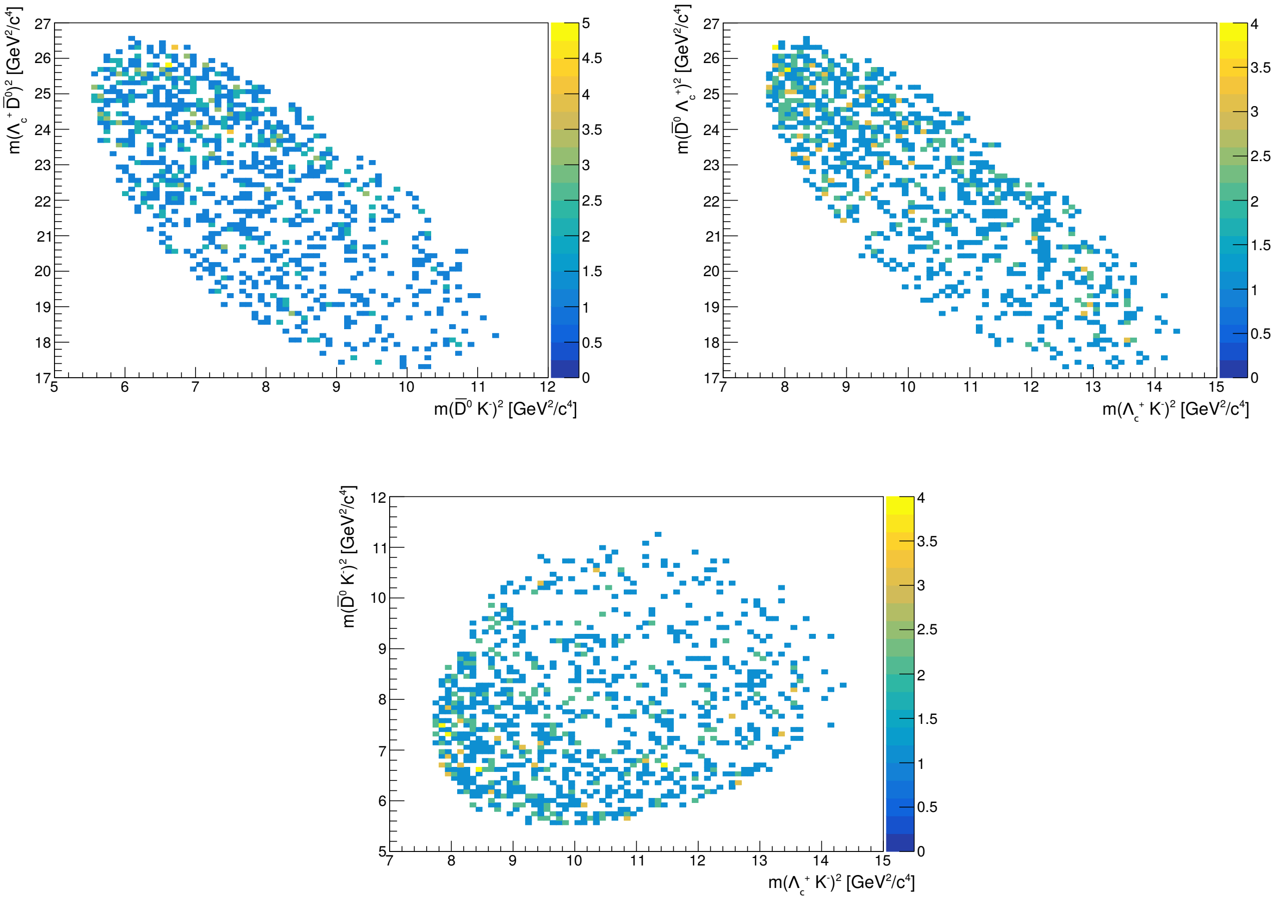

Figure 54: Distributions of the Dalitz variables from sidebands candidates.

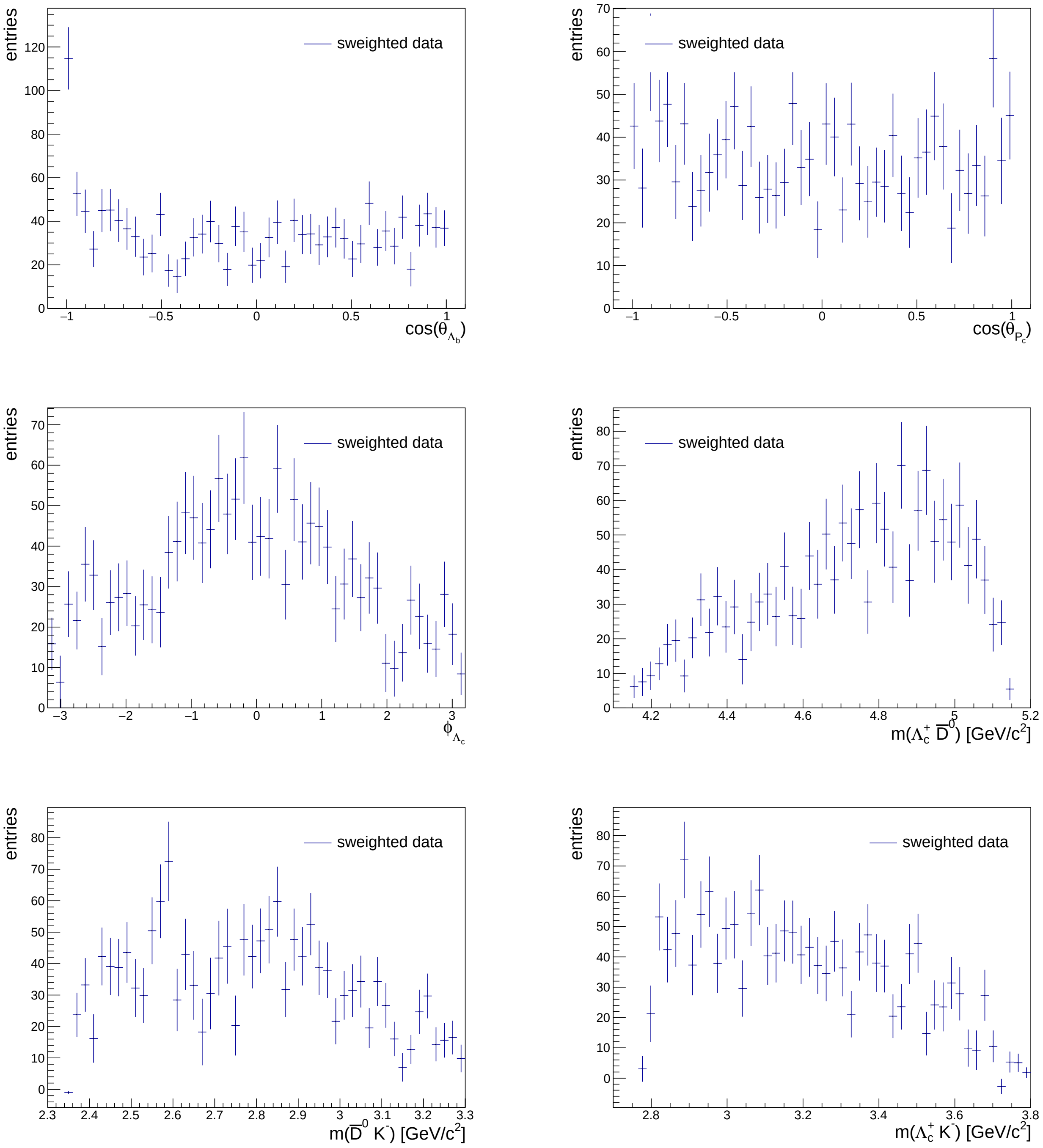

Figure 55: Angular and invariant mass distributions on s-weighted-background candidates.

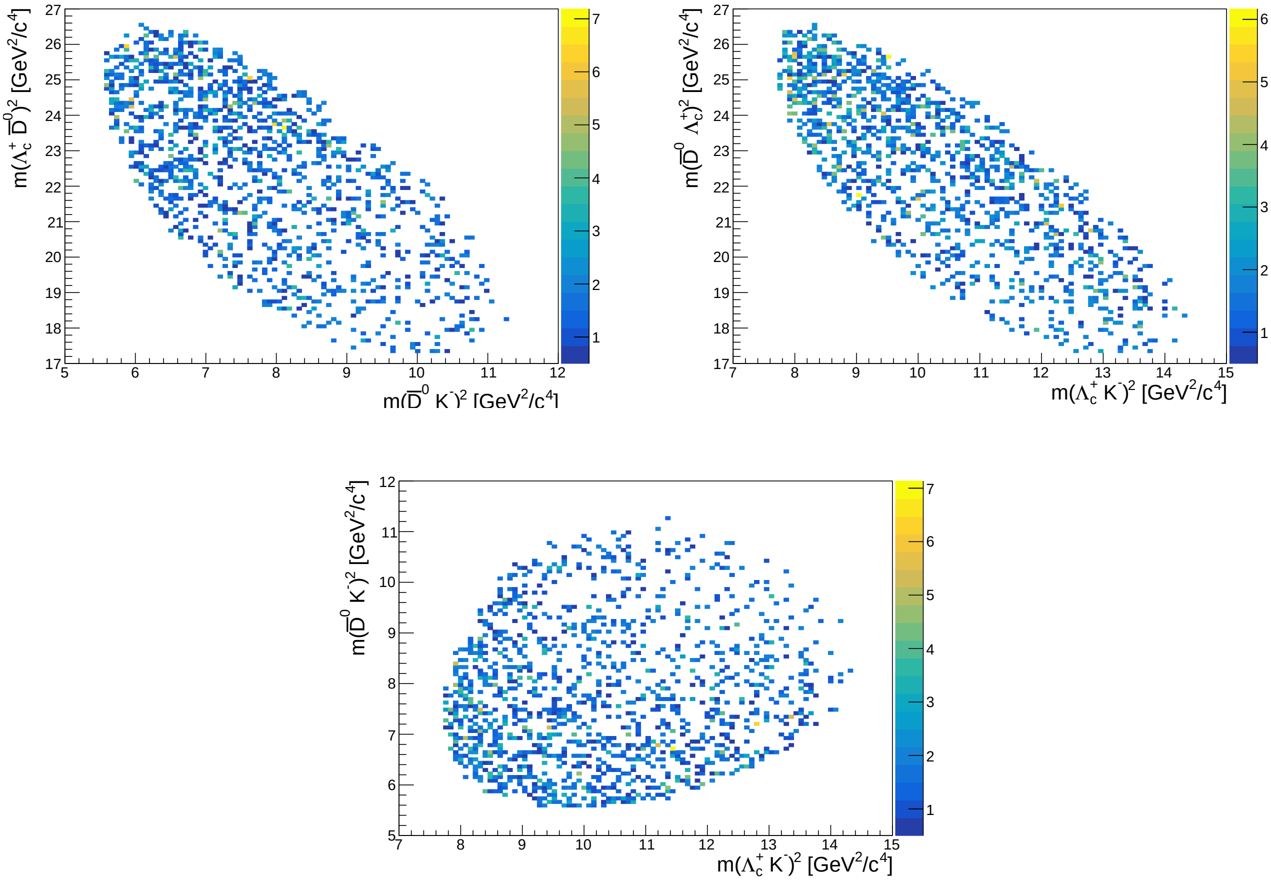

Figure 56: Distributions of the Dalitz variables on *s*-weighted-background candidates.

7.1.10 Check of the *s*-weighting procedure

The amplitude fit of this analysis relies on a previously-*s*-weighted data set, in which candidates have been categorised as signal- or background-like. As described in Section 3.2.3, in the *s*-weighting procedure the control variables, i.e. the Λ_b^0 invariant mass in this case, are assumed to be independent of the discriminating variables, which in this analysis are the $\Lambda_c^+\overline{D}^0$, $\Lambda_c^+K^-$ and $\overline{D}^0K^-$ invariant masses. This is checked by plotting the Λ_b^0 invariant mass distribution in equally-populated slices of the $\Lambda_c^+\overline{D}^0$, $\Lambda_c^+K^-$ and $\overline{D}^0K^-$ invariant mass projections, as shown in Figure 57.

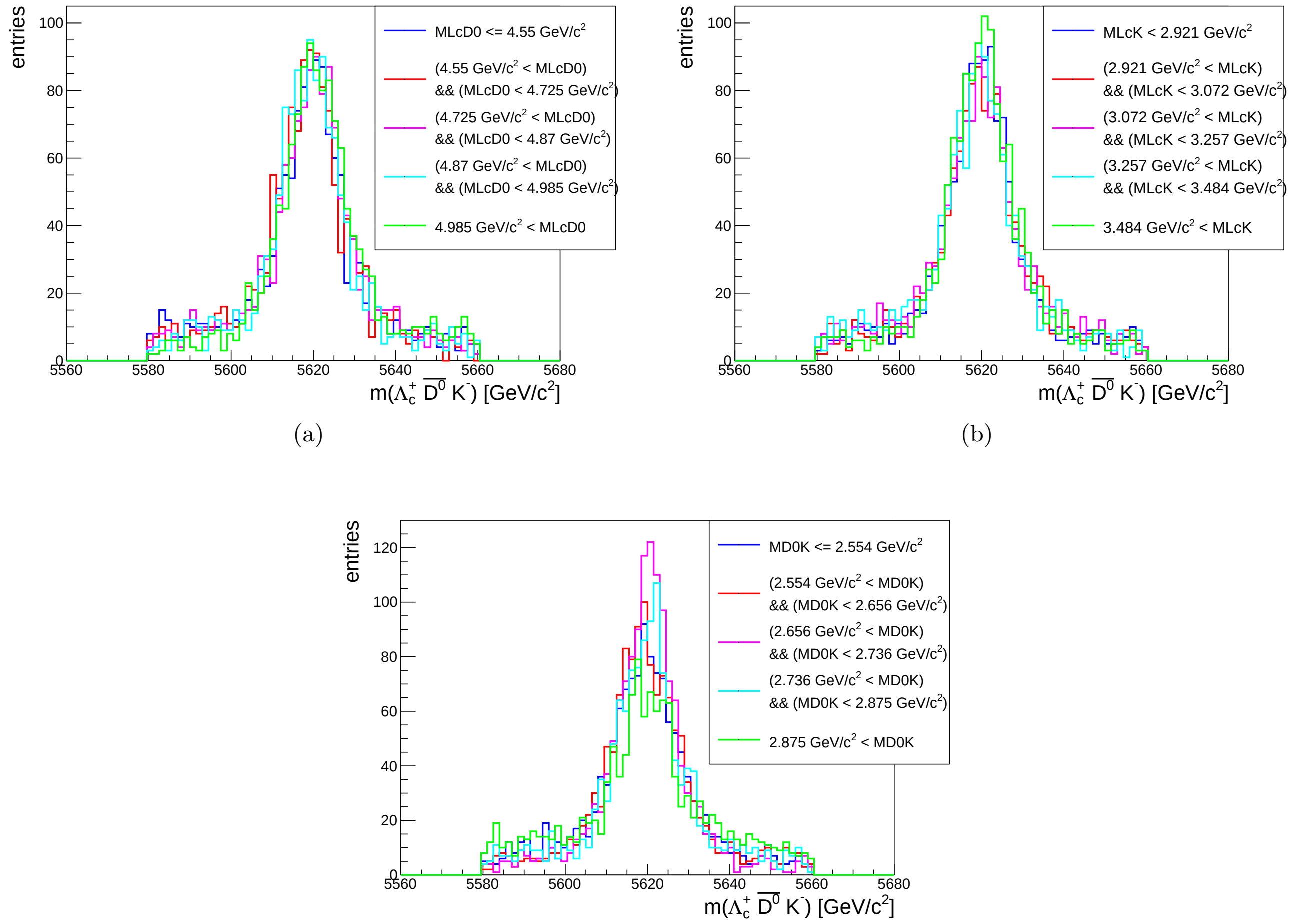

(a)

(b)

(c)

Figure 57: Λ_b^0 invariant mass distribution in equally-populated slices of the $\Lambda_c^+\overline{D}^0$ (a), $\Lambda_c^+K^-$ (b) and $\overline{D}^0K^-$ (c) invariant mass projections.

Under the assumption of the control variable being independent of the discriminating ones, the signal and background shapes of the Λ_b^0 invariant mass distribution in the above-mentioned slices should be comparable, thus should overlap. Nevertheless, the results show that the Λ_b^0 peaking shape differ in the $m(\overline{D}^0K^-) < 2.875$ GeV$/c^2$ and 2.656 GeV$/c^2 < m(\overline{D}^0K^-) < 2.736$ GeV$/c^2$ regions. Thus, the *s*-weighting procedure could in principle lead to problematic behaviours.

The validity of the *s*-weighting procedure is verified by removing background candidates from the sidebands of the Λ_b^0 invariant mass distribution. A tighter Λ_b^0 mass cut in the [5600, 5640] MeV$/c^2$ range is applied for this purpose. However, in this way combinatorial background candidates under the Λ_b^0 peaking shape are not removed from the data set. An amplitude fit to the resulting data set is performed without weighting candidates. The fit results are listed in Table 40, and the fit projections are shown in Figure 58. The amplitude fit describes the unweighted data sample reasonably well, given the presence of combinatorial background candidates which now are fitted as signal ones. Overall, the fit to the unweighted sample gives consistent results with the amplitude fit performed on the weighted sample, thus the *s*-weighting procedure is considered to work properly.

Component	Baseline weighted fit	unweighted fit
$\mathrm{D}^*_{\mathrm{s}0}(2317)$	0.099 ± 0.013	0.119 ± 0.080
$\mathrm{D_s}$ K-matrix	0.862 ± 0.029	0.854 ± 0.074
$\mathrm{D}^*_{\mathrm{s}3}(2860)$	0.0181 ± 0.0077	0.0136 ± 0.0083
$\Xi^0_\mathrm{c}(2790)$	0.0257 ± 0.0051	0.021 ± 0.013
Sum	1.0029 ± 0.0041	1.0072 ± 0.0061

Table 40: Fitted resonance fractions obtained *s*-weighting the data set, and with an unweighted amplitude fit.

7.1.11 Studies on the normalisation samples

As described in Section 6.2, the simulated samples used as normalisation of the signal *pdf* are generated with different detector conditions. In order to use them as a unique sample in the signal *pdf*, their consistency in shapes of the amplitude variables is checked. Figure 59 shows their distributions for all the simulated conditions. The samples show a good agreement in all the variables, allowing to merge them and use them together.

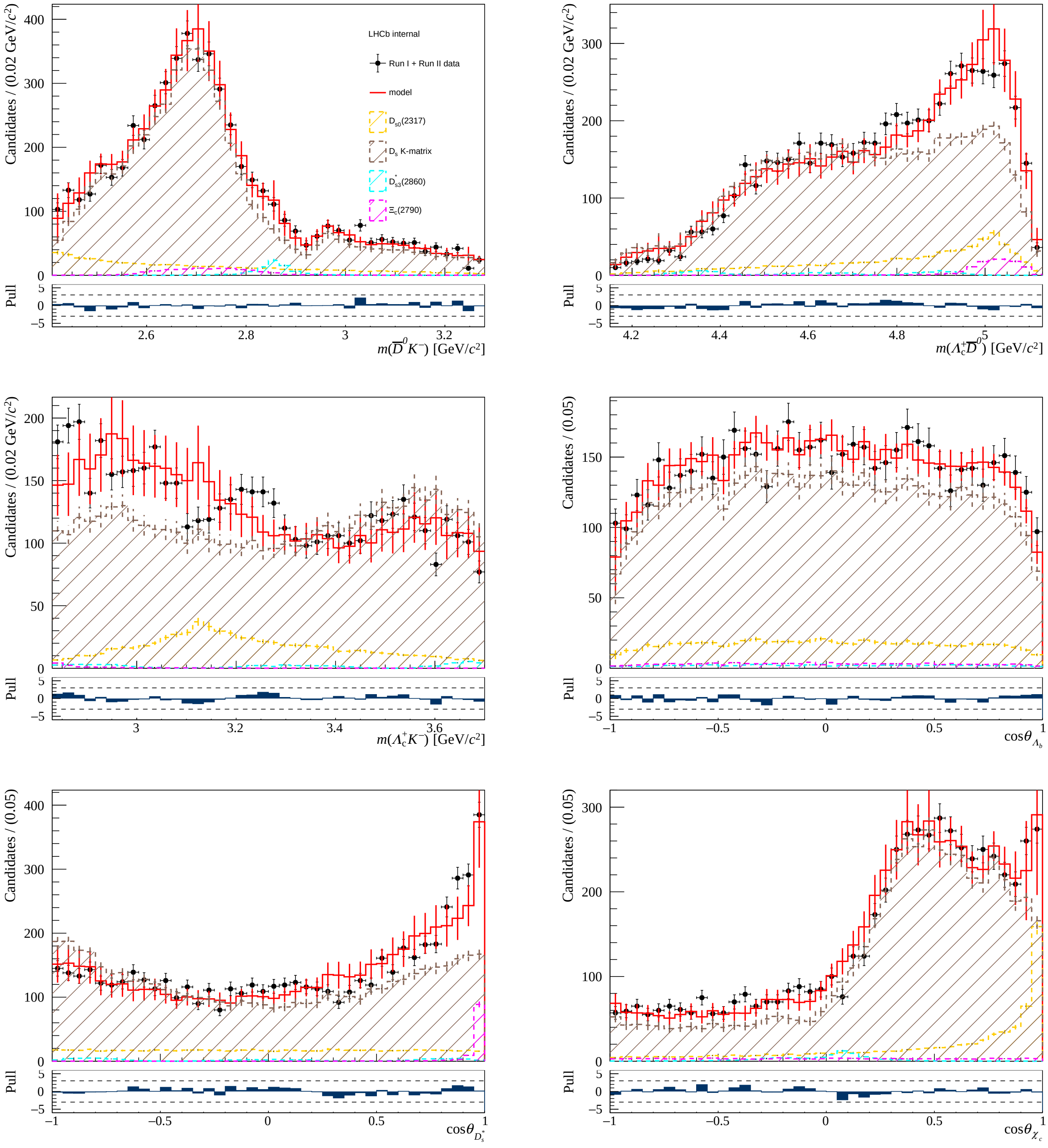

Figure 58: Projections of the amplitude fit to the unweighted data set.

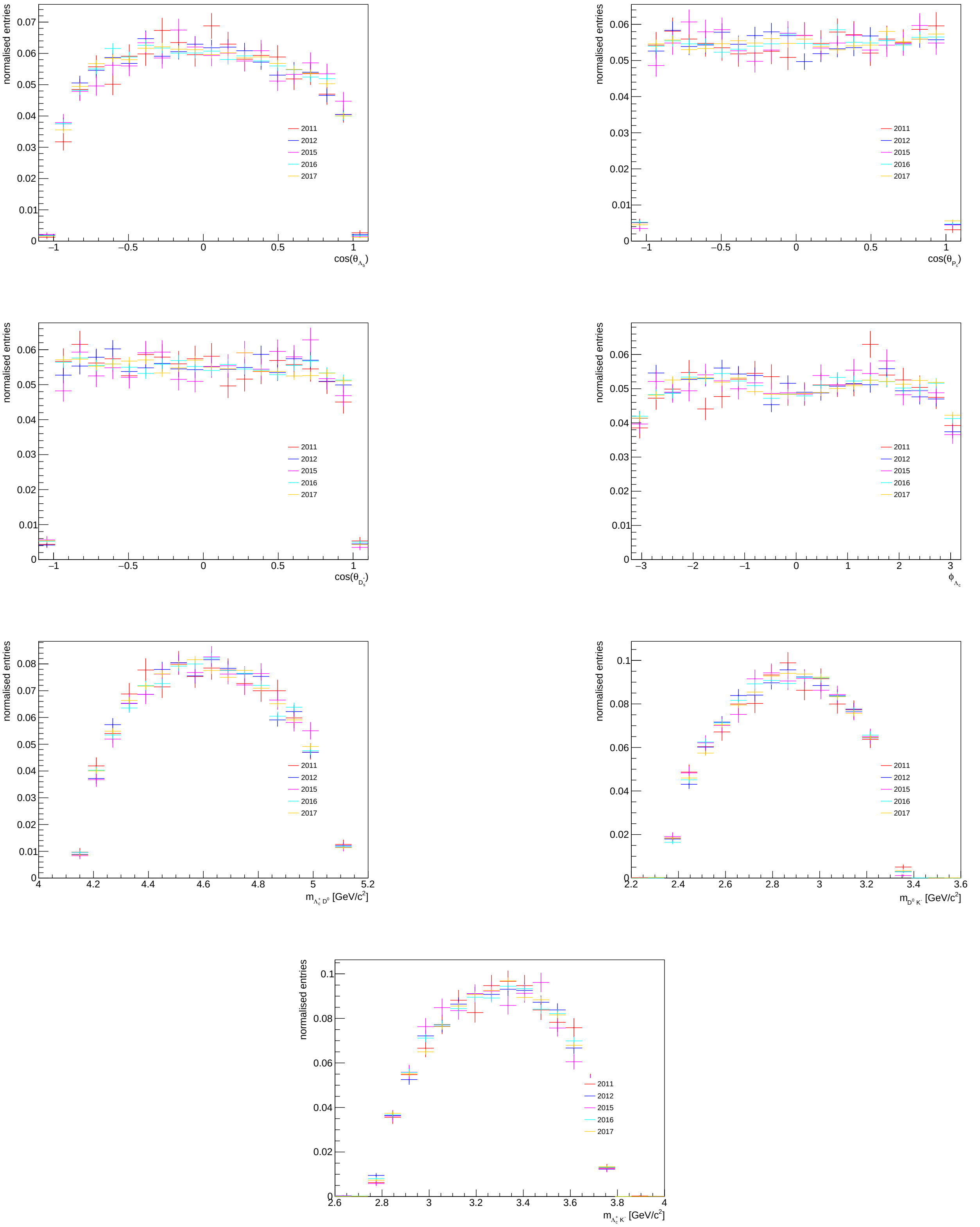

Figure 59: Distributions of the amplitude variables of the normalisation samples simulating different data taking conditions.

7.1.12 Fits to LHC Run 1 and Run 2 data sets

The amplitude fit presented in Chapter 6 is performed to data taken by LHCb during LHC Run 1 and Run 2, with different beam and data taking conditions. The results are checked by performing mass and amplitude fits to the LHC Run 1 and Run 2 data sets separately. The same mass and amplitude fit models are employed, as for the baseline fits. Figure 60 shows the mass fits to the two split data sets, and the fit results are reported in Table 41. Both the fit shapes and the results obtained from the two samples are in good agreement, and they are compatible within their uncertainties. In particular, the sum of the signal and background yields on the two split data sets is compatible with the results obtained on the full LHCb data set.

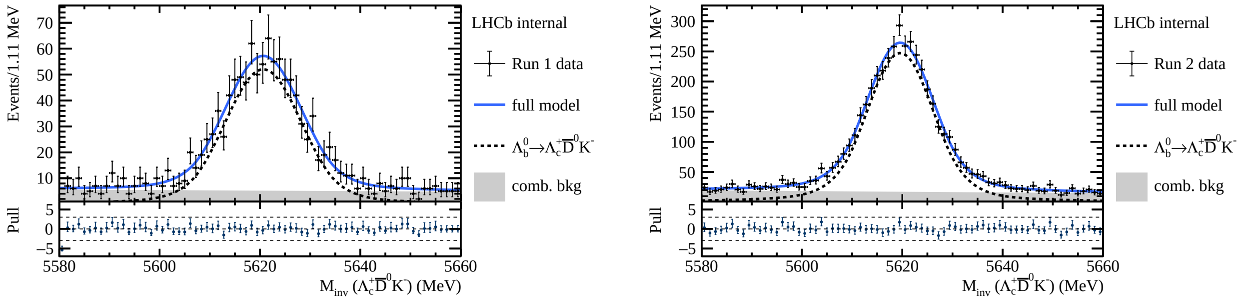

Figure 60: Fits to the $m(\Lambda_c^+\overline{D}^0K^-)$ invariant mass distribution for split LHC Run 1 (left) and Run 2 (right) data sets.

Fit parameter	Full data set	Run 1 data set	Run 2 data set
$N_{\Lambda_b^0}$	4971 ± 92	938 ± 41	4006 ± 81
N_{bkg}	1594 ± 71	376 ± 34	1244 ± 62
$\mu_{\Lambda_b^0}$	5619.78 ± 0.13	5620.66 ± 0.34	5619.59 ± 0.14
$\sigma_{\Lambda_b^0}$	6.84 ± 0.14	7.6 ± 0.34	6.65 ± 0.15
$\tau_{\Lambda_b^0}$	-0.0031 ± 0.0013	-0.0019 ± 0.0026	-0.0034 ± 0.0015

Table 41: Results of the fits to the $m(\Lambda_c^+\overline{D}^0K^-)$ invariant mass distribution for split LHC Run 1 and Run 2 data sets, compared to the fit results to the full LHCb data set.

Table 42 lists the fitted fit fractions over the two data sets. The results of the amplitude fits show good agreement between the split and combined data sets.

Component	Full data set	Run 1 data set	Run 2 data set
$D_{s0}^*(2317)$	0.099 ± 0.013	0.112 ± 0.036	0.096 ± 0.018
D_s K-matrix	0.862 ± 0.029	0.854 ± 0.054	0.853 ± 0.024
$D_{s3}^*(2860)$	0.0181 ± 0.0077	0.0245 ± 0.0083	0.0137 ± 0.0032
$\Xi_c^0(2790)$	0.0257 ± 0.0051	0.0155 ± 0.0082	0.0286 ± 0.0064
Sum	1.0029 ± 0.0041	1.0064 ± 0.0071	0.9911 ± 0.0049

Table 42: Comparison of the resonance fractions obtained by fitting the complete LHCb data set, and fitting the split Run 1 and Run 2 data sets.

7.2 Source of systematic uncertainties

The procedures followed to asses the systematic uncertainties on the results of this analysis are detailed in this Section. The resulting uncertainties are summarised in Section 7.3.

7.2.1 Size of the normalisation sample

The finite size of the normalisation sample used in the amplitude fit affects the precision on the results, representing a source of systematic uncertainty. The impact of such effect is evaluated by performing pseudo-experiments. One signal sample is simulated with the same amplitude model resulting from the amplitude fit to data, and with same number of signal candidates as in the data sample. Phase-space samples are generated with different sizes, and used as normalisation sample in the signal *pdf.* For a fixed number of normalisation events, 250 phase-space samples are generated with different generation seeds. Amplitude fits are performed to the signal sample afore-mentioned employing the same amplitude model used to fit the data, and different normalisation samples are used. The difference between the generated and fitted values of the resonance fractions and interference terms, relative to their generated values, are computed. Finally, the standard deviation of the above-mentioned distributions are plotted versus all the combination of signal and normalisation sample sizes. Figure 61 shows the obtained results for the fit fractions; the interference terms show similar dependence on the normalisation sample size.

The values obtained for the combination of 5,000 signal events and 89,000 normalisation events, which represent best the size of the samples used in the amplitude fit to data, are quoted as a systematic uncertainty due to the finite size of the normalisation sample. They are quoted in Tables 43-44.

7.2.2 Efficiency shapes of the selections based on Boosted Decision Trees classifiers and particle identification

The binning schemes of the *D-from-B* BDT and PID efficiency maps chosen to correct the signal *pdf* (Eq. 143) could affect the efficiency shapes. Hence, they represent sources of systematics uncertainties on the final results.

The systematic effects related to the *D-from-B* BDT efficiency binning are studied by varying the binning of the 2-dimensional *D-from-B* BDT efficiency map in the $\cos(\theta_{P_c})$ and $m(\Lambda_c^+\overline{D}^0)$ variables, from a 8x8 binning scheme to 22x22 bins in units of 2 bins. The default binning scheme used in the nominal amplitude fit is 15x15 bins. Amplitude fits are performed to data with the resulting efficiency look-up tables, making use of the default binning for the PID efficiency maps. The differences between the obtained results and the nominal fit fractions and interference terms are computed, and the standard deviation of their distributions are quoted as a systematic uncertainty to the BDT efficiency binning.

The effect of the PID efficiency binning is examined by creating efficiency look-up tables from the *PIDCalib* software package (Sec. 3.3.1) with different binning schemes in momentum and pseudo-rapidity of the bachelor K^-, and in the number of tracks of the events. Schemes from the 25x25x5 to the 35x35x5 binnings in steps of 5 bins in the first two variables, the momentum p and pseudo-rapidity η of the K^-, are investigated. The binning in the number of tracks is kept constant. The default binning in the nominal fit is 30x30x5 bins. For each of the above-mentioned binning schemes, the 2-dimensional efficiency maps in $\cos(\theta_{P_c})$ and $m(\Lambda_c^+\overline{D}^0)$ are binned from a 10x10 bins scheme to 20x20 bins in units of 2 bins, with 15x15 bins being the default scheme. Amplitude fits are performed to data with all combinations of the resulting PID efficiency maps, making use of the default *D-from-B* BDT efficiency look-up tables. The differences between the obtained results and the nominal fit fractions and interference terms are computed, and the standard deviation of their distributions are quoted as systematic uncertainty to the PID efficiency binning.

The systematic uncertainties of assigned to the efficiency shapes of the *D-from-B* BDT and PID selections are quoted in Tables 43-44.

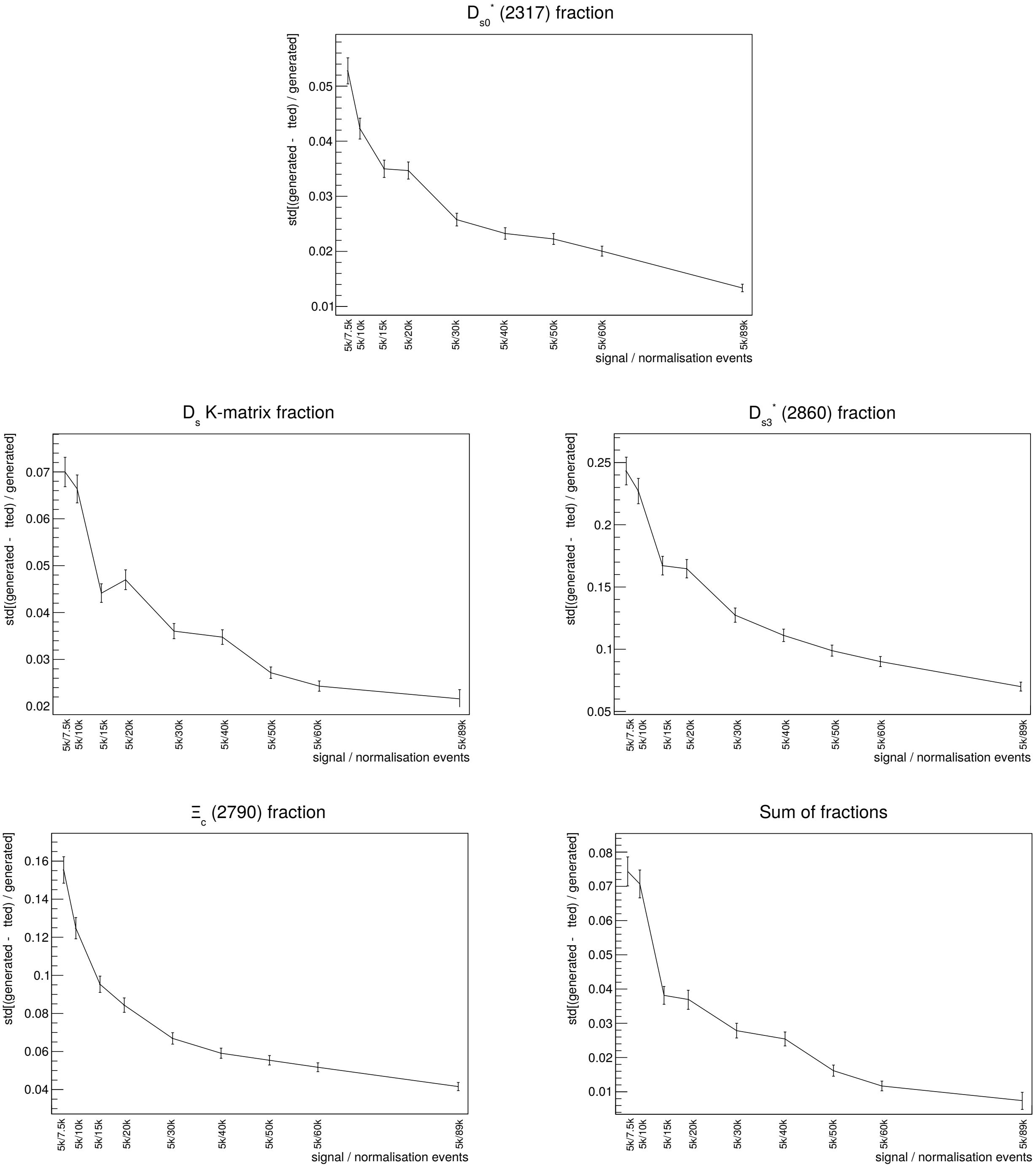

Figure 61: Distributions of the standard deviations of the difference between generated and fitted resonance fractions, depending on the size of the normalisation sample. The size of the signal sample is kept constant. The distributions are obtained from pseudo-experiments, in which the same amplitude model used to fit the data has been employed. The last points (to the right) of the distributions reflect the sizes of the signal and normalisation samples used in this analysis. They are quoted as a systematic uncertainty of the fit to data related to the finite size of the normalisation sample.

7.2.3 Line shape of the $D^*_{s0}(2317)$ state

The line shape of the $D^*_{s0}(2317)$ state is described in the baseline amplitude model by a Flatté distribution. An alternative parametrisation makes use of a sub-threshold Breit-Wigner distribution, where an effective pole mass $\tilde{m}$ is defined as in Equation 88, and it is used to evaluate the parameter p_0 in Equation 84. The rest of the line shape function keeps the same form as for the base relativistic Breit-Wigner shape used to describe over-threshold states. An amplitude fit with this alternative parametrisation of the $D^*_{s0}(2317)$ resonance is performed, and the fit projections are presented in Appendix A.7. The differences between these results and the baseline amplitude fit are quoted as systematic uncertainties on the measured fit fractions and interference terms. They are reported in Tables 43-44.

The quoted systematic uncertainties also include components of statistical errors, when assessed following the above-described method. A more precise evaluation would involve fits to pseudo-experiments. However, the values obtained are relatively small with respect the other contributions of systematic uncertainties, hence this effect is not considered relevant in this case.

7.2.4 Fit biases

The amplitude fit could in principle introduce biases in the measurements of the parameters, fit fractions and interference terms. Eventual fit biases are investigated by employing pseudo-experiments. The fitted parameters of the amplitude model are sampled in the uncorrelated space following the same method introduced in Section 6.4, and 250 models are defined accordingly. For each of them, a pseudo-experiment is performed generating signal and normalisation samples with same number of candidates as in the fit to data. The generated samples are fitted using the baseline amplitude model. The distributions of the differences between the generated and fitted quantities are computed. The mean values of such distributions represent the fit biases on the parameters under interest, and are quoted in Tables 43-44. Once the fit biases are known, the fit results can be corrected for them. However, additional systematics uncertainties would be introduced by this correction procedure. Since the measured fit biases are small relatively to the absolute values of the fitted quantities, the fit biases themselves are quoted as systematic uncertainties.

7.3 Systematic uncertainties

A summary of the systematic uncertainties is presented in Tables 43-44 for the fit fractions and the interference terms, respectively. The uncertainty related to the normalisation sample size is the most relevant for the K-matrix contribution and for the $D^*_{s0}(2317)$ fit fraction. However, it could be easily reduced by employing simulated samples of larger size. The uncertainties assigned to the *D-from-B* BDT and PID efficiency shapes are the leading ones for the $D^*_{s3}(2860)$ and $\Xi^0_c(2790)$ fit fractions. It is believed that there is room for improvement on them. The estimated fit biases are the least contributing to the systematic uncertainties, for all the states.

The individual systematic uncertainties are assumed to be uncorrelated and summed in quadrature, leading to the final results presented in Tables 45-46. All interference terms are compatible with zero. The resonance fit fractions are limited by the statistical uncertainties, apart by the $D^*_{s0}(2317)$ contribution which have statistical and systematic errors of the same order.

Fit fraction	Fitted value	Norm. sample size	BDT eff. shape	PID eff. shapes	$\mathrm{D}^{*}_{\mathrm{s}0}(2317)$ line shape	Fit biases
$\mathrm{D}^{*}_{\mathrm{s}0}(2317)$	0.099	0.014	0.003	0.003	0.0008	0.0002
$\mathrm{D_s}$ K-matrix	0.862	0.018	0.005	0.003	0.007	0.01
$\mathrm{D}^{*}_{\mathrm{s}3}(2860)$	0.0181	0.0009	0.0005	0.0009	0.0004	0.0002
$\Xi^{0}_{\mathrm{c}}(2790)$	0.0257	0.0001	0.0034	0.0015	0.0005	0.0012
Sum	1.0029	0.0100	0.0022	0.0031	0.0080	0.0044

Table 43: Fitted values of the fit fractions and list of systematic uncertainties.

Interference term	Fitted value	Norm. sample size	BDT eff. shape	PID eff. shapes	$\mathrm{D}^{*}_{\mathrm{s}0}(2317)$ line shape	Fit biases
$\mathrm{D}^{*}_{\mathrm{s}0}(2317)$ - $\mathrm{D_s}$ K-matrix	-0.012	0.0002	0.000002	0.00002	0.0006	0.0003
$\mathrm{D}^{*}_{\mathrm{s}0}(2317)$ - $\mathrm{D}^{*}_{\mathrm{s}3}(2860)$	0.00006	0.00003	0.0002	0.00354	0.000003	0.000003
$\mathrm{D}^{*}_{\mathrm{s}0}(2317)$ - $\Xi^{0}_{\mathrm{c}}(2790)$	-0.0059	0.00001	0.0002	0.0029	0.0007	0.000005
$\mathrm{D_s}$ K-matrix - $\mathrm{D}^{*}_{\mathrm{s}3}(2860)$	-0.00015	0.00013	0.000005	0.00012	0.000007	0.00001
$\mathrm{D_s}$ K-matrix - $\Xi^{0}_{\mathrm{c}}(2790)$	0.0059	0.0007	0.0002	0.0014	0.0099	0.0005
$\mathrm{D}^{*}_{\mathrm{s}3}(2860)$ - $\Xi^{0}_{\mathrm{c}}(2790)$	0.0021	0.0006	0.00006	0.0017	0.0006	0.0002

Table 44: Fitted values of the interference terms and list of systematic uncertainties.

Component	Fit fraction
$\mathrm{D}^{*}_{\mathrm{s}0}(2317)$	0.099 ± 0.013 (stat.) ± 0.015 (syst.)
$\mathrm{D_s}$ K-matrix	0.862 ± 0.029 (stat.) ± 0.022 (syst.)
$\mathrm{D}^{*}_{\mathrm{s}3}(2860)$	0.0181 ± 0.0077 (stat.) ± 0.0014 (syst.)
$\Xi^{0}_{\mathrm{c}}(2790)$	0.0257 ± 0.0051 (stat.) ± 0.0039 (syst.)
Sum	1.0029 ± 0.0041 (stat.) ± 0.0141 (syst.)

Table 45: Fit fractions with statistical and systematic uncertainties.

	$\mathrm{D_s}$ K-matrix	$\mathrm{D}^{*}_{\mathrm{s}3}(2860)$	$\Xi^{0}_{\mathrm{c}}(2790)$
$\mathrm{D}^{*}_{\mathrm{s}0}(2317)$	-0.012 ± 0.015 (stat.) ± 0.0007 (syst.)	0.00006 ± 0.00079 (stat.) ± 0.00356 (syst.)	-0.0059 ± 0.0021 (stat.) ± 0.0030 (syst.)
$\mathrm{D_s}$ K-matrix	/	-0.00015 ± 0.00053 (stat.) ± 0.01612 (syst.)	0.0059 ± 0.0099 (stat.) ± 0.0101 (syst.)
$\mathrm{D}^{*}_{\mathrm{s}3}(2860)$	/	0.0021 ± 0.0013 (stat.) ± 0.0019 (syst.)	

Table 46: Fitted interference terms between the components of the amplitude model.

8 Search for pentaquark states

Amplitude fits neglecting any contributions from eventual pentaquark states have been performed so far. This Chapter presents the statistical tests performed to asses the significance for the observation of pentaquark states in $\Lambda_b^0 \to \Lambda_c^+ \overline{D}^0 K^-$ decays. Pentaquark candidates with same properties as observed in $\Lambda_b^0 \to J/\psi p K^-$ decays [1, 2] are tested The possible presence of hidden-charm pentaquark states are investigated in Section 8.4.

8.1 Expectations from the theory models

It is possible to estimate the number of reconstructed $P_c(4380)^+$ and $P_c(4450)^+$ pentaquark candidates that are expected to be observed in the $\Lambda_b^0 \to \Lambda_c^+ \overline{D}^0 K^-$ channel, using the theoretical predictions for their decay widths (Sec. 1.4, Tab. 4, [39]), and the measured properties from their first observation [1]. Assuming the theory model presented in Section 1.4 to be valid, a naïve extrapolation of the reconstructed P_c yields in the data set used in this analysis is given by:

$$\begin{aligned} N_{P_c,9.1fb^{-1}}(\Lambda_b^0 \to \Lambda_c^+ \overline{D}^0 K^-) = & \frac{\mathcal{B}_{th}(P_c \to \Lambda_c^+ \overline{D}^0)}{\mathcal{B}_{th}(P_c \to J/\psi p)} \cdot \frac{N_{9.1fb^{-1}}(\Lambda_b^0 \to \Lambda_c^+ \overline{D}^0 K^-)}{N_{3fb^{-1}}(\Lambda_b^0 \to J/\psi K^- p)} \\ & \cdot \frac{\mathcal{B}(\Lambda_b^0 \to J/\psi K^- p)}{\mathcal{B}(\Lambda_b^0 \to \Lambda_c^+ \overline{D}^0 K^-)} \cdot N_{P_c,3fb^{-1}}(\Lambda_b^0 \to J/\psi K^- p) \end{aligned} \tag{163}$$

where the ratio of the B_{th} terms represents the predicted relative branching fractions of the P_c states decaying in $\Lambda_c^+ \overline{D}^0$ and $J/\psi p$ as presented in Table 4. The yield of reconstructed candidates for a specific decay, at a given integrated luminosity, is represented by the $N_{lumi}(decay)$ term. The $N_{P_c,lumi}(decay)$ factor is the number of observed P_c candidates for the specified decay and integrated luminosity. In particular, $N_{P_c,3fb^{-1}}(\Lambda_b^0 \to J/\psi K^- p)$ is derived from:

$$N_{P_c,3fb^{-1}}(\Lambda_b^0 \to J/\psi K^- p) = \mathcal{F}_{P_c,3fb^{-1}}(\Lambda_b^0 \to J/\psi K^- p) \cdot N_{\Lambda_b^0 \to J/\psi K^- p,3fb^{-1}} \tag{164}$$

with $\mathcal{F}_{P_c,3fb^{-1}}(\Lambda_b^0 \to J/\psi K^- p)$ being the fit fraction of the P_c state measured in its first observation. Using values $N_{3fb^{-1}}(\Lambda_b^0 \to J/\psi K^- p) = 26,000$, $N_{9.1fb^{-1}}(\Lambda_b^0 \to \Lambda_c^+ \overline{D}^0 K^-) = 5,000$, $\mathcal{F}_{P_c(4380)^+,3fb^{-1}}(\Lambda_b^0 \to J/\psi K^- p) = 4.2\%$, $\mathcal{F}_{P_c(4450)^+,3fb^{-1}}(\Lambda_b^0 \to J/\psi K^- p) = 8.1\%$, $\mathcal{B}(\Lambda_b^0 \to J/\psi K^- p) = 3.2 \cdot 10^{-4}$ and $\mathcal{B}(\Lambda_b^0 \to \Lambda_c^+ \overline{D}^0 K^-) = 1.5 \cdot 10^{-3}$, it is possible to estimate the yields of the $P_c(4380)^+$ and $P_c(4450)^+$ states expected to be reconstructed in the data sample of this analysis. The estimated yields and corresponding fit fractions are presented in Table 47. These are basic extrapolations which might be not precise and affected by uncertainties. Nevertheless, the molecular model presented in Section 1.4 would expect a significant pentaquark signal in the $\Lambda_b^0 \to \Lambda_c^+ \overline{D}^0 K^-$channel. Hence, the reconstructed yield of the P_c states in the data sample of this analysis are the most relevant quantity for the statistical tests.

8.1.1 Amplitude model with pentaquark states

A variety of hypotheses concerning the possible decays of pentaquark states in the $\Lambda_b^0 \to \Lambda_c^+ \overline{D}^0 K^-$ channel are investigated employing profile likelihood ratio tests, as presented in Section 3.2.5.

Model	$P_c(4380)^+, J^P = \frac{3}{2}^-$	$P_c(4450)^+, J^P = \frac{3}{2}^-$	$P_c(4450)^+, J^P = \frac{5}{2}^+$
$\Sigma_c^*\overline{D}$	29 / 0.6%	-	-
$\overline{D}^*\Sigma_c$	185 / 3.6%	222 / 4.3%	419 / 8.2%

Table 47: Expected yields and fit fractions of the $P_c(4380)^+$ and $P_c(4450)^+$ states in the data sample of this analysis, following the predictions by the $\Sigma_c^*(2520)\overline{D}$ and $\Sigma_c(2455)\overline{D}^*$ molecular models [39].

First, the hypotheses of having independent contributions of the $P_c(4380)^+$, $P_c(4450)^+$, $P_c(4312)^+$, $P_c(4440)^+$, $P_c(4457)^+$ states in the $\Lambda_b^0 \to \Lambda_c^+\overline{D}^0K^-$ channel are studied. The properties measured in the respective first observations (Tables 2-3) are used to characterise these states. Only upper limits have been assigned to the widths of the $P_c(4312)^+$, $P_c(4440)^+$, $P_c(4457)^+$ states, and their upper boundaries are quoted as width values here.

Secondly, the hypotheses of having both the $P_c(4380)^+$ and $P_c(4450)^+$, or the $P_c(4312)^+$, $P_c(4440)^+$ and $P_c(4457)^+$ contributions, are investigated. The relative fit fractions between the states are fixed to what has been measured in their first observations [1]- [2].

The matrix elements of the P_c states are build analogously to what has been done in Chapter 6 for the other resonances, and are added coherently to the complete matrix element (Eq. 153). The B_{LS} couplings of the Λ_b^0 and P_c decays are listed in Table 48. Only the partial waves corresponding to the lowest values allowed of the orbital angular momentum are considered. From [2], the J^P assignments of the $P_($4440$)^+$ and $P_c(4457)^+$ states are not uniquely determined, and values $J^P = \frac{1}{2}^-, \frac{3}{2}^-$ are considered plausible: in the following, both the hypotheses are tested.

Decay	B_{LS} couplings
$\Lambda_b^0 \to P_c(4380)^+K^-$	$B_{1,\frac{3}{2}}^{\Lambda_b^0\to P_c(4380)^+K^-}$, $B_{2,\frac{1}{2}}^{P_c(4380)^+\to\Lambda_c^+\overline{D}^0}$
$\Lambda_b^0 \to P_c(4450)^+K^-$	$B_{2,\frac{5}{2}}^{\Lambda_b^0\to P_c(4450)^+K^-}$, $B_{3,\frac{1}{2}}^{P_c(4450)^+\to\Lambda_c^+\overline{D}^0}$
$\Lambda_b^0 \to P_c(4312)^+K^-$	$B_{0,\frac{1}{2}}^{\Lambda_b^0\to P_c(4312)^+K^-}$, $B_{0,\frac{1}{2}}^{P_c(4312)^+\to\Lambda_c^+\overline{D}^0}$
$\Lambda_b^0 \to P_c(4440)^+K^-$, $J^P(P_c(4440)^+) = \frac{1}{2}^-$	$B_{0,\frac{1}{2}}^{\Lambda_b^0\to P_c(4440)^+K^-}$, $B_{0,\frac{1}{2}}^{P_c(4440)^+\to\Lambda_c^+\overline{D}^0}$
$\Lambda_b^0 \to P_c(4440)^+K^-$, $J^P(P_c(4440)^+) = \frac{3}{2}^-$	$B_{1,\frac{3}{2}}^{\Lambda_b^0\to P_c(4440)^+K^-}$, $B_{2,\frac{1}{2}}^{P_c(4440)^+\to\Lambda_c^+\overline{D}^0}$
$\Lambda_b^0 \to P_c(4457)^+K^-$, $J^P(P_c(4457)^+) = \frac{1}{2}^-$	$B_{0,\frac{1}{2}}^{\Lambda_b^0\to P_c(4457)^+K^-}$, $B_{0,\frac{1}{2}}^{P_c(4457)^+\to\Lambda_c^+\overline{D}^0}$
$\Lambda_b^0 \to P_c(4457)^+K^-$, $J^P(P_c(4457)^+) = \frac{3}{2}^-$	$B_{1,\frac{3}{2}}^{\Lambda_b^0\to P_c(4457)^+K^-}$, $B_{2,\frac{1}{2}}^{P_c(4457)^+\to\Lambda_c^+\overline{D}^0}$

Table 48: Couplings of the decays including P_c contributions.

8.2 Likelihood ratio test implementation

Profile likelihood ratio tests are performed, as introduced in Section 3.2.5. They are employed to build confidence belts which allow to determine either confidence intervals for the observation of pentaquark states, or upper limits. A variety of methods have been developed to perform such statistical tests. Particular popular are asymptotic methods such as described in [83]. However they are not well suited for this analysis, since the observable under test, namely the yield (i.e. the fit fraction) of pentaquark candidates in the data set, are derived from the fitted parameters in a non-straightforward way. Therefore, an alternative approach must be followed.

A pseudo-experiment is performed, and a sample is generated with the same amplitude model as fitted to the data from Table 32. On top of the states fitted to data, a pentaquark contribution with a given contribution f_{P_c} is added. An amplitude fit to such a sample is performed, with the same amplitude model used to fit the data but with the addition of the pentaquark contribution. The maximum likelihood estimator used as denominator in the likelihood ratio (Eq. 53) is obtained by fitting the B_{LS} couplings of the pentaquark contribution. As said in Section 8.1.1, pentaquarks with properties as measured in [1, 2] are tested, thus their mass and width values are not fitted here. The constrained likelihood fits (representing the numerator of the likelihood ratio in Equation 53) are performed on the same simulated sample, but now fixing the couplings of the pentaquark component. This translates into fixing the contribution $\tilde{f}_{P_c}$ of the P_c signal. Scanning a range of values $\tilde{f}_{P_c}$ over a physically-allowed region, the *pdf* distribution of the likelihood ratio, given the *true value* f_{P_c}, is obtained and the statistical test can be performed.

The above-described procedure is used to build confidence belts as introduced in Section 3.2.5. In fact, this method allows to determine a single horizontal slice of the confidence, corresponding to the *true value* of the pentaquark contribution f_{P_c}. A complete confidence belt can be constructed by iterating this procedure for many values of f_{P_c}, which corresponds to scan the confidence belt in slices.

However, some “technical issues” arise when applying this procedure to the specific case of this analysis. First, as already said the observable of interest, namely the pentaquark fit fraction, is not directly fit but it is derived from the fitted B_{LS} couplings of the pentaquark component. Therefore, the likelihood ratio has to be profiled in the couplings, and the result translated into values of fit fractions. More importantly, the free parameters which are needed to describe a single pentaquark contribution are four, namely the magnitudes and phases (or real and imaginary parts) of the two B_{LS} couplings per P_c state, as listed in Table 48. The same reasoning applies when testing hypotheses involving more than one P_c state, for which the number of P_c fit parameters increases linearly. Despite the fact that in principle it is possible to profile the likelihood ratio in a multi-dimensional space, in fact this would dramatically increase the computational resources required to perform the statistical tests with respect to a one-dimensional profiling.

To overcome the difficulties of performing multi-dimensional tests, an approximated method is followed. Let us consider testing the hypothesis of observing an individual pentaquark state in the $\Lambda_{\mathrm{b}}^0 \to \Lambda_{\mathrm{c}}^+ \overline{\mathrm{D}}{}^0 \mathrm{K}^-$ channel. An amplitude fit to the data is first performed including the pentaquark contribution of interest, and fitting the magnitude and phases of the related couplings. Then, the ratio of the two magnitudes $\tilde{m}$ and the difference between the two phases $\tilde{\phi}$ of the P_c contribution are taken:

$$\begin{aligned} \tilde{m} &\equiv \frac{mag_{\Lambda_{\mathrm{b}}^0}}{mag_{P_c}} \\ \tilde{\phi} &\equiv \phi_{\Lambda_{\mathrm{b}}^0} - \phi_{P_c} \end{aligned} \tag{165}$$

where the Λ_{b}^0 and P_c subscripts indicate the components of the B_{LS} couplings for the Λ_{b}^0 and the P_c decays, respectively. The likelihood ratio is finally profiled in $\tilde{m}$, keeping constant $\tilde{\phi}$. In this way the likelihood ratio is profiled in only one dimension, and in a quantity which is directly related to the pentaquark fit fraction.

A similar approach is followed in case of testing the hypothesis of multiple pentaquark signals, such as the joint presence of the $P_c(4438)^+$ and $P_c(4450)^+$ or of the $P_c(4312)^+$, $P_c(4440)^+$ and $P_c(4457)^+$ states. First, amplitude fits are performed to data fitting all the parameters of the P_c states. The ratios of the magnitudes $\tilde{m}_i$ and phases $\tilde{\phi}_i$ of the couplings are considered, for each of the ith pentaquark contribution. The ratios $\tilde{\phi}_i$ are kept fixed similarly to the previous case. The ratios $\tilde{m}_i$ are now constrained in such a way to obtain relative fit fractions of the P_c candidates similar to what has been measured in [1] for the $P_c(4438)^+$ and $P_c(4450)^+$ states and in [2] for the $P_c(4312)^+$, $P_c(4440)^+$ and $P_c(4457)^+$ states. Once the ratios $\tilde{m}_i$ are fixed relatively to each others, their absolute scaling is varied and used to profile the likelihood ratio. In this way confidence belts can be build for testing the hypotheses of observing the $P_c(4438)^+$ and $P_c(4450)^+$ or the $P_c(4312)^+$, $P_c(4440)^+$ and $P_c(4457)^+$ states with relative fractions as measured in [1,2].

8.3 Hypothesis testing

The presence of the $P_c(4380)^+$ and $P_c(4450)^+$ states in $\Lambda_b^0 \to \Lambda_c^+\overline{D}^0K^-$ decays is tested first. Table 49 reports the results of amplitude fits to data in the hypotheses of having one P_c only at time, and in the case of adding both of them. The mass, width and spin assignments are fixed to the values reported in Table 2, as measured in their first observation [1]. To describe the other states, the baseline amplitude model used to fit the data in Chapter 6 is used. The fit projections over the $m(\Lambda_c^+\overline{D}^0)$ invariant mass distribution are shown in Figure 62.

Hypothesis	$P_c(4380)^+$ fit fraction	$P_c(4450)^+$ fit fraction
$P_c(4380)^+$ only	$0.0018^{+0.0022}_{-0.0018}$	/
$P_c(4450)^+$ only	/	$0.0023^{+0.0025}_{-0.0023}$
$P_c(4380)^+$ and $P_c(4450)^+$	$0.0023^{+0.0032}_{-0.0023}$	$0.00015^{+0.00021}_{-0.00015}$

Table 49: Fitted values of the $P_c(4380)^+$ and $P_c(4450)^+$ fit fractions, for different hypotheses. Only the statistical uncertainties are shown.

Amplitude fits to the data are performed adding independently the two states to the amplitude model, and the ratios of magnitudes and differences of phases (Eq. 165) of the couplings are determined. About twenty pseudo-experiments are performed generating samples and varying uniformly the ratio of the couplings magnitude $\tilde{m}$ of the pentaquark candidate under test, as described in the previous section. This corresponds to making hypotheses about a range of P_c fractions. For each of them, one unconstrained-likelihood fit is performed fitting the ratio m of the P_c contribution and all the other parameters of the model. One hundred fits with fixed values of the ratio of magnitudes m are performed, and their results combined to build a 95% confidence level interval for the corresponding generated value $\tilde{m}$. The m values defining the lower and upper boundaries of the CI are then translated to values of pentaquark fit fractions. The procedure is iterated for all the hypothesised $\tilde{m}$ values, finally defining a confidence belt as shown in Section 3.2.5.

Figure 63 shows the confidence belts in the fit fraction space for the $P_c(4380)^+$ and $P_c(4450)^+$ pentaquark candidates. The fit fractions of these states measured on data are represented by vertical lines. The general trend of the confidence belts reflects the expected behaviour for such a statistical test, as in Figure 21. Nevertheless they are affected by fluctuations of the intervals, caused by the uncertainties related to the amplitude fits and to the statistical size of the fitted samples. The intersections of the lines corresponding to the measured fractions with the confidence belts determine 95% CL upper limits for the observation of the two states in the $\Lambda_b^0 \to \Lambda_c^+\overline{D}^0K^-$ channel:

$$\begin{aligned} P_c(4380)^+ \text{ fit fraction} < 0.0125 \text{ (95\%CL)} \\ P_c(4450)^+ \text{ fit fraction} < 0.007 \text{ (95\%CL)} \end{aligned} \tag{166}$$

The same procedure is repeated testing the hypothesis of observing both the $P_c(4380)^+$ and $P_c(4450)^+$, with their relative fit fractions constrained to the value $\mathcal{R}(P_c(4380)^+/P_c(4450)^+) = 2.05$ as measured in their first observation. The resulting confidence belts are shown in Figure 64, and the corresponding upper limits on fit fractions of the pentaquark states result to be:

$$\begin{aligned} P_c(4380)^+ \text{ fit fraction} < 0.0095 \text{ (95\%CL)} \\ P_c(4450)^+ \text{ fit fraction} < 0.0047 \text{ (95\%CL)} \end{aligned} \tag{167}$$

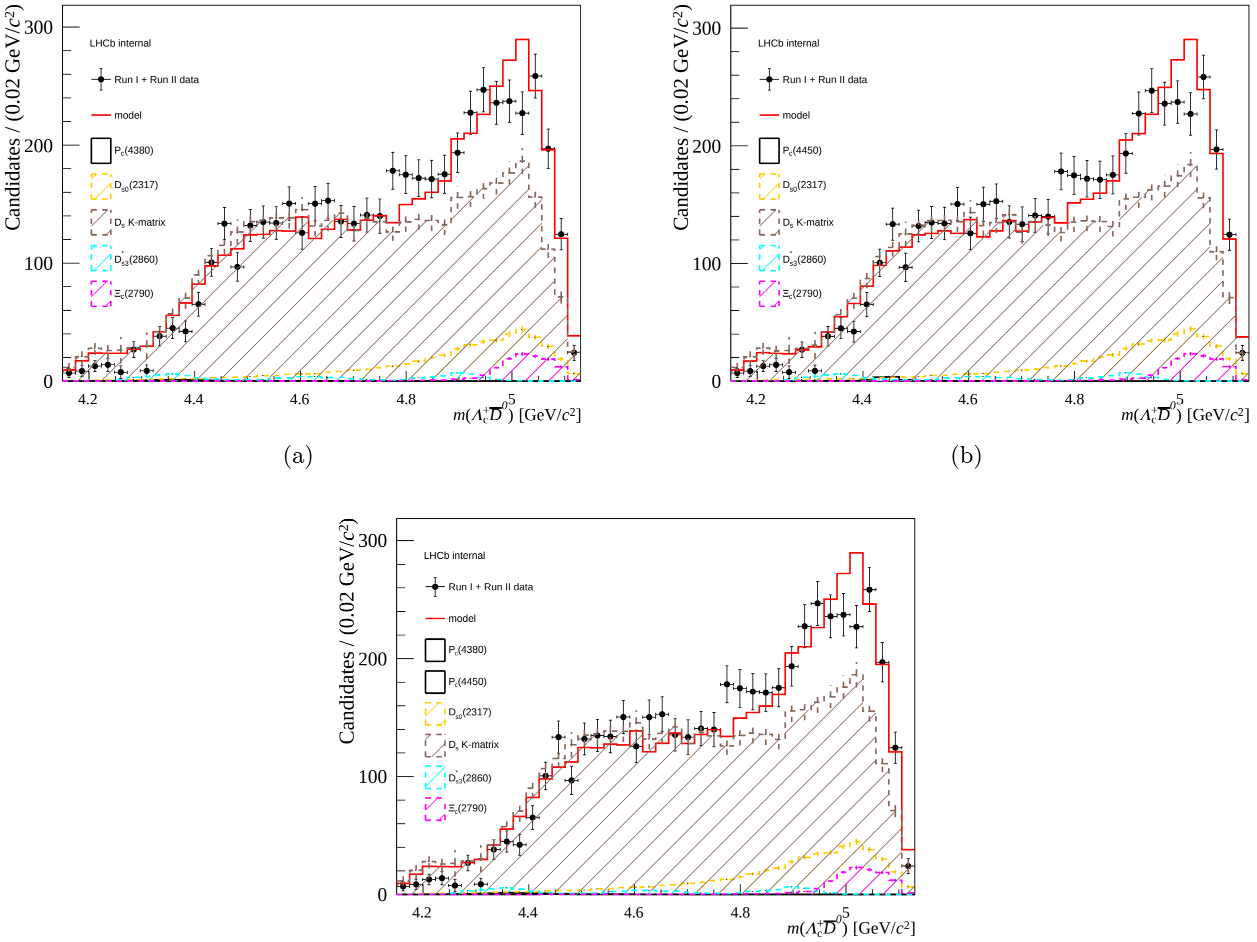

(a)

(b)

(c)

Figure 62: Projections of the amplitude fits over the $m(\Lambda_c^+\overline{D}^0)$ invariant mass distribution, including the $P_c(4380)^+$ and $P_c(4450)^+$ pentaquark states. a) The $P_c(4380)^+$ state is included in the model. b) The $P_c(4450)^+$ state is included in the model. c) The $P_c(4380)^+$ and $P_c(4450)^+$ states are included in the model.

The individual presence of the $P_c(4312)^+$, $P_c(4440)^+$ and $P_c(4457)^+$ states is tested analogously. Both the $J^P = \frac{1}{2}^-, \frac{3}{2}^-$ assignments are tested for the $P_c(4440)^+$ and $P_c(4457)^+$ states. The results of the amplitude fits to data adding these pentaquark contributions are listed in Table 50. The projections of the fits over the $m(\Lambda_c^+\overline{D}^0)$ invariant mass distributions are shown in Figures 65-66. Confidence belts are shown in Figure 67, resulting in the following upper limits:

$$\begin{aligned}
&P_c(4312)^+ \text{ fit fraction} < 0.004 \text{ (95\%CL)}\\
&P_c(4440)^+, J^P = \frac{1}{2}^- \text{ fit fraction} < 0.006 \text{ (95\%CL)}\\
&P_c(4440)^+, J^P = \frac{3}{2}^- \text{ fit fraction} < 0.0045 \text{ (95\%CL)}\\
&P_c(4457)^+, J^P = \frac{1}{2}^- \text{ fit fraction} < 0.0045 \text{ (95\%CL)}\\
&P_c(4457)^+, J^P = \frac{3}{2}^- \text{ fit fraction} < 0.008 \text{ (95\%CL)}
\end{aligned} \tag{168}$$

Hypothesis	$P_c(4312)^+$ fit fraction	$P_c(4440)^+$ fit fraction	$P_c(4457)^+$ fit fraction
$P_c(4312)^+$ only	$0.0009^{+0.0013}_{-0.0009}$	/	/
$P_c(4440)^+$ ($J^P = \frac{1}{2}^-$) only	/	$0.0015^{+0.0021}_{-0.0015}$	/
$P_c(4440)^+$ ($J^P = \frac{3}{2}^-$) only	/	$0.000024^{+0.000025}_{-0.000024}$	/
$P_c(4457)^+$ ($J^P = \frac{1}{2}^-$) only	/	/	0.0015 ± 0.00015
$P_c(4457)^+$ ($J^P = \frac{3}{2}^-$) only	/		0.00026 ± 0.0021
$P_c(4312)^+$, $P_c(4440)^+$ ($J^P = \frac{1}{2}^-$), $P_c(4457)^+$ ($J^P = \frac{1}{2}^-$)	0.0023 ± 0.0018	0.00034 ± 0.00027	0.000090 ± 0.000071
$P_c(4312)^+$, $P_c(4440)^+$ ($J^P = \frac{3}{2}^-$), $P_c(4457)^+$ ($J^P = \frac{3}{2}^-$)	$0.0024^{+0.0025}_{-0.0024}$	0.0019 ± 0.0019	$0.00010^{+0.00011}_{-0.00010}$

Table 50: Fitted values of the $P_c(4312)^+$, $P_c(4440)^+$ and $P_c(4457)^+$ fit fractions, for different hypotheses. Only statistical uncertainties are shown.

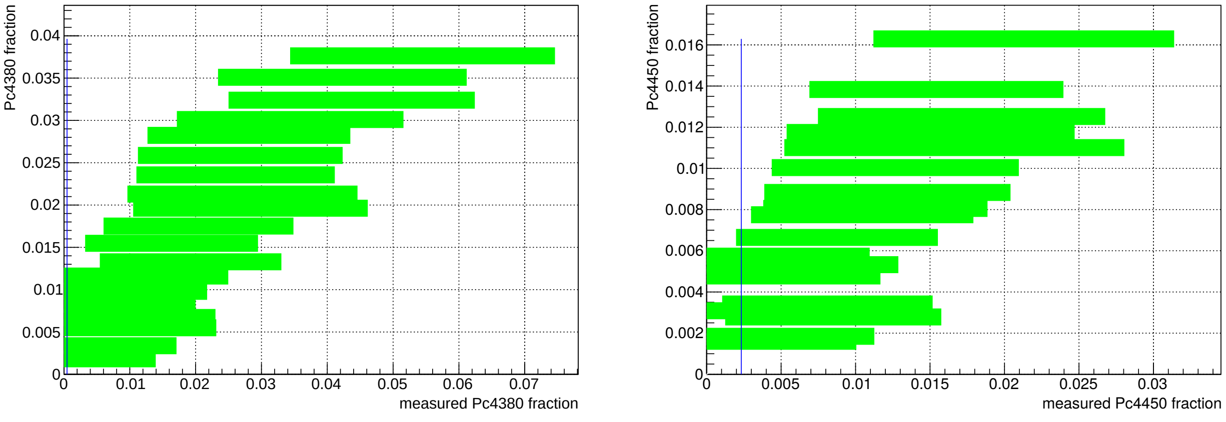

(a) (b)

Figure 63: Confidence belts for the $P_c(4380)^+$ (a) and $P_c(4450)^+$ (b) fit fractions at 95% confidence level, under the hypothesis of observing only one of them in $\Lambda_b^0 \to \Lambda_c^+ \overline{D}^0 K^-$ decays. The blue vertical lines indicate the fit fraction values measured on data.

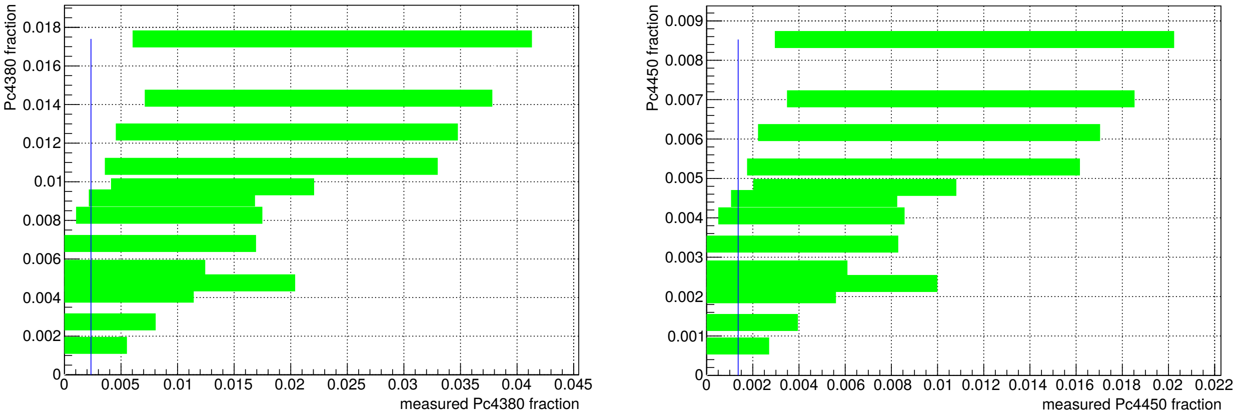

(a)

(b)

Figure 64: Confidence belts for the $P_c(4380)^+$ (a) and $P_c(4450)^+$ (b) fit fractions at 95% confidence level, under the hypothesis of observing both of them in $\Lambda_b^0 \to \Lambda_c^+\overline{D}^0K^-$ decays. The blue vertical lines indicate the fit fraction values measured on data. The ratio between the P_c fit fractions is fixed to the results obtained in [1].

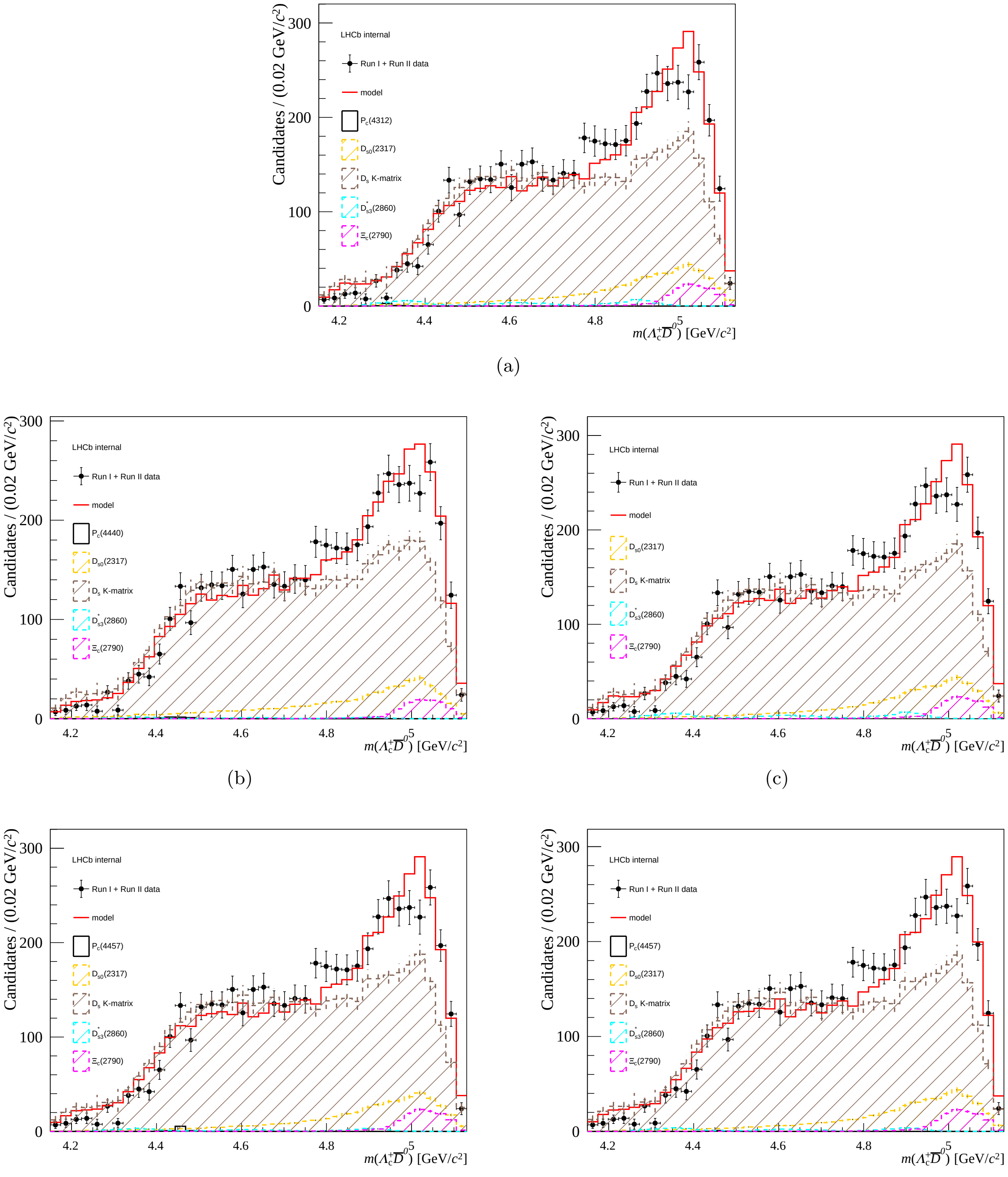

(a)

(b)

(c)

(d)

(e)

Figure 65: Projections of the amplitude fits over the $m(\Lambda_c^+\overline{\mathrm{D}}^0)$ invariant mass distribution, including the $P_c(4312)^+$, $P_c(4440)^+$, $P_c(4457)^+$ states in the amplitude model. a) The $P_c(4312)^+$ state is included in the model. b) The $P_c(4440)^+$ state is included in the model, with $J^P = \frac{1}{2}^-$ assignment. c) The $P_c(4440)^+$ state is included in the model, with $J^P = \frac{3}{2}^-$ assignment. d) The $P_c(4457)^+$ state is included in the model, with $J^P = \frac{1}{2}^-$ assignment. e) The $P_c(4457)^+$ state is included in the model, with $J^P = \frac{3}{2}^-$ assignment.

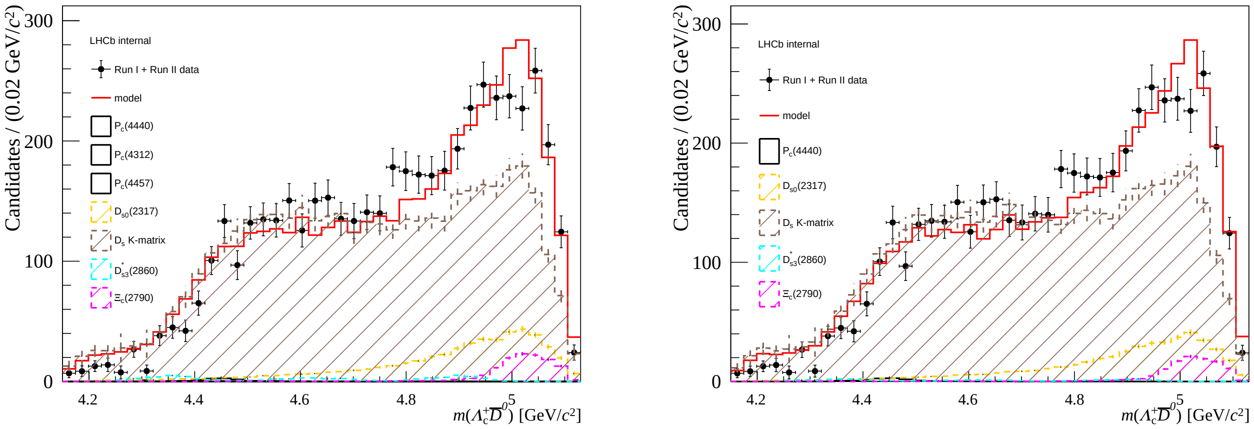

(a)

(b)

Figure 66: Projections of the amplitude fits over the $m(\Lambda_c^+\overline{\mathrm{D}}^0)$ invariant mass distribution, including the $P_c(4312)^+$, $P_c(4440)^+$, $P_c(4457)^+$ states in the amplitude model. a) The $P_c(4312)^+$, $P_c(4440)^+$, $P_c(4457)^+$ states are included in the model, with $J^P = \frac{1}{2}^-$ assignment for the $P_c(4440)^+$ and $P_c(4457)^+$ states. b) The $P_c(4312)^+$, $P_c(4440)^+$, $P_c(4457)^+$ states are included in the model, with $J^P = \frac{3}{2}^-$ assignment for the $P_c(4440)^+$ and $P_c(4457)^+$ states.

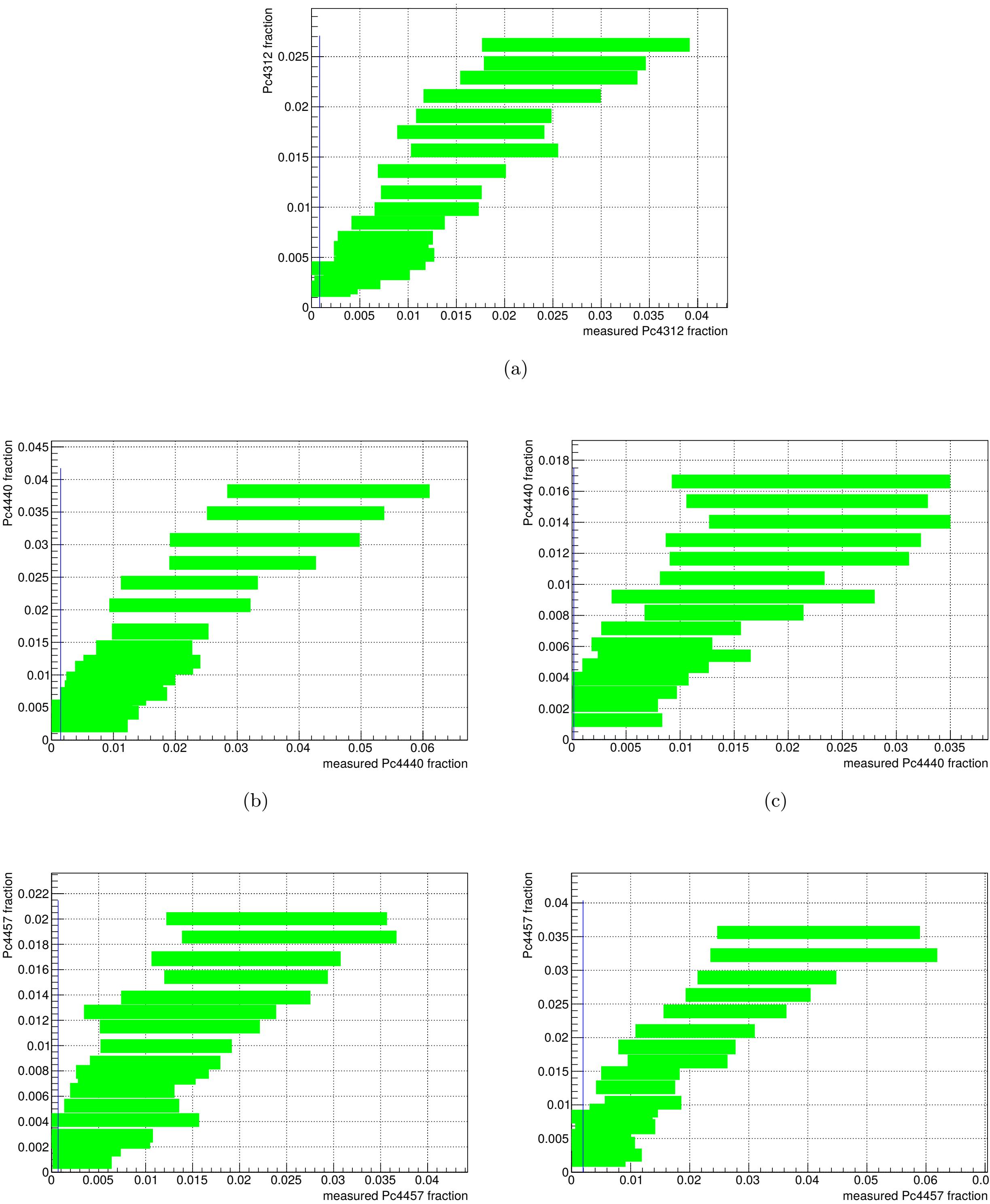

(a)

(b)

(c)

(d)

(e)

Figure 67: Confidence belts for the $P_c(4312)^+$ (a), $P_c(4440)^+$ ($J^P = \frac{1}{2}^+$ (b), $J^P = \frac{3}{2}^+$ (c)) and $P_c(4457^+)$ ($J^P = \frac{1}{2}^+$ (d), $J^P = \frac{3}{2}^+$ (e)) fit fractions at 95% confidence level, under the hypothesis of observing only one of them in $\Lambda_b^0 \to \Lambda_c^+ \overline{D}^0 K^-$ decays. The blue vertical lines indicate the fit fraction values measured on data.

Unfortunately, the procedure described in Section 8.2 for assessing the statistical significance for the combined observation of $Pc(4312)^+$, $P_c(4440)^+$ and $P_c(4457^+)$ states does not lead to stable results. This can be related to the model becoming too complex, which would require a different approach for constructing the confidence intervals or a modification of the amplitude model. However, based on the results obtained for testing these states individually, upper limits with upper boundary at per-cent level are expected. A complete derivation is addressed to future studies.

The above results are in contrast with the expectations from the majority of the $\Sigma^{(*)}\overline{\mathrm{D}}^{(*)}$ molecular models of the pentaquark candidates observed by LHCb. Visible pentaquark signals decaying to the $\overline{\mathrm{D}}^0\mathrm{K}^-$ system have been predicted by such models, in a quantitative way for the $P_c(4380)^+$ and $P_c(4450)^+$ states ([39], Section 8.1), and more qualitatively for the $P_c(4312)^+$, $P_c(4440)^+$ and $P_c(4457)^+$ pentaquarks [55, 56, 133].

On the other hand, the results support the predictions of the $\Sigma^{(*)}\overline{\mathrm{D}}^{(*)}$ molecular model from [59], in which the couplings of the P_C states to the $\Lambda_c^+\overline{\mathrm{D}}^0$ system are predicted to be small. As introduced in Section 1.5, this work makes use of the most recent LHCb data to tune the constants involved in the loop predictions.

8.4 Extra hidden-charm pentaquarks

The eventual presence of hidden-charm pentaquark states such as predicted in [40] is also tested. The parametrisation of the states as described in [40] is not straightforward to implement in the amplitude model of this analysis. Nevertheless, Breit-Wigner distributions are good approximations for the line shapes of the first states (see Figure 5 in [40]). Thus, three states $P_{c,s11}$, $P_{c,d11}$, $P_{c,d13}$ are described by making use of Breit-Wigner line shapes and resonance parameters as listed in Table 51. An amplitude fit with the newly-defined model is performed to data.

State	Mass [MeV/c^2]	Width [MeV/c^2]	J^P
$P_{c,s11}$	4295	7.4	$\frac{1}{2}^-$
$P_{c,d11}$	4334	56.	$\frac{1}{2}^-$
$P_{c,d13}$	4395	108.	$\frac{3}{2}^-$

Table 51: Parameters used to describe the first partial waves described in [40].

The results of the amplitude fit to the data, including the three extra-hidden charm pentaquarks, are listed in Table 52. The pentaquark contributions are compatible with zero within the related statistical uncertainties.

Component	Fit fraction
$P_{c,s11}$	$0.00075^{+0.00087}_{-0.00075}$
$P_{c,d11}$	$0.0004^{+0.0017}_{-0.0004}$
$P_{c,d13}$	$0.00022^{+0.00047}_{-0.00022}$
$\mathrm{D}^*_{s0}(2317)$	0.107 ± 0.047
D_s K-matrix	0.856 ± 0.039
$\mathrm{D}^*_{s3}(2860)$	0.0153 ± 0.0045
$\Xi_c^0(2790)$	0.022 ± 0.010
Sum	1.0015 ± 0.0078

Table 52: Fit results for the resonance fractions of the baseline amplitude model and hidden-charm pentaquark states. Only statistical uncertainties are shown.

9 Conclusions

This thesis reports the amplitude analysis of $\Lambda_{\mathrm{b}}^0 \to \Lambda_{\mathrm{c}}^+ \overline{\mathrm{D}}^0 \mathrm{K}^-$ decays collected by the LHCb experiment in LHC Run 1 and Run 2, corresponding to an integrated luminosity of 9.1 fb^{-1}. This channel is important to discriminate between models which attempt to describe the nature of the pentaquark candidates observed by LHCb in 2015 and in 2019.

The measured fit fractions of the intermediate resonances used to describe the data are reported in the following:

$$\begin{aligned}
&\mathrm{D}_{\mathrm{s}0}^*(2317) \text{ fit fraction} = 0.099 \pm 0.013 \text{ (stat.)} \pm 0.015 \text{ (syst.)}\\
&\mathrm{D}_{\mathrm{s}}\ K-\text{matrix fit fraction} = 0.862 \pm 0.029 \text{ (stat.)} \pm 0.022 \text{ (syst.)}\\
&\mathrm{D}_{\mathrm{s}3}^*(2860) \text{ fit fraction} = 0.0181 \pm 0.0077 \text{ (stat.)} \pm 0.0014 \text{ (syst.)}\\
&\Xi_{\mathrm{c}}^0(2790) \text{ fit fraction} = 0.0257 \pm 0.0051 \text{ (stat.)} \pm 0.0039 \text{ (syst.)}
\end{aligned} \tag{169}$$

where the K-matrix term describes the contributions from the $\mathrm{D}_{\mathrm{s}1}^*(2700)$ and $\mathrm{D}_{\mathrm{s}1}^*(2860)$ states. The interference terms between the above states are consistent with zero.

Upper limits have been derived on the presence of pentaquark states in the data set used in this analysis. Under the hypothesis of observing the decay of only one pentaquark contribution in the $\Lambda_{\mathrm{b}}^0 \to \Lambda_{\mathrm{c}}^+ \overline{\mathrm{D}}^0 \mathrm{K}^-$ channel, the upper limits on their observation are found to be:

$$\begin{aligned}
&P_c(4380)^+ \text{ fit fraction} < 0.0125 \text{ (95\%CL)}\\
&P_c(4450)^+ \text{ fit fraction} < 0.007 \text{ (95\%CL)}\\
&P_c(4312)^+ \text{ fit fraction} < 0.004 \text{ (95\%CL)}\\
&P_c(4440)^+, J^P = \frac{1}{2}^- \text{ fit fraction} < 0.006 \text{ (95\%CL)}\\
&P_c(4440)^+, J^P = \frac{3}{2}^- \text{ fit fraction} < 0.0045 \text{ (95\%CL)}\\
&P_c(4457)^+, J^P = \frac{1}{2}^- \text{ fit fraction} < 0.0045 \text{ (95\%CL)}\\
&P_c(4457)^+, J^P = \frac{3}{2}^- \text{ fit fraction} < 0.008 \text{ (95\%CL)}
\end{aligned} \tag{170}$$

assuming mass and widths of the pentaquark states as measured in [1, 2].

Under the assumption of observing both the $P_c(4380)^+$ and $P_c(4450)^+$ states with relative fit fractions as measured in [1], upper limits are set for their observation in $\Lambda_{\mathrm{b}}^0 \to \Lambda_{\mathrm{c}}^+ \overline{\mathrm{D}}^0 \mathrm{K}^-$ decays:

$$\begin{aligned}
&P_c(4380)^+ \text{ fit fraction} < 0.0095 \text{ (95\%CL)}\\
&P_c(4450)^+ \text{ fit fraction} < 0.0047 \text{ (95\%CL)}
\end{aligned} \tag{171}$$

The above results are in contrast with the expectations from the majority of the $\Sigma\overline{\mathrm{D}}^*$-$\Sigma^*\overline{\mathrm{D}}$ molecular models of the pentaquark candidates observed by LHCb. Given the statistics of $\Lambda_{\mathrm{b}}^0 \to \Lambda_{\mathrm{c}}^+ \overline{\mathrm{D}}^0 \mathrm{K}^-$ channel studied in this analysis, [39] predicted in a quantitative way visible signals of the $P_c(4380)^+$ and $P_c(4450)^+$ states decaying to $\Lambda_{\mathrm{c}}^+ \overline{\mathrm{D}}^0$. In these models, the pentaquarks are described as loosely-bound states of $\Sigma_c^*(2520)\overline{\mathrm{D}} - \Sigma_c(2455)\overline{\mathrm{D}}^*$ hadrons in non-relativistic regime. Only more qualitative expectations for the $P_c(4312)^+$, $P_c(4440)^+$ and $P_c(4457)^+$ are available at this time. Nevertheless, large couplings of the pentaquarks to the $\Lambda_c^+\overline{D}^0$ system have been predicted by [55] using an effective range expansion of the dynamics around the $\Sigma_c\overline{D}^{(*)}$ threshold region, and by [56] making use of an extended chromomagnetic model. Also, the results of this analysis are not in line with the predictions of the hadrocharmonium description of the P_cs as modelled in [58].

On the other hand, the results corroborate the predictions of the $\Sigma^{(*)}\overline{D}^{(*)}$ molecular hypothesis as presented in [59]. In this work, by tuning to the most recent LHCb data the constants involved in the loop calculations, the couplings of the P_c states to the $\Lambda_c^+\overline{D}^0$ system are predicted to be small. More conclusive statement can only be made with the predictions of P_c branching fractions rather than couplings, which are not available yet.

Similarly, the contributions from additional hidden-charm pentaquarks predicted in [40], which describes reasonably well the observed $P_c(4380)^+$, result to be negligible in $\Lambda_b^0 \to \Lambda_c^+\overline{D}^0K^-$ decays.

A Appendices

A.1 Data distributions with finer binning

Figure 68 shows the distributions of the s-weighted signal candidates, with finer binning (400 bins) with respect to the default plots (40 bins) shown in Figure 42. Distributions from phase-space simulated samples are overimposed.

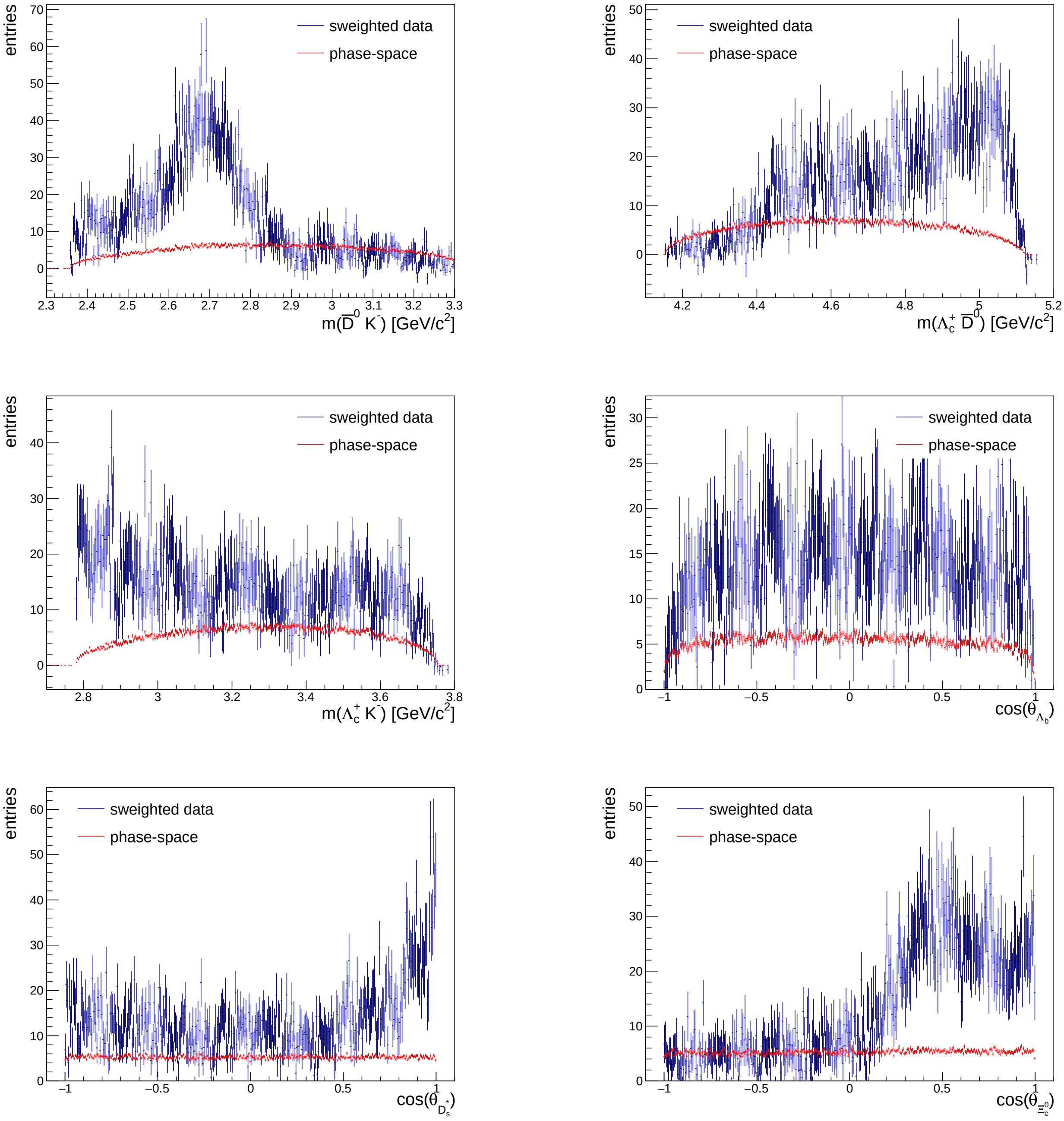

Figure 68: Distributions of the amplitude variables on s-weighted signal candidates compared to the distributions from the phase-space simulated sample.

A.2 Fit distributions with finer binning

Figure 69 shows the projections of the amplitude fit to data with 60 bins. The default projections shown in Figure 44 have 40 bins. The baseline amplitude model is considered.

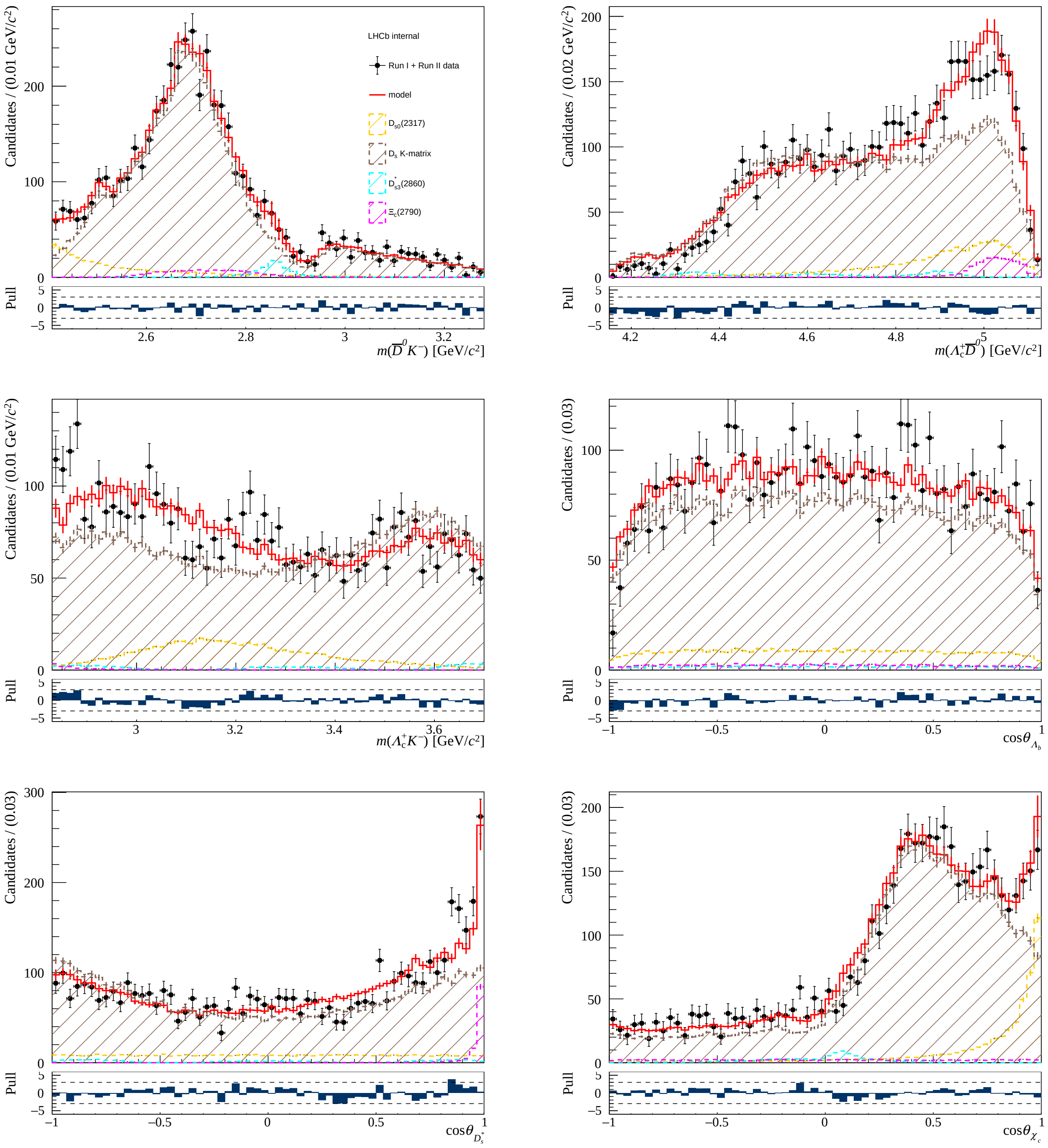

Figure 69: Projections of the baseline amplitude fit over the amplitude variables, overimposed to the data. 60 bins are used.

Figure 70 shows the $m(\Lambda_c^+\overline{D}^0)$ projection of the amplitude fits to data replacing the $D^{*0}(2007)K^-$ channel in the K-matrix amplitude by the $D_1^0(2420)K^-$ channel. Two different binning schemes are proposed.

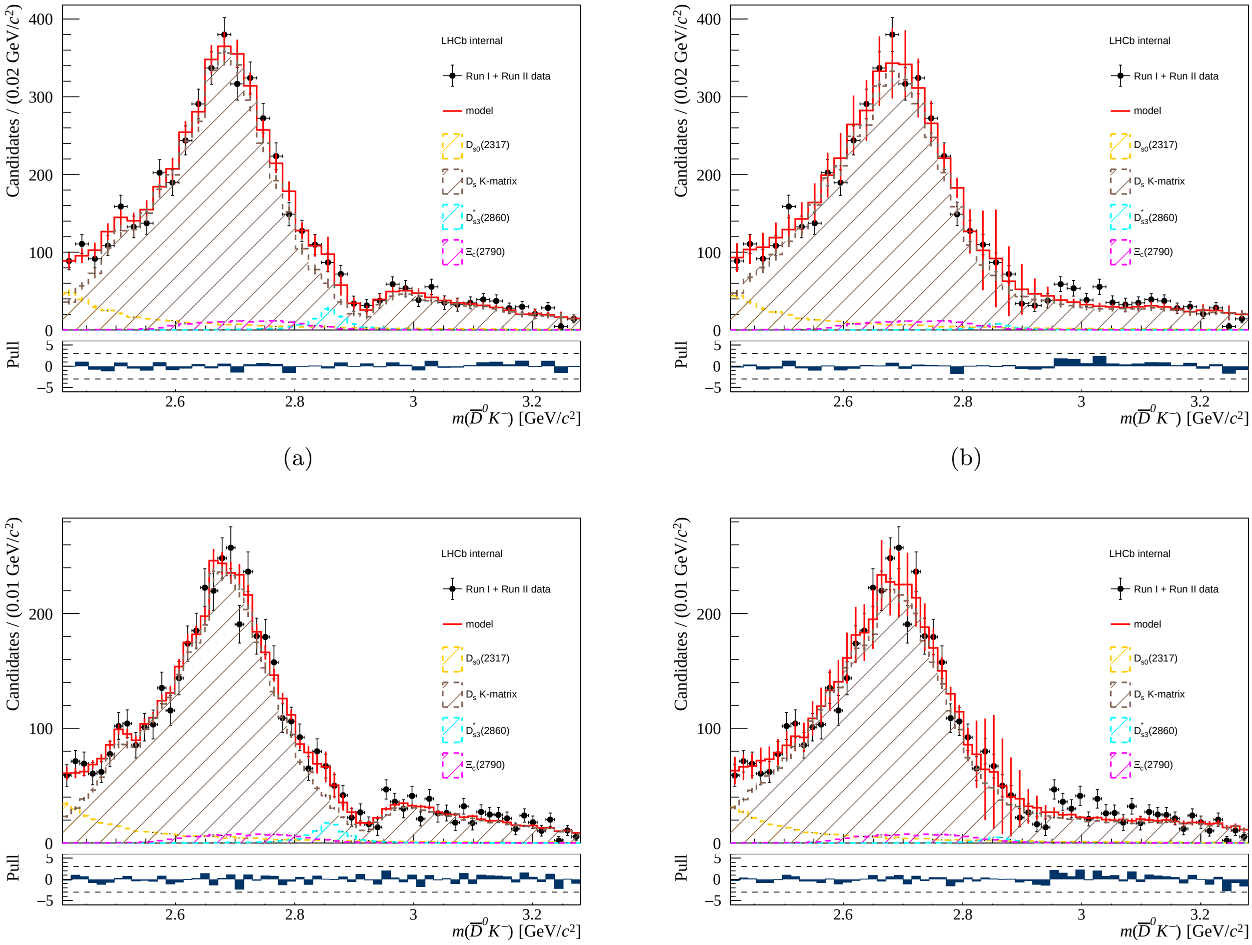

(a)

(b)

(c)

(d)

Figure 70: Projections of the amplitude fit over the $m(\overline{D}^0K^-)$ invariant mass distribution, overimposed to the data. 40 bins (a, b) and 60 bins (c, d) are used. a, c) Baseline amplitude model, with the $D^{*0}(2007)K^-$ and $\overline{D}^0K^-$ channels included in the K-matrix amplitude. b, d) The $D^{*0}(2007)K^-$ channel in the K-matrix amplitude has been replaced by the $D_1^0(2420)K^-$ channel.

A.3 Efficiency maps of the Λ_c^+ and $\overline{D}^0$ selections based on Boosted Decision Trees classifiers

Efficiency maps of the individual and combined *D-from-B* BDT selections of the Λ_c^+ and $\overline{D}^0$ are shown in Figures 71-72-73 over the angular variables, invariant mass distributions and Dalitz plots, respectively. The efficiency values are weighted by the candidate *s*-weights.

The efficiency shapes of the individual classifiers are compatible with each other. The efficiency shape of the combined selection show a similar trend to the efficiency of the individual classifiers, and its average efficiency is equal to the product of the mean efficiencies of the latter. Hence, the two BDT classifiers factorise and the related efficiency terms in the signal *pdf* (Eq. 143) can be expressed as a simple product.

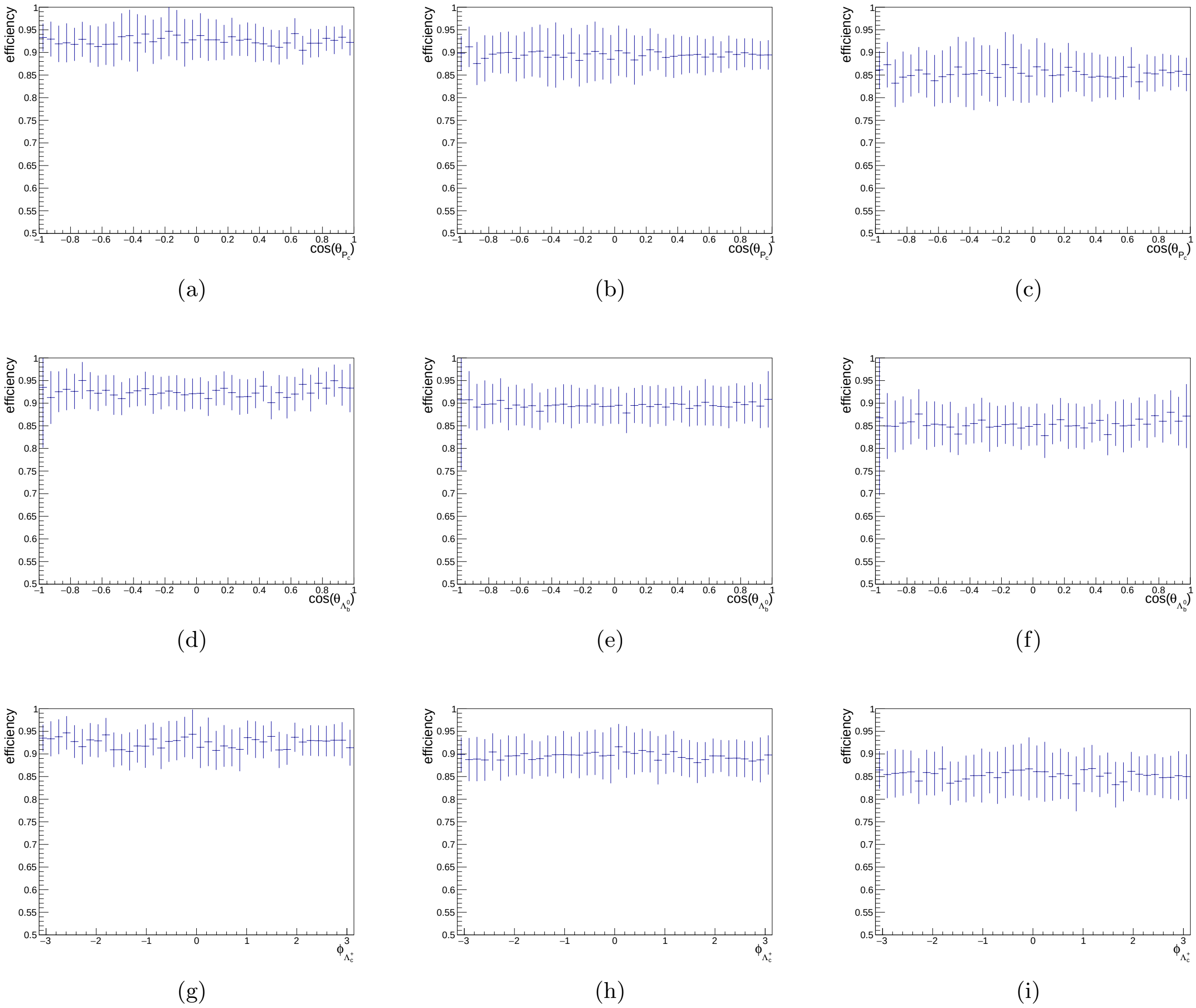

(a) (b) (c)

(d) (e) (f)

(g) (h) (i)

Figure 71: Efficiency over the angular variables of the default *D-from-B* BDT selection of the *c*-hadrons. a, d, g) Individual efficiency of the $\overline{D}^0$ selection. b, e, h) Individual efficiency of the Λ_c^+ selection. c, f, i) Efficiency of the combined selections of the Λ_c^+ and $\overline{D}^0$ hadrons.

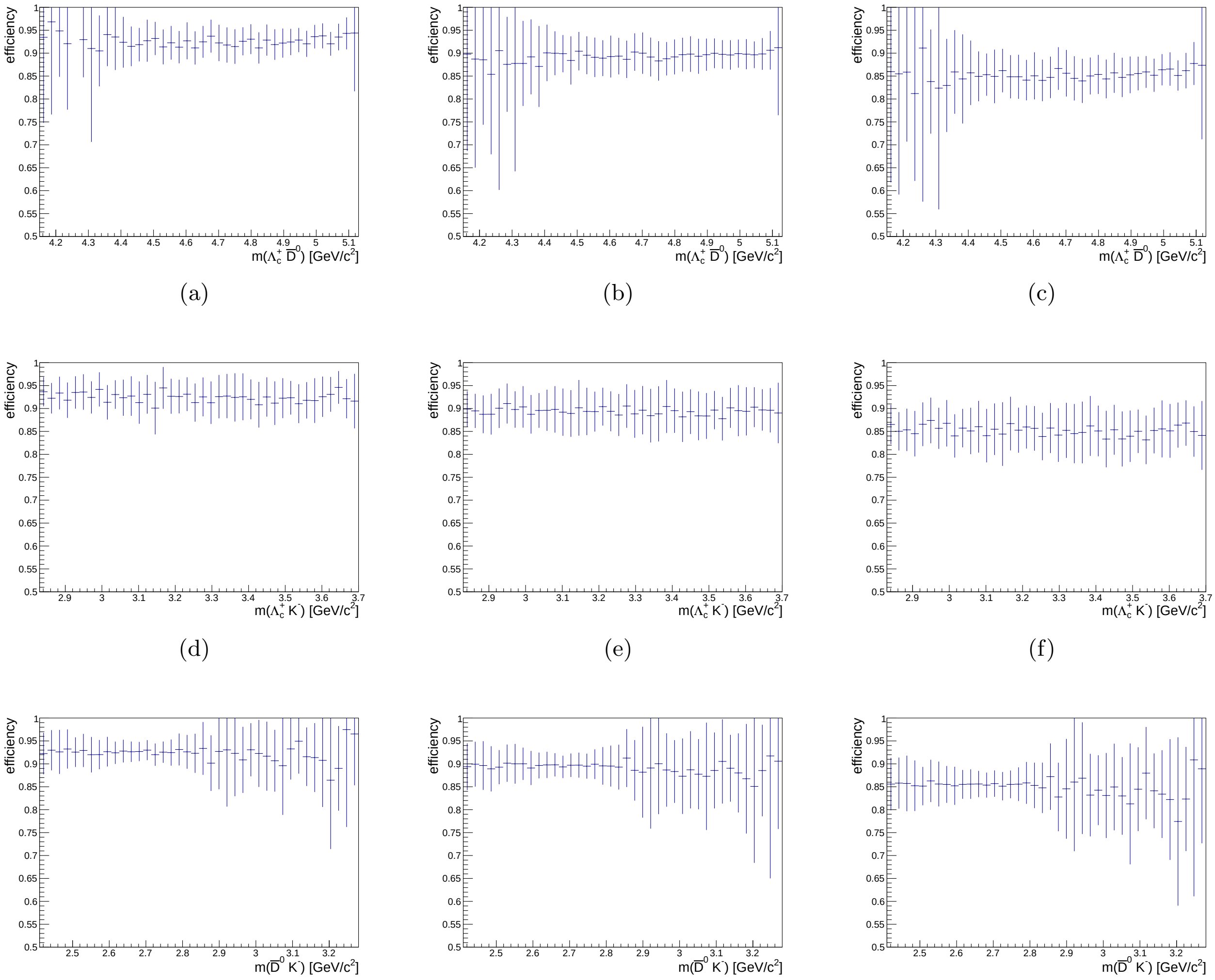

(a) (b) (c)

(d) (e) (f)

(g) (h) (i)

Figure 72: Efficiency of the default *D-from-B* BDT selection of the *c*-hadrons, over the invariant mass distributions of the final-state particles. a, d, g) Individual efficiency of the $\overline{\mathrm{D}}^0$ selection. b, e, h) Individual efficiency of the Λ_c^+ selection. c, f, i) Efficiency of the combined selections of the Λ_c^+ and $\overline{\mathrm{D}}^0$ hadrons.

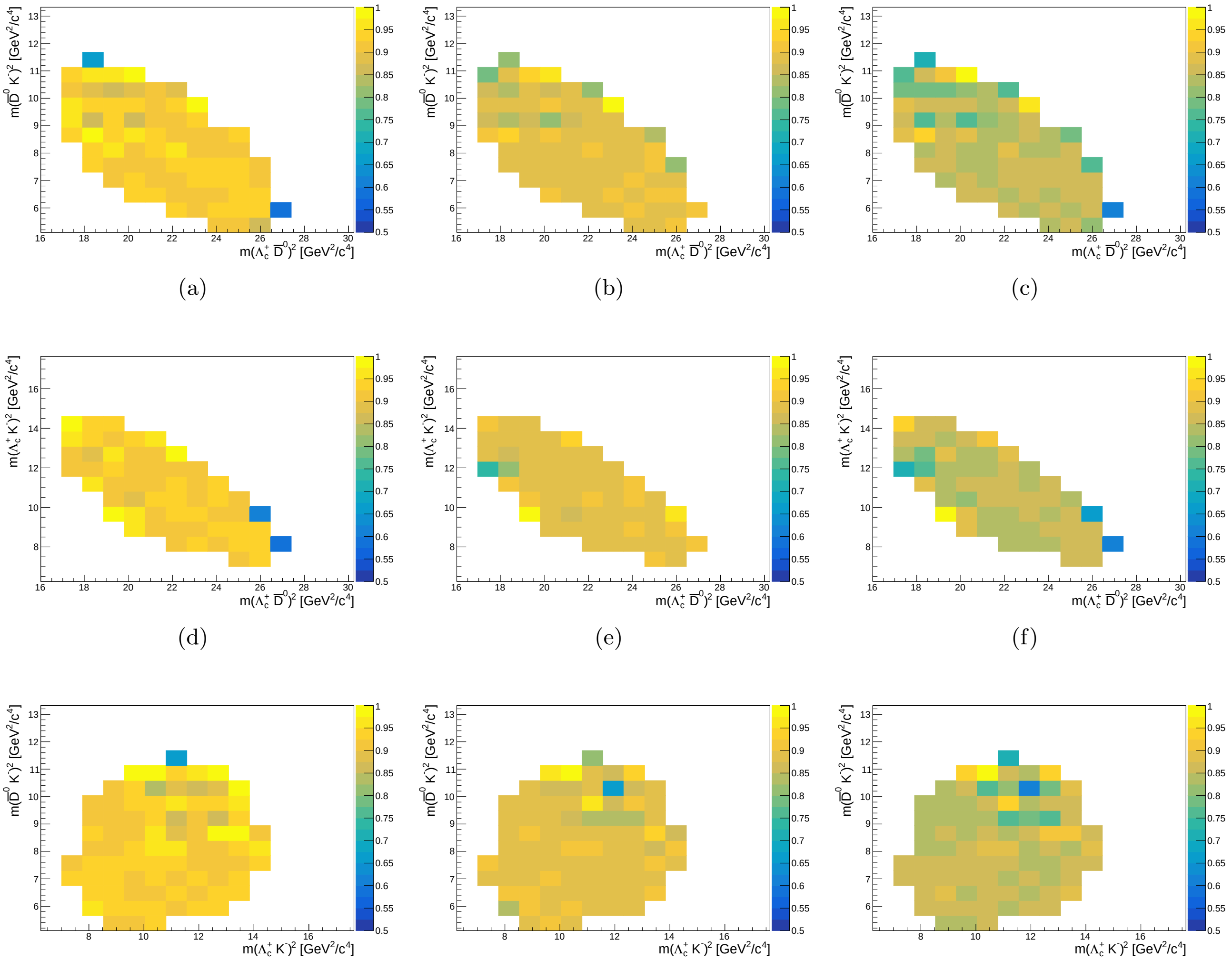

(a) (b) (c)

(d) (e) (f)

(g) (h) (i)

Figure 73: Efficiency over the Dalitz plots of the default *D-from-B* BDT selection of the *c*-hadrons. a, d, g) Individual efficiency of the $\overline{\mathrm{D}}^0$ selection. b, e, h) Individual efficiency of the Λ_c^+ selection. c, f, i) Efficiency of the combined selections of the Λ_c^+ and $\overline{\mathrm{D}}^0$ hadrons.

A.4 Efficiency maps of the K^- selection based on particle identification

Efficiency maps of the $ProbNN$ classifier for the default selection of the bachelor K^- are shown in Figures 74 over the angular variables, invariant mass distributions and Dalitz plots.

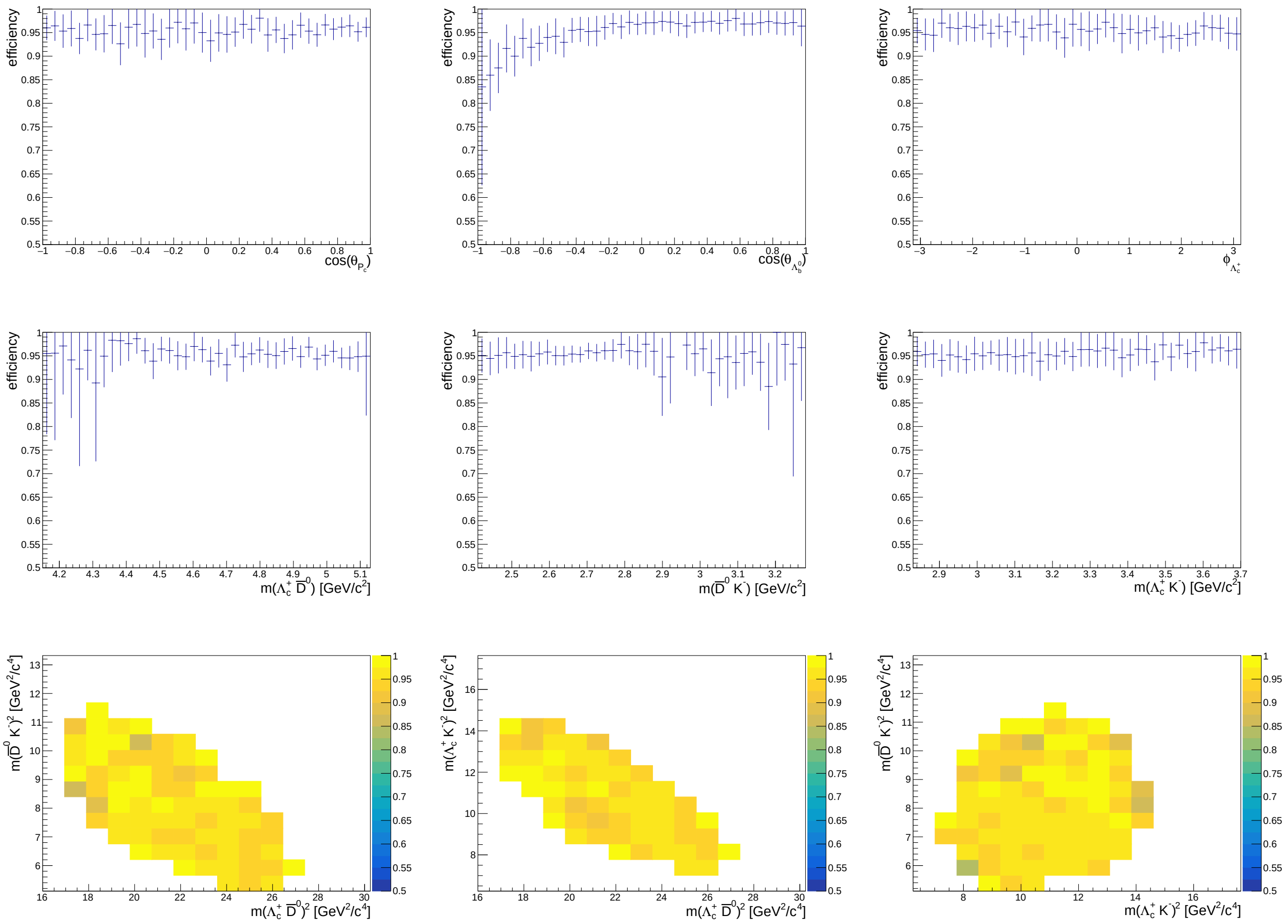

Figure 74: Efficiency over the amplitude variables of the default PID selection of the bachelor K^-.

A.5 $\mathrm{D}^{*}_{s1}(2700)$ and $\mathrm{D}^{*}_{s1}(2860)$ states parametrised by a sum of Breit-Wigner line shapes

The baseline amplitude model describes the $\mathrm{D}^{*}_{s1}(2700)$ and $\mathrm{D}^{*}_{s1}(2860)$ by a K-matrix amplitude. A more naïve approach is to consider them as two independent contributions, parametrised by Breit-Wigner line shapes. An amplitude model following the latter approach is considered, and the amplitude fit to data is repeated. The resulting fit fractions are reported in Table 53, and the interference terms in Table 54. Figure 75 shows the projections of the amplitude fit to data. A strong destructive interference between the two states is modeled by the amplitude fit, which also results in an unstable fit. In this case the Breit-Wigner approximation for the two states is failing, and it is necessary to resort to the K-matrix approach.

Component	Fit fraction
$\mathrm{D}^{*}_{s0}(2317)$	0.138
$\mathrm{D}^{*}_{s2}(2573)$	0.0104
$\mathrm{D}^{*}_{s1}(2700)$	1.21
$\mathrm{D}^{*}_{s1}(2860)$	0.340
$\mathrm{D}^{*}_{s3}(2860)$	0.0183
$\Xi^{0}_{c}(2790)$	0.0232
non-resonant	0.108
Sum	1.852781

Table 53: Fit results for the resonance fractions, parametrising the $\mathrm{D}^{*}_{s1}(2700)$ and $\mathrm{D}^{*}_{s1}(2860)$ states by two independent Breit-Wigner line shapes..

	$\mathrm{D}^{*}_{s2}(2573)$	$\mathrm{D}^{*}_{s1}(2700)$	$\mathrm{D}^{*}_{s1}(2860)$	$\mathrm{D}^{*}_{s3}(2860)$	$\Xi^{0}_{c}(2790)$
$\mathrm{D}^{*}_{s0}(2317)$	0.0001	-0.008	0.002	0.00007	0.0001
$\mathrm{D}^{*}_{s2}(2573)$	/	0.000004	-0.0001	-0.00002	0.0002
$\mathrm{D}^{*}_{s1}(2700)$	/	/	-0.93	-0.0008	0.02
$\mathrm{D}^{*}_{s1}(2860)$	/	/	/	0.0005	-0.01
$\mathrm{D}^{*}_{s3}(2860)$	/	/	/	/	0.003

Table 54: Fit results for the interference terms between the components of the amplitude model, parametrising the $\mathrm{D}^{*}_{s1}(2700)$ and $\mathrm{D}^{*}_{s1}(2860)$ states by two independent Breit-Wigner line shapes..

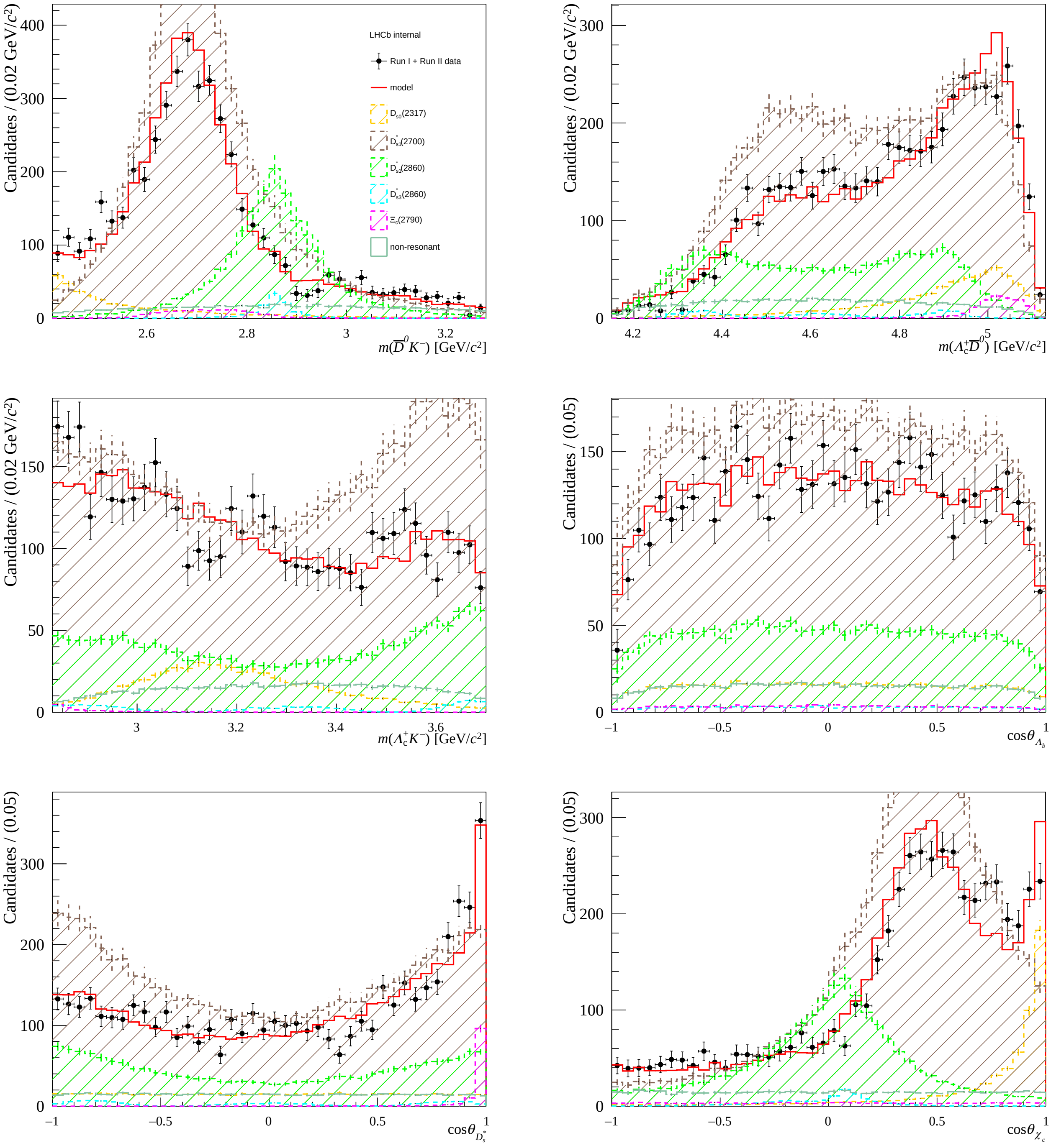

Figure 75: Projections of the amplitude fit to data. The $\mathrm{D}^*_{s1}(2700)$ and $\mathrm{D}^*_{s1}(2860)$ states are parametrised by two independent Breit-Wigner line shapes.

A.6 Fit to data with $\Xi_c^0(2970), \Xi_c^0(3055), \Xi_c^0(3080)$ states

Figure 76 shows the $m(\Lambda_c^+ K^-)$ projection of the amplitude fits to data adding the $\Xi_c^0(2970), \Xi_c^0(3055), \Xi_c^0(3080)$ states to the baseline amplitude model. All combinations of spin-parity assignment $J^P = \frac{1}{2}^-, \frac{3}{2}^-$ for these states are considered.

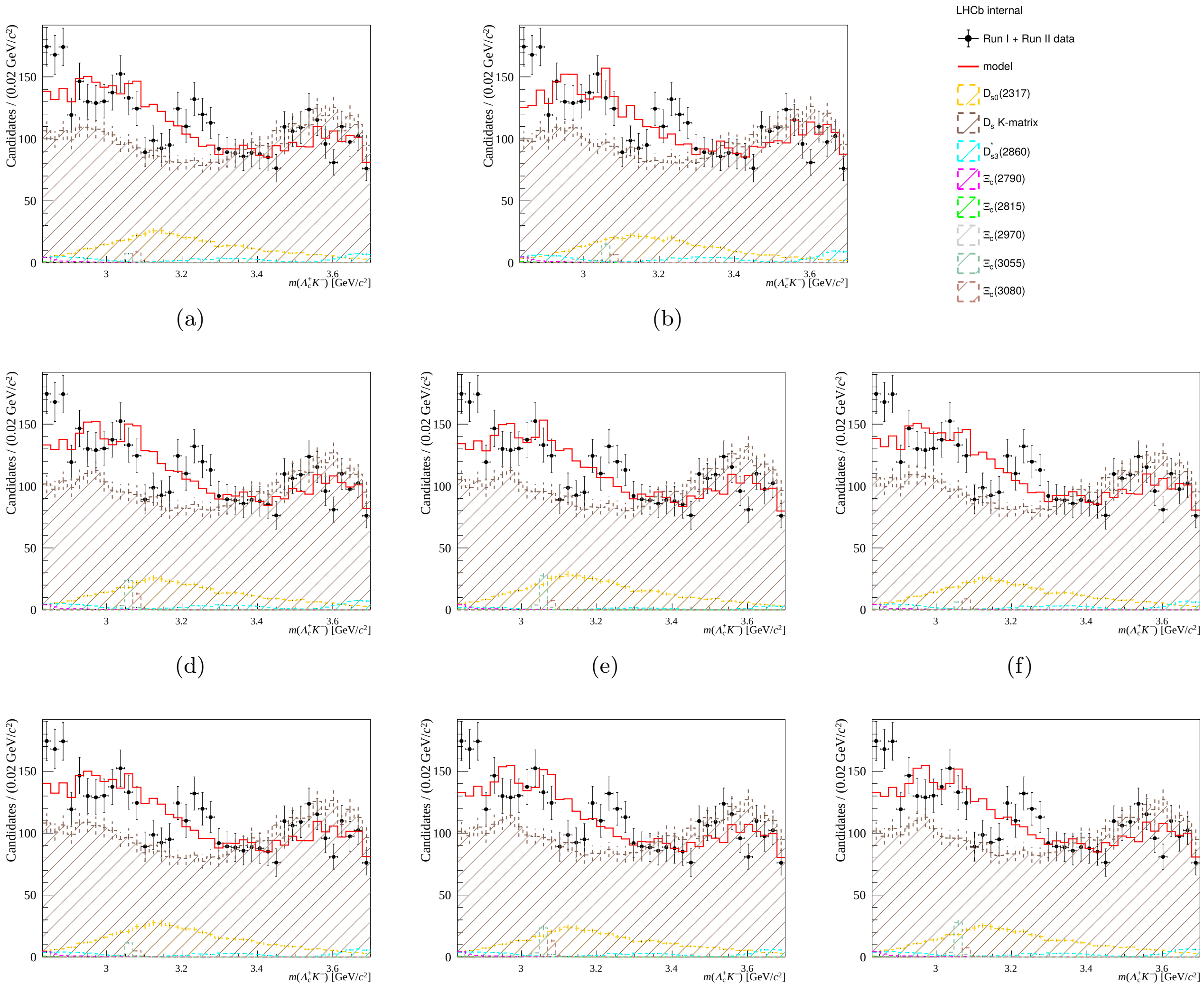

(a) (b)

(d) (e) (f)

(g) (h) (i)

Figure 76: $m(\Lambda_c^+ K^-)$ projection of the amplitude fits to data with $\Xi_c^0(2970)$, $\Xi_c^0(3055)$, $\Xi_c^0(3080)$ states for different assignments of spin.
a) $J^P(\Xi_c^0(2970)) = \frac{1}{2}^-, J^P(\Xi_c^0(3055)) = \frac{1}{2}^-, J^P(\Xi_c^0(3080)) = \frac{1}{2}^-$.
b) $J^P(\Xi_c^0(2970)) = \frac{1}{2}^-, J^P(\Xi_c^0(3055)) = \frac{1}{2}^-, J^P(\Xi_c^0(3080)) = \frac{3}{2}^-$.
c) $J^P(\Xi_c^0(2970)) = \frac{1}{2}^-, J^P(\Xi_c^0(3055)) = \frac{3}{2}^-, J^P(\Xi_c^0(3080)) = \frac{1}{2}^-$.
d) $J^P(\Xi_c^0(2970)) = \frac{1}{2}^-, J^P(\Xi_c^0(3055)) = \frac{3}{2}^-, J^P(\Xi_c^0(3080)) = \frac{3}{2}^-$.
e) $J^P(\Xi_c^0(2970)) = \frac{3}{2}^-, J^P(\Xi_c^0(3055)) = \frac{1}{2}^-, J^P(\Xi_c^0(3080)) = \frac{1}{2}^-$.
f) $J^P(\Xi_c^0(2970)) = \frac{3}{2}^-, J^P(\Xi_c^0(3055)) = \frac{1}{2}^-, J^P(\Xi_c^0(3080)) = \frac{3}{2}^-$.
h) $J^P(\Xi_c^0(2970)) = \frac{3}{2}^-, J^P(\Xi_c^0(3055)) = \frac{3}{2}^-, J^P(\Xi_c^0(3080)) = \frac{1}{2}^-$.
g) $J^P(\Xi_c^0(2970)) = \frac{3}{2}^-, J^P(\Xi_c^0(3055)) = \frac{3}{2}^-, J^P(\Xi_c^0(3080)) = \frac{3}{2}^-$.

A.7 Line shape of the $D^*_{s0}(2317)$ state parametrised by a sub-threshold Breit-Wigner distribution

In the baseline amplitude model, the line shape of the $D^*_{s0}(2317)$ state is parametrised by a Flatté distribution. The projections of an amplitude fit where the Flatté line shape is replaced by a sub-threshold Breit-Wigner function are presented in Figure 77.

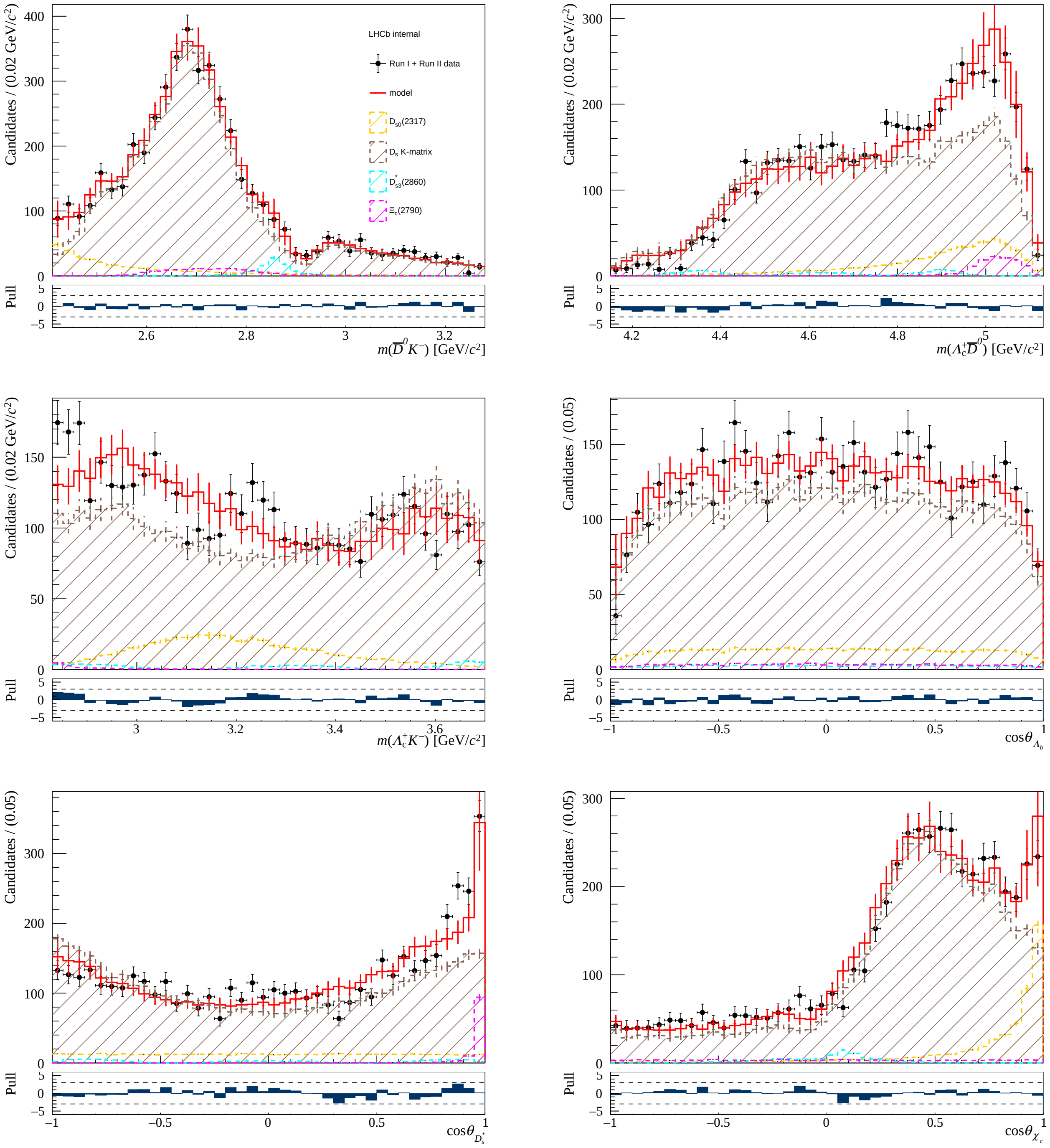

Figure 77: Projections of the amplitude fit parametrising the $D^*_{s0}(2317)$ state by a sub-threshold Breit-Wigner distribution.

References

[1] LHCb collaboration, R. Aaij *et al.*, *Observation of $J/\psi p$ resonances consistent with pentaquark states in $\Lambda_b^0 \to J/\psi K^- p$ decays*, Phys. Rev. Lett. **115** (2015), no. LHCB-PAPER-2015-029 `arXiv:1507.03414`.

[2] LHCb collaboration, R. Aaij *et al.*, *Observation of a narrow pentaquark state, $P_c(4312)^+$, and of two-peak structure of the $P_c(4450)^+$*, Phys. Rev. Lett. **122** (2019), no. LHCB-PAPER-2019-014, CERN-EP-2019-058 , `arXiv:1904.03947`.

[3] Belle Collaboration, S.-K. Choi *et al.*, *Observation of a Narrow Charmonium-like State in Exclusive $B^\pm \to K^\pm\pi^+\pi^- J/\psi$ Decays*, Phys. Rev. Lett. **91** (2003), no. BELLE-CONF-0352 262001, `arXiv:0308029`.

[4] Belle Collaboration, S.-K. Choi *et al.*, *Observation of a resonance-like structure in the $\pi^\pm\psi'$ mass distribution in exclusive $B \to K\pi^\pm\psi'$ decays*, Phys. Rev. Lett. **100** (2008), no. BELLE-CONF-0773 142001, `arXiv:0708.1790`.

[5] K. Peters, *A Primer on Partial Wave Analysis*, Int. J. Mod. Phys. A **21** (2006) , `arXiv:physics/0412069`.

[6] M. Stahl, *First observation of the decays $\Lambda_b^0 \to \Lambda_c^+ \overline{D}^{0(*)} K^-$*, PhD thesis, July, 2018, Presented 11 July 2018.

[7] *Tensorflow main webpage*, https://www.tensorflow.org/.

[8] LHCb collaboration, *LHCb Tracker Upgrade Technical Design Report*, CERN-LHCC-2014-001. LHCb-TDR-015.

[9] *Website of the GEANT simulation framework*, https://geant4.web.cern.ch/.

[10] A. Piucci, A. Mogini, S. Esen, and T. Nikodem, *A study on Scintillating Fiber tracker optimisation for the LHCb upgrade*, Tech. Rep. LHCb-PUB-2017-016, 2017.

[11] C. N. Yang and R. L. Mills, *Conservation of Isotopic Spin and Isotopic Gauge Invariance*, Phys. Rev. **96** (1954) 191.

[12] *Einstein notation of summation*, https://en.wikipedia.org/wiki/Einstein_notation.

[13] M. Gell-Mann, *Symmetries of baryons and mesons*, Phys. Rev **125** (1962) .

[14] Particle Data Group, M. Tanabashi *et al.*, *Review of Lattice Quantum Chromodynamics*, Phys. Rev. D **98** (2018) 030001.

[15] Particle Data Group, M. Tanabashi *et al.*, *Review of Quantum Chromodynamics*, Phys. Rev. D **98** (2018) 030001.

[16] A. Deur, S. J. Brodsky, and G. F. de Téramond, *The QCD running coupling*, Progress in Particle and Nuclear Physics **90** (2016) 1.

[17] Particle Data Group, C. Patrignani *et al.*, *2017 Review of Particle Physics*, Chin. Phys. **C40** (2017), no. 10 100001.

[18] W. A. Bardeen, A. J. Buras, D. W. Duke, and T. Muta, *Deep-inelastic scattering beyond the leading order in asymptotically free gauge theories*, Phys. Rev. D **18** (1978) 3998.

[19] *Quark model*, https://en.wikipedia.org/wiki/Quark_model.

[20] M. Fierz, *Über die relativistische Theorie kräftefreier Teilchen mit beliebigem Spin*, Helvetica Physica Acta **12** (1939) 3.

[21] W. Pauli, *The Connection Between Spin and Statistics*, Phys. Review **58** (1940) 716.

[22] Particle Data Group, M. Tanabashi *et al.*, *Review of Charmonium System*, Phys. Rev. D **98** (2018) 030001.

[23] Particle Data Group, M. Tanabashi *et al.*, *Review of Spectroscopy of Mesons Containing Two Heavy Quarks*, Phys. Rev. D **98** (2018) 030001.

[24] J. M. Richard, *Exotic hadrons: review and perspectives*, `arXiv:1606.08593`.

[25] D. Dlakonov, V. Petrov, and M. Polyakov, *Exotic Anti-Decuplet of Baryons: Prediction from Chiral Solitons*, Z. Phys. A **359** (1997) 305.

[26] M. Praszałowicz, *Successes and Problems of Chiral Soliton Approach to Exotic Baryons*, Acta Physica Polonica B **36** (2005), no. 5.

[27] LEPS Collaboration, T. Nakano *et al.*, *Evidence for Narrow $S = +1$ Baryon Resonance in Photo-production from Neutron*, Phys. Rev. Lett. **91** (2003) 012002, `arXiv:0301020`.

[28] LEPS Collaboration, Y. Ohashi *et al.*, *Exotic State Searches at the SPring-8: Observation of a Pentaquark State Θ^+ Baryopn*, `arXiv:0402005`.

[29] CLAS Collaboration, S. Stepanyan *et al.*, *Observation of an Exotic $S = +1$ Baryon in Exclusive Photoproduction from the Deuteron*, Phys. Rev. Lett. **91** (2003) 252001.

[30] DIANA Collaboration, V. V. Barmin *et al.*, *Observation of a baryon resonance with positive strangeness in K+ collisions with Xe nuclei*, Physics of Atomic Nuclei **66** (2003) 1715, `arXiv:0304040`.

[31] ELSA Collaboration, J. Barth *et al.*, *Evidence for the positive-strangeness pentaquark Θ^+ in photoproduction with the SAPHIR detector at ELSA*, Phys. Lett. B **572** (2003) 127.

[32] LHCb Collaboration, R. Aaij *et al.*, *Model-Independent Evidence for $J/\psi p$ Contributions to $\Lambda_b^0 \to J/\psi p K^-$ decays*, Phys. Rev. Lett. **117** (2016) .

[33] Y. Gao *et al.*, *Amplitude analysis of the $\Lambda_b^0 \to J/\psi p \pi^-$ decay and the $J/\psi p$ pentaquark candidates*, .

[34] A. Ali, I. Ahmed, M. J. Aslam, and A. Rehman, *Heavy quark symmetry and weak decays of the b baryons in pentaquarks with a $c\bar{c}$ component*, Phys. Rev. D **94** (2016) 054001.

[35] L. Maiani, A. D. Polosa, and V. Riquer, *The New Pentaquarks in the Diquark Model*, Phys. Lett. B **749** (2015) , `arXiv:1507.04980`.

[36] R. Zhu and C.-F. Qiao, *Pentaquark states in a diquark-triquark model*, Phys. Rev. B **756** (2015) , `arXiv:1510.08693`.

[37] V. Kubarovsky and M. B. Voloshin, *Formation of hidden-charm pentaquarks in photon-nucleon collisions*, Phys. Rev. D **92** (2015) 031502, `arXiv:1508.00888`.

[38] Guo, F. K. and Meißner, U. G. and Wang, W. and Yang, Z. , *How to reveal the exotic nature of the $P_c(4450)$*, Phys. Rev. D **92** (2015) .

[39] Y. H. Lin, C. W. Shen, F. K. Guo, and B. S. Zou, *Decay behaviors of the P_c hadronic molecules*, Phys. Rev. D. **95** (2017) 114017, `arXiv:1703.01045`.

[40] C. W. Shen, D. Ronchen, U.-G. Meißner, and B. S. Zou, *Exploratory study of possible resonances in the heavy meson - heavy baryon coupled-channel interactions*, Chin. Phys. C (2018) 023106.

[41] H. X. Chen *et al.*, *Towards Exotic Hidden-Charm Pentaquarks in QCD*, Phys. Rev. Lett. **115** (2015) 172001.

[42] J.-J. Wu, R. Molina, E. Oset, and B. S. Zou, *Prediction of Narrow N^* and Λ^* Resonances with Hidden Charm above 4 GeV*, Phys. Rev. Lett. **105** (2010) 232001, `arXiv:1007.0573`.

[43] J.-J. Wu, R. Molina, E. Oset, and B. S. Zou, *Dynamically generated N^* and Λ^* resonances in the hidden charm sector around 4.3 GeV*, Phys. Rev. C **84** (2011) 015202, `arXiv:1011.2399`.

[44] W. L. Wang, F. Huang, Z. Y. Zhang, and B. S. Zou, *$\Sigma_c\overline{D}$ and $\Lambda_c\overline{D}$ states in a chiral quark model*, Phys. Rev. C **84** (2011) .

[45] Z. Y. Zhang, P. Wang, Y. Y. Wen, and L.-R. Dai, *An Extended Chiral SU(3) Quark Model*, Communications in Theoretical Physics **39** (2003) .

[46] F. Huang, D. Zhang, and Y. W. Yu, *Coupled-channels study of ΛK and ΣK states in the chiral SU(3) quark model*, Phys. Rev. C **71** (2005) .

[47] F. Huang, W. L. Wang, Z. Y. Zhang, and Y. W. Yu, *Preliminary study of the $\overline{K}N$ interaction in a chiral constituent quark model*, Phys. Rev. C **76** (2007) .

[48] A. D. Jackson, D. O. Risk, and B. Verwest, *Meson exchange model for the nucleon-nucleon interaction*, Nuclear Physics A **249** (1975) 397.

[49] Z. C. Yang *et al.*, *The possible hidden-charm molecular baryons composed of anti-charmed meson and charmed baryon*, `arXiv:1105.2901arXiv:1105.2901`.

[50] J. J. Wu, T. S. H. Lee, and B. S. Zou, *Nucleon resonances with hidden charm in coupled-channel models*, Phys. Rev. C **85** (2012) .

[51] Lü, Q. F. and Dong, Y. B. , *Strong decay mode $J/\psi p$ of hidden charm pentaquark states $P_c(4380)^+$ and $P_c(4450)^+$ in $\Sigma_c D^{0*}$ molecular scenario*, Phys. Rev. D **93** (2016) , `arXiv:1603.00559`.

[52] C. W. Shen, G. F. G. J. J. Xle, and B. S. Zou, *Disentangling the hadronic molecule nature of the $P_c(4380)^+$ pentaquark-like structure*, Nucl. Phys. A (2016) , `arXiv:1603.04672`.

[53] D. Rönchen *et al.*, *Coupled-channel dynamics in the reactions $\pi N \to \eta N, K\Lambda, K\Sigma$*, Nucl. Phys. A (2012) , `arXiv:1211.6998`.

[54] T. M. Allev, K. Azizi, M. Savcl, and V. S. Zamiralov, *Analysis of heavy spin-3/2 baryon-heavy spin-1/2 baryon-light vector meson vertices in QCD*, Phys. Rev. D (2011) , `arXiv:1102.0416`.

[55] Z.-H. Guo and J. A. Oller, *Anatomy of the newly observed hidden-charm pentaquark states: $P_c(4312)$, $P_c(4440)$ and $P_c(4457)$*, Phys. Lett. B **793** (2019) 144, `arXiv:1904.00851`.

[56] X.-Z. Weng, X.-L. Chen, W.-Z. Deng, and Z. S.-L. *Hidden-charm pentaquarks and P_c states*, `arXiv:1904.09891`.

[57] B. Silvestre-Brac, *Systematics of $Q^2(\overline{q}^2)$ systems with a chromomagnetic interaction*, Phys. Rev. D **46** (1992) 2179.

[58] M. I. Eldes, V. Y. Petrov, and M. V. Polyakov, *New LHCb pentaquarks as hadrocharmonium states*, `arXiv:1904.11616`.

[59] C. W. Xiao, J. Nieves, and E. Oset, *Heavy quark spin symmetric molecular states from* $\overline{D}^{(*)}\Sigma_c^{(*)}$ *and other coupled channels in the light of the recent LHCb pentaquarks*, `arXiv:1904.01296`.

[60] A. A. J. Alves and L. Collaboration, *The LHCb Detector at the LHC*, Journal of Instrumentation **3** (2008), no. 08 S08005.

[61] C. Parkes, T. Ruf, and T. Szumlak, *Reconstruction of Cluster Positions in the LHCb Velo*, Tech. Rep. LHCb-2007-151, CERN-LHCb-2007-151, 2007.

[62] B. Storaci, *Optimization of the LHCb track reconstruction*, Journal of Physics: Conference Series **664** (2015), no. 7 072047.

[63] S. Benson, V. Gligorov, M. A. Vesterinen, and J. M. Williams, *The LHCb Turbo Stream*, J. of Physics **664**.

[64] R. Aaij *et al.*, *A comprehensive real-time analysis model at the LHCb experiment*, Journal of Instrumentation **14** (2019) .

[65] R. E. Kalman, *A new approach to linear filtering and prediction problems*, J. Basic Eng. **82** (1960) 35.

[66] J. Brehmer, J. Albrecht, and P. Seyfert, *Ghost probability: an efficient tool to remove background tracks*, Tech. Rep. LHCb-INT-2012-025. CERN-LHCb-INT-2012-025, CERN, Geneva, Sep, 2012.

[67] M. De Cian, S. Farry, P. Seyfert, and S. Stahl, *Fast neural-net based fake track rejection in the LHCb reconstruction*, Tech. Rep. LHCb-PUB-2017-011, 2017.

[68] M. Kucharczyk, P. Morawski, and M. Witek, *Primary Vertex Reconstruction at LHCb*, Tech. Rep. LHCb-PUB-2014-044, CERN-LHCb-PUB-2014-044, 2014.

[69] F. R. Hamper, E. M. Ronchetti, P. J. Rousseeuw, and W. A. Stahel in *RobustStatistics, The Approach Based on the Inuence Function* (J. Wiley and Sons, eds.). 1986.

[70] LHCb RICH Group, M. Adinolfi *et al.*, *Performance of the LHCb RICH detector at the LHC*, Eur. Phys. J. **C73** (2013), no. CERN-LHCB-DP-2012-003, LHCB-DP-2012-003 2431, `arXiv:1211.6759`.

[71] L. Anderlini, S. Benson, and L. Gligorov, *Computing strategy for PIDcalibration samples for LHCb Run 2*, Tech. Rep. LHCb-PUB-2016-020, 2016.

[72] D. M. Brundnoy, *Isobar Model for Resonance Scattering*, Phys. Rev. **145** (1966) 1229.

[73] W. Jacob and G. C. Wick, *On the General Theory of Collisions for Particles with Spin*, Annals of Physics **7** (1959) 404.

[74] O. Behnke, K. Kröninger, G. Schott, and T. Schörner-Sadenius in *Data Analysis in High Energy Physics* (Wiley-Vch, ed.). 2015.

[75] H. Cramer, *Mathematical Methods of Statistics*, 1999.

[76] R. C. Radhakrishna, *Information and the accuracy attainable in the estimation of statistical parameters*, Bull. Calcutta Math. Soc. **37** (1945).

[77] J. Aldrich, *R. A. Fisher and the Making of Maximum likelihood*, Statistical Science **12** (1997), no. 3 496.

[78] R. Barlow, *Extended maximum likelihood*, NIMPR **297** (1990) 496.

[79] M. Pivk and F. R. L. Diberder, *Plots: A statistical tool to unfold data distributions*, Nuclear Instruments and Methods in Physics Research Section A: Accelerators, Spectrometers, Detectors and Associated Equipment **555** (2005), no. 1 356.

[80] J. Neyman and E. Pearson, *On the problem of the most efficient tests of statistical hypotheses*, Phil. Trans. of the Royal Society A **231** (1933) 289.

[81] R. A. Fisher in *Statistical Methods for Research Workers* (Oliver and Boyd, eds.). 1925.

[82] J. Neyman, *Outline of the theory of statistical estimation based on the classical theory of probability*, Phil. Trans. of the Royal Society A **236** (1937) 333.

[83] G. Cowan, K. Cranmer, E. Gross, and O. Vitells, *Asymptotic formulae for likelihood-based tests of new physics*, Eur. Phys. J. C **71** (2011) , `1007.1727`.

[84] S. S. Wilks, *The Large-Sample Distribution of the Likelihood Ratio for Testing Composite Hypotheses*, Ann. Math. Statis. **9** (1938), no. 1 60.

[85] G. J. Feldman and R. D. Cousins, *A unified approach to the classical statistical analysis of small signals*, Phys. Rev. D **57** (1999) 3873, `arXiv:physics/9711021`.

[86] C. Gini in *Variabilità e mutabilità: contributo allo studio delle distribuzioni e delle relazioni statistiche* (T. di P.C̃uppini, ed.). 1912.

[87] J. H. Friedman, *Greedy Function Approximation: A Gradient Boosting Machine*, Ann. Stat. **29** (2001) 1189.

[88] L. Breiman, *Bagging Predictors*, Tech. Rep. 421, Department of Statistics, University of California, 1994.

[89] L. Anderlini, A. Contu *et al.*, *The PIDCalib package*, Tech. Rep. LHCb-PUB-2016-021, 2016.

[90] M. Williams, *Generic D from B Selections*, Tech. Rep. CERN-LHCb-INT-2012-002, 2012.

[91] M. Stahl *et al.*, *Identification of non-prompt charm hadrons*, Tech. Rep. LHCb-INT-2018-033, CERN-LHCb-INT-2018-033, 2018.

[92] *Google Brain Project main webpage*, https://ai.google/research/teams/brain.

[93] *TensorflowAnalysis GitLab repository*, https://gitlab.cern.ch/poluekt/TensorFlowAnalysis.

[94] *GitLab repository of the TOAST amplitude fitter*, https://gitlab.cern.ch/apiucci/toast.

[95] *Website of the PyROOT extension to ROOT*, https://root.cern.ch/pyroot.

[96] *Website of the Minuit minimisation package*, https://seal.web.cern.ch/seal/snapshot/work-packages/mathlibs/minuit/.

[97] *Website of the ROOT implementation of Minuit*, https://root.cern.ch/doc/master/classTMinuit.html.

[98] *Website of the CERN* lxplus *service*, http://information-technology.web.cern.ch/services/lxplus-service.

[99] *Website of the CERN batch service*, http://information-technology.web.cern.ch/services/batch.

[100] *Description of the Git submodules*, https://git-scm.com/book/it/v2/Git-Tools-Submodules.

[101] *Reference of the GNU Lesser General Public License*, https://www.gnu.org/licenses/lgpl-3.0.en.html.

[102] C. Xiaoli *et al.*, *Open is not enough*, Nature Physics **15** (2019) 113.

[103] *GitLab repository of the current analysis*, https://gitlab.cern.ch/lhcb-bandq-exotics/Lb2LcD0K-Amplitude.

[104] *GitLab website*, https://about.gitlab.com/.

[105] *Website of the CERN Virtual Machines service*, http://cernvm.cern.ch/.

[106] *Website of the CERN OpenStack service*, https://cernvm.cern.ch/portal/openstack.

[107] *Snakemake website*, https://snakemake.readthedocs.io/en/stable/.

[108] *Docker website*, https://www.docker.com.

[109] *EOS website*, http://information-technology.web.cern.ch/services/eos-service.

[110] V. Gligorov, C. Thomas, and M. Williams, *The HLT inclusive B triggers*, Tech. Rep. LHCb-PUB-2011-016, 2011.

[111] M. Williams *et al.*, *The HLT2 Topological Lines*, Tech. Rep. LHCb-PUB-2011-002, CERN-LHCb-PUB-2011-002, 2011.

[112] M. Needham, *Clone Track Identification using the Kullback-Liebler Distance*, Tech. Rep. LHCb-2008-002. CERN-LHCb-2008-002. LPHE-2008-002, CERN, Geneva, Jan, 2008.

[113] LHCb Collaboration, R. Aaij *et al.*, *Measurement of the $B^{\pm}$ production asymmetry and the CP asymmetry in $B^{\pm} \to J/\psi K^{\pm}$ decays*, Phys. Rev. D **95** (2017) 052005.

[114] L. C. Andrews in *Special functions of mathematics for engineers* (S. Press, ed.). 1997. doi: 10.1117/3.270709.

[115] *Unbinned PID resampling using kernel density estimation*, https://twiki.cern.ch/twiki/bin/view/LHCb/MeerkatPIDResampling.

[116] M. A. Morrison and G. A. Parker, *A Guide to Rotations Quantum Mechanics*, Aus. J. Physics **40** 465.

[117] J. M. Blatt and V. F. Weisskopf in *Theoretical Nuclear Physics* (Springer, ed.). 1979.

[118] S. M. Flatté, *Coupled - Channel Analysis of the pi eta and K anti-K Systems Near K anti-K Threshold*, Phys. Lett. B **63** (1976) 224.

[119] Particle Data Group, M. Tanabashi *et al.*, *Review of Resonances*, Phys. Rev. D **98** (2018) 030001.

[120] R. G. Newton, *Optical theorem and beyond*, American Journal of Physics **44** (1976) 639.

[121] M. R. Pennington, T. Mori, S. Uehara, and Y. Watanabe, *Amplitude analysis of high statistics results on $\gamma\gamma \to \pi^+\pi^-$ and the two photon width of isoscalar states*, Eur. Phys. J. C **56** (2008) .

[122] J. A. Oller and E. Oset, *N/D description of two meson amplitudes and chiral symmetry*, Phys. Rev. D **60** (1999) .

[123] N. N. Achasov and A. A. Kozhevnikov, *Electromagnetic form factor of the pion in the field-theory-inspired approach*, Phys. Rev. D **83** (2011) .

[124] A. V. Anisovich, V. A. Nikonov *et al.*, *Analysis of the meson-meson data in the framework of the dispersion D-matrix method*, Phys. Rev. D **84** (2011) .

[125] LHCb collaboration, R. Aaij *et al.*, *Measurements of the* $\Lambda_b^0 \to J/\psi\Lambda$ *decay amplitudes and the* Λ_b^0 *polarisation in pp collisions at* $\sqrt{s} = 7$ *TeV*, Phys. Lett. **B724** (2013) 27, `arXiv:1302.5578`.

[126] LHCb collaboration, R. Aaij *et al.*, *Measurements of the* $\mathit{\Lambda}_b^0 \to J/\psi \mathit{\Lambda}$ *decay amplitudes and the* $\mathit{\Lambda}_b^0$ *polarisation in pp collisions at* $\sqrt{s} = 7$ *TeV*, Physics Letters B **724** (2012) 27, `arXiv:1302.5578`.

[127] F. Hu and J. Zidek, *The Weighted Likelihood*, The Canadian Journal of Statistics **30** (2002) 347.

[128] X. Wang and J. Zidek, *Selecting likelihood weights by cross-validation*, Annals of Statistics **33** (2005) 463, `arXiv:math/0505599`.

[129] *GitLab repository of the 2DAdaptiveBinning libraries*, https://gitlab.cern.ch/mstahl/2DAdaptiveBinning.

[130] *Website of the ROOT implementation of the kernel algorithm for smoothing 2-dimensional histograms*, https://root.cern.ch/doc/master/TH2_8cxx_source.html#l02530.

[131] S.-C. L. *et al.*, *Strong decays of* $D_J(3000)$ *and* $D_{sJ}(3040)$, Phys. Rev. D **97** (2018) .

[132] G. Feng-Kun and M. Ulf-G. *More kaonic bound states and a comprehensive interpretation of the* D_{sJ} *states*, Phys. Rev. D **84** (2011) .

[133] J.-B. Cheng and Y.-R. Liu, $P_c(4457)^+$*,*$P_c(4440)^+$*, and* $P_c(4312)^+$*: molecules or compact pentaquarks?*, `arXiv:1905.08605`.